Ordering and dynamics of strongly correlated transition metal oxides

Thomas Ronald Caverley Forrest

A Thesis presented for the degree of
Doctor of Philosophy

For my parents: Elizabeth Whitelegg and David Forrest.

I, Thomas Ronald Caverley Forrest, confirm that the work presented in this thesis is my own. Wherever information has been derived from other sources, this has been indicated in the thesis.

Abstract

This thesis describes a series of synchrotron based X-ray experiments on the lattice dynamics or magnetic ordering of several strongly correlated electron systems. Firstly, it will provide an introduction to the strongly correlated electron materials that were studied. After which a description of the experimental techniques used, specifically resonant X-ray scattering (RXS) and X-ray inelastic scattering (IXS), will be given. Finally the results of these experiments will be set out and evaluated. The experiments were as follows:

X-ray inelastic scattering measurements on the effects of fluorine doping on the lattice dynamics of the newly discovered iron pnictide superconducting compound, $SmFeAsO_{0.6}F_{0.35}$ and its antiferromagnetic parent compound, SmFeAsO. The results from these experiments demonstrate the importance of antiferromagnetic fluctuations in understanding the lattice dynamics of this class of crystals. This result has been demonstrated for the '122' class of pnictide crystals, but until now has not been shown for the '1111' class of pnictides.

Resonant X-ray scattering in the vicinity of the Mn L_2 and L_3 resonant enhancements was used to reassess the magnetic structure of multiferroic $TbMnO_3$. The results indicate that the commonly accepted magnetic structure is modified, with additional a and c axis magnetic components. Therefore the ferroelectric polarisation in $TbMnO_3$ arises from a phase transition between two non-collinear magnetic structures. It was previously believed that this phase transition was between a collinear and a non-collinear magnetic structure.

Resonant X-ray scattering measurements were also taken on $TbMnO_3$'s sister compound, $DyMnO_3$. Data was recorded at the Mn K and Dy L_3 resonant enhancements. Several unidentified incommensurate reflections, independent of this compound's magnetic phases, were detected with photon energies close to the Mn K edge. What these reflections represent is still a mystery, although they do make a compelling case for further experimental work.

Acknowledgements

During the course of my Ph.D. studies I have been helped by a number of people at UCL and the various research facilities where my experiments were conducted. Unfortunately I do not have enough space to include everybody's name here. There are however a number of people who have significantly contributed to my understanding of X-ray scattering and condensed matter physics. The first and most important person was my supervisor, Desmond McMorrow. Without his guidance and patience I doubt that I would have been able to complete my studies, so thank-you Des! I would also like to thank my secondary supervisor Gerrit van der Laan, especially for his contributions in interpreting the $TbMnO_3$ results. Another person who has my gratitude is Helen Walker, who was instrumental in helping me to understand resonant X-ray scattering. I would also like to thank the various members of the experimental collaborations which I was lucky enough to be a part of. For the work on $SmFeAsO_{1-x}F_y$ these people were Mathieu Le Tacon, Christian Rüegg, John Hill, Andrew Walters, Michael Krisch, Alexi Bossak and all the other members of ID28. For the resonant X-ray scattering work on $TbMnO_3$ I would like to thank my collaborators at Durham University, Peter Hatton, Tom Beale and Stewart Bland. Also Stuart Wilkins for his advice and insight that was extremely useful. Danny Mannix also deserves my gratitude. In addition I must thank the beamline staff at ID08, 5U.1 and XM11A, especially Urs Staub. For the work conducted on $DyMnO_3$, I am indebted to the staff at ID20 and I16, especially Federica Fabrizi. Also a special mention has to go to the crystal growers, without whom I would not have been able to perform the experiments described in this thesis. These include Prabhakaran and Andrew Boothroyd at Oxford University, who provided the $TbMnO_3$ crystals. Karpinski's group at ETH for the $SmFeAsO_{1-x}F_y$ crystals. Tokura's group at the University of Tokyo for the $DyMnO_3$ crystals. In addition to those who helped me with the experimental work, I would also like to thank Bob Aldus, Stuart Calder and Duc Lee for their friendship and advice; good luck for the future guys! Finally a huge thank you must go to my parents, Conway Moore and all my friends in Milton Keynes for their support over the last three and a half years.

Contents

List of Figures

List of Tables

Chapter 1

Introduction

Strongly correlated electron systems encompass a broad group of materials which exhibit unusual electrical and/or magnetic properties. The term 'strongly correlated' refers to the fact that these unusual properties, arise from interactions between a multiple number of electrons. Therefore, such systems cannot be adequately described by simple one-electron models, such as the Hartree-Fock or local density approximations. Often, these multiple electron interactions manifest themselves in interesting and useful macroscopic properties. Examples include, high temperature superconductivity, combined magnetic, ferroelectric and/or ferroelastic order (multiferroic), gigantic and colossal magnetoresistance effects. Throughout the course of my Ph.D. studies, I have used high intensity synchrotron X-ray sources to investigate the atomic properties of two classes of strongly correlated electron systems.

The first such system are the iron pnictide, high temperature superconductors. This recently discovered class of materials, display superconductivity at relatively high temperatures. Superconductivity is observed upon doping with fluorine ions [1] or, in some cases, the application of hydrostatic pressure [2, 3]. The appearance of high temperature superconductivity in these materials has generated a great deal of excitement amongst the strongly correlated electron community. It is believed that the iron pnictides may offer an important insight into the superconducting mechanism of other classes of high tempera-

ture superconductors, such as the cuprates [4]. Theoretical calculations [5] has shown that standard Bardeen, Cooper and Schrieffer (BCS) electron-phonon coupling, is unlikely to be responsible for the iron pnictide's high superconducting temperatures. Experimental studies however, indicate that the lattice, and therefore its dynamics, still plays an important role in the superconductivity of these materials [6]. To this end, I have performed a series of inelastic X-ray scattering (IXS) experiments, to investigate the effects of fluorine doping on the lattice dynamics of single crystal samples of the iron pnictides: SmFeAsO and $SmFeAsO_{0.60}F_{0.35}$. These experiments are summarised in chapter 3. The theoretical background of IXS is given in the second half of chapter 2. Currently, single crystal samples of this class of iron pnictide are only available in extremely small sizes (μm^3). Therefore, neutron inelastic scattering is precluded. X-rays on the other hand, make an ideal probe of the lattice dynamics, and IXS has a proven track record in investigating samples of a similar size [7, 8].

These IXS studies have been published in *Physical Review B* as a rapid communication and editor's suggestion [9]. Results show an interesting renormalisation of certain optical phonon modes, these modes are believed to be coupled to the magnetic iron sublattice. An additional optical mode, which is not connected to the magnetic sublattice, shows no doping induced renormalisation effects. It is speculated that the observed spin-lattice coupling, could strongly enhance the electron-phonon coupling in these materials.

The second class of strongly correlated electron materials to be studied, were the manganite magnetoelectric multiferroics: $ReMnO_3$ (Re is Tb or Dy). Upon a low temperature magnetic phase transition, these materials become ferroelectric [10, 11]. In addition, upon the application of a relatively weak magnetic field, the direction of the electrical polarisation may be rotated by 90°. This strong cross coupling between the magnetic and electrical order, is believed to be caused by the formation of an cycloidal antiferromagnetic structure, on the manganese sublattice. This new magnetic structure breaks inversion symmetry, with the ferroelectric polarisation being caused by the inverse Dzyaloshinskii-Moriya interaction between the manganese spins. The theory of how a cycloidal magnetic structure induces the ferroelectric polarisation has been established for some time (2005). However, it is important to note that the original determination of the cycloidal magnetic

structure, was based upon representation analysis of the neutron diffraction pattern of $TbMnO_3$ [12]. This neutron work only studied two types of incommensurate antiferromagnetic reflections, (A and G type). However, other neutron diffraction measurements of $TbMnO_3$, show that all four types of antiferromagnetic reflections are present in this material (A,C,F and G type) [13]. The third chapter of this thesis, describes a series of experiments which measured the F and C type antiferromagnetic reflections of $TbMnO_3$, through the technique of resonant X-ray scattering. The theoretical background of this technique is described in the first half of chapter 2. Specifically, measurements were taken at the Mn L_2 & L_3 and Tb M_4 & M_5 resonant enhancements, using soft X-rays. The advantage of performing resonant X-ray scattering measurements at these resonant energies, is that, information on the localised Mn $3d$ and Tb $4f$ electronic states, is provided. Experimental results showed, in a model independent way, that the F and C type reflections correspond to additional components of the manganese magnetic structure. These additional magnetic components, modify the previously determined magnetic structures above and below the ferroelectric phase transition. These experiments have yielded two journal articles, which have been published in *The Journal of Physics: Condensed Matter* as a Fast Track Communication [14] and *Physical Review Letters* [15].

The penultimate chapter (chapter number 5) will focus on resonant and non-resonant X-ray scattering experiments from $TbMnO_3$'s sister compound: $DyMnO_3$. Like $TbMnO_3$, the ferroelectric polarisation is believed to arise from a transition to a manganese cycloidal magnetic structure that breaks inversion symmetry. However, because of dysprosium's high elastic neutron absorption cross-section, the number of neutron diffraction experiments have been limited [16]. It is possible to perform neutron experiments on isotropically enriched $DyMnO_3$, however this means a significant increase in the price of crystal samples. In addition, recent experimental results have suggested that the dysprosium magnetic moments may also form a cycloidal magnetic structure in $DyMnO_3$'s ferroelectric phase [17]. Resonant X-ray scattering would therefore seem to be an ideal tool to study this compound. This is because X-rays do not suffer from the same absorption problem as neutrons. Also, by tuning the X-ray's energies to a specific resonant edge of the sample, it is possible to separate the magnetic ordering of $DyMnO_3$'s magnetic ions

(i.e. Mn and Dy). Unlike the resonant X-ray scattering studies of $TbMnO_3$, which are described in chapter 4, the experiments on $DyMnO_3$ were performed with much higher energy X-rays. Specifically, in the vicinity of the Mn K and Dy L_3 absorption edges. Therefore, the volume of reciprocal space that one may probe, is greatly increased. This allows for measurements on all four types of antiferromagnetic reflections that may be present (A,C,F and G type). However, the electric-dipole selection rules means that, one is primarily probing the Mn $4f$ and Dy $5d$ delocalised electronic states.

Results from these studies were something of a mixed bag. Specifically, data taken at the Dy L_3 resonant enhancement showed a number of strange peaks which could not be classified. Data taken at the Mn K resonant enhancement, did however, confirm a b-c cycloidal magnetic structure of the manganese sublattice. This is the first time that such a cycloidal structure has been confirmed, with microscopic measurements in $DyMnO_3$. Even so, other data taken at the Mn K resonant enhancement identified a number of interesting incommensurate reflections. These reflections seem to be independent of the compound's magnetic phases. What these results represent is still a mystery, although they do make a compelling case for further experimental work.

The final chapter of this thesis will give an overall conclusion of the experimental studies. Suggestions of possible future experimental work which would help to advance our understanding of these intriguing systems, will also be given here.

Chapter 2

Theory of X-ray scattering

2.1 X-rays, a probe of atomic structures and dynamics

X-rays are an ideal probe for studying the properties of condensed matter systems. This is because an X-ray's wavelength is comparable to the interatomic distances of both liquids and solids. Thus, scattering of X-rays from condensed matter systems produces an interference effect which contains detailed information on the material's structure or dynamics. This concept was first experimentally demonstrated in 1912 by two separate groups. Firstly, by a group lead by M. von Laue, who measured a diffraction pattern from $CuSO_4$ crystals, and secondly, by W.L. Bragg and W.H. Bragg, in their pioneering research on the structure of sodium chloride (NaCl). For this work, von Laue was awarded the Nobel prize for physics in 1914, while the Braggs were awarded the same prize a year later. Subsequently, X-rays have been used to determine the structure of a wide range of organic and inorganic materials. Specific examples include, benzene, DNA, complex ionic crystals such as MgSn and the allotropes of carbon i.e. graphite and diamond.

Today, the extremely high flux and tunable energy which are available at synchrotron X-ray sources, have led to a vast increase in the number of X-ray techniques that can be used to study condensed matter systems. For further information on synchrotron radiation, readers should refer to the second chapter of *Elements of modern X-ray physics*

by Als-Nielsen and McMorrow [18].

The rest of this chapter will be split into three sections. The first section provides a theoretical introduction to the X-ray photon-electron interaction. The other two sections describe specific examples of such interactions. Firstly, the elastic interaction between an X-ray photon and a sample's magnetic dipole, which gives rise to X-ray magnetic scattering and X-ray resonant exchange scattering. Secondly, the interaction between a photon and phonon lattice dynamics, resulting in inelastic X-ray scattering.

2.2 X-ray scattering: a theoretical introduction

The process of a single photon scattering from a sample, can be described with the following Quantum Mechanical (QM) notation. An incident photon (momentum $\mathbf{q} = \hbar\mathbf{k}$ & polarisation ϵ) is scattered from its initial state: $|\hbar\mathbf{k_i}, \epsilon_i\rangle$, undergoing a transition, to its final state: $|\hbar\mathbf{k_f}, \epsilon_f\rangle$. Meanwhile, the sample can also undergo a change in QM states, due the scattering process. Starting with: $|a\rangle$ and changing to: $|b\rangle$. Thus the entire photon-sample system can be written as: $|i\rangle$=$|a, \hbar\mathbf{k_i}, \epsilon_i\rangle$ for the initial state and $|f\rangle$=$|b, \hbar\mathbf{k_f}, \epsilon_f\rangle$ for the final state, after the photon is scattered.

The partial differential cross-section for this scattering process, where the scattered photons have an energy range of E to $E + dE$, and are scattered into a solid angle $d\Omega$, is:

$$\frac{d^2\sigma}{d\Omega dE} = \frac{W\rho(E_f)}{I_0} \tag{2.1}$$

Here I_0(=c/V) gives the incident flux, $\rho(E_f)$ is the density of the states of $|f\rangle$. Finally, W gives a probability that the electron-photon system will undergo a transition from the initial state $|i\rangle$ to the final state $|f\rangle$. This transition probability (W) can be calculated using Fermi's Golden Rule. For the present purpose W is taken to the 2nd order:

$$W = \frac{2\pi}{\hbar}\left|\langle f|\,\mathcal{H}'\,|i\rangle + \sum_{n,i}\frac{\langle f|\,\mathcal{H}'\,|n\rangle\,\langle n|\,\mathcal{H}'\,|i\rangle}{E_i - E_f}\right|^2 \delta(E_i - E_f) \tag{2.2}$$

Here $|n\rangle$ is a possible intermediate state that the system may occupy between states $|i\rangle$ and $|f\rangle$. Also, $E_i = E_a + \hbar\omega_{ki}$ and $E_f = E_b + \hbar\omega_{kf}$.

The Hamiltonian ($\mathcal{H}'$) in equation 2.2 describes the interactions between the system's electrons and the electromagnetic field of the X-ray photons. $\mathcal{H}'$ may be calculated from the Hamiltonian for electrons in a quantised electromagnetic field ($\mathcal{H}$), which contains three general terms:

1. $\mathcal{H}_e$: The Hamiltonian of the electrons, without electron-photon interactions.
2. $\mathcal{H}_\gamma$: The Hamiltonian of the photons, without electron-photon interactions.
3. $\mathcal{H}'$: The Hamiltonian of the electron-photon interaction, this will be relativity small and can be treated as a perturbation.

Mathematically, this total Hamiltonian can be written as [19]:

$$\begin{aligned}\mathcal{H} = \quad & \textstyle\sum_j \frac{1}{2m}\left(\mathbf{P}_j - \frac{e}{c}\mathbf{A}(\mathbf{r}_j)\right)^2 + \sum_{ij} V(\mathbf{R}_{ij}) \\ & -\tfrac{e\hbar}{2mc}\textstyle\sum_j \mathbf{s_j}\cdot\nabla\times\mathbf{A}(\mathbf{r}_j) \\ & -\tfrac{e\hbar}{2(mc)^2}\textstyle\sum_j \mathbf{s}_j\cdot\mathbf{E}(\mathbf{r}_j)\times\left(\mathbf{P}_j - \frac{e}{c}\mathbf{A}(\mathbf{r}_j)\right) + \sum_{\mathbf{q}\epsilon}\hbar\omega_k(c^\dagger_{\mathbf{q}\epsilon}c_{\mathbf{q}\epsilon} + \tfrac{1}{2})\end{aligned} \tag{2.3}$$

$\mathbf{A}(\mathbf{r_j})$ is the vector potential of a photon's electromagnetic field and $\mathbf{E}(\mathbf{r_j})$ is the electric field of the photons. ($\mathbf{P_j}$-$\frac{e}{c}\mathbf{A}(\mathbf{r_j})$) is the electron's canonical momentum when it is in the presence of the photon's electromagnetic field. Finally, $c_{\mathbf{q}\epsilon}$ and $c^\dagger_{\mathbf{q}\epsilon}$ are respectively, the photon (momentum $\mathbf{q}$, polarisation ϵ) creation and annihilation operators.

The separate terms in this Hamiltonian (equation 2.3) represent the following. The first term gives the kinetic energy of an electron at position $\mathbf{r_j}$. The second term is the potential energy of the electron in the electromagnetic field that is created by the other electrons. Specifically, $\mathbf{V}(\mathbf{R_{ij}})$ is the potential for an electron-electron interaction. Since Maxwell's definition of the magnetic vector potential is $\nabla\times\mathbf{A} = \mu\mathbf{H} = \mathbf{B}$. The third term in equation 2.3 gives the Zeeman interaction, between the electron spin and the magnetic field of the

photons, $\mathbf{s_j} \cdot \mathbf{B}$. The fourth term describes the spin-orbit interaction, i.e. the coupling between the electron's magnetic moment and the magnetic field that it feels due to its motion. Finally, the fifth term in equation 2.3 represents the energy of the electromagnetic field itself, with the 1/2 representing zero point energy.

The X-ray photon's electric field $\mathbf{E}(\mathbf{r_j})$, may be written in terms of the Coulomb potential ϕ, and the differential of the vector potential: $\dot{\mathbf{A}}(\mathbf{r_j})$.

$$\mathbf{E}(\mathbf{r_j}) = -\nabla\phi - \frac{1}{c}\dot{\mathbf{A}}(\mathbf{r_j}) \tag{2.4}$$

By using this relationship and expanding the kinetic energy term given in equation 2.3, one can express the Hamiltonian $\mathcal{H}$ in terms of the three general Hamiltonians: $\mathcal{H}_e$, $\mathcal{H}_\gamma$, $\mathcal{H}'$. For this thesis however, only the the interaction Hamiltonian $\mathcal{H}'$, will be described. A full derivation of all three Hamiltonians is given in Blume [19]. This interaction Hamiltonian may be separated into several different terms which correspond to: 1) The photon's electromagnetic field interaction with an electron's charge, which leads to Thomson charge scattering ($\mathcal{H}'_1$ & $\mathcal{H}'_2$). 2) The Zeeman interaction ($\mathcal{H}'_3$). 3) The spin-orbit coupling of the sample's electrons ($\mathcal{H}'_4$).

$$\begin{aligned}\mathcal{H}' = \; & \underbrace{\frac{e^2}{2mc^2}\sum_j \mathbf{A}^2(r_j)}_{\mathcal{H}'_1} \underbrace{- \frac{e}{mc}\sum_j \mathbf{A}(r_j)\cdot\mathbf{P}_j}_{\mathcal{H}'_2} \\ & \underbrace{- \frac{e\hbar}{mc}\sum_j \mathbf{s}_j \cdot [\nabla \times \mathbf{A}(r_j)]}_{\mathcal{H}'_3} \underbrace{- \frac{e\hbar}{2(mc)^2}\frac{e^2}{c^2}\sum_j \mathbf{s}_j \cdot [\dot{\mathbf{A}}(r_j) \times \mathbf{A}(r_j)]}_{\mathcal{H}'_4}\end{aligned} \tag{2.5}$$

Furthermore, the vector potential of a photon's electromagnetic field, may be expressed in terms of the photon creation (c) and annihilation ($c^\dagger$) operators. In the volume V, $\mathbf{A}(\mathbf{r_j})$ is:

$$\mathbf{A}(\mathbf{r}) = \sum_{q,\sigma}\left(\frac{2\pi\hbar c^2}{V\omega_q}\right)^{1/2}[\epsilon(\mathbf{q}\sigma)c(\mathbf{q}\sigma)e^{i\mathbf{q}\cdot\mathbf{r}} + \epsilon^*(\mathbf{q}\sigma)c^\dagger(\mathbf{q}\sigma)e^{-i\mathbf{q}\cdot\mathbf{r}}] \tag{2.6}$$

Here the polarisation vector of a photon, with momentum $\mathbf{q}$ and polarisation state σ, is: $\epsilon(\mathbf{q}\sigma)$.

The vector potential, $\mathbf{A}(\mathbf{r_j})$, shown in equation 2.6 is linear in both the photon creation and annihilation operators. Therefore, terms which are linear in $\mathbf{A}(\mathbf{r_j})$ ($\mathcal{H}'_2$ & $\mathcal{H}'_3$), will change the number of photons in the system. Thus, these terms can only contribute to the 2^{nd} order section of equation 2.2, where they appear twice. Terms which are quadratic in $\mathbf{A}(\mathbf{r_j})$ ($\mathcal{H}'_1$ & $\mathcal{H}'_4$), conserve the overall number of photons, and contribute to the 1^{st} order terms of equation 2.2.

$$W = \frac{2\pi}{\hbar}\left|\langle f|\left(\mathcal{H}'_1+\mathcal{H}'_4\right)|i\rangle + \sum_{n,i}\frac{\langle f|\left(\mathcal{H}'_2+\mathcal{H}'_3\right)|n\rangle\langle n|\left(\mathcal{H}'_2+\mathcal{H}'_3\right)|i\rangle}{E_i-E_f}\right|^2\delta(E_i-E_f) \quad (2.7)$$

This transition probability, can be used to derive the scattering cross-section for many different X-ray scattering processes. However, for the remainder of this chapter, I will restrict myself to specific examples. The first example is for X-ray magnetic scattering (XRMS) and X-ray resonant exchange scattering (XRES). This will make use of all the Hamiltonian terms described in equation 2.7. The second example will focus on deriving the dynamical structure factor, which is used to describe phonon lattice dynamics. This is observed through the technique of inelastic X-ray scattering (IXS).

2.3 X-ray magnetic scattering

Traditionally neutrons have been used to study magnetic structures. However, the routine investigation of magnetic, charge and other forms of multipolar ordering is now possible with X-rays. This section will describe the historical background of X-ray scatting studies of long range magnetic order. It will also show how the transition probability, given in equation 2.7, can be used to determine the cross-section of scattering of both the spin ($\mathbf{S}$) and orbital ($\mathbf{L}$) components of a magnetic structure. Also, a discussion of the resonant

X-ray scattering (RXS) cross-section and selection rules will be given. In addition to studying magnetic order, RXS is capable of providing information on many other different forms of long range order. Finally, a description of the ID20 X-ray magnetic scattering beamline, and the different types of measurement performed during a resonant X-ray scattering experiment, will be provided.

It was not until the theoretical work of Platzman and Tzoar in 1970 [20], that magnetic scattering of X-ray photons was considered to be practical. Neutrons however, were first used to study magnetic order by Shull and collaborators in the late 1940s [21]. Earlier theoretical work [22, 23] had included magnetic terms in the cross-section of a photon scattering from a free charge. Platzman and Tzoar's work however, was the first to conclude that magnetic densities, giving rise to magnetic Bragg scattering, could be studied with X-rays. This result is not entirely unexpected, as X-rays have both electric and *magnetic* fields. Thus, an interaction with a sample's magnetic properties (in addition to the charge density) seems reasonable. In fact, the X-ray scattering amplitude f may be written as:

$$f \approx f^0 + f' + if'' + f^{spin} \tag{2.8}$$

$f_0 \propto -Zr_0$ is the Thomson charge scattering contribution, Z is the atomic number and r_0 is the classical electron radius. f' and if'' are the respective contributions from the dispersive and absorptive processes. The f^{spin} represents the amplitude of scattering which explicitly contains the electron-spin operator. Unfortunately, the intensity of this magnetic scattering was estimated to be 10^{-6}-10^{-9} smaller than the intensity of classical Thomson charge scattering. Even so, the first experimental observation of X-ray magnetic scattering in NiO, was made by de Bergevin and Brunel [24] only two years after Platzman and Tzoar's work. By 1983 de Bergevin and Brunel had completed a series of experiments [25], that had demonstrated all the effects predicted by Platzman and Tzoar. These original experiments amazingly used a sealed tube X-ray source. Nowadays, synchrotron radiation produces an intense flux of X-rays which are both, highly polarised and tunable in energy. These three factors now allow for detailed studies of magnetic, charge and other higher forms of ordering, in a wide range of materials.

2.3.1 The non-resonant X-ray magnetic scattering cross-section

The X-ray magnetic scattering cross-section, given in terms of photon polarisation states, was first calculated by Blume [19] and Blume & Gibbs [26]. However, the clearest explanation of this derivation can be found in the Ph.D. thesis of J. P. Hill [27]. These calculations contain all the magnetic scattering terms, and give the scattering cross-section in terms of the polarisation states of the incident and scattered photons. These polarisation states are an important aspect of X-ray magnetic scattering.

To determine the magnetic scattering cross-section, one replaces the vector potential $\mathbf{A}(\mathbf{r_j})$, in the interaction Hamiltonian with equation 2.6. As this result is derived in full by Blume [19], I shall restrict myself to a qualitative description of the scattering terms.

Starting with the first-ordering scattering terms. The term due to the $\mathcal{H}'_1$ gives Thompson scattering of photons by free electrons, multiplied by a charge density-density correlation function. This Thompson scattering term can be the dominant one in the X-ray cross-section.

The scattering arising from the $\mathcal{H}'_4$ term of the interaction Hamiltonian, is sensitive to the spin density Fourier transform. It should be noted that for this term, the scattering is proportional to the cross product of the incident and scattered X-ray polarisation vectors. This is not the case for the Thompson scattering.

Finally, there are the second order scattering terms, that arise from $\mathcal{H}'_2$ and $\mathcal{H}'_3$. These produce a term for the scattering cross-section, that contains a contribution, which is proportional to the sample's orbital angular momentum. This scattering term is of the same order of magnitude as the pure spin scattering term. Additionally, the photon's polarisation state dependence differs from the two terms described above.

By expressing the orbital ($\mathbf{L}$) and spin ($\mathbf{S}$) components of the cross-section, in terms of the Fourier transforms of their magnetisation densities ($\mathbf{L}(\mathbf{Q})$ and $\mathbf{S}(\mathbf{Q})$ respectively), the magnetic scattering amplitude can be rewritten as:

$$f^{mag}(Q) = ir_0 f_{dw} \frac{\hbar\omega}{mc^2} \left[\frac{1}{2}\mathbf{L}(\mathbf{Q}) \cdot \mathbf{A}'' + \mathbf{S}(\mathbf{Q}) \cdot \mathbf{B} \right] \tag{2.9}$$

The vectors $\mathbf{A}''$ and $\mathbf{B}$ describe the polarisation dependence of the X-rays, scattered from the respective orbital and spin components. These vectors can be summarised as:

$$\begin{aligned} \mathbf{A}'' = &\quad 2(1 - k_i \cdot k_f)(\epsilon_f \times \epsilon_i) - (k_i \times \epsilon_i)(k_i \cdot \epsilon_f) + (k_f \times \epsilon_f)(k_f \cdot \epsilon_i) \\ \mathbf{B} = &\quad (\epsilon_f \times \epsilon_i) + (k_f \times \epsilon_f)(k_f \cdot \epsilon_i) - (k_i \times \epsilon_i)(k_i \cdot \epsilon_f) - (k_f \times \epsilon_f) \times (k_i \times \epsilon_i) \end{aligned} \tag{2.10}$$

This result is derived in full by Blume and Gibbs [26], readers should refer to this paper for further information. It is useful to express these polarisation vectors as 2×2 matrices. For synchrotron experiments, the obvious choice is a basis which has components parallel (π) and perpendicular (σ) to the scattering plane. This basis is shown in figure 2.1. Equation 2.11 shows what scattering channels the different matrix elements represent.

$$\begin{pmatrix} \sigma - \sigma' & \pi - \sigma' \\ \sigma - \pi' & \pi - \pi' \end{pmatrix} \tag{2.11}$$

In this format $\mathbf{A}''$ and $\mathbf{B}$ are:

$$\begin{aligned} \mathbf{A}'' &= \tfrac{Q^2}{2k^2} \begin{pmatrix} 0 & -(k_i + k_f) \\ k_i + k_f & 2k_i \times k_f \end{pmatrix} \\ \mathbf{B} &= \begin{pmatrix} k_i \times k_f & -k_i(1 - k_i \cdot k_f) \\ k_f(1 - k_i \cdot k_f) & k_i \times k_f \end{pmatrix} \end{aligned} \tag{2.12}$$

Therefore equation 2.9 can be written as:

$$f^{mag}(Q) = ir_0 f_{dw} \tfrac{\hbar\omega}{mc^2} \times$$

$$\begin{pmatrix} \mathbf{S}(\mathbf{Q}) \cdot (k_i \times k_f) & -\frac{Q^2}{2k^2}\left[\left(\frac{\mathbf{L}(\mathbf{Q})}{2} + \mathbf{S}(\mathbf{Q})\right) \cdot k_i + \frac{\mathbf{L}(\mathbf{Q})}{2} \cdot k_f\right] \\ \frac{Q^2}{2k^2}\left[\left(\frac{\mathbf{L}(\mathbf{Q})}{2} + \mathbf{S}(\mathbf{Q})\right) \cdot k_i + \frac{\mathbf{L}(\mathbf{Q})}{2} \cdot k_f\right] & \left[\frac{Q^2}{2k^2}\mathbf{L}(\mathbf{Q}) + \mathbf{S}(\mathbf{Q})\right] \cdot (k_i \times k_f) \end{pmatrix} \tag{2.13}$$

The next step is to rewrite the scattering amplitude in terms of the coordinate system of

figure 2.1. This is achieved by using the following geometrical relations:

$$\begin{aligned}
\hat{U}_1 &= \tfrac{(k_i+k_f)}{(2\cos(\theta))} \\
\hat{U}_2 &= \tfrac{(k_i\times k_f)}{(\sin(2\theta))} \\
\hat{U}_3 &= \tfrac{(k_i-k_f)}{(2\sin(\theta))} \\
\tfrac{Q^2}{2k^2} &= 2\sin^2(\theta) \\
(1 - k_i \cdot k_f) &= 2\sin^2(\theta)
\end{aligned} \tag{2.14}$$

By using these geometric relationships, one arrives at the final expression for the cross-section of X-ray non-resonant magnetic scattering:

$$f^{mag} = ir_0 f_{dw} \tfrac{\hbar\omega}{mc^2} \times \begin{pmatrix} S_2 \sin 2\theta & -2\sin^2\theta[(L_1+S_1)\cos\theta - S_3\sin\theta] \\ 2\sin^2\theta[(L_1+S_1)\cos\theta + S_3\sin\theta] & \sin 2\theta[2\sin^2\theta L_2 + S_2] \end{pmatrix} \tag{2.15}$$

Here r_0 is the classical electron radius and f_{dw} is the Debye-Waller factor, this accounts for a reduction in scattering due to thermal vibrations.

As equation 2.15 shows, the orbital and spin angular moments have different polarisation dependences. It is therefore possible to determine the different magnetic contributions to the scattered signal. Before continuing, it should be noted that the $\frac{\hbar\omega}{mc^2}$ prefactor in equation 2.15 does not appear in the Thomson charge scattering amplitude. Therefore, the ratio of magnetic to charge scattering intensity is approximately: $\left(\frac{\hbar\omega}{mc^2}\right)^2$, for a 10 keV photon, this ratio is: $\sim 4\times10^{-4}$. This explains why magnetic scattering is so much weaker than charge scattering.

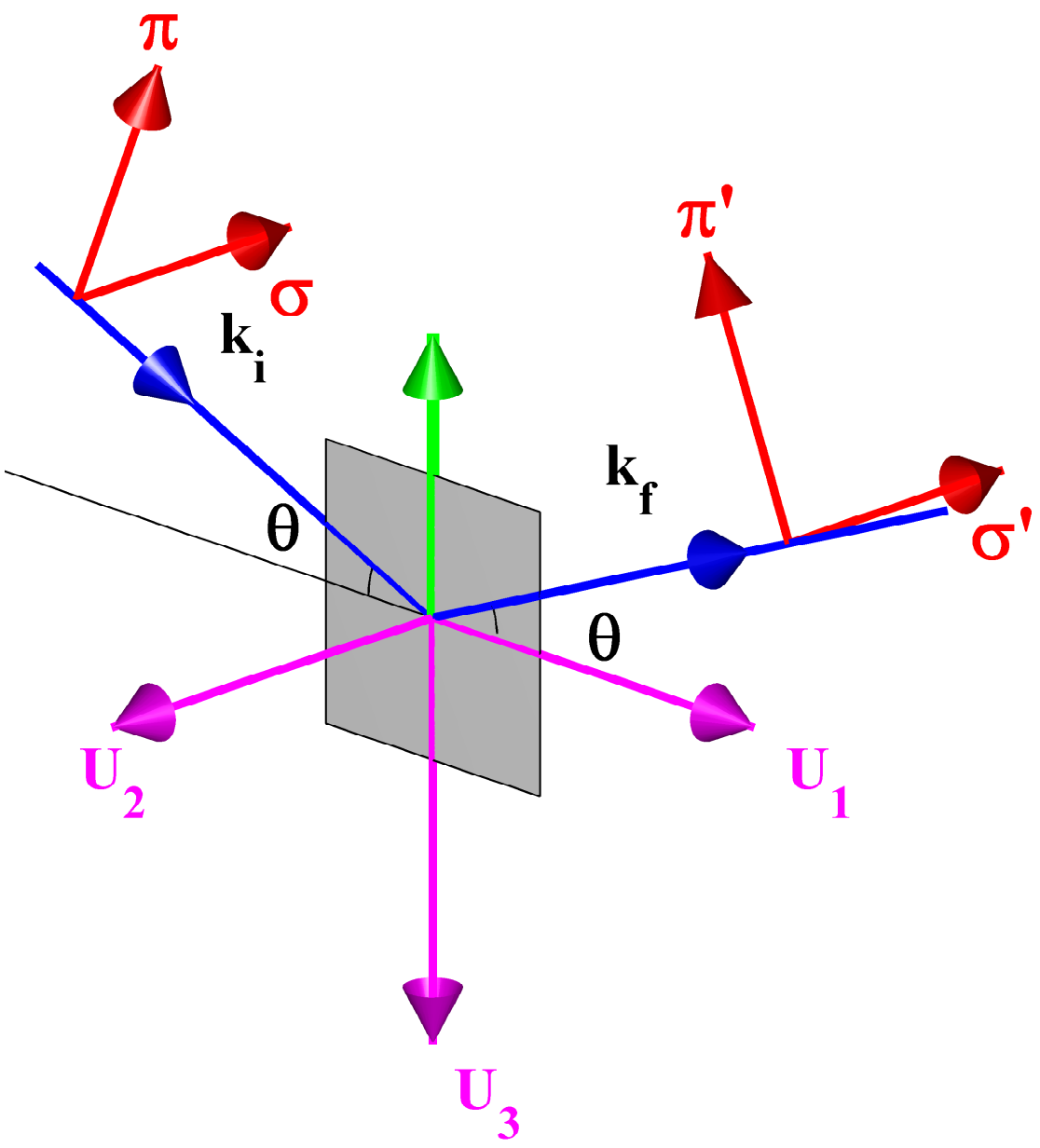

Figure 2.1: A diagram of the vertical scattering plane used in X-ray magnetic scattering experiments. The coordinate system ($\mathbf{U_1}, \mathbf{U_2}, \mathbf{U_3}$) is denoted by purple arrows, the incident ($\mathbf{k_i}$) and scattered ($\mathbf{k_f}$) wavevectors are denoted by the blue arrows. The polarisation states (σ,π) are denoted by the red arrows. The scattering angle is θ, and the green vertical arrow represents the wavevector transfer $\mathbf{q}$. The vectors $\mathbf{U}$ define a basis for the magnetic structure being studied. This basis can be expressed in terms of the incident and scattered wavevectors.

2.3.2 Resonant X-ray scattering

By tuning the energy of the incident X-ray photon through a sample's atomic absorption edge, an additional resonant contribution to the scattering amplitude can be seen. This contribution can enhance the scattered signal by several orders of magnitude. The first resonant X-ray scattering study was performed in 1985, by Namikawa *et al.* [28]. This work showed a resonant enhancement of the (2 2 0) Bragg reflection, in the vicinity of the K-absorption edge of ferromagnetic nickel.

The origin of the resonant scattering effect can be seen in the denominator of the 2^{nd} order terms in equation 2.7. If the combined energy of the incident photon ($\hbar\omega$) and the initial state of the electron (E_a) are equal to the energy of an intermediate electronic state. Or in other words, when $\hbar\omega = E_n - E_a$. Then the denominator will tend to zero, and the contribution to the scattering cross-section from the 2^{nd} order terms diverges. A simplistic view of the resonant scattering process is as follows. The incident photon is destroyed, transferring its energy to a ground state virtual electron ($|a\rangle$). This electron is then excited into an intermediate state ($|n\rangle$). If the process is elastic, this electron will decay back to its initial ground state, where it will emit a second photon. Thus, resonant X-ray scattering can be thought of as a probe of the intermediate electronic state of the specific element. In addition to studying long range static correlations, as in the case of standard X-ray diffraction, RXS provides information on the local site symmetry of a sample's electronic states. This is similar to spectroscopy experiments, such as XMCD and XANES. What is more, at resonant energies, the atomic structure factors transform into a tensor, reflecting the anisotropy of the intermediate electronic state. This anisotropy could be due to low site symmetry, Jahn-Teller distortions, magnetic ordering or electronic orbital ordering [29, 30, 31, 32, 33].

Selection rules

There are two factors controlling which intermediate states one can observe. Firstly, since electrons are fermions, the Pauli Exclusion Principle states that, the resonant electron

can only be excited into an unoccupied intermediate state. Secondly, there are certain *selection rules* that determine which electronic transitions are 'allowed', and which are 'forbidden'. I will now derive the selection rules for the most commonly studied RXS transition, the electric-dipole transition (E1). The derivation shown in this section follows the one given on pages 170-172 of *Quantum Mechanics* by A. Rae [34].

An electromagnetic wave (angular frequency ω) where the electric field (E) is parallel to the z direction, may be described as:

$$E = E_0 \cos(\mathbf{k} \cdot \mathbf{r} - \omega t) \tag{2.16}$$

If one assumes that the wavelength of the electromagnetic wave is much greater than an atom's radius, then $e^{ik \cdot r} \approx 1$. This is known as the electric dipole approximation. Also near the resonance condition, the $\mathcal{H}_2$ Hamiltonian dominates the scattering cross-section (equation 2.7) [35]. Combining these two facts gives:

$$\begin{aligned} \langle n| \mathcal{H}_2 |i\rangle \propto \langle n| \epsilon \cdot P_j |i\rangle \quad &= m \langle n| \epsilon \cdot \dot{r}_j |i\rangle \\ &= \tfrac{-im}{\hbar} \langle n| \epsilon \cdot [r_j, \mathcal{H}_{el}] |i\rangle \\ &= \tfrac{im}{\hbar} (E_n - E_i) \langle n| \epsilon \cdot r_j |i\rangle \end{aligned} \tag{2.17}$$

Here $\mathcal{H}_{el}$ is the Hamiltonian for an isolated electron. The energy factor (E_n-E_i) can be taken outside the matrix elements, this is because both the ground and intermediate electronic states are eigenstates. The relationship given in equation 2.17 shows that, to describe resonant scattering within the electric-dipole approximation, one needs to know an electron's position, but not its momentum. For the case of the electromagnetic wave described above, this Hamiltonian will be:

$$\hat{\mathcal{H}}' = eEz \approx eE_0 z \cos(\omega t) \tag{2.18}$$

Furthermore, the time independent Hamiltonian will be:

$$\hat{\mathcal{H}}'' = eE_0 z \tag{2.19}$$

This may be treated as a perturbation.

The next step is to calculate the value of $\hat{\mathcal{H}}''$ for a perturbation that corresponds to an electronic transition from a ground state, described by the quantum numbers (n_1,l_1,m_1), to an excited state, described by the quantum numbers (n_2,l_2,m_2). This is achieved by using the standard one electron wavefunction in spherical polar co-ordinates (r,θ,ϕ), see chapter 3 of [34]. Here $\hat{\mathcal{H}}''$ is calculated like any other quantum mechanical expectation value:

$$\begin{aligned}
\hat{\mathcal{H}}''_{12} &= eE_0 \int u^*_{n_1 l_1 m_1} z u_{n_2 l_2 m_2} d\tau \\
&= eE_0 \left[\int_0^\infty R^*_{n_1 l_1}(r) R_{n_2 l_2}(r) r^3 dr\right] \\
&\times \left[\int_0^\pi P_{l_1}^{|m_1|}(\cos(\theta)) P_{l_2}^{|m_2|}(\cos(\theta)) \cos(\theta)\sin(\theta) d\theta\right] \\
&\times \left[\int_0^{2\pi} e^{i(m_2 - m_1)\phi} d\phi\right]
\end{aligned} \tag{2.20}$$

$u_{n,l,m}$ is the electron's total wavefunction. $R_{nl}(r)$ represents the radial component of the electron's wavefunction, and $P_l^{|m|}$ the Legendre functions.

Clearly an electronic transition is only allowed if all three of the integrals given in equation 2.20 are non-zero. Starting with the integral over ϕ, it is clear that this term vanishes unless m_1=m_2. Furthermore, the integral with respect to θ can be evaluated using the relationship:

$$(2l+1)\cos(\theta) P|m|_l = (l - |m| + 1) P|m|_{l+1} + (l + |m|) P|m|_{l-1} \tag{2.21}$$

By using this relationship and assuming that m_1=m_2, the integral over θ becomes:

$$\frac{l_2 - |m| + 1}{2l_2 + 1} \int_0^{\pi} P_{l_1}^{|m_1|} P_{l_2+1}^{|m_1|} \sin(\theta) d\theta + \frac{l_2 + |m|}{2l_2 + 1} \int_0^{\pi} P_{l_1}^{|m_1|} P_{l_2-1}^{|m_1|} \sin(\theta) d\theta \tag{2.22}$$

The integrals shown above, are in general difficult to evaluate. However, one may use the fact that Legendre functions having the same values of m but different values of l are orthogonal. Therefore the integral over θ will be zero, unless l_1=l_2+1 or l_1=l_2-1.

Thus for a electric-dipole transition to be allowed (for $E//z$), the angular quantum number (l) must only change by ± 1 and the magnetic quantum number (m) must be unchanged. However, it should be noted that, for an electromagnetic wave whose electric field is polarised in the x direction, the integral over ϕ is:

$$\frac{1}{2} \int_0^{2\pi} (e^{i(m_2 - m_1 + 1)\phi} + e^{i(m_2 - m_1 - 1)\phi}) d\phi \tag{2.23}$$

This will be zero unless m_1=$m_2 \pm 1$.

Therefore, the full selection rules of the electric-dipole transition, for an arbitrary electric field polarisation are:

$$\begin{aligned} \Delta l &= \pm 1 \\ \Delta m &= \pm 1 \ or \ 0 \end{aligned} \tag{2.24}$$

It is also worth noting that the integral of r in equation 2.20 is always finite. Thus, there is no selection rule for the principle quantum number, n.

As I have stated previously, these selection rules only apply to the electric-dipole transition. There are however, other higher order transitions that may occur. For example, if $\mathbf{k} \cdot \mathbf{r}$ is assumed to be small rather than zero, the electric field may be expressed as a power series:

$$E = E_0 \left[\cos(\omega t) + (\mathbf{k} \cdot \mathbf{r}) \sin(\omega t) - \frac{1}{2} (\mathbf{k} \cdot \mathbf{r})^2 \cos(\omega t) + \cdots \right] \tag{2.25}$$

The first term in the square brackets corresponds to the electric-dipole transition, while the other terms will lead to higher order transitions, called the electric-quadrupole, electric-octopole, etc. In addition, the atomic electrons may interact with the magnetic field of

the electromagnetic wave, leading to a different set of transitions which are known as the magnetic-dipole, magnetic-quadrupole, etc. All of these transitions will have different selection rules to the electric-dipole transition.

The X-ray resonant exchange scattering cross-section

If the excited electronic state is split by magnetic interactions, then the resonant X-ray scattering becomes a probe of magnetic order. This is known as X-ray resonant exchange scattering (XRES). The X-ray resonant exchange scattering cross-section was first calculated by Hannon and co-workers [36], using the same method that had been previously used to described resonant γ-ray scattering [37, 38]. By considering the resonant terms that arise from the $\mathbf{A}\cdot\mathbf{P}$ operator of the interaction Hamiltonian ($\mathcal{H}'_2$ in equation 2.5). Hannon and co-workers [36] showed that the resonant contribution for an electric $2^{\Delta l}$ resonance (El), of which the electric-dipole transition (Δl=1) is a member, to the scattering amplitude is [36, 37, 38]:

$$f_{El} = 4\pi\lambda f_{dw} \sum_{m=-l}^{l} \left[\epsilon_i^* \cdot Y_{lm}\left(\hat{k_f}\right) Y_{lm}^*\left(\hat{k_i}\right) \cdot \epsilon_i\right] F_{lm}\left(\omega\right) \tag{2.26}$$

Where F_{lm} is:

$$F_{lm}(\omega) = \sum_{a,n} \frac{P_a P_{a(n)} \Gamma_x(amn, El)/\Gamma}{x(a,n) - i} \tag{2.27}$$

λ is the X-ray photon's wavelength, Y_{lm} are the vector spherical harmonics for the El transition. f_{dw} is the Debye-Waller factor, this accounts for the reduction in scattering intensity due to thermal vibrations of ions about their equilibrium positions. Here, $\hat{\epsilon}$, ionic states a and n, energies E_a and E_n are the same as in section 2. P_a is the statistical probability for the initial state $|a\rangle$, while $\mathrm{P}_{a(n)}$ gives the probability that a transition into the excited ionic state ($|n\rangle$) is allowed from state a. $\mathrm{P}_{a(n)}$ is therefore determined by the overlap integrals of the unoccupied electronic state, when the system is in a ground state ($|a\rangle$), and of the same electronic state, when the system is in a excited state ($|n\rangle$),

i.e. when the electronic states are in the presence of a core hole. When summed over the magnetic quantum number m, the quantity $\Gamma_x(amn, El)$ gives the partial width for a specific El decay, i.e. $|n\rangle \rightarrow |a\rangle$. For the sum over m to be non-zero however, there must be spin-orbit correlations of either the ground or excited state. The variable Γ is the total width for all decay processes, these may be both radiative (from any shell) and non-radiative (i.e. Auger, Coaster-Kronig) de-excitations of $|n\rangle$. Finally the $x(a, n)$ term in the denominator of equation 2.27 can be written as $2(E_a - E_n - \hbar\omega)/\Gamma$, and gives the deviation from the resonance in units of $\Gamma/2$.

Although this scattering amplitude equation is non-trivial, what is clear, is that the amplitude of scattering is determined by the detailed electronic structure of the sample, which are described by the F_{lm} factors given in equation 2.27. Usually these factors are determined by *ab-initio* calculations. The polarisation dependence of the scattering however, is determined through the vector spherical harmonics of equation 2.26, and is independent of the F_{lm} factors. Both the energy widths Γ_x and Γ, are dependent on matrix elements of the initial and excited electronic states. For the partial width Γ_x, this can be seen in equation 2.28:

$$\Gamma_x(amn, El) = 8\pi \left(\frac{e^2}{\lambda}\right) \left(\frac{l+1}{l}\right) \left| \langle a| \sum_i J_l(kr_i) Y_{lm}(\widehat{r}_i) |n\rangle \right|^2 \tag{2.28}$$

j_l is the spherical Bessel function of order l.

It therefore follows that the greater the overlap between the initial and excited state's wavefunctions, the greater the resonant scattering intensity will be.

The electric-dipole transition (E1)

For most cases the electric-dipole transition (Δl=1, Δm=$\pm$1 or 0) dominates the resonant scattering cross-section. For such a transition, Hannon *et al.* [36] showed that:

$$\begin{aligned}\left[\hat{\epsilon}'^{*}\cdot Y_{1\pm1}\left(\hat{k}'\right)Y^{*}_{1\pm1}\left(\hat{k}\right)\cdot\hat{\epsilon}\right] &= \left[\tfrac{3}{16\pi}\right]\left[\hat{\epsilon}'^{*}\cdot\hat{\epsilon}\mp i\left(\hat{\epsilon}'^{*}\times\hat{\epsilon}\right)\cdot\hat{z}_j-\left(\hat{\epsilon}'^{*}\cdot\hat{z}_j\right)\left(\hat{\epsilon}\cdot\hat{z}_j\right)\right]\\ \left[\hat{\epsilon}'^{*}\cdot Y_{10}\left(\hat{k}'\right)Y^{*}_{10}\left(\hat{k}\right)\cdot\hat{\epsilon}\right] &= \left[\tfrac{3}{8\pi}\right]\left[\left(\hat{\epsilon}'^{*}\cdot\hat{z}_j\right)\left(\hat{\epsilon}\cdot\hat{z}_j\right)\right]\end{aligned} \tag{2.29}$$

To clearly show the polarisation dependence of the electric-dipole transition, the scattering amplitude can be written as:

$$\begin{aligned}f_{E1}= \;& \tfrac{3}{4}\lambda\left\{\hat{\epsilon}'^{*}\cdot\hat{\epsilon}\left[F_{11}+F_{1-1}\right]-i\left(\hat{\epsilon}'^{*}\times\hat{\epsilon}\right)\cdot\hat{z}_j\left[F_{11}-F_{1-1}\right]\right.\\ &\left.+\left(\hat{\epsilon}'^{*}\cdot\hat{z}_j\right)\left(\hat{\epsilon}\cdot\hat{z}_j\right)\left[2F_{10}-F_{11}-F_{1-1}\right]\right\}\end{aligned} \tag{2.30}$$

Which may be rewritten in terms of linear combinations of the F_{lm} factors:

$$f_{E1}=\left(\hat{\epsilon}'\cdot\hat{\epsilon}\right)F^{(0)}-i\left(\hat{\epsilon}'\times\hat{\epsilon}\right)\cdot\hat{z}_jF^{(1)}+\left(\hat{\epsilon}'\cdot\hat{z}_j\right)\left(\hat{\epsilon}\cdot\hat{z}_j\right)F^{(2)} \tag{2.31}$$

$\hat{z}_j$ is a unit vector which is parallel to the total magnetic moment. For example $\hat{z}_1$ is parallel to the vector $\hat{U}_1$ as shown in figure 2.1.

Finally by using the geometric relationships given in equations 2.14, the electric-dipole scattering amplitude was further rewritten in terms of linear photon polarisation states, by Hill and McMorrow [39]. These scattering amplitudes are given in the same matrix format as the non-resonant scattering amplitude (equation 2.15).

$$\begin{aligned}f^{res}_{E1}= \;& F^{(0)}\begin{pmatrix}1 & 0\\ 0 & \cos2\theta\end{pmatrix}\\ & -iF^{(1)}\begin{pmatrix}0 & z_3\sin\theta-z_1\cos\theta\\ z_1\cos\theta+z_3\sin\theta & -z_2\sin2\theta\end{pmatrix}\\ & +F^{(2)}\begin{pmatrix}{z_2}^2 & -z_2(z_1\sin\theta-z_3\cos\theta)\\ z_2(z_1\sin\theta+z_3\cos\theta) & -\cos^2\theta({z_1}^2\tan^2\theta+{z_3}^2)\end{pmatrix}\end{aligned} \tag{2.32}$$

The first matrix of equation 2.32 contains no terms which are dependent on the magnetic moments, hence this term will contribute to scattering from a charge Bragg peak. For an incommensurate antiferromagnet (as is the case for $TbMnO_3$ and $DyMnO_3$) the second matrix, which is linear in the power of z, produces the first-harmonic magnetic satellite peak. This term is responsible for the magnetic circular dichroic effect seen in ferromagnets. This is because $F^{(1)}$ depends on the difference in resonance strengths between states with Δm=+1 and Δm=-1 e.g $[F_{11} - F_{1-1}]$. The third term which is quadratic in the power of z will produce the second harmonic magnetic satellite peak. This term is related to magnetic linear dichroism.

The electric-quadrupole transition (E2)

Another common resonance transition is the electric-quadrupole (E2) which contains 13 distinct polarisation terms in the scattering amplitude. These terms vary in the power of $\hat{z}_j$ from 0 to 4. Thus, for an incommensurate antiferromagnet, the electric-quadrupole transitions will produce up to four distinct satellite peaks. All of these peaks will have different polarisation dependences [40]. Hill and McMorrow also derived the cross-section for the electric-quadrupole (E2) transition in terms of the photon scattering channels, σ-σ', σ-π', π-σ' and π-π'. However, these equations are not given here.

2.3.3 ID20, an X-ray magnetic scattering beamline

The ESRF's ID20 X-ray magnetic scattering beamline is one of the world's premier scientific instruments, for the investigation of magnetic and other higher forms of order. The beamline's energy range of 3-25keV, its high brilliance and large flux, enable the routine measurement of the resonant enhancement of scattering, at the actinide M-edges, lanthanide L-edges and transition metal K-edges. A large choice of sample environments are available to prospective users. These include a 10 Tesla magnetic field, pressures up to 30 kbar, the use of a diamond phase plate to produce circularly polarised light. Also, a closed cycle refrigerator with a ^{4}He Joule-Thomson evaporation stage, can reduce the temperature of the sample environment to 1.5 K. Because of this large variety of choice,

I will restrict my description of the beamline to the equipment that was used for my investigation of the magnetic ordering in $DyMnO_3$. For a more complete description of the beamline, please refer to the article of Paolasini *et al.* [41].

The beamline receives its photons from three linear undulators. The maximum flux available for 10 keV photons is 10^{14} photon s^{-1} at the beam's focal point, this is only possible however when the synchrotron has a current of 200 mA. ID20's monochromator is a Si(1 1 1) double crystal, the first of which is cooled with liquid nitrogen, while the second is mounted on a bender for tunable focusing. By finely rotating the two-crystal assembly, one is able to perform experimental measurements between 3.4 and 25keV. This gives a resolution of less than 10 eV (for example ΔE=8eV at 10 keV). A pair of 1m long silicon mirrors, one before and one after the monochromator, are used to provide vertical focusing, and to reject higher order harmonic reflections from the monochromator. After the second focusing mirror, the beam passes through a 500μm thick beryllium window and enters the first experimental hutch (EH1). The focused beam size at the sample position is $250\mu m$ (vertical) and $300\mu m$ (horizontal). Located inside EH1 is a Micro-Controle diffractometer, the diffractometer is commonly used in the four circle mode (FOURC), with a vertical scattering geometry (see figure 2.2). For this mode, the free angles of rotation are: θ, 2θ, χ and ψ. In addition the polarisation analyser crystal can be rotated about the scattered wavevector ($\mathbf{k_f}$), this angle of rotation is labelled η.

Polarisation analysis

To perform X-ray magnetic and resonant scattering experiments, the polarisation state of the scattered X-rays needs to be measured. ID20 achieves this by utilising a polarisation analyser crystal (PA), which is located at the end of the 2θ-arm. The PA is a high quality single crystal mounted on a motorised stage. A specific crystal is chosen for a specific photon energy, so that the Bragg scattering angle is approximately 45°. Because of this condition, each polarisation analyser crystal is limited to a narrow energy band, meaning that a large collection of crystals is needed to study the different absorption edges. To perform the polarisation analysis of the scattered wavevector, the polarisation

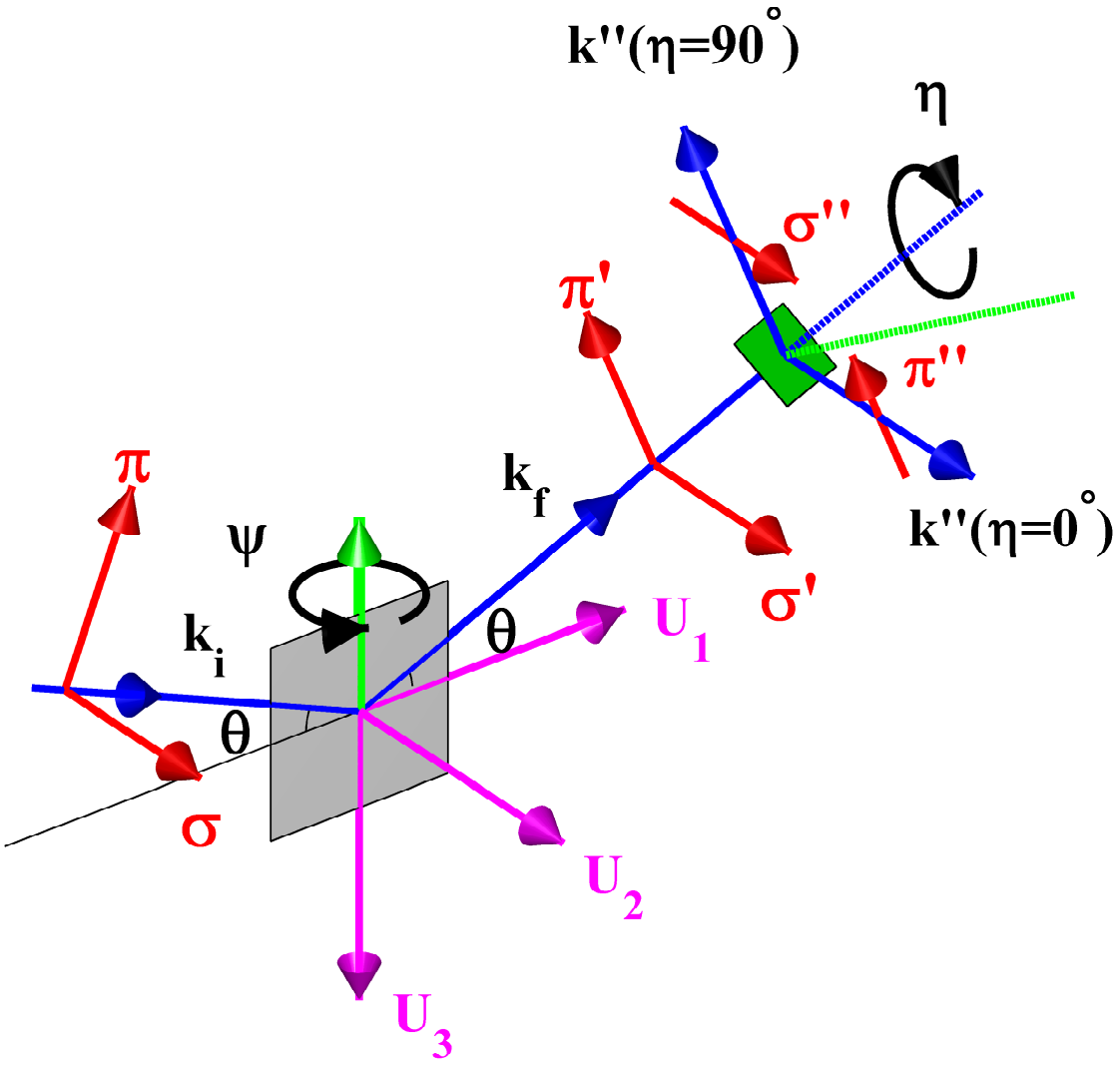

Figure 2.2: A diagram of the vertical scattering geometry with polarisation analysis set-up, used on ID20. Again the coordinate system ($\mathbf{U_1}$,$\mathbf{U_2}$,$\mathbf{U_3}$) is denoted by purple arrows. The incident ($\mathbf{k_i}$) and scattered ($\mathbf{k_f}$) wavevectors are denoted by the blue arrows, and polarisation states (σ,π) are denoted by the red arrows. The scattering angle is θ. The motor movements of the diffractometer are shown as black arrows. The green vertical arrow represents the wavevector transfer $\mathbf{q}$. The polarisation analyser crystal (green rectangle), is selected and oriented for a given energy so its Bragg scattering angle is $\theta_{pol} \approx 45°$. In order to select a specific polarisation channel, the polarisation analyser crystal is rotated about the scattered wavevector (angle η).

analyser crystal is rotated about the scattered wavevector ($\mathbf{k_f}$), this is η in figure 2.2. For horizontally (σ') polarised photons, η=0°, while for vertically (π') polarised photons η=90°. The photons, scattered by the PA, are detected by a solid state Silicon Avalanche Photo Diode (APD) device.

Types of measurement performed on ID20

Because of its high flux, the beamline can be used to perform non-resonant X-ray magnetic scattering experiments [42]. But the primary activity of the ID20 instrument, is to measure the enhancement in the scattering intensities, when the incident photon energy is tuned through an absorption edge of a sample's elemental species. The scattered intensity now provides information on broken lattice symmetries which could be due to charge, magnetic or a higher multipole form of order. As described earlier, this information is collected through the characterisation of the scattered X-ray. Specifically, the angular dependence about the scattering vector (azimuthal dependence) and energy dependence of the intensity of scattering, across an absorption edge. The azimuthal dependence, with polarisation analysis, is a method which directly measures the symmetries of the tensors involved in resonant scattering amplitudes. In practice, the azimuthal dependence is determined by measuring the scattered intensity of a specific polarisation state, upon rotating the sample about the scattering vector. For the case of specular reflections, this can be done by rotating the sample around the ψ-axes. However, for non-specular reflections, a computational macro calculates the crystal sample's UB matrix as a function of ψ, thus giving the desired θ, 2θ and χ motor positions. For ID20, this macro allows one to measure the azimuthal dependences of reflections which are up to $\pm 20^\circ$ off-specular. Examples of azimuthal scans, with a complete analysis of the results, are presented in chapters 4 and 5. The energy dependence of the intensity of scattering, is determined by varying the energy of the incident photons, while maintaining a constant wavevector transfer. The incident energy is controlled by the main monochromator, while the scattering vector is kept constant through adjustments of the diffractometer's angular motors.

2.4 Inelastic X-ray scattering

Highly intense X-rays can also be complementary to neutrons for the investigation, of lattice dynamics. For the remainder of this chapter, I will describe both the theoretical and experimental background of inelastic X-ray scattering (IXS) from phonon excitations. Firstly, I will give a brief introduction and historical overview to IXS. I will also compare IXS to other methods of studying lattice dynamics, such as inelastic neutron scattering (INS) and light scattering techniques, such as Raman and Brillouin scattering. Secondly, the inelastic X-ray cross-section will be derived from the interaction of X-rays with electrons, which I have previously discussed in section 2.2. Finally, I will discuss some of the practical challenges of measuring phonons with X-rays, and describe a model IXS beamline: ID28 at the ESRF.

The inelastic scattering process is schematically depicted in figure 2.3. Both, INS and IXS measure the dynamic structure factor S($\mathbf{Q}$,E), where $\mathbf{Q}$ is the total momentum transfer and E is the energy of the excitation. S($\mathbf{Q}$,E) is actually the space and time Fourier transform of the density-density correlation function. Both INS and IXS are able to measure the entire phonon dispersion. Brillouin or Raman scattering, by contrast, can only measure specific phonon modes, close to the centre of the Brillouin zone (the Γ-point). For the general case, neutrons are advantageous to X-rays when studying excitations, as one is able to detect other forms of excitations aside from phonons. However, the scattering between the target sample's nucleus and neutron is relatively weak. When this is combined with the fact that neutron sources have a relatively low flux (when compared to X-ray sources), INS experiments require a sample volume of several mm^3. IXS measurements, by contrast, can be made on significantly smaller volumes, 10^{-5}-10^{-4} mm^3. Thus, IXS allows for the investigation of materials which are only available in very small amounts, such as the iron pnictides described in chapter 3. In addition, this small sample volume allows one to study materials under extreme conditions, for example high pressure. Another advantage of X-rays is that the IXS dynamic structure factor is highly coherent. This is not the case with neutrons, where it is sometimes necessary to separate the coherent and incoherent contributions to S($\mathbf{Q}$,E).

The possibility of performing inelastic X-ray measurements on previously unmeasurable samples, provided the main motivation for scientists to develop an inelastic X-ray scattering instrument. This represented a considerable effort on the behalf of these scientists, as in order to be comparable to a neutron triple-axis spectrometer, the incident photon wavelength would have to be ≈1Å, which requires a photon energy of 12 keV. Thus to study meV phonon excitations, the energy bandwidth of these new machines would have to be: $\Delta E/E=10^{-7}$. Notwithstanding this difficult task, researchers began in the 1980s to build the first IXS machine. Initially attempts were made to build a laboratory based instruments, using a rotating anode as the X-ray source. This produced an instrument with an energy resolution of 42 meV. Unfortunately, the rotating anode source gave an insufficient photon flux for practical experiments [43]. It was not until the first synchrotron based instrument, located on a bending magnet source at HASYLAB with ΔE=55 meV, that the photon flux and energy resolution, allowed for the first IXS experiments. These experiments were conducted on graphite [44] and beryllium [44, 45]. After these initial successes, a dedicated IXS beamline with a wiggler insertion device (ID) was constructed at HASYLAB. This new beamline had both a greater photon flux and a vastly improved energy resolution of 9 meV. Modern day IXS instruments have improved significantly on these initial machines. Thanks to the immense flux produced by 3^{rd} generation synchrotrons, the high brilliance of new undulator IDs, and advances in X-ray optics, inelastic X-ray scattering experiments are now routinely performed on extremely small samples (μm^3), with energy resolutions of 1.5 meV or less.

2.4.1 The inelastic X-ray scattering cross-section

I will now discuss the theory of inelastic scattering of X-rays, and describe how this leads to the determination of the dynamic structure factor ($S(\mathbf{Q},E)$). This relies on the theoretical background of electron-photon interactions, which has been presented in section 2.2.

Equation 2.5 describes the Hamiltonian, in the weak relativistic limit, of the electron-photon interaction. For most IXS research, experiments are performed with photon energies that are not in the vicinity of a sample's absorption edge. Therefore, the Hamiltonian

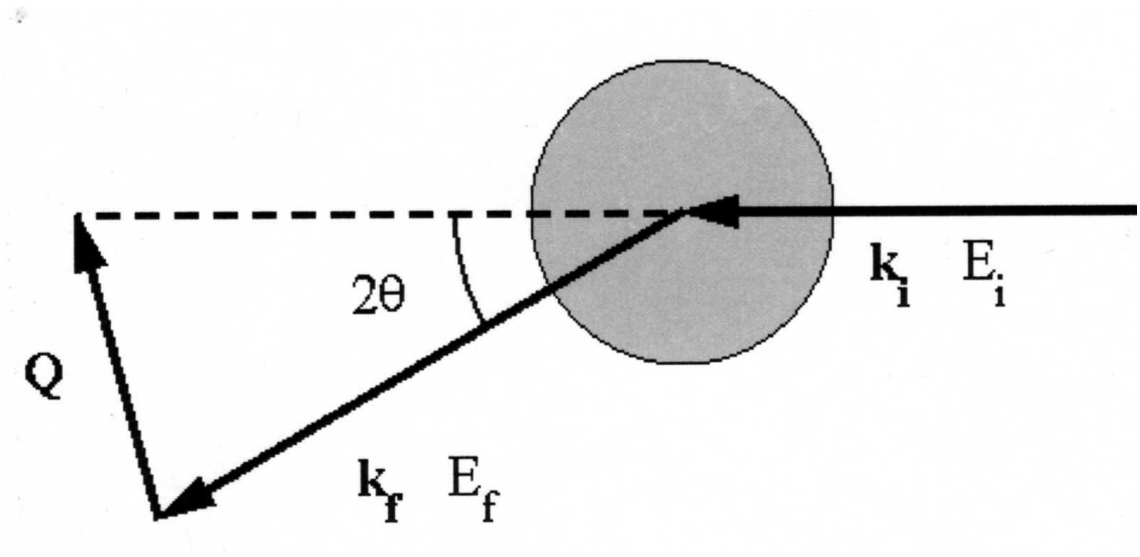

Figure 2.3: A diagram of the inelastic scattering process, $\mathbf{k_{i(f)}}$ and $E_{i(f)}$ are the wavevector and energy of the incident (scattered) photon. 2θ is the scattering angle and $\mathbf{Q}$ is the momentum transfer due to the scattering process. This diagram is a slightly modified version of the one found in *Inelastic x-ray scattering from phonons* [46].

terms $\mathcal{H}_2$ and $\mathcal{H}_3$ in equation 2.5 can be ignored. In addition, if the IXS experiment is being used to study the lattice dynamics of a system, the much weaker spin interactions described by $\mathcal{H}_4$, are not included. Thus the only interaction term which is of interest, is the one arising from the Thomson charge scattering ($\mathcal{H}_1$):

$$\mathcal{H}_1 = \frac{1}{2} r_0 \sum_j \mathbf{A}^2(r_j) = \frac{e^2}{2mc^2} \sum_j \mathbf{A}^2(r_j) \tag{2.33}$$

$\mathbf{A(r}_j\mathbf{)}$ is the same vector potential defined in equation 2.6, r_0 is the classical electron radius.

The probability that the electron-photon system will transform from its initial state $|i\rangle$ to a final state $|f\rangle$, can again be calculated by Fermi's golden rule. However, as one is only interested in the $\mathcal{H}_1$ term, the transition probability (W) needs to be calculated to the first order only. By inserting the expression for $\mathbf{A(r_j)}$ from equation 2.6 into the Thomson Hamiltonian, and remembering that the only terms of interest are the $cc^\dagger$ $c^\dagger c$ terms, which do not change the photon number, $\mathcal{H}_1$ becomes:

$$\begin{aligned}\langle f|\,\mathcal{H}_1\,|i\rangle = \; & r_0\tfrac{2\pi\hbar c^2}{V}\,\langle b,\hbar\mathbf{k_f},\epsilon_f|\sum_{\mathbf{jq}\sigma\mathbf{p}\gamma}\tfrac{1}{(\omega_q\omega_p)^{1/2}}\Big[\epsilon_{\mathbf{q}\sigma}\cdot\epsilon^*_{\mathbf{p}\gamma}c_{\mathbf{q}\sigma}c^\dagger_{\mathbf{p}\gamma}e^{i(\mathbf{q}-\mathbf{p})\cdot\mathbf{r_j}} \\ & +\epsilon^*_{\mathbf{q}\sigma}\cdot\epsilon_{\mathbf{p}\gamma}c^\dagger_{\mathbf{q}\sigma}c_{\mathbf{p}\gamma}e^{-i(\mathbf{q}-\mathbf{p})\cdot\mathbf{r_j}}\Big]\,|a,\hbar\mathbf{k_i},\epsilon_i\rangle\end{aligned} \tag{2.34}$$

$\mathbf{q_i} = \hbar\mathbf{k_i}$ and $\mathbf{q_f} = \hbar\mathbf{k_f}$ are the respective momenta of the incident and scattered photons, also σ and γ are the polarisation states of the photons. The wavefunctions of the initial and final states have also been separated into the constituent atomic and photon parts. This equation will only be non-zero, if a photon with a momentum of $\hbar\mathbf{k_i}$ is annihilated and another with momentum $\hbar\mathbf{k_f}$ is created. In addition, although it is not explicitly shown here, the creation and annihilation can be written in terms of photon numbers. Using these two facts one can simplify equation 2.34 to:

$$\langle f|\,\mathcal{H}_1\,|i\rangle = r_0\frac{2\pi\hbar c^2}{V}\left(\frac{n_{\mathbf{k}}}{\omega_i\omega_f}\right)^{1/2}\langle b|\sum_j(\epsilon_i\cdot\epsilon_f)e^{i\mathbf{Q}\cdot\mathbf{r_j}}\,|a\rangle \tag{2.35}$$

$\mathbf{Q}$=$\hbar\mathbf{k_f}$-$\hbar\mathbf{k_i}$ being the momentum transfer, the i and f subscripts refer to the initial and final states. Substituting this expression into equation 2.1, and defining $\rho(E_f)$ to be the number of photon states, in a shell in k-space with a thickness of dk:

$$\rho(E_f) = \frac{V\omega_i^2}{8\pi^2\hbar c^3} \tag{2.36}$$

The double differential cross-section for this scattering process is:

$$\frac{d^2\sigma}{d\Omega dE} = r_0^2(\epsilon_i\cdot\epsilon_f)^2\frac{k_i}{k_f}\sum_{i,f}P_i\left|\langle b|\sum_j e^{-i\mathbf{Q}\cdot\mathbf{r_j}}\,|a\rangle\right|^2\delta(E-E_f-E_i) \tag{2.37}$$

The initial and final states are summed in order to take the thermodynamic average of the electronic states, with P_i being the thermal population of the initial states. This allows for the calculation of the double differential cross-section in different experimental conditions,

i.e. temperature, pressure etc. As described in the introduction of this section, IXS measures the dynamical structure factor of a system. Currently, the double differential cross-section describes the interaction between photons and electrons, not excitations. The next step therefore, is to obtain an equation for S(**Q**,E) from the double differential cross-section shown above. This may be achieved if the following two criteria are met:

1. Since all forms of X-ray scattering arise from an interaction between a photon and the sample's electrons (not the nucleus), it is difficult to justify a model where the scattering originates from a single point or delta function. However, by making an assumption known as the adiabatic approximation, which suggests that, if the movement of the electrons are fast enough to average out over the time scale of the lattice vibrations, then it is fair to model the X-ray scattering process as originating from a point charge. This approximation allows one to separate a system's quantum state into two parts. Firstly, the electronic part $|S_e\rangle$, and secondly the nuclear part $|S_n\rangle$, where $|S_{atom}\rangle$=$|S_e\rangle|S_n\rangle$.

2. We assume that the electronic part of the total wavefunction remains unchanged by the scattering process. The only difference in the wavefunction is therefore due to the excitation of the nuclear part (atomic density fluctuations).

By using these two approximations, equation 2.37 may be rewritten in terms of the atomic densities:

$$\frac{d^2\sigma}{d\Omega dE} = r_0^2(\epsilon_i \cdot \epsilon_f)^2 \frac{k_i}{k_f} \left\{ \sum_{in,fn} P_{In} \left| \langle b_n | \sum_m f_m(Q) e^{-i\mathbf{Q}\cdot\mathbf{R_m}} |a_n\rangle \right|^2 \delta(E - E_f - E_i) \right\} \quad (2.38)$$

Here $f_m(Q)$ is atom m's atomic form factor, R_m is the position vector of the same atom's nucleus (not the electron). The dynamical structure factor S(**Q**,E) is contained within the curly brackets of this equation. By assuming that scattering units of the system are equal, equation 2.38 may be simplified to:

$$\frac{d^2\sigma}{d\Omega dE} = r_0^2(\epsilon_i \cdot \epsilon_f)^2 \frac{k_i}{k_f} |f(Q)|^2 S(\mathbf{Q}, E) \quad (2.39)$$

The first three terms may be grouped as the Thomson scattering cross-section for photons by free electrons. This is separate from the dynamic properties of the system. The atomic form factor appears here only as a multiplication factor, but this is only when the scattering units of the system are equal. If this is not the case, the atomic form factor is contained within the dynamical structure factor. By rewriting the double differential cross-section in this form, one may separate the scattering contributions of the individual scatters or elemental species $f(\mathbf{Q})$, from the collective properties of the system, S($\mathbf{Q}$,E).

Assuming that the phonon vibrations are harmonic in nature, i.e. $\mathrm{E}_{p.e.} \propto \delta x^2$. Then for the single photon scattering process, the dynamical structure factor may be rewritten as [46]:

$$S(\mathbf{Q}, E) = \sum_m \left\langle n(E) + \frac{1}{2} \pm \frac{1}{2} \right\rangle (E_j(\mathbf{q})^{-1} F_{in}(\mathbf{Q}))\delta(E \pm E_j(q)) \tag{2.40}$$

The sum extends over the $3m$ phonon modes within a crystal of m atoms per unit cell. The three terms in the large angular brackets describe the phonon mode population. The first term is the Bose factor: $1/(1 - e^{-E/k_B T})$, which gives the phonon population at a specific temperature. The 1/2 represents zero point fluctuations. The plus or minus sign indicates whether a phonon has been respectively created or destroyed, during the scattering process. Outside of the angular brackets are a further two terms, which contain different definitions for the momentum transfer. The first term represents the energy transfer at which the phonon exists. $\mathbf{q}$ is the reduced momentum transfer, which is related to the total momentum transfer ($\mathbf{Q}$) by $\mathbf{Q}$=$\mathbf{G}$+$\mathbf{q}$, where $\mathbf{G}$ is a reciprocal lattice vector. Hence, the energy of a phonon $E_j(\mathbf{q})$ is independent of Brillouin zone. Finally, $F_{in}(\mathbf{Q})$ is the inelastic structure factor, this describes the scattering strength of different phonon excitations. $F_{in}(\mathbf{Q})$ may be written as:

$$\mathbf{F_{in}}(\mathbf{Q}) = \left| \sum_m M_m^{-\frac{1}{2}} f_m(\mathbf{Q}) \left[e_m^j(\mathbf{q}) \cdot \mathbf{Q} \right] e^{i\mathbf{Q}\cdot\mathbf{r_m}} f_{dw} \right|^2 \tag{2.41}$$

This expression contains a number of important pieces of information. Working through the equation systematically, one sees that again the phonon mode j is summed over all

atoms in the crystal's unit cell, denoted by m. The intensity of scattering from the phonon mode is related to a number of factors. Firstly, intensity is inversely proportional to the mass of the nuclei M_m involved in the excitation. Secondly, the intensity is proportional to the square of the Fourier transform of the electron density, f_m. The term contained within the square brackets is perhaps the most important term, here $e_m^j(\mathbf{q})$ is the eigenvector of a specific phonon mode of the m^{th} atom, at the reduced momentum $\mathbf{q}$, while $\mathbf{Q}$ is again the total momentum transfer. Put simply, to observe a specific phonon mode, the momentum transfer must not be perpendicular to the direction of vibration of the mode. Furthermore, while it might be possible to measure a phonon mode in one Brillouin zone, the same mode could be much more intense in a different zone. Conversely, if one is measuring a number of phonon modes that have similar energies, it might be worth choosing a Brillouin zone where a mode's intensity might be less, but where the contrast between the intensities of the different phonon modes is greatest. This will allow for the disentanglement of the different phonon branches. Since a system's phonon wavevector is non-trivially related to the system's symmetries, it is best to use an *a priori* lattice dynamics calculation to choose the best zone to work in. These calculations are based on theoretical models such as Density Functional Theorem (D.F.T.), and should be performed before the experiment. Finally, the f_{dw} term in equation 2.41 accounts for the thermal vibrations of an atom about its equilibrium position, which can not be described by a specific phonon excitation. This term is known as the Debye-Waller factor, and has been encountered previously in section 2.3.2.

With all the terms now described, the double differential cross-section in its entirety is:

$$\frac{d^2\sigma}{d\Omega dE} = r_0^2(\epsilon_i \cdot \epsilon_f)^2 \frac{k_i}{k_f} \sum_m \left\langle n(E) + \frac{1}{2} \pm \frac{1}{2} \right\rangle (E_j(\mathbf{q})^{-1} F_{in}(\mathbf{Q}))\delta(E \pm E_j(q)) \qquad (2.42)$$

2.4.2 The triple-axis spectrometer

Advances in the brilliance of modern synchrotron X-ray sources, has allowed for the construction of IXS spectrometers with a high enough incident flux and a meV energy resolution. These machines are now comparable to inelastic neutron scattering spectrometers.

For the remainder of this chapter, I will describe the basic attributes that a instrument needs to measure crystallographic excitations. This could be for X-rays or neutrons. In addition, I will also discuss a specific IXS instrument, ID28 which is located at the ESRF.

To study a crystallographic excitation, with either X-ray or neutron scattering probes, several pieces of information need to be extracted. Specifically, the incident and scattered momenta (or wavevectors) and the incident and final energies of the probe, are needed. A simple diagram of the inelastic scattering process is shown in figure 2.3. By using the cosine rule, it is easy to show from the figure that:

$$Q^2 = k_i^2 + k_f^2 - 2k_i k_f \cos(2\theta) \tag{2.43}$$

2θ is the scattering angle and Q, k_i and k_f are as previously defined. As the energy of a photon E is related to its wavevector k, through the expression $E = \hbar ck$, equation 2.43 can be rewritten in terms of energy. Thus, the simplest way to perform an inelastic scattering experiment is to fix the incident wavevector k_i (which also defines E_i), the final scattered wavevector k_f and the scattering angle 2θ. An instrument capable of achieving this is a triple-axis spectrometer (TAS), which was first developed for neutron studies by Brockhouse *et al.* [47]. The same basic design however can also be used for IXS. Triple-axis means that these instruments have three axes, which are used to control the wavevector, energy and scattering angle of the probe. The first axis is located at the instrument's monochromator, the second at the sample goniometer and the third at the crystal analysers. The incident energy and wavevector of the probe are defined by a specific value of 2θ for a high-quality single crystal, which is the monochromator. For X-rays this is usually a Bragg reflection of a silicon or diamond crystal. The final energy is set by a Bragg reflection of the analyser crystal. Finally, the scattering angle 2θ, the final piece of information to find Q, is determined from the relative positions of the other two axes.

Before I begin to describe a specific IXS instrument, it is worth noting that for phonon excitations, the energy of the phonon excitation is always much less than the energy of incident X-ray. Thus, by setting $k_i \approx k_f$, equation 2.43 reduces to Bragg's law.

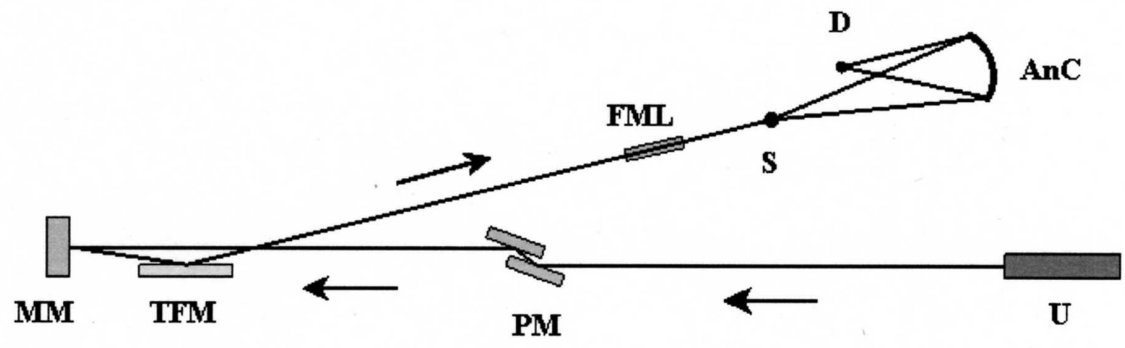

Figure 2.4: A schematic diagram of the ID28 instrument. The initials stand for the following, **U**: undulator, **PM**: pre and post monochromator, **MM**: main monochromator, **TFM**: toroidal focusing mirror, **FML**: focusing multilayer, **S**: sample, **AnC**: analyser crystals and finally **D** is the array of detectors. This diagram is a slightly modified version of the one found in *Inelastic x-ray scattering from phonons* [46]. The sizes, lengths and angles are not to scale.

$$\left(\frac{Q}{k_i}\right) = 2\sin\left(\frac{2\theta}{2}\right) \tag{2.44}$$

Therefore, the ratio of the exchange to incident momentum is dependent only on the scattering angle (2θ), not the energy. Thus, for IXS phonon measurements, there are no limitations in the energy transfer at a specific Q-point. This is in strong contrast to INS measurements, where there is a strong relationship between the energy and momentum transfer.

2.4.3 ID28, an inelastic X-ray scattering beamline

A schematic diagram of the ESRF's ID28 beamline is given in figure 2.4. I will begin my description at the beamline's source of X-rays, its undulators, and work systematically down the beamline.

ID28 receives its X-rays from three undulators of a 32mm magnetic period. This magnetic period allows for a choice of X-ray energies from 13.8 to 25.7 keV. All photons produced by these undulators are polarised in the horizontal plane. Because of the meV energy resolution requirements, the incident energy of the photons must be monochromated to

a high degree of certainty. Before this can be achieved however, the beam must be premonochromated, so the energy of the photons impinging on the main monochromator is well defined. In addition, so that the heat load of the white beam will not damage the main monochromator. To achieve this premonochromation, a silicon (1 1 1) channel-cut double-crystal monochromator, denoted PM in figure 2.4, is used. The crystal gives a relative band width of: $\Delta E/E \approx 2 \times 10^{-4}$, and is cooled to a temperature of 100 K by a closed loop liquid nitrogen system. At this temperature silicon demonstrates a maximum in thermal conductivity and a minimum in the linear thermal expansion coefficient. Thus, the thermal deformation of the silicon crystal is maintained below the limits where the loss of photons, with the correct energy, may occur. After the high heat load premonochromator, the beam's heat load may need to be reduced even further. This stops thermal broadening of the energy resolution. This procedure is optional and may be achieved through the use of a second pair silicon monochromators, cut with a (3 3 1) channel. This second premonochromator gives a relative band width of: $\Delta E/E \approx 2 \times 1.44^{-5}$.

In order to attain meV energy resolution, the beam must then be monochromated even further. This is achieved through the use of a high quality large silicon single crystal, denote MM in figure 2.4. To act as a monochromator, the crystal operates at a Bragg angle of 89.98° and utilises a silicon (n n n) reflection to select the energy resolution (see table 2.1). This is the first of the triple axes. The resolving power of such a silicon reflection is given by [48]:

$$\frac{\Delta E}{E} = \frac{d_{hkl}}{\pi \Lambda_{ext}} \tag{2.45}$$

d_{hkl} is the lattice spacing for a specific (hkl) reflection. Λ_{ext} is the primary extinction length [48], which increases with increasing reflection order. Thus, to improve the resolving power of the main monochromator, it is necessary to increase the order of the silicon (n n n) reflection. The silicon Bragg reflection is selected by tuning the incident photon energy. This is done by the previous monochromators. The incident energy can then be finely tuned by varying the main monochromator's temperature (ΔT), as this causes the silicon crystal's d-spacing to change, thus changing the energy of the Bragg reflection:

Si (n n n)	E (KeV)	ΔE (meV)	ΔT (mK)	ΔE/E	Flux (s^{-1})
Si(7 7 7)	13.840	5.30	150	3.8×10^{-7}	10.5×10^{10}
Si(8 8 8)	15.817	4.40	109	2.8×10^{-7}	9×10^{10}
Si(9 9 9)	17.794	2.20	48	1.2×10^{-7}	2.70×10^{10}
Si(11 11 11)	21.747	0.83	15	4.7×10^{-8}	6.6×10^{9}
Si(12 12 12)	23.725	0.73	12	3.1×10^{-8}	5.85×10^{9}
Si(13 13 13)	25.704	0.50	7.6	1.9×10^{-8}	1.47×10^{9}

Table 2.1: A table showing the properties of the different Si (n n n) reflections available from the main backscattering monochromator at ID28. ΔE is the energy resolution, ΔT is the temperature equivalent of ΔE in mK. Experimental conditions: two 1.6 m U32 undulators, ring current: 200 mA, primary slits aperture: 1.6 mm (horizontal)×0.7 mm (vertical), secondary slits aperture: 2.4 mm (horizontal)×1.0 mm (vertical). This table was copied from the beamline's website [50]. The table clearly shows that, increasing the photon energy and hence the order of the silicon reflection, produces a better energy resolution. However, with a better resolution, the flux is reduced.

$$\frac{\Delta E}{E} = \alpha \Delta T \tag{2.46}$$

The constant of proportionality, $\alpha = 2.58 \times 10^{-6} K^{-1}$, is the thermal expansion coefficient of silicon at room temperature. Practically, to perform a high quality experiment, one needs to record steps in energy of approximately one tenth of the energy resolution. Therefore, the temperature of the main monochromator and analysers must be controlled to a precision of at least 0.5 mK [49].

In addition to the necessity of precise temperature control, geometrical factors also limit the energy resolution. Through the differentiation of Bragg's law, the relative energy resolution due to angular divergence ($\Delta\theta$) of an X-ray beam impinging on a crystal is [46, 51]:

$$\frac{\Delta E}{E} = cot(\theta_B)\Delta\theta \tag{2.47}$$

θ_B is the scattering angle of a monochromator's silicon (n n n) Bragg reflection.

To minimise this effect on the energy resolution, the term must be less than the monochromator's intrinsic energy resolution. This is achieved by placing the monochromator crystal

in a extreme back scattering orientation, hence $\theta_B = 89.98°$ so that $cot(89.98°) \approx 10^{-4}$. This scattering geometry allows for the angular divergence to be comparable to the divergence from undulator source. After undergoing the back scattering, the beam's direction is reversed, so that these highly monochromated X-rays now travel towards the beamline's front end. Before reaching the sample, the beam can be additionally focused through the use of toroidal mirror (vertical focusing), which is located directly after the main monochromator, and a Ru/B_4C multilayer (horizontal focusing), which is located just before the sample's goniometer.

Samples are mounted on a goniometer in the horizontal scattering geometry (S in figure 2.4). This goniometer is the second of the three TAS axes, and allows for rotations about the θ, χ and ψ axes and for translations in all three directions (x, y and z). In addition, the axis of rotation of the spectrometer's arm (2θ) also intersect at the sample position. Because of the backscattering geometry, the white beam transfer line crosses close to the goniometer. This configuration places some restrictions on the θ motor. Thus, an additional sample rotation stage (additional θ) has been installed to allow for a greater degree of freedom.

Once the X-rays have been scattered by the sample, they pass into the beamline's 12 metre long spectrometer arm. This arm is positioned on rails on top of marble tables, and is moved along the rails through the use of a motorised screw. The far end of the arm contains nine silicon crystal analysers (not to be confused with the polarisation analyser crystals described in section 2.3.3). These crystal analysers are the third TAS axis, which reflect the X-rays with a back scattering geometry ($\theta_B = 89.98°$) onto a corresponding solid-state detector. These detectors are located at the front end of the spectrometer arm. Multiple crystal analysers are used, so that several momentum transfers can be recorded simultaneously. The purpose of the analyser crystal is to again select a specific energy and wavevector which are relative to the incident energy, hence the need for precise temperature control between the main monochromator and the analyser crystals. In fact, these analyser crystals are not one large single crystal, but a number of undistorted perfectly flat crystals which have been placed onto a spherical surface. The reason for this design is that the analysers require a very high angular acceptance, which is well above accepted values.

Thus, the only way to obtain such a high value is to use a focusing system. However, one cannot simply use an elastically bent crystal, as this would induce damaging strain effects on the crystallographic structure meaning a reduction in energy resolution. The solution to this problem, is to use an array of approximately 12000 high quality flat silicon crystals glued onto a spherical substrate.

All IXS measurements are made by performing constant Q scans, otherwise known as energy scans. This can be achieved by changing the incident energy, through fine adjustments of the main monochromator's temperature, while keeping the analyser's acceptance energy constant. As I have stated previously (equation 2.44), for phonon excitations the relationship between the exchange energy and Q is negligible. Therefore, to perform a scan, one needs to move to the intended Q position and then scan the monochromator energy. Results are then shown as the difference in energy between the incident (monochromator energy) and the final energy (acceptance energy of the analyser crystal).

Chapter 3

Inelastic X-ray scattering studies of $SmFeAsO_{1-x}F_y$

3.1 Iron pnictides: an introduction

This Chapter will focus on a group of transition metal compounds which display quantum effects on a macroscopic scale: the superconducting iron pnictides. The first half of this chapter contains an introduction and a review of the theoretical modes, that are used to explain possible superconducting mechanisms. In addition, previous experimental work on the lattice dynamics of these materials will be described. The second half of this chapter will describe the results of inelastic X-ray scattering (IXS) measurements of the phonon lattice dynamics, in two specific pnictide compounds: SmFeAsO and $SmFeAsO_{0.60}F_{0.35}$. The first of these compounds is non-superconducting, instead forming a antiferromagnetic spin-density wave metal below 130 K. The second fluorine-doped compound is a superconductor below 53 K [52]. IXS measurements were taken at room temperature, where both compounds are paramagnetic. Particular attention was paid to the dispersions along the [100] direction of three optical modes, close to an energy transfer of 23 meV. Two of these three modes corresponded to vibrations of the As-Sm atoms, for one of the modes the atoms vibrate in phase with one another, while for the other the atomic vibrations are out-

of-phase. The third mode corresponds to in-phase vibrations of the Fe-O atoms. All three phonon modes are polarised out of the Fe-As planes. Interestingly, two of these modes are strongly renormalised upon fluorine doping, with one mode softening and the other hardening upon doping. The two phonon modes which show the doping renormalisation effects are also believed to be linked to the magnetic moments of the Fe ions via structural distortions. Therefore, these results point towards the significance of magnetism in understanding the electron coupling of these systems. This experimental work has recently been published in *Physical Review B* as a Rapid Communication [9].

3.1.1 The discovery of superconductivity in the pnictides

During the early part of 2008, Kamihara and co-workers [1] reported the discovery of superconductivity in the oxypnictide compound $LaFeAsO_{1-x}F_x$ (x=0.05-0.12). Resistivity and diamagnetic susceptibility measurements showed that a superconducting state appeared below 26 K, when the polycrystalline samples were doped with F^- ions at the O^{2-} sites, to a level between 5-11 %. This discovery was made while working on the $LaOMP_n$ (M=Mn, Fe, Co or Ni and P_n=P or As) oxypnictide family of compounds. Superconductivity had already been discovered in several of these samples, however transition temperatures (T_c) were relatively low, for example T_c=5 K for LaOFeP [53]. Thus, a T_c of 26 K was seen as a major advance. Shortly afterwards, the T_c in $LaFeAsO_{1-x}F_x$ was shown to increase further to 43 K when the sample was placed under a pressure of 4 GPa [54]. Furthermore, other superconducting $ReFeAsO_{1-x}F_x$ compounds, where Re is a rare earth ion, were quickly identified. The maximum T_c was found to be 55 K, when Re=Sm [55], this is the highest known superconducting temperature outside of the cuprates.

These initial discoveries generated a great deal of excitement, sparking a gold rush in research within the strongly correlated electron community, reminiscent of the discovery of superconductivity in the cuprates 20 years before. It was originally hoped that a pnictide based superconductor with a T_c exceeding that of the cuprates may be found, so far however, 55 K has proved to be the upper limit. This initial burst of research has not been in vain however, as several new classes of iron based superconductors, with different

crystal structures have been identified. These include:

- $ReFeAsO_{1-x}F_x$ and $AFe_{1-x}Co_xAsF$ (Re=rare earth, A=Ca or Sr) compounds which form a ZrCuSiAs-type structure. This is commonly referred to as the '1111' structure.
- $A_{1-x}B_xFe_2As_2$ (A=Ba, Sr, Ca and B=K, Cs, Na) compounds which have a $ThCr_2Si_2$-type structure. This is commonly referred to as the '122' structure.
- XFeAs (x=Li or Na) compounds with a Cu_2Sb-type structure. Referred to as the '111' structure.
- The α-FeSe compounds, which have a α-PbO-type structure. Referred to as the '11' structure.
- The newly discovered Sr_2DO_3FeAs (D=Sc or V) compounds, which has a K_2NiF_4-type structure. This compound is referred to as the '21311' structure or the '42622', as the unit cell contains two formula units.

Despite the failure to raise the maximum superconducting temperature above 55 K, research into the iron pnictides still proceeds at a pace. It is now hoped that these compounds might act as a *'Rosetta stone'* [4], in decoding the mysteries of unconventional superconductivity.

3.1.2 The crystal structure and phase diagram of the pnictides

This section will be used to describe the crystal structure and physical properties of the '1111' iron pnictides, as my research was conducted on such a compound: $SmFeAsO_{1-x}F_x$. However, as these FeAs-based superconductors are relatively new, a discussion of the results taken on the '122' structures has also been included. This is because the underlying mechanism of superconductivity in these two classes is believed to be same. At the time of writing, superconductivity has been observed in approximately 300 oxypnictide compounds which have the '1111' structure [56]. A diagram of the room temperature crystal

structure for these compounds is given in figure 3.1. As the figure shows, the unit cell is a tetragonal, with the crystal structure belonging to the $P4/nmm$ space group. This crystal structure has two different layers in the $a-b$ plane, one consisting of covalently bonded Re and O atoms (green sheet in fig 3.1), with the other consisting of covalently bonded Fe and As atoms (cyan sheet in fig 3.1). These layers are alternatively stacked along the c-direction, with a slight charge difference between the two layer types, hence the interlayer bonding is ionic in nature. In these compounds, the charge carriers are electrons which are confined to the Fe-As layers. The Re-O layers act as a 'charge reservoir' [52], when it is doped with extra electrons. This electron doping can be achieved through the partial substitution of the O^{2-} ions with the singularly charged F^{-} ions, or by the application of high pressures (60kbar) [57], which generate oxygen vacancies in the crystal structure. In fact, all five of the pnictide structures described above contain a charge carrying 2D layer. This suggests that, the physical properties of these compounds might be two-dimensional in nature. This two-dimensionality is similar to what is observed in other unconventional superconductors, such as the cuprates, ruthenates and cobalts.

A phase diagram of fluorine doping in $LaFeAsO_{1-x}F_x$ ($0 \leq x \leq 0.2$) is shown in figure 3.2. An initial inspection of the phase diagram suggest similarities to the cuprates. For example, the parent compound of both materials are antiferromagnetic, with this ordering suppressed by doping. In addition, there is experimental evidence for the existence of a *pseudogap* region just above T_c [58]. On closer inspection however, many of these similarities become superficial. Starting with the parent compound, while it is true to say that both the underdoped cuprates and iron pnictides are antiferromagnets, they are completely different types. The cuprates exists as a Mott insulator: antiferromagnets with a large on site Coulomb energy, which prevents electrons from moving freely throughout crystal structure. The ReFeAsO's, in contrast, form electrically conducting antiferromagnetic spin-density-wave (SDW) metals, below approximately 150 K. Here, the Fe spins are periodically modulated. What is more, for the ReFeAsO's, these spins alternate in direction from one Fe-As layer to the next, giving a stripe-like structure. Whereas the cuprates have a up-down chequerboard-like spin pattern. In addition, the transition to the SDW state in the ReFeAsO compounds appear to be related to a tetragonal to orthorhombic

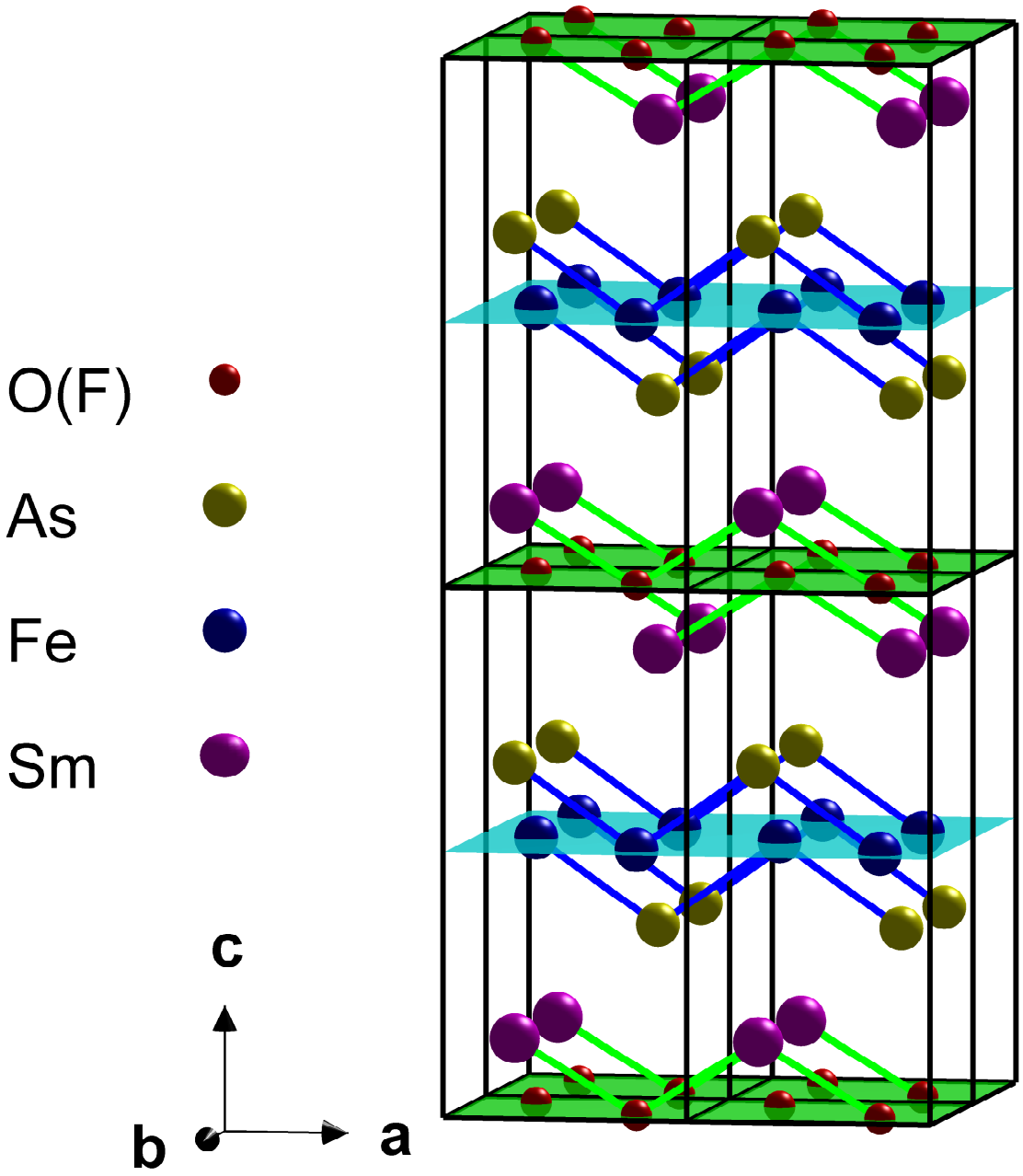

Figure 3.1: A 2×2×2 supercell of the high temperature tetragonal structure of $SmFeAsO_{1-x}F_x$ (space group $P4/nmm$). The atomic positions were taken from Zhigadlo *et al* [52]. The cyan sheets represent the As-Fe charge carrying layers, while the green sheets represent the Sm-O charge reservoir layers.

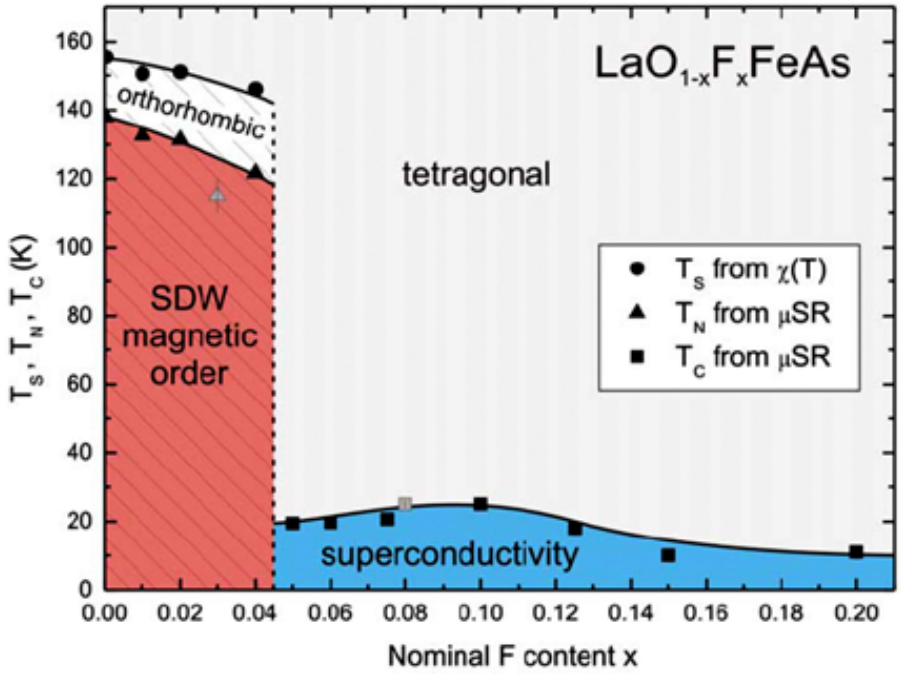

Figure 3.2: The phase digram of $LaFeAsO_{1-x}F_x$, as determined from susceptibility and μSR experiments. The figure was taken from [60].

structural phase transition [59]. This new orthorhombic structure has the *Cmma* space group.

The effects of fluorine doping on the $ReFeAsO_{1-x}F_x$ compounds will now be discussed. With doping levels of approximately 5%, the orthorhombic phase transition is suppressed and these materials are no longer an antiferromagnet, instead becoming a superconductor below T_c. The nature of how the magnetic order disappears varies between compounds. For some (e.g. Re=La) [60] an abrupt first-order change is observed, while other compounds (e.g. Re=Ce) exhibit a gradual decrease in Fe magnetic moment which is more second-order in nature [61]. In fact, for Re=Sm there have been reports [62] of a coexistence between static antiferromagnetic order and the superconducting state. The difference between the behaviour of the magnetic order with doping could be due to varying sample qualities, or slight and subtle differences between their crystal structures.

Upon further doping, the T_c of the superconducting state rises slightly, until a doping level of about 10% is reached. The phase diagram of the $ReFeAsO_{1-x}F_x$ compounds above a

doping level of 20% is unknown, due to a lack of crystal samples.

Specific heat measurements of the upper critical field, H_{C2} (the strength of magnetic field required to destroy the superconducting state), for $NdFeAsO_{1-x}F_x$, has shown only a modest superconducting anisotropy of $\gamma \equiv H_{c2}^{ab}/H_{c2}^{c} \approx 4.3$ [63]. The superconducting anisotropy for the cuprates, by contrast, can be as high as 8 [64]. The low anisotropy of the pnictides suggests that, unlike the cuprates, the superconductivity in these compounds is three dimensional. The concept of 3D superconductivity amongst the 2D pnictide layered structure, has been supported by electrical resistivity measurements made on $(Ba,K)Fe_2As_2$ [65]. Recent angle-resolved photoemission spectroscopy (ARPES) studies of $Ba_{0.6}K_{0.4}Fe_2As_2$ [66] and $NdFeAsO_{0.9}F_{0.1}$ [67], have also shown little anisotropy in the superconducting energy gap (Δ). This 3D superconductivity may be understood from the knowledge that, unlike the 2D cuprates, which have only one band of charge carriers, the pnictides have multiple bands. In fact, all five of the Fe $3d$ orbitals are believed to contribute to the electronic structure near the Fermi level [5]. Thus, the pnictides are multi-band superconductors, with the predicted number of bands varying between two and five, depending on the theoretical calculations.

3.1.3 Theoretical modes of pnictide superconductivity

Using BCS theory, McMillan [68] determined that the maximum transitions temperature for electron-phonon superconductors occurs when the coupling constant (see section 3.1.4) is 2. Practically, this places an upper limit on the superconducting transition temperature of approximately 30K. The high (i.e. >30K) superconducting temperatures observed in the pnictides, therefore suggest that an exotic, non BCS electron-phonon, coupling mechanism is responsible for the superconductivity. In fact, one of the leading contenders for the superconducting order parameter suggests this mechanism to be spin-lattice coupling [5]. This order parameter, named the $s_{\pm}$ state, can be visualised using the schematic representation of a pnictide's a-b Fermi surface at k_z=0, which is shown in figure 3.3.

The basic idea is that, the order parameter and the superconducting energy gap has one sign at the hole Fermi surface, which is in the shape of two cylinders, at the central (Γ)

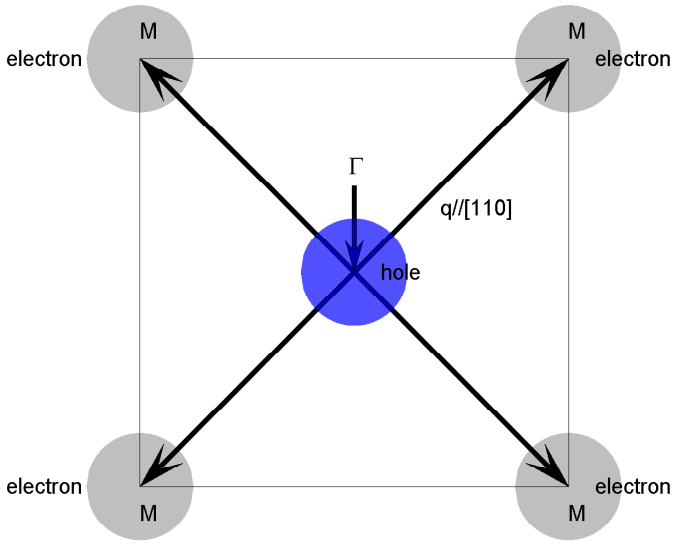

Figure 3.3: A Schematic representation of the a-b Fermi surface of LaFeAsO, with the hole and electron Fermi surfaces, as calculated by Singh and Du [5]. The figure also shows that it is possible for a spin density wave of wavevector q, to nest between the hole and electron Fermi surfaces.

point of the Brillouin zone. Conversely, the order parameter and superconducting energy gap has the opposite sign for the two electron Fermi surface cylinders, at each of the Brillouin zone's corners, the M-points. This sign reversal is discontinuous between the Fermi surfaces, hence it is different to other multiband s-wave superconductors, such as MgB_2. The superconducting energy gap (Δ) is therefore proportional to the modulus of this order parameter.

The superconducting order parameter, based on the $s_{\pm}$ gap symmetry, was originally proposed by Singh and Du from D.F.T. band structure calculations, within the local spin density approximation on LaFeAsO [5]. Results from this work, showed that the low lying electronic states come from the five Fe d-bands, with the Fermi surface cylinders at Γ and M mainly coming from the d_{xz} and d_{yz} electronic states. The O-As hybridised p states however, are well below the Fermi energy.

If the $s_{\pm}$ gap symmetry is correct, the superconducting pairing is achieved via antiferromagnetic fluctuations, which are in turn coupled to the lattice. The superconductivity is then induced, if this order parameter changes sign under a translation from the electron to hole pockets. In real space, this produces to an oscillating potential which may be

attractive for certain spacings of the Cooper pair electrons. The connecting of different parts of the Fermi surface by a fixed wavevector is known as nesting. Nesting can drive the formation of a spin density wave of wavevector (q). This is because in the presence of a varying magnetic field, such as the one caused by the spin-density wave, instabilities arise in the inverse q-dependent (dynamic) paramagnetic susceptibility. For one dimensional materials, this is known as the Kohn anomaly. These effects may lower the total energy the electrons, resulting in an energy gap at the Fermi level along the region where the Fermi surface nesting occurs. As there is no angular anisotropy of this superconducting state's symmetry, the energy gap will have no nodes, i.e. there is no point in reciprocal space where the superconducting energy gap is zero.

A theoretical understanding of superconductivity in the iron pnictides is still in its infancy however. Indeed, the $s_{\pm}$ state is not the only order parameter to have been suggested, other examples include p-wave [69], d-wave and mixed symmetry sates [70, 71], some of which have nodes. Therefore, a large amount of experimental evidence is needed to determine the pairing state of these compounds. Recently, inelastic neutron scattering measurements, which are sensitive to the phase of the energy gap on separate Fermi surface regions, has detected the existence of a magnetic resonance in $Ba_{0.6}K_{0.4}Fe_2As_2$ [72] below T_c. Further single crystal measurements, have shown that this resonance is located at the Fermi surface pockets at a wavevector of (0.5 0.5 L) [73]. This magnetic resonance is believed to arise from an enhancement of the dynamic magnetic susceptibility, due to the Fermi surface nesting described above. This result when combined with APRES measurements [74], seem to point towards $s_{\pm}$ wave symmetry. Knowing the order parameter of the pnictides will not be the end of the story however. For example, the d-wave symmetry of the cuprates has been known for over a decade [75], yet a microscopic mechanism for the superconductivity in these compounds is still undetermined. Thus, a clarification of the multiband structure, and the unusual interactions between the Fe spins and the crystal structure in the pnictides, is vital for a complete understanding of the superconducting mechanism.

3.1.4 Previous studies of the pnictide's lattice dynamics

The previous section has shown that one possible mechanism for superconductivity in the pnictides may involve a coupling between the spin and lattice degrees of freedom. However, recent experimental evidence has established that the lattice, and therefore phonons, may still contribute to the electron coupling in the pnictides. In particular, neutron diffraction measurements [76] of powder samples of $RFeAsO_{1-\delta}$ (R=La or Nd), have shown that superconductivity is closely related to the As-Fe-As bond angle (α). The T_c of several pnictide structures [77] is a maximum when the $FeAs_4$ tetrahedron approaches a regular tetrahedron in shape (α=109.47°). Furthermore, EXAFS measurements on $LaFeAsO_{0.93}F_{0.07}$ [78] have shown a significant reduction in the mean-squared relative displacement of the Fe-As bond, at the onset of superconductivity. Finally, strong evidence for at least some electron-phonon coupling, can be found in isotopic substitution measurements made by Liu and co-workers. Here, the ^{16}O atoms were replaced by ^{18}O isotopes in $SmFeAsO_{1-x}F_x$ (x=0 & 0.15) and the ^{56}Fe atom was replaced by ^{54}Fe isotopes in $Ba_{1-x}K_xFe_2As_2$ (x=0 & 0.4) [79]. Resistivity measurements on these compounds showed slight but significant increases in T_N (x=0) and T_c ($x\neq0$). While these results suggest that electron-phonon coupling cannot be completely ignored, there is also significant evidence which suggests that this coupling is too weak to cause the superconductivity in these compounds. Most notably, the D.F.T. band structure calculations on LaFeAsO by Singh and Du [5] were extended by Boeri *et al* [80], who used density function perturbation theory to estimate the electron-phonon coupling strength. This work found that the coupling was evenly distributed amongst all phonon modes. This result allows one to approximate the spectral density function $\alpha^2F(\omega)$, the bare phonon density of states weighted by the electron-phonon coupling matrix elements (α^2), to the experimentally determined value of the phonon density of states (PDOS). Thus one can determine the strength of electron-phonon coupling (λ) by integrating the experimental PDOS over all mode frequencies:

$$\lambda = 2\int_0^\infty \frac{\alpha^2F(\omega)}{\omega}d\omega \tag{3.1}$$

Where $\alpha^2F(\omega)$ is replaced by the experimental PDOS.

Boeri *et al.* [80] calculated a theoretical value of 0.21 for λ. This indicates that the electron-phonon interaction is much weaker than any other electron-phonon superconductors. By using the Allen-Dynes approximation (equation 3.2), which is based upon the Eliashberg equations and used to estimate the critical temperature of BCS superconductors [81], Boeri and co-workers estimated a superconducting transition temperature due to BCS electron-phonon coupling of 0.5 K. This value was deduced from a logarithmic phonon average [82] of ω_{ln}=205 K and a Coulomb repulsion of μ^*=0.

$$k_B T_c = \frac{\hbar\omega_{ln}}{1.2} exp\left[-\frac{1.04(1+\lambda)}{\lambda - \mu^*(1+0.62\lambda)}\right] \tag{3.2}$$

These theoretical predictions of a weak electron phonon coupling strength, are supported by PDOS measurements on $LaFeAsO_{1-x}F_x$ (x=0 & 0.1) by Christianson *et al.* [83]. It is important to remember however, that both the experimental and theoretical determinations of the electron-phonon coupling strength are based on the assumption that this strength is equal for all phonon modes. For most superconductors this has shown to be correct, however there are exceptions, for example MgB_2 [7, 8]. Therefore, if this assumption proves to be incorrect, the strength of electron-phonon coupling may have been significantly underestimated.

While the work described so far might seem to be contradictory, it is clear that further studies of the pnictide's lattice dynamics are needed. In particular single crystal measurements, which allows one to determine the strength of electron-phonon coupling for individual phonon modes, are extremely important. Experimental techniques that observe the lattice dynamics include inelastic neutron and X-ray scattering, and optical scattering techniques, such as Raman scattering. The majority of lattice dynamics measurements have been conducted on the '122' class of compounds. This is because samples of the '1111' compounds are extremely small ($\approx$100$\times$100$\times$50μm), making single crystal neutron measurements impossible and measurements with other scattering probes very difficult.

Starting with inelastic scattering studies of the '122' compounds. Recent inelastic neutron scattering (INS) [84] and inelastic X-ray scattering (IXS) [85] experiments on $CaFe_2As_2$,

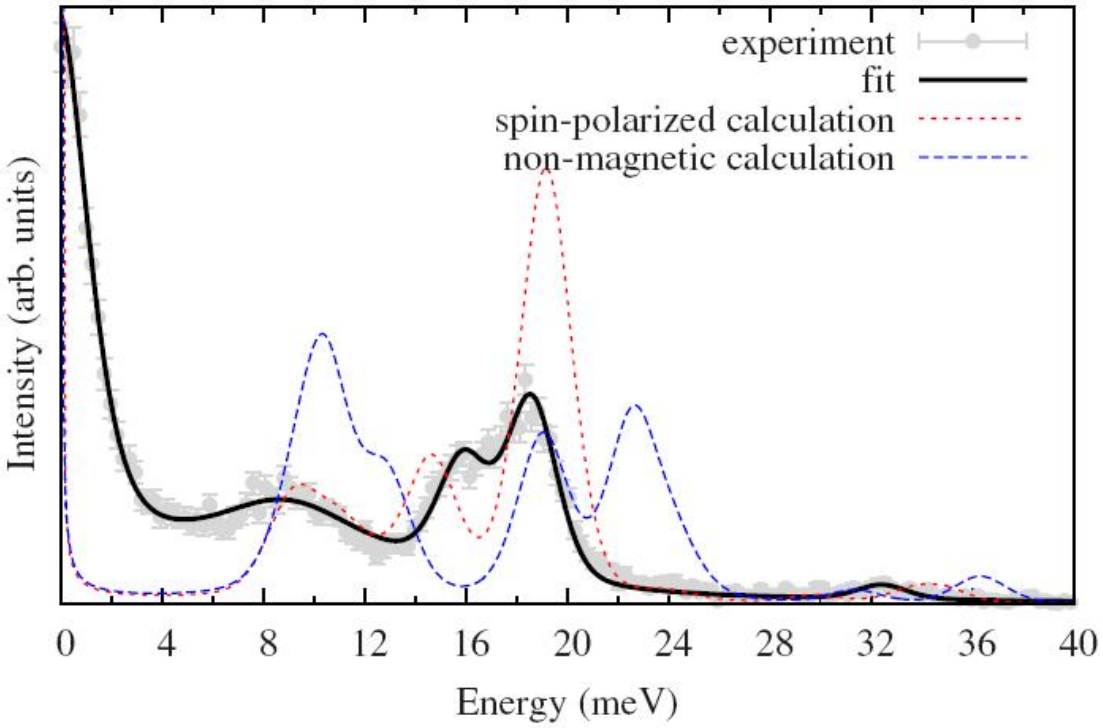

Figure 3.4: A room temperature IXS spectrum of $CaFe_2As_2$, taken at Q=(1.5 0 3), by Hahn *et al.* [85]. The experimental data is shown by the grey points, while the pseudo-Voigt fits of this data are shown by the black solid line. Calculations of the phonon structure factor with (red dashed line) and without (blue dashed line) spin-polarisation are also shown. Neither set of calculations completely agree with the experimental data, however the spin-polarised calculation is clearly in better agreement. This result indicates that the effects of magnetic interactions are needed to understand the lattice dynamics of these systems.

have shown that to gain a better description of the room temperature phonon dispersion, density functional theory calculations, which also take into account the local spin density in the exchange correlation, are needed (see figure 3.4). Thus, due to the strong relationship between the Fe-As bond length and Fe spin state, a significant spin-lattice coupling could indirectly contribute to superconductivity [86]. Furthermore, an INS measurement on $BaFe_2As_2$ [87] has found spin-wave excitations above 100 meV, this suggests that spin-fluctuations are a serious candidate in mediating superconductivity in the pnictides.

In addition, the phonon density of states (PDOS) in $BaFe_2As_2$ [88], $Sr_{0.6}K_{0.4}Fe_2As_2$ and $Ca_{0.6}Na_{0.4}Fe_2As_2$ [89], were measured by inelastic neutron scattering. Comparisons be-

tween the PDOS in the parent and doped compounds show a renormalisation of phonon modes around 20 meV. Although, no anomalous effects upon the superconducting transition were detected in the doped compound. Raman scattering however, showed abnormalities and renormalisations at the parent compound's magnetic and doped compound's superconducting transitions in $Sr_{1-x}K_xFe_2As_2$ [90, 91], $Ba_{1-x}K_xFe_2As_2$ [91] and $Ba(Fe_{1-x}Co_x)_2As_2$ [92].

The room temperature PDOS of $LaFeAsO_{1-x}F_x$ (x=0 & 0.1) has also been investigated with neutron [83] and X-ray inelastic scattering [93]. INS results from Christianson and co-workers [83] found little difference in phonon frequencies between the parent and superconducting compounds, while the superconducting compound showed only a small variation with temperature. Comparisons between the experimental PDOS and first-principle calculations of Boeri *et al.* [80] gave excellent agreement for values of electron-phonon coupling strength (λ), and T_c.

In addition, IXS measurements were performed on the same compounds by Fukuda *et al.* [93], also the phonon dispersion along the [1 0 0] direction of a single crystal of the oxygen deficient pnictide, $PrFeAsO_{0.9}$, was measured. PDOS measurements on $LaFeAsO_{1-x}F_x$ showed the existence of three phonon modes at 13, 23 and 30 meV. The modes at 13 and 23 meV were again in good agreement with the calculations of Boeri *et al.* [80]. Although, the third mode at 30 meV was softer with respect to the theoretical calculations. The authors account for this difference, by reducing the Fe-As nearest neighbour force constant by 30%. The softening of this mode was reduced upon cooling to 35 K, but no other changes were observed in the PDOS. The disagreement between theory and experimental data could be explained by the sensitivity between the Fe spin state and the Fe-As bond length. As the *ab initio* calculations underestimate the size of the Fe magnetic moment [94], this in turn will lead to a underestimation of the bond length.

The effect of fluorine doping on phonon modes has also been investigated by Raman scattering, in microscopic grains of polycrystalline $CeFeAsO_{1-x}F_x$ and $LaFeAsO_{1-x}F_x$ [95]. This paper identifies several Raman active modes, the authors report a noticeable change in the La E_g and A_{1g} mode frequencies upon fluorine doping. These changes were

associated with the fluorine ion entering the Re-O layer. Meanwhile, little changes were seen in the Raman active modes, which are associated with the motions of the ions in the Fe-As layer.

In addition, the fluorine doping effects on the room temperature phonon density of states, in powder samples of $NdFeAsO_{1-x}F_x$ ($x = 0$ & 0.15), were investigated by inelastic X-ray and Raman scattering by Le Tacon *et al.* [6]. In agreement with the work of Fukada *et al.* [93], the authors report that IXS measurements showed three peaks in the parent compound's PDOS spectrum. These peaks were located close to 13, 24 and 32 meV, again the energy peak at 32 meV is softer than theoretically predicted. The effect of fluorine substitution on the PDOS of $NdFeAsO_{1-x}F_x$ is shown in figure 3.5(a). As the figure indicates, there are no major changes in the PDOS peaks at 13 and 32 meV. However, the peak at 24 meV shows a significant change with doping, as an extra feature in the PDOS around 21 meV is seen. The same effect is also seen in $SmFeAsO_{1-x}F_x$ (figure 3.5(b)). The phonon modes around 24 meV were initially studied in the parent compounds LaFeAsO and SmFeAsO by Hadjiev *et al.* [96]. This work assigned three Raman active optical phonon modes to this energy region. Specifically, group theory calculations showed that these modes correspond to the *c*-axis polarised motions of the rare earth (A_{1g} symmetry), As (A_{1g} symmetry) and Fe (B_{1g} symmetry) atoms. Thus, the differences seen in the PDOS corresponds to the softening of at least one of these modes. The Raman scattering measurements of Le Tacon *et al.* [6] used these classification to characterise the three zone-centred modes, observed in NdFeAsO between 15 and 30 meV. The first line had an energy of 20.5 meV, and corresponds to the A_{1g} mode of Nd. The second mode close to 24.5 meV was associated with the As A_{1g} mode. Finally, the third mode at 25.3 meV corresponds to the Fe B_{1g} mode. It should be noted however, that since this initial research, lattice dynamical calculations which give a more precise value for the eigendisplacements of each mode, have shown that: the rare earth A_{1g} mode also has *As* atoms moving in-phase with it, the As A_{1g} mode also contains out-of-phase motions of the rare earth atoms, finally the Fe B_{1g} mode also contains the motions of surrounding oxygen atoms. Therefore, these modes will now be referred to as: the in-phase A_{1g} (*Re*,*As*), the out-of-phase A_{1g} (*Re*,*As*) and the B_{1g} (*Fe*,*O*) modes respectively. Schematic representations of these three modes

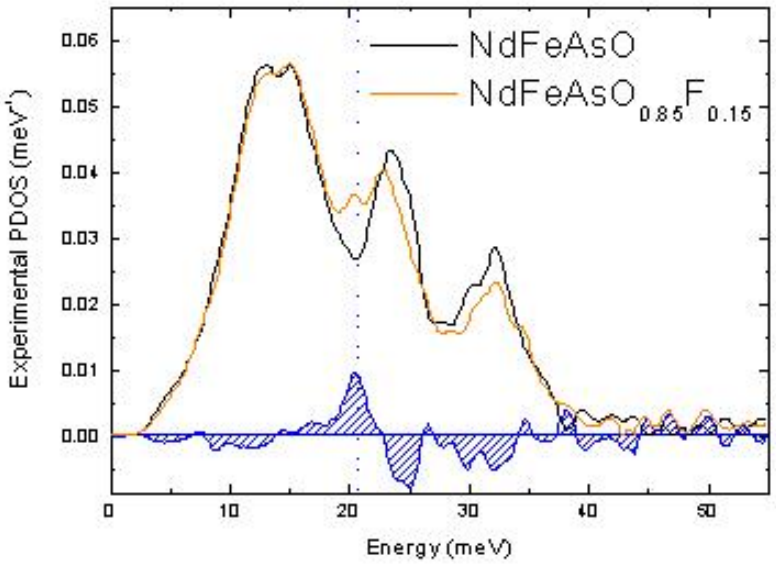

(a)

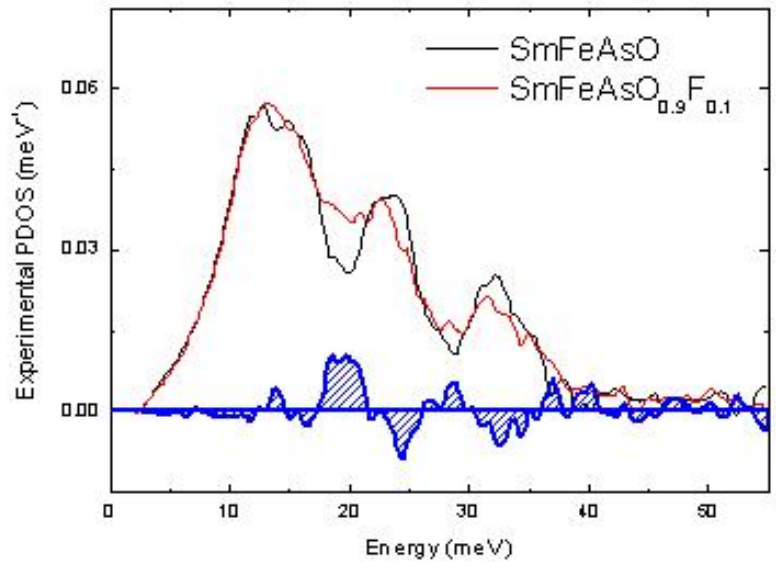

(b)

Figure 3.5: 3.5(a) PDOS of NdFeAsO and $NdFeAsO_{0.85}F_{0.15}$ [6] and 3.5(b) PDOS of SmFeAsO and $SmFeAsO_{0.9}F_{0.1}$ (unpublished). The figures show a difference between the density of states of the parent and superconducting compounds at 21 meV, this corresponds to a doping induced softening of at least one of the three optical phonon modes, identified by Hadjiev *et al.* [96]. Schematic representations of these modes are shown in figure 3.6.

at $q = 0$ are shown in figure 3.6.

Upon doping, Raman scattering measurements showed that the in-phase A_{1g} (Nd,As) phonon softens by 0.3 meV. Le Tacon *et al.* [6] state that this effect may be explained by an increase in the Nd-O distance due to fluorine doping. Similarly, a small softening was also expected for the other two branches, due to a corresponding increase in the Fe-As distance. Experimental results however, show that these two branches harden by 0.6 meV. The authors suggest, that this hardening may be explained by the compound becoming more metallic with doping. Consequently, the Coulomb screening is modified, changing the phonon frequency. As the states close to the Fermi level originate from the Fe $3d$ bands, this effect is greatest for atoms of the Fe-As layer. The authors conclude the paper, by stating that single crystal dispersion measurements are needed to fully explain these renormalisations.

3.2 Experimental details

The PDOS results presented by Le Tacon *et al.* [6], demonstrate that the lattice dynamics of the pnictides are affected by fluorine doping. In order to determine the relevance of this doping-induced renormalisation to the superconducting mechanism, single crystal IXS measurements, which can display the effects of fluorine on the individual phonon modes, are required. The remainder of this chapter will be used to describe such a single crystal IXS study, on the pnictide compounds: SmFeAsO and $SmFeAsO_{0.60}F_{0.35}$.

3.2.1 Crystal growth and characterisation

High quality single crystal samples of both SmFeAsO and $SmFeAsO_{0.60}F_{0.35}$, with dimensions of $100 \times 100 \times 50 \mu m^3$, were grown by Kapmski's group at ETH, Zürich, Switzerland [52]. The samples were grown in a NaCl/KCl flux, by placing powders of the starting materials (SmAs, FeAs, Fe_2O_3, Fe and SmF_3) into a BN crucible. Six tungsten carbide anvils were then used to provide a pressure of 3 GPa at room temperature. While keeping

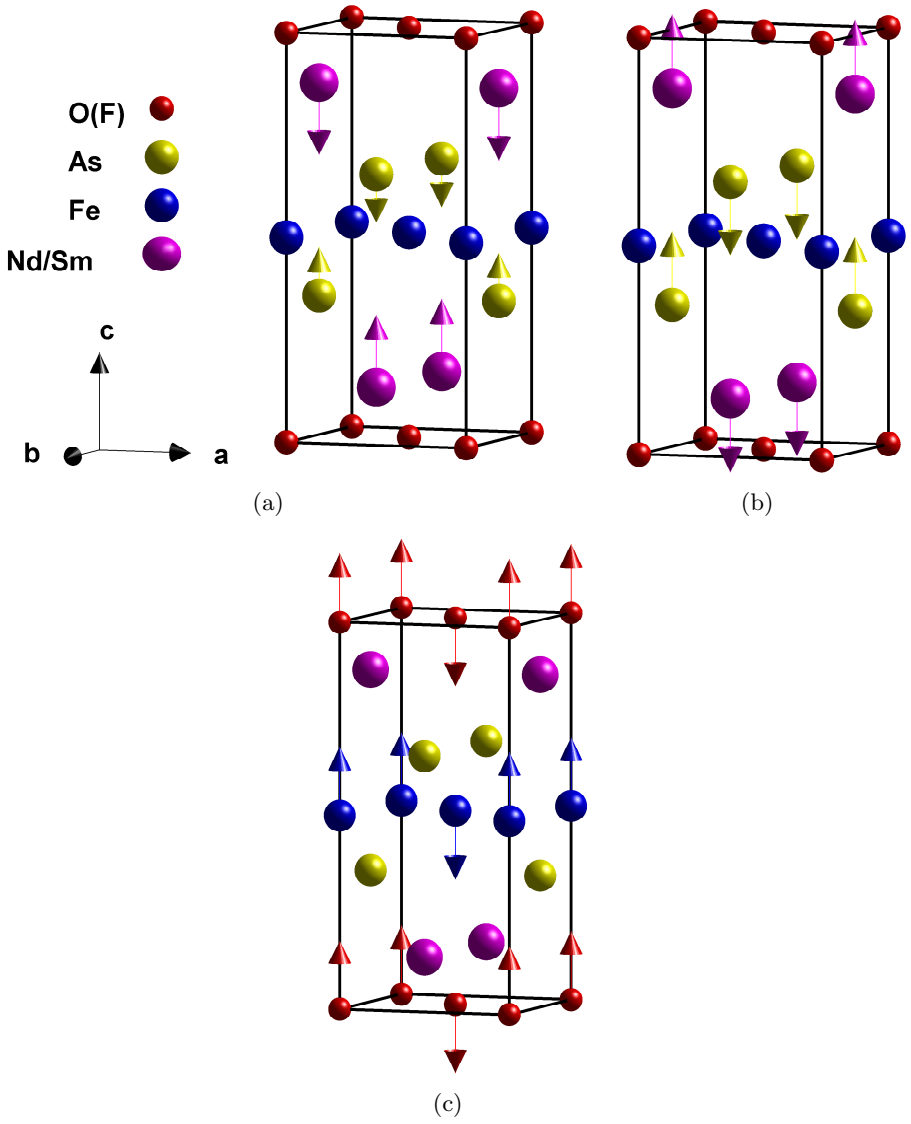

Figure 3.6: Schematic representations of the three c-axis polarised Raman active modes (at $q = 0$), identified by Hadjiev and co-workers [96]. These modes are: 3.6(a) the in-phase A_{1g} (As,Sm) mode, 3.6(b) the out-of-phase A_{1g} (As,Sm) mode, 3.6(c) the B_{1g} (Fe,O) mode.

the pressure constant, the temperature inside the crucible was increased to 1350-1450°C, then maintained for 4-10 hours, after which it was slowly reduced to room temperature. The NaCl/KCl flux was then dissolved in water. Structural refinements were performed using a lab based X-ray diffractometer, with a CCD area detector. Results from these refinements showed the samples had the correct crystallographic structure, with negligible flux impurities. SQUID measurements gave a magnetic ordering temperature of T_N=130 K for SmFeAsO, and a superconducting transition temperature of T_c=53 K for $SmFeAsO_{0.60}F_{0.35}$. Both of these transition temperatures are in agreement with published research [55, 97].

For the IXS experiments described in this chapter, the crystal samples were initially mounted by sandwiching them inside two sheets of $20\mu m$ thick Kapton film. However, locating the crystal samples with this mounting proved to be extremely difficult. In addition, the samples were free to move during an experimental run. By trial and error, a solution was found by fixing a crystal's c-face onto a small piece of Kapton film approximately $250 \times 250\mu m^2$ in surface area. The opposite end of this film was then fixed to the end of a small plastic rod (diameter $500\mu m$), whose tip was melted to a point. Pictures of the mounted sample can be found in figure 3.7. Both the sample and plastic rod were fixed to the Kapton with Araldite adhesive. This set up allowed the sample to be fixed securely and easy to locate. In addition, this sample mounting allows for the experiments to be conducted in both reflection and transmission geometries.

3.2.2 Spectrometer configuration and scattering geometry

All experimental measurements were conducted on the ID28 beamline, at the ESRF (see section 2.4.3). In order to utilise the Si(11 11 11) backscattering reflection, an incident photon energy of 21.747 keV was selected, this set-up provided an energy resolution of 2 meV. The X-ray beam was focused down to $50 \times 40\mu m^2$, through the use of the toroidal mirror and W/C multilayer. Initial elastic scattering measurements of the (004) Bragg reflection, in both samples, gave rocking curves with a FWHM of 0.5°. This gives a resolution along the c-axis of 0.202Å^{-1} or 0.27 reciprocal lattice units. In addition, rocking

curves of the (200) Bragg reflection gave FWHM of 0.25°, indicating that the resolution along the a-axis was 0.076Å^{-1} or 0.05 reciprocal lattice units.

It has already been established, in section 2.4, that the intensity of scattering from a phonon mode is proportional to $(\mathbf{Q} \cdot \sigma_{\mathbf{n}})^2$. Therefore, to maximise the intensity of scattering from the three c-axis polarised modes, measurements should be taken in the Brillouin zone with a large Q_c component. However, because of the proximity of these three modes to one another, *a priori* lattice dynamics calculations are also extremely useful in suggesting which Brillouin zones provide the best contrast between the different modes. These lattice dynamics calculations were based upon D.F.T. performed on a 2×2×1 supercell of $LaFeAsO_{1-x}F_x$, where fluorine doping was accounted for by replacing one oxygen atom with a fluorine atom. This D.F.T. work was performed by Noffsinger *et al.* [98] using the QUANTUM-ESPRESSO package. The ground electronic structure was calculated within the local density approximation (LDA), while the lattice dynamical properties were calculated by density-functional perturbation theory. It should be noted that these calculations were not spin polarised.

In order to determine the optimal Brillouin zone in which to measure the c-polarised optical modes, Bossoft (written by Alexei Bosak, ID28, ESRF), a parasitic *a priori* lattice dynamics program. Specifically, this program calculates the IXS spectrum as a function of the total momentum transfer Q. This is achieved by using the eigenfrequencies and eigenvectors from the output of *ab-initio* (or non-*ab-initio*) programs, such as AbInit, CASTEP, Phonon or Unisoft, to calculate the dynamic structure factor S(Q,E), within the limit of one-phonon scattering:

$$S(\mathbf{Q}, E) = \sum_m \left\langle n(E) + \frac{1}{2} \pm \frac{1}{2} \right\rangle (E_j(\mathbf{q})^{-1} F_{in}(\mathbf{Q})) \delta(E \pm E_j(q)) \tag{3.3}$$

Here F_{in} is:

$$\mathbf{F_{in}}(\mathbf{Q}) = \left| \sum_m M_m^{-\frac{1}{2}} f_m(\mathbf{Q}) \left[e_m^j(\mathbf{q}) \cdot \mathbf{Q} \right] e^{i\mathbf{Q}\cdot\mathbf{r_m}} f_{dw} \right|^2 \tag{3.4}$$

Thus when calculating the inelastic scattering spectrum, this program also takes into account the scattering strength of each phonon due to the elemental species involved,

through the crystal's atomic form factor, which is a function of Q and the electron charge density. In addition, the atomic mass (or more precisely $M_n^{-1/2}$) is also entered. The effects of temperature are accounted for through the Debye-Waller factor (f_{dw}) which describes non-phonon thermal vibrations, and Bose factor ($n(E)$) which gives the phonon population at a specific temperature.

Once Bossoft has these initial parameters, it can calculate not only the IXS spectrum for individual Q points, but also compare spectra for a given reduced q in different Brillouin zones, or produce an E-Q intensity map for a given set of Q and Brillouin zone. Perhaps more importantly, for a given reduced momentum transfer (q) and specific phonon mode, the Bossoft program will determine in which Brillouin zone the mode's intensity will be maximum, or where the contrast with respect to other modes is greatest.

Results from these *a priori* calculations suggest that the zone around the (1 0 12) Γ-point, was a good choice for the IXS measurements. This was due to the zone having a large Q_c component, and calculated Q-points which had significant contrast between the three optical modes. In addition, for the $P4/nmm$ crystal structure, (1 0 12) is a forbidden reflection, thus the elastic line at low q should not have an extra component arising from a Bragg peak's tail. Practically, this choice of Brillouin zone corresponded to a challenging quasi-grazing incidence reflection geometry. With such small samples, this meant that even a small rotation in θ could lead to the sample precessing out of the beam, thus it was extremely important to align the sample as close to the diffractometer's centre of rotation as possible. In addition, a fluorescence detector was installed at the front of the 2θ detector arm during the second half of the experiment. This also helped to locate the sample. All measurements were taken at room temperature, in the paramagnetic phase. Lattice constants were determined from elastic scattering measurements, also taken on ID28. In the tetragonal unit cell, these were: a=b=3.939Å, c=8.485Å for SmFeAsO and a=b=3.931Å, c=8.472Å for $SmFeAsO_{0.60}F_{0.35}$.

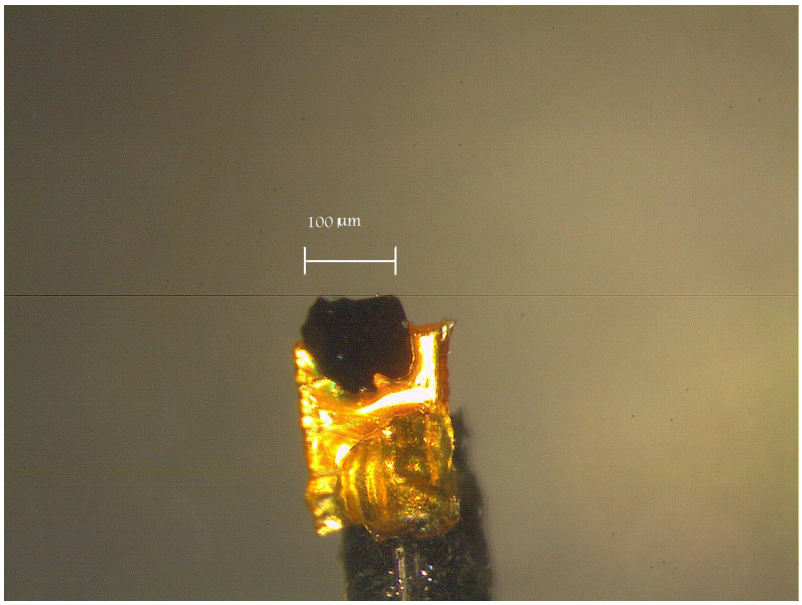

(a)

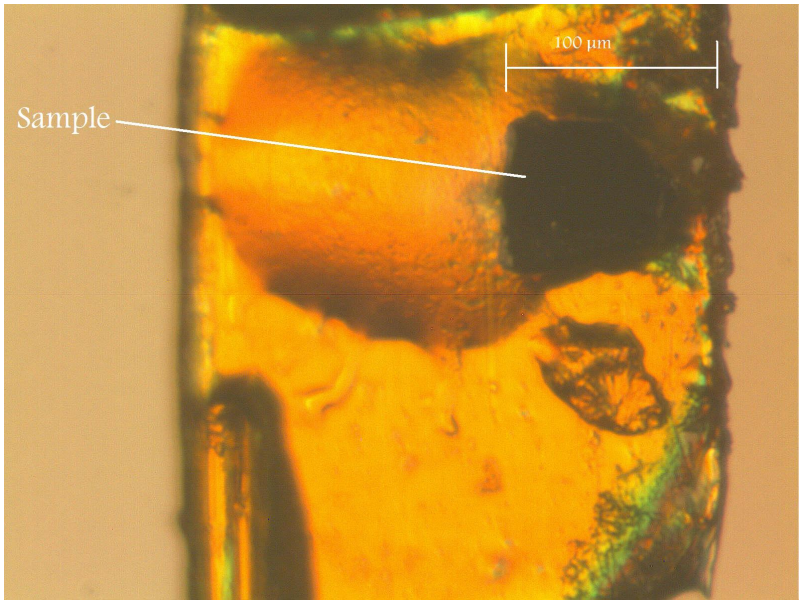

(b)

Figure 3.7: photographs taken under an approximate magnification of 1000×. 3.7(a) is the superconducting compound: $SmFeAsO_{0.60}F_{0.35}$. 3.7(b) is the parent compound: SmFeAsO.

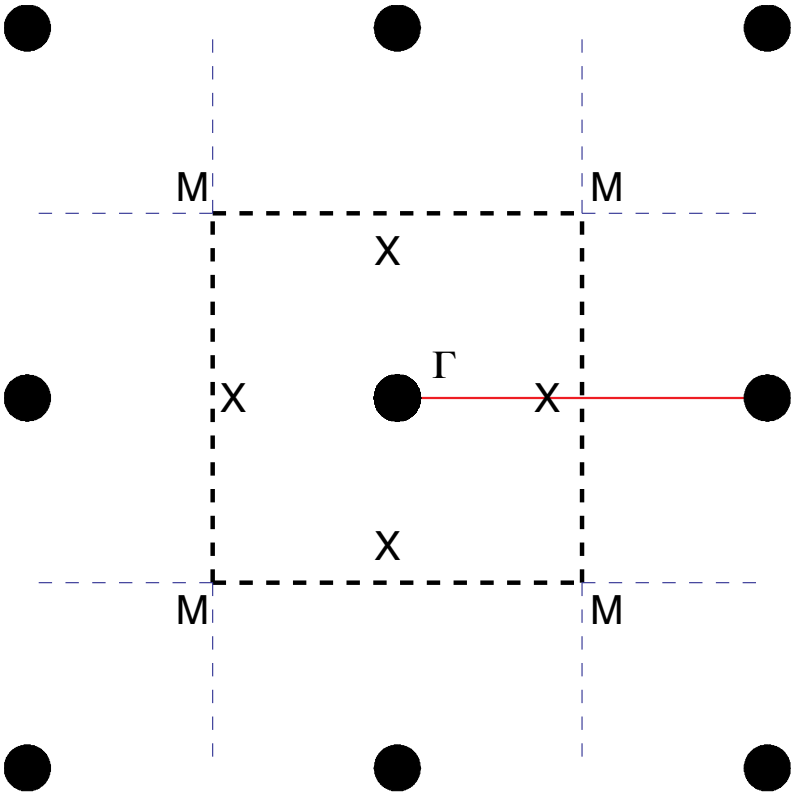

Figure 3.8: A diagram of the a^*-b^* plane Brillouin zone for $SmFeAsO_{1-x}F_y$. The black circles represent reciprocal lattice points, while the black dashed square is the boundary of the first Brillouin zone, The blue lines represent the boundary of other zones. The centre (Γ), edge centre (M) and corner (R) points of the Brillouin zone are also labelled. Finally, the red line represents the direction along which the IXS dispersion, of the optical phonon modes, was measured.

3.3 Experimental results

After two partially successful experiments, the majority of results were taken during an experimental run in February 2009. Although, some additional measurements were taken during in-house time in March and April 2009. During these experiments, IXS spectra were taken at several Q-points. Specifically, these were: (0.6 0 12), (0.7 0 12) and (0.8 0 12) for the superconducting compound, and (0.6 0 12) and (0.8 0 12) for the parent compound. In addition, by utilising ID28's eight crystal analysers (one analyser was broken), multiple Q-points could also be measured simultaneously. Maps of the different analyser positions in the q_a-q_c plane are shown in figure 3.9, the resolution along q_a and q_c at each q-point is also shown. Because the crystal structure of these compounds is primitive, the Brillouin zones boundary is at q_x=q_y=q_z=0.5 r.l.u. This is shown in figure 3.8. Thus, any q-point which has a component greater than 0.5 r.l.u., will have this component reflected back into the first Brillouin zone, for example q=(0.6 0 0.55) will transformed to q=(0.4 0 0.45).

Figure 3.10 shows an example IXS spectrum of SmFeAsO at Q=(0.6 0 12) (q=(0.4 0 0)), with the 23 meV optical phonon region magnified. The spectrum shows that, in addition to the three optical modes, there is clearly at least one acoustic mode close to an energy transfer of 11 meV.

3.3.1 Analysis of the IXS spectra

All experimental spectra were initially fitted with resolution limited pseudo-Voigt functions, using a least squares approach. This was achieved by using the Spec1d routine. Spec1d, written by Des McMorrow and Henrik Rønnow, is designed to perform efficient non-linear least squares analysis of one dimensional (i.e. x, y, error) data sets from the command line in MATLAB. During the non-linear least squares fitting, the change in a fitting parameter at each iterative step is determined using the LevenbergMarquardt algorithm, which is a combination of the Gaussian-Newton algorithm and method of gradient descent [99]. The goodness of fit between the experimental data and the theoretical

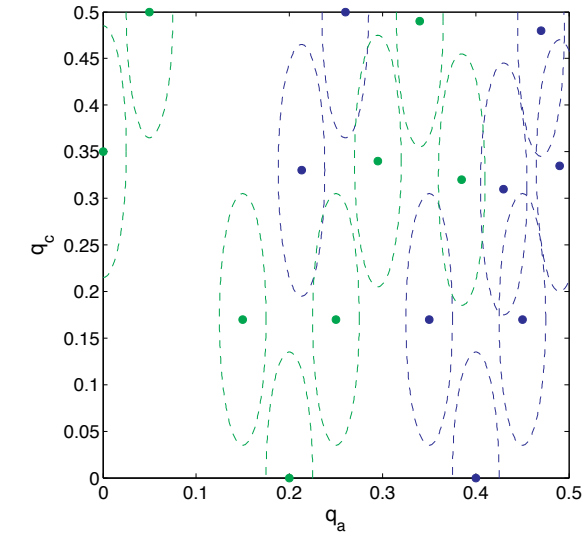

(a)

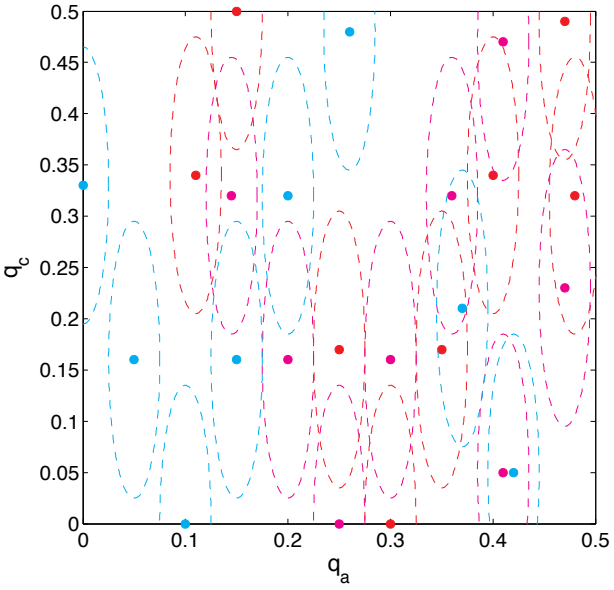

(b)

Figure 3.9: A map of ID28's eight analyser position (analyser number 4 was broken during the experimental run), in the reduced q_a-q_c plane. Also included in the figure are ellipses, which represent the resolution at each q-point. Figure 3.9(a) represents the measured q-points in both the parent and the superconducting samples. The blue data points represent the eight analyser positions when analyser number 3 was at Q=(0.6 0 12). The green data points for analyser 3 at Q=(0.8 0 12). Figure 3.9(b) represents q-points which were measured in the superconducting sample only. The red data represent the eight analyser positions when analyser 3 was at Q=(0.7 0 12). The maroon data points for analyser 2 at Q=(1.25 0 11). The cyan data points for analyser 2 at Q=(1.1 0 11).

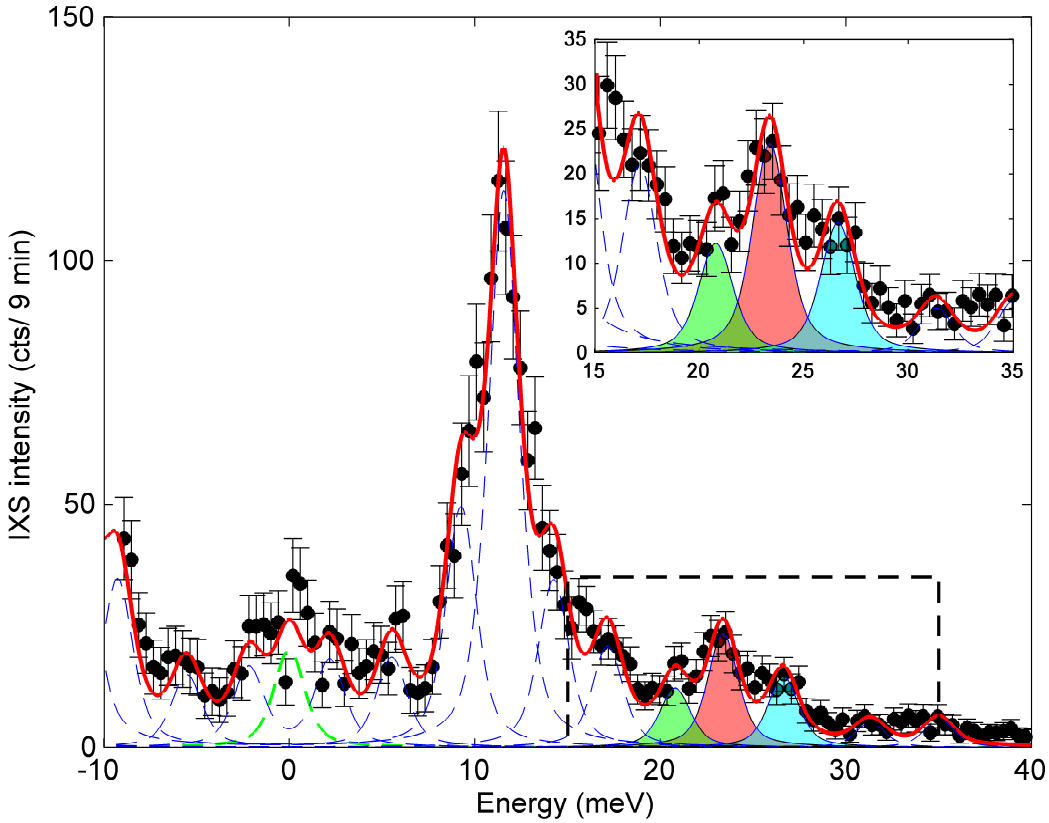

Figure 3.10: A example of a typical IXS spectrum of SmFeAsO at q=(0.4 0 0). The three c-axis optical modes are magnified and highlighted. In addition, the large peak at 11 meV corresponds to the transverse acoustic mode along the [001] direction.

distribution, i.e. the pseudo-Voigt functions, is defined by the reduced χ^2 value:

$$\chi^2 = \frac{1}{\nu}\sum_{k=1}^{m}\frac{(y_k - f(a_0, ..., a_n; x_k))^2}{\sigma^2} \tag{3.5}$$

x_k and y_k are the experimental data points, $f(a_0, ..., a_n; x_k)$ is the fitted function of the parameters, a_n. σ^2 is the variance of the observations, which is useful, as it weights each of the data points according to the accuracy/error of each measurement. Finally, the variable ν is the degrees of freedom of the fit, such that:

$$\nu = M - (N + 1) \tag{3.6}$$

M is the number of data points and N is the number of free parameters. Thus, the reduced χ^2 values allows one to compare the goodness of the fit to different sets of data, which may vary in the number of features to be fitted. A fit was determined to have converged with the experimental data, when the difference in the reduced χ^2 between two successive iterations, denoted by g, was less than a predefined fraction (τ) of the last iteration:

$$\frac{\chi^2(g) - \chi^2(g+1)}{\chi^2(g+1)} \leq \tau \tag{3.7}$$

Usually τ is set to a very small value, for most of the fitting performed in this thesis, τ=1×10^{-10}.

Confidence limits

After convergence of the fit is reached, it is important to determine an error for the fitted parameters. However, because the data set (i.e. x, y, $error$) used to determine the parameters contain random measurement errors, it will be just one of a range of data sets. The same is also true for the corresponding fitting parameters, because, if the experiment was repeated again one would generate, from the new data set, different values for the fitted parameters through the χ^2 minimisation process. Thus, each set of free fitting parameters are part of the probability distribution, which is contained within a multiple-dimension space of all the possible parameters values. Instead of presenting the full details of the

probability distribution, one usually summaries the distribution in terms of confidence limits. These are limits, within which there is a region of the multi-dimension parameter space that contains a certain percentage of the total probability distribution. In one dimension, this is usually represented by a line centred on the experimentally determined parameter value. For higher dimensions, ellipses or ellipsoids are used to represent the confidence regions.

A confidence region can therefore be defined in terms of χ^2. As the fitting parameters are found my minimising the χ^2 value (χ^2_{min}), if these parameter values are altered slightly then the value of χ^2 will increase, thus: $\Delta\chi^2$=χ^2-χ^2_{min}. A confidence region may therefore be defined as a region where the increase in χ^2 is less than or equal to a specific choice of $\Delta\chi^2$, which corresponds to a certain confidence percentage. For the fitting shown in this chapter, one is not interested in the limits (error) associated with the confidence region of the overall fit, rather limits (errors) associated with the individual confidence regions of each the parameter taken separately. For such a case, the confidence region for each parameter is a projection of the multi-dimensional regions, defined by $\Delta\chi^2$, onto the one dimensional parameter space. Specifically, for the Spec1d routine, the error of the parameters is defined as the change in the parameter which produced $\Delta\chi^2$=1. For a one-dimensional confidence interval, this corresponds to an line containing 68.3% of the data. Thus, this gives a confidence of 68.3% that the true parameter value lies within the range of data specified by fitted parameter value and the errors. A confidence of 68.3% is used because it corresponds to one normal standard error from the fitted parameter value.

3.3.2 Comparisons between experiment and *ab-initio* calculations

In order to identify the phonon modes, the experimental IXS spectra were compared to the theoretical phonon spectra, produced by the Bossoft *a-priori* program from Noffsinger *et al.*'s [98] D.F.T. work. Particular attention was paid to the optical mode region of the IXS spectra, close to 23 meV. Below is a step by step account of the method used to fit the experimental data to the theoretical calculations.

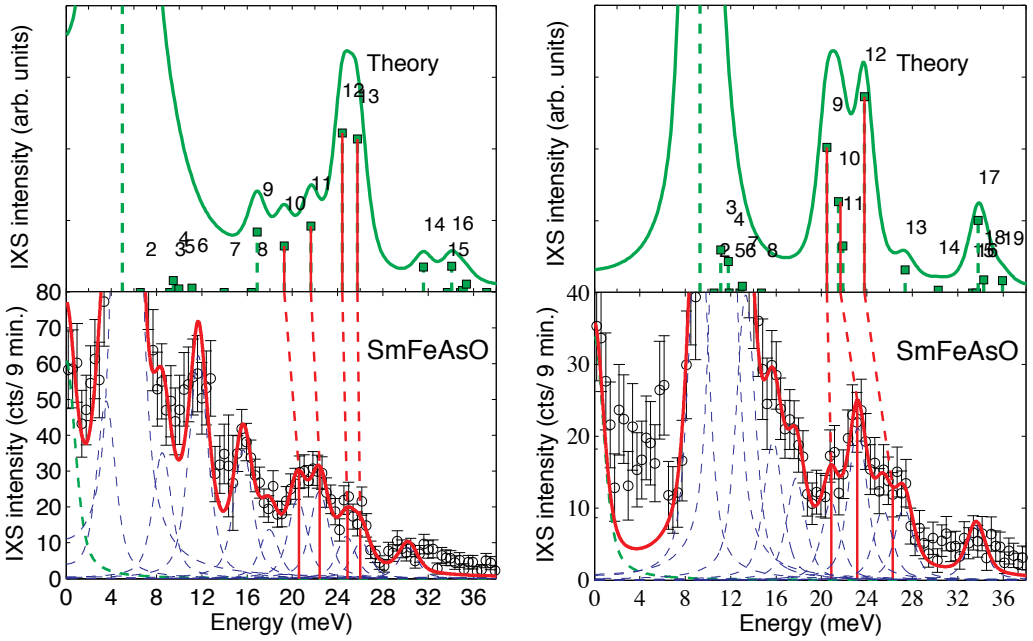

Figure 3.11: A comparison between the theoretical IXS spectra, in the 23 meV optical phonon region. The D.F.T. calculations on LaFeAsO [98] are shown in the top panels, and the experimental IXS spectra of the SmFeAsO are shown in the bottom panels. The spectra correspond to two q-points: 3.11(a) q=(0.2 0 0) and 3.11(b) q=(0.4 0 0). As the figure shows, agreement between theory and experimental data is poor for the 23 meV region.

- Step 1: Start with inelastic spectrum where the calculations only give one strong optical mode. Identify this strong mode with the corresponding peak in the experimental data. The next step is to determine if the positions of the phonon mode, given in the experiment, are the same as the calculations, or have they changed (i.e. softened or hardened).

- Step 2: Now look at the inelastic spectra which have similar reduced wavevector transfer as the spectrum in step 1, but where the calculations give more than one strong optical mode. Apply the same (approximate) softening or hardening to the modes that were identified in step 1. Try to identify the remaining peaks in the experimental data with the previously uncharacterised phonon modes. Also try to be consistent with other spectra at similar wavevector transfers.

- Step 3: Fit the experimental phonon modes with pseudo-Voigt distributions (widths are fixed by the analyser resolution). Finally, use the positions and intensities of the modes characterised in steps one and two as start points, but let them vary.

An example of this procedure is shown in figure 3.11. As the figure shows, the experimental data of SmFeAsO and theoretical calculations on LaFeAsO in the 23 meV region, do not agree. Indeed, the theoretical calculations failed to reproduce the experimental spectra for any measured Q-point throughout the entire Brillouin zone.

3.3.3 Acoustic modes

In addition to measurements of the optical phonon modes, ID28 in-house time was used to measure three acoustic modes, at several q-points along the [100] direction, in both samples. The first acoustic mode to be measured was a longitudinal type (LA), where the in-phase vibrational displacement of all the atoms are parallel to the direction of the mode's propagation, i.e. the [100] direction. IXS spectra of this acoustic mode were recorded in the Brillouin zone centred at the (4 0 0) Γ-point. Specifically, at two points which correspond to Q=(4.15 0 0) and Q=(4.4 0 0), for ID28's crystal analyser number 2. The full list of analyser positions are given in the tables 3.1 & 3.2.

Analyser 1	Analyser 6	Analyser 2	Analyser 7	Analyser 3
3.976	4.063	4.15	4.237	4.323
0.003	0.001	0	-0.001	-0.003
0.120	0.0612	0	-0.064	-0.130
Analyser 8	Analyser 4	Analyser 9	Analyser 5	
4.657	4.741	4.827	4.911	
-0.005	-0.006	-0.008	-0.010	
-0.200	-0.270	-0.343	-0.420	

Table 3.1: Position of the analysers for the longitudinal phonon modes, around Q=(4.15 0 0).

Analyser 1	Analyser 6	Analyser 2	Analyser 7	Analyser 3
4.227	4.314	4.4	4.486	4.572
0.003	0.001	0	-0.001	-0.003
0.120	0.061	0	-0.064	-0.130
Analyser 8	Analyser 4	Analyser 9	Analyser 5	
4.657	4.742	4.827	4.911	
-0.005	-0.006	-0.008	-0.010	
-0.199	-0.270	-0.343	-0.420	

Table 3.2: Position of the analysers for the longitudinal phonon modes, around Q=(4.4 0 0).

An example IXS spectrum of the longitudinal acoustic mode at Q=(4.4 0 0), is shown in figure 3.12. As the figure shows, there is no renormalisation of this mode upon fluorine doping. This was true for measurements taken throughout the Brillouin zone.

The second acoustic mode to be measured was a transverse type (TA2). Here, the vibrational displacements of all atoms are perpendicular to the phonon mode's direction of propagation. Specifically these displacements are along the [001] direction. For this acoustic mode, IXS spectra were recorded in the Brillouin zone centred around the (1 0 12) Γ-point. Specifically, at five Q-points corresponding to: Q=(0.9 0 12), (0.8 0 12), (0.7 0 12), (0.6 0 12) and (0.5 0 12) for the number 3 crystal analyser. Because these modes are highly dispersive along the [001] direction, only the scans from the number 3 crystal analyser can be used to determine the dispersion of this mode along [q_a00]. Figure 3.13 shows an example of the a IXS spectrum of this phonon taken at q=(0.2 0 0).

The IXS spectra of the TA1 mode shows the existence of two phonon modes in the doped sample. The second phonon at an energy transfer 8 meV, in the doped sample, is most likely the second transverse acoustic mode (see below). The fact that the second phonon mode is visible in these IXS spectra, is most likely due to the mosaic of the crystal sample, thus a small part of the b-axis direction might be included in the scattering plane.

Finally, the third acoustic mode to be measured, was again of a transverse type (TA2). Here, the vibrational displacements of all atoms, are along the [010] direction. Like the longitudinal mode, IXS spectra were recorded in the Brillouin zone centred at the (4 0 0) Γ-point, this time at five Q-points corresponding to: Q=(4 0.1 0), (4 0.2 0), (4 0.3 0),

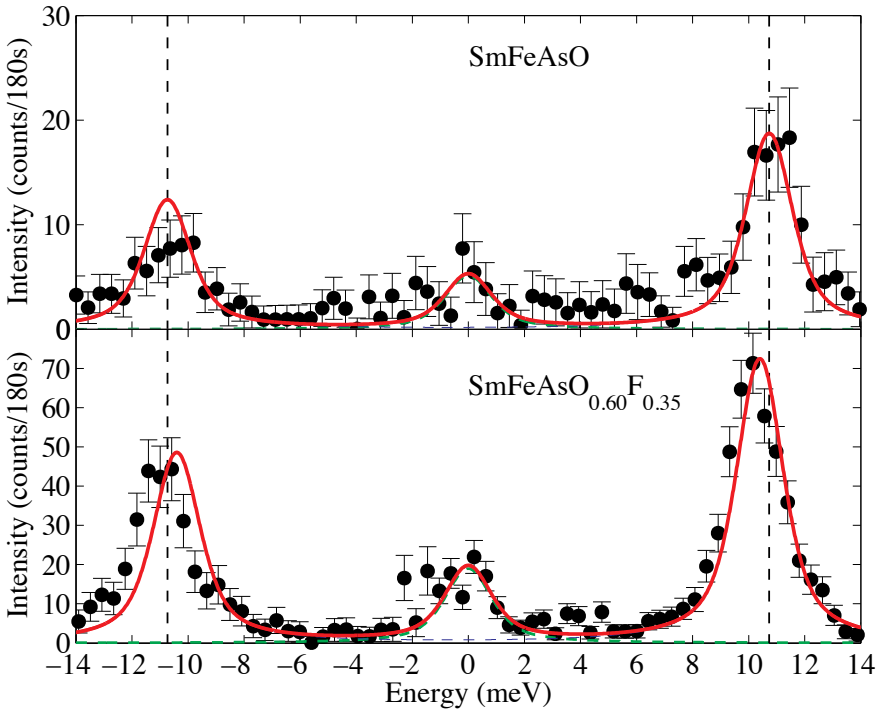

Figure 3.12: IXS spectra of the longitudinal acoustic modes (LA) in (a) SmFeAsO and (b) $SmFeAsO_{0.60}F_{0.35}$ at q=(0.2 0 0). This data was taken at Q=(4.4 0 0), during the April 2009 experiment. The phonons and elastic line were fitted with a Lorentzian profile. The figure shows little or no doping induced renormalisation of this mode.

(4 0.4 0) and (4 0.5 0) for the number 2 crystal analyser. Figure 3.14 shows an example of the a IXS spectra of this phonon, at q=(0 0.2 0).

Figure 3.14 shows little evidence for a renormalisation of the second transverse acoustic mode upon fluorine doping.

The dispersion of the three acoustic modes is included in figure 3.17. The figure shows that the experimental data essentially follow the theoretically predicted dispersion [98].

3.3.4 Optical modes

Clearly, the experimental IXS spectra have failed to reproduce the theoretical phonon spectra of LaFeAsO [98]. However, one is still able to identify the c-axis polarised optical phonon modes [6, 96]. Figure 3.10 shows that at q=(0.4 0 0), all three of the optical

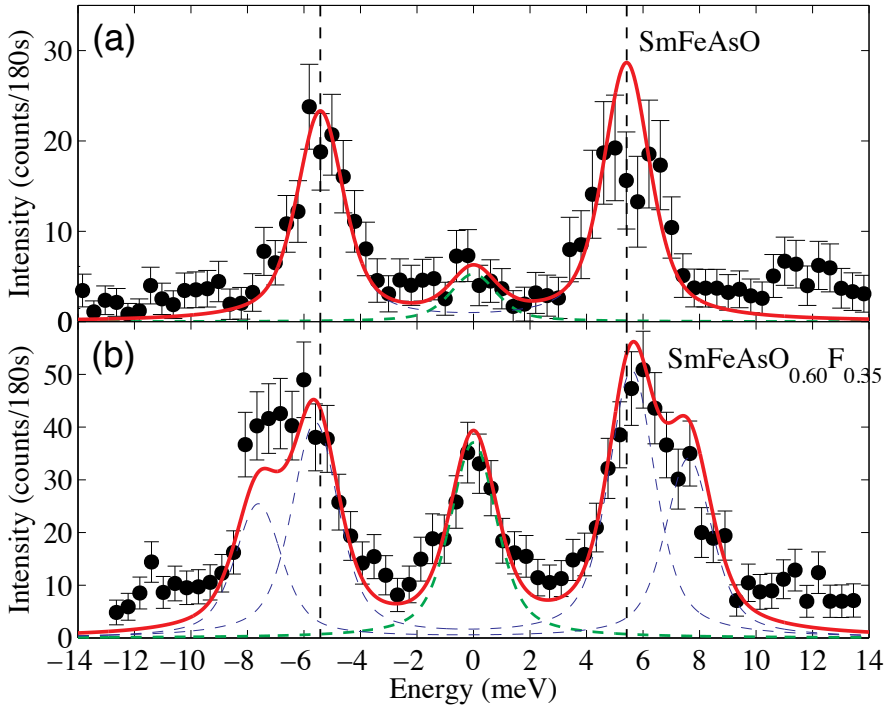

Figure 3.13: IXS spectra of the first transverse acoustic modes (TA1) in (a) SmFeAsO and (b) $SmFeAsO_{0.60}F_{0.35}$ at q=(0.2 0 0), this data was taken during the April 2009 experiment. The phonons and elastic line were fitted with a Lorentzian profile. The figure shows an extra phonon in the doped compound at an energy transfer of 8 meV.

phonon modes are clearly visible. With this result in mind, the optical phonon modes were fitted for all recorded IXS spectra. This time, the spectra were fitted independently of the theoretical calculations. By starting with a experimental spectrum, such as the one in figure 3.10, that clearly shows all three optical phonon modes. The positions of the phonon modes in these experimental spectra, were again re-used as the starting values for the phonon positions, for experimental spectra taken close by. In addition, instead of fitting the spectra with pseudo-Voigt functions, the phonons were analysed by fitting a series of Lorentzian profiles. The change in fitting profiles was due to the fact that the fitting was no longer performed with a fixed width. This time the fits were performed using the multifit routine, written by Toby Perring. Like Spec1d, multifit performs non-linear least squares analysis from the Matlab command line, again using the LevenbergMarquardt algorithm.

The multifit routine may perform non-linear least square fitting, where the parameters are

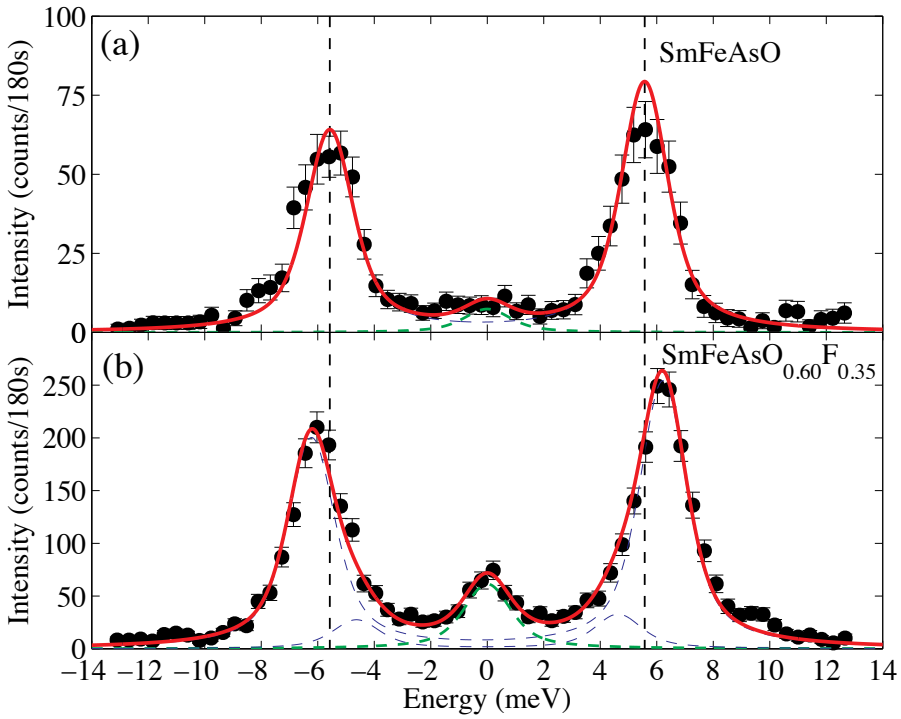

Figure 3.14: IXS spectra of the second transverse acoustic modes (TA2) in (a) SmFeAsO and (b) $SmFeAsO_{0.60}F_{0.35}$ at q=(0 0.2 0), this data was taken during the April 2009 experiment. The phonons and elastic line were fitted with a Lorentzian profile.

either completely free to vary or are fixed to their initial values. These programs however, are not constructed to perform constrained fits, i.e. where a parameter is free to vary inside a given range. Constrained fits are important when fitting the phonon modes in SmFeAsO and $SmFeAsO_{0.60}F_{0.35}$, as fitting the data with a fixed width of the analyser resolutions gave poor values of χ^2, while fits with a freely varying parameter gave phonon modes with unphysically large widths. To overcome this problem, an *if* statement was placed into the fitting function file. If the program tries to perform a fit where the width parameter is greater or less than a percentage of the starting value (usually 10%), then this statement will add a constant to the fitting function that is proportional to the difference between the current (not allowed) width, and the upper limit of the allowed width parameter. This has the effect of increasing the χ^2 value of the fit, forcing the program to modify the width parameter back to the previous value, which is in the allowed range. The effects of this *if* statement can be seen in figure 3.15. This is a plot of parameter space for a Lorentzian curve, where the central position of the curve has been fixed.

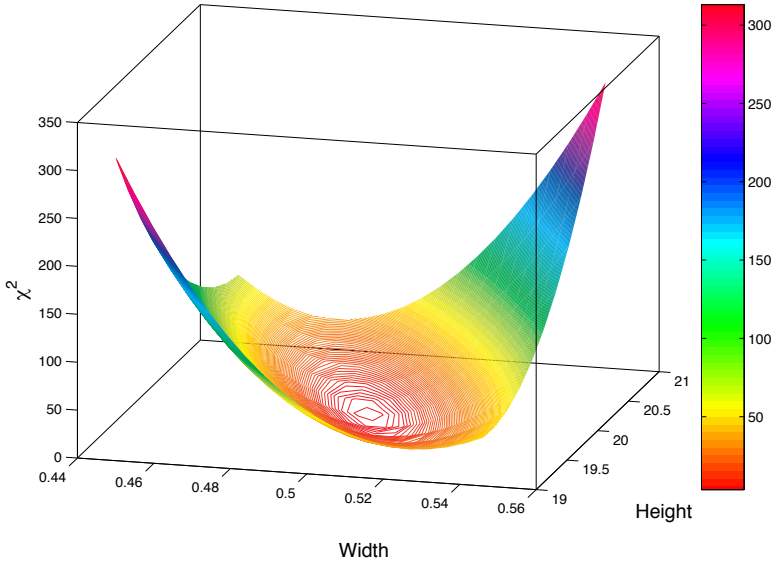

(a)

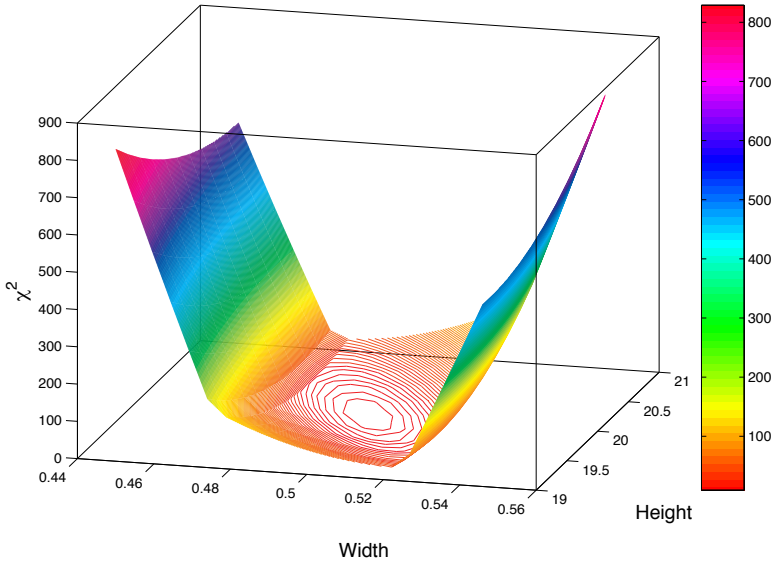

(b)

Figure 3.15: Parameter space (width and height) plots of the verses χ^2 of a Lorentzian curve which has the parameters, amplitude=20, FWHM=0.5, centre=0 (fixed). The upper panel is the χ^2 surface for a completely unconstrained fit (except for the curve's centre). The lower panel is the χ^2 surface, where the width parameter is constrained to the range $0.5\pm5\%$. As the figure shows, through the addition of the if statement, the χ^2 surface can be heavily modified, forcing the program to fit a chosen parameter to the predefined range.

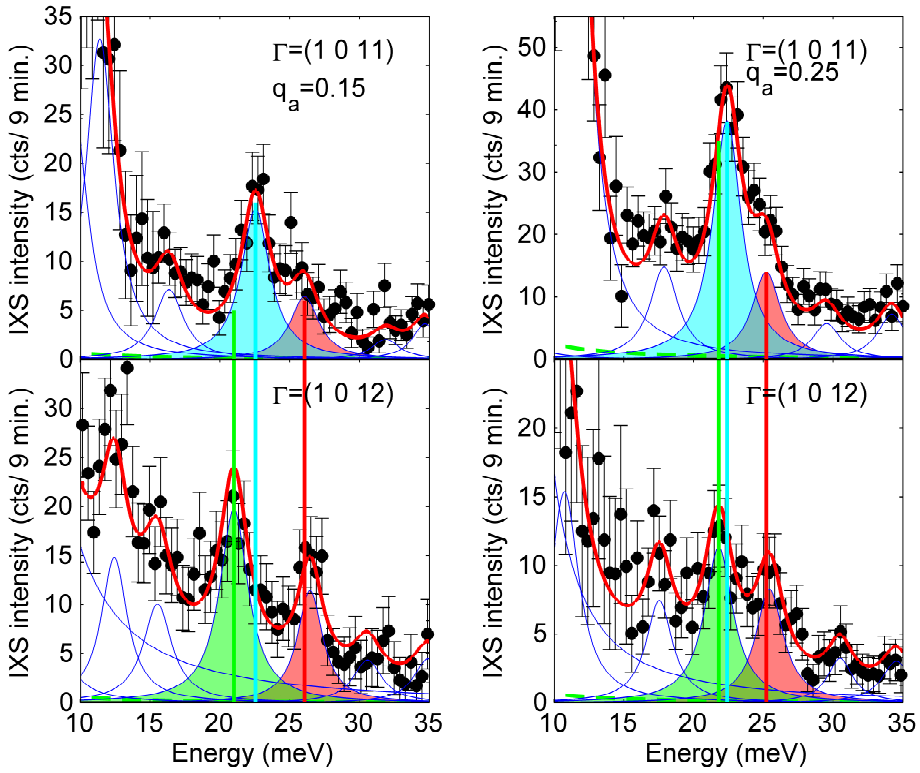

(a) (b)

Figure 3.16: Experimental IXS spectra of $SmFeAsO_{0.60}F_{0.35}$ for q=(0.15 0 0.17) (left) and q=(0.25 0 0.17) (right), in two different Brillouin zones: Γ=(1 0 11) (upper panel) and Γ=(1 0 12) (lower panel). The red line is the result of the total fit, and the thin blue lines represent individual phonons. The three optical phonon modes around 23 meV are highlighted.

With the exception of the elastic line, the line widths of the fits were allowed to broaden by 10 to 20% of their resolution-limited values. A similar broadening effect, which had previously been reported in $CaFe_2As_2$ [84], might provide useful information in phonon coupling in these materials. However, due to the low counting statistics, it was not possible to extract these widths with any precision. Thus, only the phonon frequency was analysed.

Figure 3.10 clearly shows all three optical phonon modes. This is not the case for all IXS spectra taken in the (1 0 12) Brillouin zone however. Specifically, the central mode around 23 meV is only visible for q_a >0.3 a^*, for most experimental spectra. It should be noted however, that all three optical modes seem to be visible in the IXS spectrum at

q=(0.05 0 0.17). Thus, the underlying factor as to whether a mode is visible, seems to be both q_a and q_c. Since most scans taken close to the (1 0 12) Γ-point, show only two of the three optical modes, addition measurements were made in the (1 0 11) Brillouin zone, specifically at: (1.1 0 11) and (1.25 0 11). The purpose of these additional scans, was to allow an unambiguous assignment of all three modes to the zone-centred Raman modes, shown in figure 3.6. Due to time constraints however, measurements in this Brillouin zone were only performed for the $SmFeAsO_{0.60}F_{0.35}$ sample.

A comparison between the doped sample's IXS spectra, at q_a=0.15 (left) and q_a=0.25 (right), in the two different Brillouin zones is given in figure 3.16. As I have explained previously, the energy of each phonon mode is independent of the total momentum transfer Q, and therefore should be independent of the Brillouin zone. The 26 meV mode is seen in both zones at low q_a, while the mode close to 23 meV is observed in the (1 0 11) zone. The mode close 21 meV is observed in the (1 0 12) zone, at q_a=0.15 and 0.25.

3.3.5 Phonon dispersion

The dispersion of these modes along (q_a 0 0), with $q_c \leq 0.17$ r.l.u., for both compounds (as determined from the second fitting method) is summarised in figure 3.17. Also included in this figure are the theoretical dispersion of LaFeAsO, provided by Noffsinger *et al.* [98]. The branches corresponding to the optical modes are also highlighted and may be considered as a guide to the eye.

Firstly, figure 3.17 shows that the dispersion of the acoustic modes is in good agreement with the theoretical calculations of Noffsinger *et al.* [98]. In addition, the dispersion of the optical modes at 26 meV follows the corresponding theoretical branch quite well. However, the same cannot be said for the other two optical branches. It should also be noted that the data suggests a possible crossing or mixing of the two A_{1g} (As,Sm) modes at q_a=0.25 a^*. To clarify this point, additional experimental data with a higher energy resolution needs to be taken. Finally, the zone centre Raman modes (diamonds) identified by Hajiev *et al.* [96] for SmFeAsO, are also included in the figure. The experimental data extrapolates well to these zone centre measurements, which allows for a precise

assignment of the experimental branches to the three c-axis polarised Raman modes. The 21 meV mode (green) corresponds to the in-phase A_{1g} (As,Sm) mode, the 23 meV mode (cyan) to the out-of-phase A_{1g} (As,Sm) mode and the 26 meV (red) to the B_{1g} (Fe,O) mode. In addition to the three Raman modes and the strong transverse acoustic branch at approximately 10 meV (see figure 3.10), several other branches are plotted on the dispersion. One mode close to 12 meV could possibility be assigned to the IR-active c-axis polarised A_{2u} (Sm,Fe,As) mode [100], while the another at 17 meV has the correct energy for the in-plane polarised E_g mode. A precise identification of these additional two modes remains challenging, due to the low counting statistics and the significant discrepancies between the mode intensities predicted by the DFT calculations and the experimental data. In fact, some of these modes seem to display doping dependencies and renormalisations of their phonon intensities, this indicates that there may be some additional changes in the lattice dynamics upon fluorine doping. However, due to the proximity of these modes to the strong transverse acoustic mode, a complete description of these phenomena is currently not possible. To achieve this, higher energy resolution measurements, or measurements in a Brillouin zone without a strong acoustic mode (if one exists) are required.

3.3.6 The effects of fluorine doping

Examples of IXS spectra of both compounds taken in the (1 0 12) Brillouin zone are shown in figure 3.18. The figure reveals the effects of fluorine doping on the three c-polarised optical modes, this is the main result of the study. Here, two of the optical modes display a clear doping dependence, with the phonon located close to 21 meV systematically softening with doping, while the mode close to 26 meV hardens. The third mode essentially shows no doping dependence, accept for a slight softening of 0.5 meV at q=(0.45 0 0.17) (not shown in figure 3.18).

To further investigate the effects of fluorine doping on the two optical modes that display the strongest renormalisation effects, namely the in-phase A_{1g} (As,Sm) mode around 21 meV and the B_{1g} (Fe,O) mode around 26 meV. ID28's eight working analysers were used

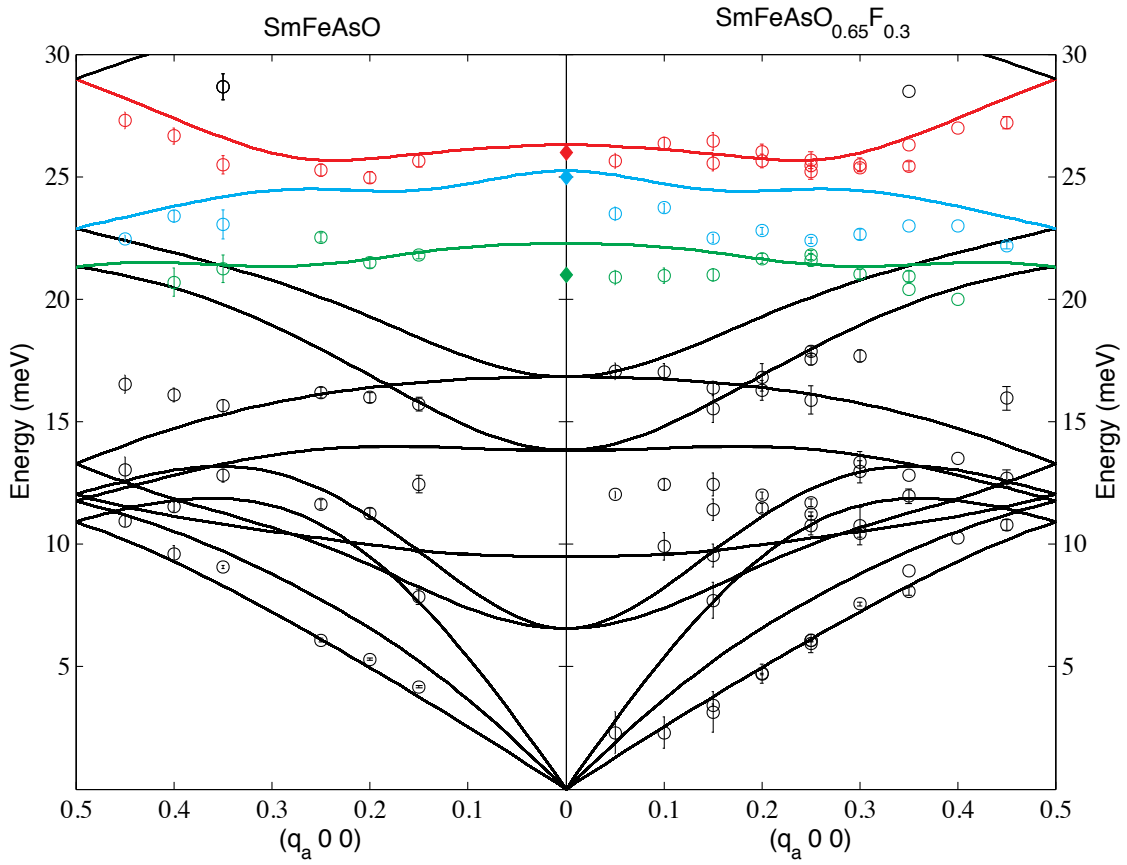

Figure 3.17: The room temperature phonon dispersion along the [100] direction of SmFeAsO (left panel) and $SmFeAsO_{0.60}F_{0.35}$ (right panel). All q-points with $q_c \leq 0.17$ c* are included in the figure. In addition, the zone centred Raman modes (diamonds) identified by Hadjiev *et al.* [96] and the theoretical dispersion of LaFeAsO (solid lines), are included [98]. Finally, the doubling of some data points are due to measurements with different values of q_c.

to map out the q-dependence of the amplitude of the doping-induced energy shift of these two modes, in the (q_a 0 q_c) plane. The figure was produced by creating an array of points. Each point is separated by resolution in each direction divided by 5 along the a-axis and 10 along the c-axis, inside the elliptical resolution centred at measured position, the doping amplitude is therefore constant within the ellipse. If two ellipse intersect, then the two nearest points are averaged. The doping induced renormalisations between the ellipses are then interpolated using a cubic function. The results of this mapping, shown in figure 3.19, reveal a clear doping-induced renormalisation of both modes which varies strongly with momentum transfer. For the in-phase A_{1g} (As,Sm) mode, the maximum amplitude of

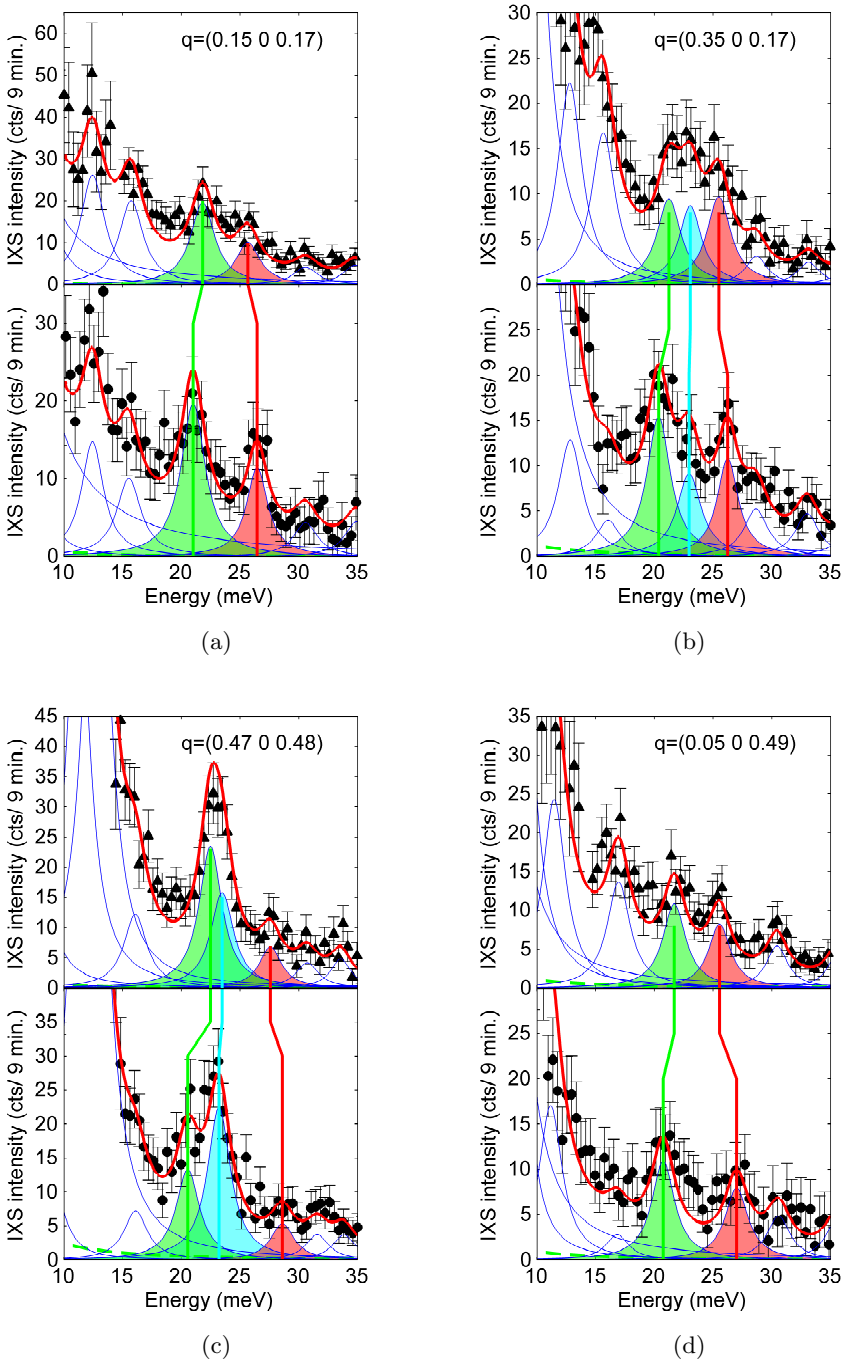

Figure 3.18: A comparison between the IXS spectra of SmFeAsO (upper panel) and $SmFeAsO_{0.60}F_{0.35}$ (lower panel) at four q-points, given on the figures. The figures show a significant softening of the in-phase A_{1g} (Sm,As) mode, and a hardening of the B_{1g} (Fe,O) mode for all four q-points. The out-of-phase A_{1g} (Sm,As) mode essentially shows no change upon fluorine doping.

softening was found to be 1.9 meV close to q=(0.47 0 0.48), while the maximum amplitude of hardening for the B_{1g} (Fe,O) mode, was found to be 1.4 meV close to q=(0.38 0 0.32). It should be noted, the doping dependence of the B_{1g} (Fe,O) mode is in contrast to recent nuclear inelastic scattering measurements [101], which gave no indication of doping effects on the Fe partial PDOS in $LaFeAsO_{1-x}F_x$.

These doping induced renormalisations are clearly at odds with the original first principle calculations [5, 80]. However, the D.F.T. work in the local density approximation (LDA) by Noffsinger and co-workers, has explicitly accounted for fluorine doping in 2×2×1 supercell of $LaFeAsO_{1-x}F_x$ [98]. Results from this work were compared to the PDOS data presented by Le Tacon *et al.* [6], with the theoreticians concluding that the doping induced changes were due to a structural relaxation only. Specifically, it was predicted that this relaxation would produce a hardening of the out-of-phase A_{1g} (As,Sm) and B_{1g} (Fe,O) modes and a splitting of the in-phase A_{1g} (As,Sm) mode. Experimentally, a hardening of the B_{1g} (Fe,O) mode is indeed observed, however the out-of-phase A_{1g} (As,Sm) mode shows no conclusive doping induced renormalisations. Furthermore, there is no evidence for the splitting of the in-phase A_{1g} (As,Sm) mode, as there is a one-to-one correspondence between features in the parent and doped IXS spectra. It should be noted however, that due to the low counting statistics of these results, it is difficult to be absolutely certain of this. Therefore, one should conclude that a structural relaxation is most likely not the cause of the doping induced renormalisations reported in this chapter, but this may not be completely ruled out.

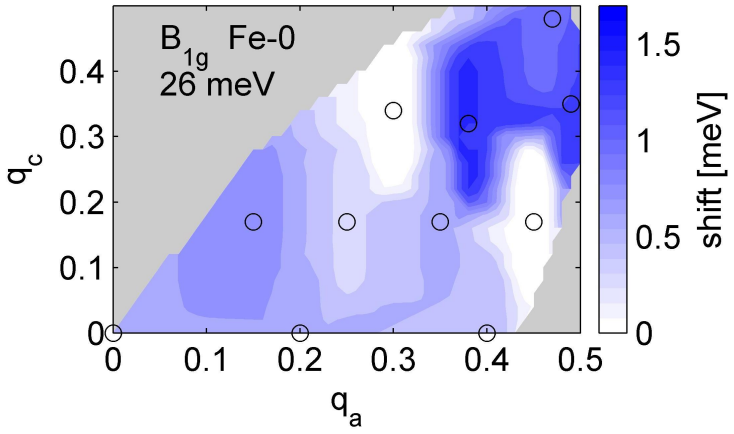

(a)

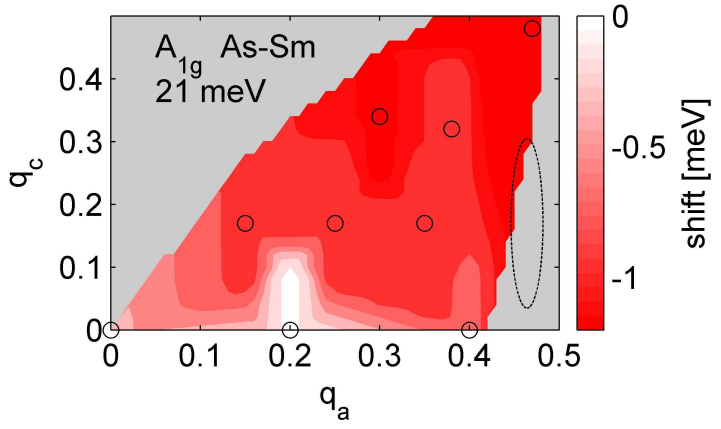

(b)

Figure 3.19: Momentum dependence of the doping induced renormalisation of the 21 meV, A_1g (figure 3.19(a)) and 26 meV , B_{1g} (figure 3.19(b)) modes, in the (q_a 0 q_c) plane. The white areas corresponds to no doping induced renormalisation, while the darker the blue (red) areas are, the greater the doping induced hardening (softening) is. The dashed ellipse indicates the q-resolution, and the grey areas where there is insufficient data.

3.4 Conclusion

As I have stated previously, spin-polarised calculations have been successful in generating a better agreement between experimental and theoretical phonon spectra, in the '122' compounds. Thus, it seems reasonable to suggest that the inclusion of magnetism is needed to describe the renormalisation effects shown in this chapter. As theoretical work [102, 103] has proposed that the magnetic ground state is closely related to the *c*-axis Fe-As distance, the atomic vibrations that modulate this distance, specifically the in-phase A_{1g} (As,Sm) and B_{1g} (Fe,O) modes, should be coupled to the Fe moments [104]. However, the out-of-phase A_{1g} (As,Sm) mode is predicted to have only a weak effect on the Fe-As tetrahedron structure, and therefore is not strongly coupled to the Fe moments. It would seem that the experimental data supports this hypothesis, as little or no renormalisation effects are seen in this mode, upon fluorine doping. This would also support the assumption that the two A_{1g} modes do not cross at q_a=0.25 a^*.

Since there are antiferromagnetic fluctuations present in the room temperature paramagnetic phase, the doping effects presented here suggests a coupling of the electronic system to the crystal lattice, through these fluctuations.

There are two pieces of evidence which provide information as to the form of this coupling:

1. The opposite shift of the two magnetically active phonons is very unusual, and implies that there might be some kind of resonance of the electronic system around 23 meV. This resonance may be similar in nature to the resonant magnetic excitation observed by Christianson *et al.* in $Ba_{0.6}K_{0.4}Fe_2As_2$ [72]. The opposite shift might therefore be explained by the two magnetically sensitive phonon modes, lying either side of this resonance. In fact, by scaling the 15 meV resonance energy observed in $Ba_{0.6}K_{0.4}Fe_2As_2$ by the T_c of both compounds, a resonance energy close to 23 meV is predicted:

$$\frac{15}{38} \times 55 = 21.71\ meV \tag{3.8}$$

2. The momentum and energy dependence of the doping induced renormalisations of the magnetically sensitive modes, which are shown in figure 3.19, has two possible sources, both of which may evolve with doping. Firstly, the electron-phonon coupling $g(\mathbf{q}, \omega)$. As I have stated previously, estimations of the electron-phonon coupling parameter λ were based upon the assumption that the coupling in all modes are equal. Thus, the possibility of a varying coupling strength between different modes, would call into question the validity of the *ab initio* calculations described earlier. Secondly, these renormalisation effects might also be due to the q-dependent magnetic or electronic susceptibility $\chi(\mathbf{q}, \omega)$. It should be noted that changes in the non-interacting q-dependent magnetic susceptibility, due to alterations in the Fermi surface upon doping, have been calculated [105]. Results showed that upon doping, the Fermi hole sheets around Γ shrink while the electron sheets around M grow. This result indicates that the spin density wave no longer nests along the Γ-M direction.

   Whether one or more of these effects are responsible for the doping induced renormalisations presented in this chapter remains uncertain, and will likely remain so until phonon structure factor calculations, with spin polarisation, are produced.

To conclude, using X-ray inelastic scattering, my collaborators and I have performed a detailed investigation into the effects of fluorine doping on the lattice dynamics of single crystal samples of SmFeAsO and $SmFeAsO_{0.60}F_{0.35}$. The measurements, which were recorded at room temperature in the crystal's paramagnetic phase, revealed a strong doping dependence of three c-axis polarised optical phonon modes, between 21-26 meV. This result is in close agreement with previous PDOS work. Comparisons with previous Raman scattering data identified the modes (in ascending energy) as the: in-phase A_{1g} (As,Sm), out-of-phase A_{1g} (As,Sm) and the B_{1g} (Fe,O). A strong doping induced renormalisation of the first and third modes was detected. These renormalisations, which disagree with theoretical calculations, that assign the doping induced changes in the PDOS in $NdFeAsO_{1-x}F_x$ to structural reorganisations, have the opposite sign for the two modes and show an unexpected momentum dependence, which is currently not understood. It has been suggested that these two modes couple to the magnetic sublattice, which in turn is coupled to the electronic states, significantly enhancing the electron-phonon coupling

in this class of crystals. Thus, the evolution of this coupling, which the phonon spectra implies, may play a significant and important role in the dramatic changes of the iron pnictide's low temperature ground states.

Chapter 4

Resonant X-ray scattering studies of multiferroic $TbMnO_3$

4.1 Multiferroics: an introduction

Magnetoelectric multiferroics are a group of materials which simultaneously possess both magnetic ordering, (ferromagnetic or antiferromagnetic) and ferroelectric ordering. Often in multiferroics, these two forms of order will interact and compete with each other. This leads to the magnetoelectric effect, which is a coupling between magnetisation and electric polarisation. Often this effect can been seen through the induction of an electric polarisation by an applied magnetic field, or a change in magnetic structure by an applied electric field. Although knowledge of magnetoelectric multiferroic materials dates back to the 1950s, the recent (2003) discovery of large magnetoelectric coupling in the rare earth compounds of $TbMnO_3$ [10] and $TbMn_2O_5$ [106] has led to a significant increase in research into these materials. This is because they are of considerable interest from both a fundamental point of view, and for the potential that they offer to the field of spintronics. For a certain class of multiferroic materials, of which $TbMnO_3$ is a member, a ferroelectric polarisation is observed at the onset of the formation of a new magnetic phase. This suggests that the magnetic structure causes ferroelectric ordering. For a significant

proportion of my Ph.D. work, I have been studying $TbMnO_3$ through the technique of resonant soft X-ray scattering. These studies involve scattering at resonant energies, where the energy of an incident X-ray photon is turned through a sample's atomic absorption edge. Resonant scattering is sensitive to many forms of multipolar order, and affords the opportunity for one to study the individual electronic states of a elemental species of the sample. Thus, resonant X-ray scattering is uniquely placed to provide information, on a microscopic level, of how ferroelectric order arises in these materials. Neutron diffraction by contrast, cannot separate the contributions to the scattering from the different magnetic species in $TbMnO_3$. In this sense, these X-ray scattering studies are complementary to the previous experimental work.

The first half of this Chapter will describe the different magnetoelectric phases of $TbMnO_3$, and discuss the large amount of research that has already been conducted. This will include theoretical explanations on how ferroelectricity in $TbMnO_3$ is induced. The second half will be used to describe the results from several experiments which studied the magnetic ordering in $TbMnO_3$. Results from these experiments show that in addition to the previously proposed Manganese magnetic structure, extra canting of the Manganese spins is found for both magnetic phases. Thus, the ferroelectric polarisation in $TbMnO_3$ is driven by the transition between two non-collinear magnetic structures instead of the previously held view of a transition between a collinear and non-collinear magnetic structure. This work has been published in two journal articles [14, 15].

4.1.1 A brief history of multiferroics

The term 'multiferroic' was first used by H. Schmid in 1994 [107] to describe a material that simultaneously possesses two or three ferro properties, i.e. ferromagnetism, ferroelectricity and ferroelasticity, in a single phase. However, studies of coupling between magnetic and electric dipole ordering, which is known as the 'magnetoelectric (ME) effect', first began toward the end of the 19^{th} century [108, 109, 110]. Further research into magnetoelectrics was conducted during the 1950s and 60s. For example in 1959, Dzyaloshinskii [111] first predicted that the violation of time-reversal symmetry in the

compound Cr_2O_3, should produce a linear magnetoelectric coupling coefficient α. A year later α was experimentally observed by Astrov [112] to be non-zero ($\alpha_{max}=\partial P/\partial H \approx 4.1$ ps m^{-1}) below a Néel temperature of 307 K. The first (highly insulating) ferroelectric ferromagnetic to be identified and studied was nickel iodide boracite: $Ni_3B_7O_{13}I$. Ascher and co-workers [113] showed that below 60 K, weak magnetic and electric order occur simultaneously. In addition, a flip in electrical polarisation was observed when an external magnetic field was applied. This initial work was followed by the synthesis of numerous multiferroic boracite compounds, all of which have complex structures with many atoms per formula unit, and more than one formula unit per unit cell. The large number of inter-ionic interactions in these materials, however, prevented scientists from determining the essential factors which cause multiferroicity, and a definition of the coupling between the magnetic, electric polarisation and structural order parameters. In addition to the work on multiferroic boracite, a systematic search for other ferroelectric ferromagnetic compounds began in the former Soviet Union in the 1950s, with Smolenskii and co-workers [114] in St. Petersburg (then Leningrad), working on mixed perovskite compounds. By replacing some of the d^0B cations in a ferroelectric perovskite oxide with a magnetic d^n ion, Smolenskii's group produced the first synthetic ferroelectric ferromagnet [115]: (1-x)$Pb(Fe_{2/3}W_{1/3})_3$-x$Pb(Mg_{1/2}W_{1/2})O_3$. Here the Mg^{2+} & W^{6+} ions are diamagnetic and cause the ferroelectricity, while the Fe^{3+} ions are responsible for the ferromagnetism. Further work on these mixed perovskite compounds continued into the 1960s, examples of this research include the B-site disordered compounds: $Pb_2(FeNb)O_6$ and $Pb_2(MnNb)O_6$, which are both ferroelectric and antiferromagnetic, with a weak ferromagnetic response below 10 K.

It seems that after the initial burst of interest in these magnetoelectric materials, research into this area declined during the later half of the 1970s, and it was not until the late 1990s before interest in the ME effect was revived. According to Khomskii [116], there were three factors connected to this revival of interest. First, techniques for preparing and studying thin films of oxides (most multiferroics are oxides) were now well established. This allowed researchers to produce high quality thin films of ferroelectric materials. This led to the discovery of a giant ferroelectric polarisation in thin films of the multiferroic:

$BiFeO_3$ [117]. Second, with these advances in sample growth and experimental techniques, new classes of multiferroic systems were being discovered, which have strong coupling between the magnetic and ferroelectric degrees of freedom. Examples include the rare earth manganites: $ReMnO_3$ [10, 11], $ReMn_2O_5$ [106], (where Re=Tb, Dy, Ho, Er) and $Ni_3V_2O_8$ [118]. Third, scientists realised that multiferroics might offer a route to new and exciting applications, e.g. controlling magnetic memory with an electric field, new types of attenuators or magnetic field sensors.

4.2 Multiferroic $TbMnO_3$

In 2003 ferroelectricity was found in the antiferromagnetically ordered manganite: $TbMnO_3$ [10]. This new multiferroic compound showed a surprisingly large magnetoelectric coupling, which was illustrated by a flop (rotation by 90°) in direction of the spontaneous electrical polarisation, when an external magnetic field was applied along the direction of the crystallographic b-axis. At room temperature $TbMnO_3$ has a orthorhombically distorted perovskite crystal structure (space group: *Pbnm*, crystal symmetry: *mmm*). A diagram of the crystal structure of $TbMnO_3$ is shown in figure 4.1. There is inversion symmetry, and the system is non-polar. Each Mn ion is surrounded by an octahedron of oxygen ligands (see figure 4.1). The effect of these surrounding oxygen ligands is to induce a crystal field on the Mn $3d$ orbitals, specifically the d orbitals are split into two groups. Firstly, the t_{2g} orbitals (d_{xy}, d_{yz}, d_{xz}) which are aligned between the surrounding oxygen ions, and secondly, the e_g orbitals (d_{z^2}, $d_{x^2-y^2}$) which are aligned towards the surrounding oxygen ions. As the crystal field on the Mn ion is mostly produced by the oxygen p-orbitals, the t_{2g} orbitals will have a lower overlap with the oxygen p-orbitals than the e_g orbitals. Thus, the t_{2g} orbitals will have a lower energy than the e_g orbitals. What is more, because the Mn ions in $TbMnO_3$ are in the Mn^{3+} state (i.e. there are 4 electrons in the $3d$ orbitals), the octahedron environment will also be Jahn-Teller distorted. This is due to the fact that as the t_{2g} orbitals are the lowest in energy, three of the Mn electrons will occupy these orbitals, while the other Mn electron will occupy the e_g orbitals. If the octahedron environment is compressed in the $x-y$ plane and expanded along the z direc-

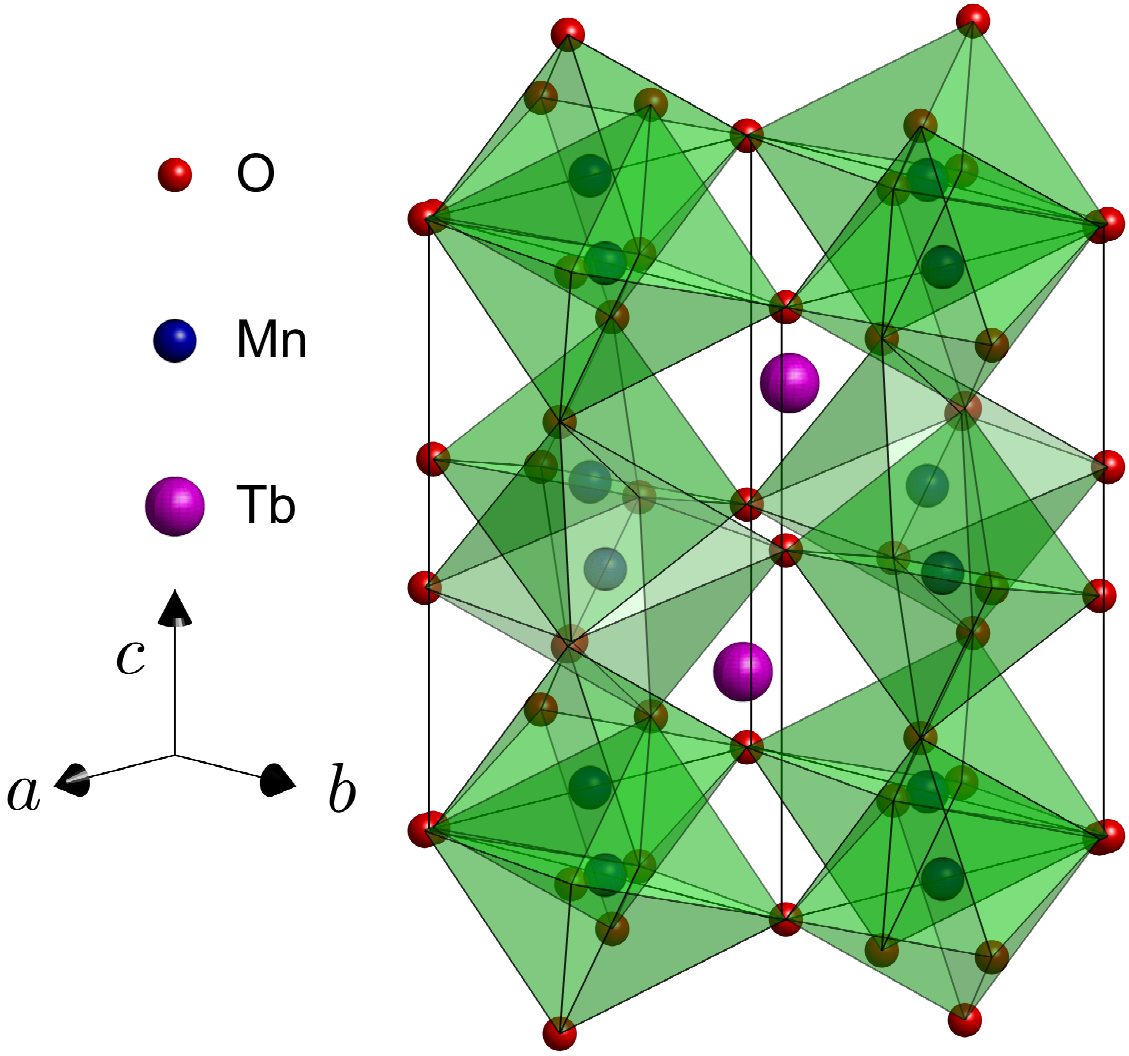

Figure 4.1: A diagram of the *Pbmn* crystal structure of $TbMnO_3$. The different elements are labelled in the legend, while the green shading represents the Jahn-Teller distorted MnO_6 octahedron crystal field environments.

tion, this will lead to a splitting in energy of the t_{2g} and e_g orbitals. For the t_{2g} orbitals this is not that important as all three orbitals are occupied, however only one of the e_g orbitals is occupied, therefore the e_g orbitals $d_{x^2-y^2}$ and d_{z^2} lose their degeneracy. Because of this expansion of the octahedron along the z-direction, there will be less of an overlap between the d_{z^2} and oxygen p orbitals. Thus, the distortion of the oxygen octahedron will lower the energy of the d_{z^2} orbital, conversely the same distortion will raise the energy of the $d_{x^2-y^2}$ orbital. To save energy, the single e_g electron will occupy the d_{z^2} orbital, this has the effect of lowering the energy of the electronic system, offsetting the increase in elastic energy that arises from the distortion.

4.2.1 The magnetic phases of $TbMnO_3$

Above 41 K, $TbMnO_3$ is both paramagnetic and paraelectric. At 41 K, $TbMnO_3$ undergoes an antiferromagnetic transition. This phase transition has been seen in anomalies in magnetisation and specific heat measurements [10, 11], which suggests that this transition is second order. Rietveld refinement of neutron powder diffraction [119] patterns has suggested that the Mn moments are aligned along the b axis (*Pbnm* notation). What is more, the magnitude of these moments show sinusoidal order, with a propagation wavevector of (0 q 0), where q is an incommensurate wavevector. At 41 K q$\sim$0.29 b^*. This wavevector should not be confused with the reduced momentum transfer of the previous Chapter. I shall refer to this phase as the **Collinear** phase, as the Mn magnetic moments are believed to be coupled in parallel or anti-parallel arrangement to their nearest neighbour. Figure 4.2(a) shows a diagram of the proposed Mn collinear magnetic structure. As the temperature is decreased from 41 K, the value of q decreases, until the temperature reaches 28 K, where a second anomaly is observed in magnetisation and specific heat, indicating another second order phase transition. At 28 K, $q\sim0.28$ b^* and remains approximately constant upon any further decrease of temperature. It is this transition at 28 K where the ferroelectric order, with a spontaneous polarisation along the crystallographic c-axis, is first detected. The magnitude of this polarisation was measured by Kimura *et al.* [10] to be 8×10^{-4} C m^{-2}, at a temperature of 4 K. Originally, it was proposed that the structure of the Mn sublattice for this 2^{nd} magnetic phase was again sinusoidally modulated [119],

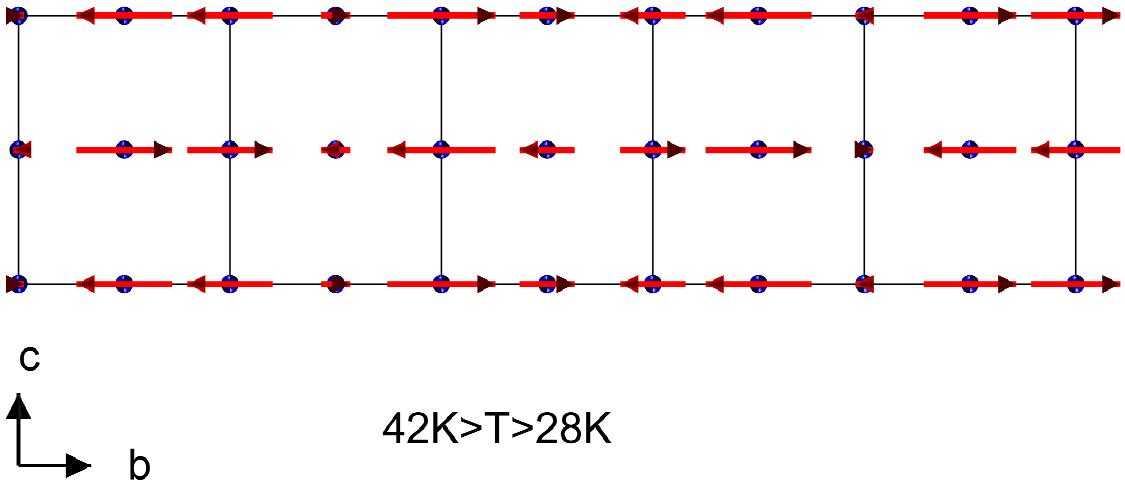

(a)

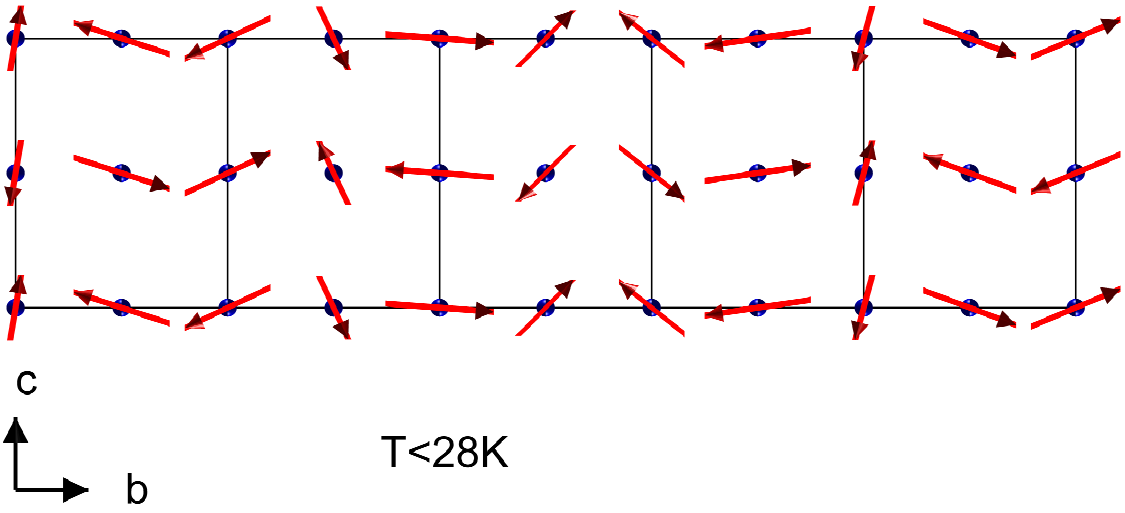

(b)

Figure 4.2: A diagram of the Mn collinear (figure 4.2(a)) and cycloidal (figure 4.2(b)) magnetic structures of $TbMnO_3$, projected onto the $b-c$ plane. The magnetic moment directions at the Mn sites are shown by the red arrows. For both phases the magnetic moments are coupled antiferromagnetically along the b and c axes, with the coupling along the b-axis being incommensurate in nature.

in a similar manner to the collinear phase. However, neutron diffraction measurements taken by Kenzelmann and co-workers [12], proposed that the magnetic structure for this phase is instead a transversely modulated spiral (or elliptically modulated cycloidal spiral) in the b-c plane. I will refer to this ferroelectric phase as the **Cycloidal** phase. Figure 4.2(b) is a diagram of the Mn cycloidal magnetic structure. Finally, a third anomaly is seen in specific heat and magnetisation data at a temperature of $\sim$7 K. This corresponds to the Tb^{3+} moments developing long-range magnetic ordering, with a propagation vector of (0 $\sim$0.42 1) r.l.u. [119].

The co-appearance of the cycloidal magnetic phase and a spontaneous electrical polarisation, suggests a strong connection between the phenomena of ferroelectricity and magnetism in this compound. In fact, polarised neutrons have been used to show that the helicity of the Mn cycloidal magnetic structure can be controlled by the application of a small external electric field (160 kV/m), when cooling the sample [120]. The same effect has also been confirmed by non-resonant scattering of circularly polarised X-rays [121].

4.2.2 Control of the electric polarisation by an external magnetic field in $TbMnO_3$

When compared with non-manganite perovskite ferroelectrics, such as $BaTiO_3$, the magnitude of the electrical polarisation seen in $TbMnO_3$ is quite small. For example, in $TbMnO_3$: P$\sim 8\times10^{-4}$ C m^{-2} at 4 K, while in $BaTiO_3$: P$\sim 2.6\times10^{-2}$C m^{-2} at 296 K. However, $TbMnO_3$ displays a strong cross coupling between the ferroelectric and magnetic order parameters. This coupling can be seen in the effects on the ferroelectric polarisation when an external magnetic field is applied [11]. $TbMnO_3$'s unusual response to an applied magnetic field (H) was first reported by Kimura *et al.* [10, 11]. In these papers, Kimura and co-workers showed that the ferroelectric polarisation could be either rotated by 90° (flopped) when H$\|$ b and H$\|$ a, *or* completely suppressed when H$\|$ c. In-field neutron and X-ray diffraction measurements have shown that this polarisation flop (for both H$\|$ a and H$\|$ b) coincides with a first order phase transition, from an incommensurate (0 q 1) to a commensurate (0 $\frac{1}{4}$ 1) magnetic structure [122, 123]. For H$\|$ c, the incommensurate

magnetic order of the Mn sublattice is replaced by a simple antiferromagnetic order, which has a (0 1 0) magnetic Bragg reflection [124].

4.2.3 Previous experiments on $TbMnO_3$

For this section I will review the research that has been used to determine the magnetic structure of $TbMnO_3$. Magnetic susceptibility and neutron diffraction measurements of $TbMnO_3$, were first performed by Quezel *et al.* [119] in 1977. The susceptibility measurements identified three transitions, at 41 K, 28 K and 7 K. The first of these transitions (41 K) was attributed to the ordering of the Mn^{3+} moments, while the transition at 7 K was attributed to antiferromagnetic ordering of the Tb^{3+} moments, the transition at 28 K was not explained. Neutron diffraction measurements taken on both powder and single crystal samples revealed the existence of two types of antiferromagnetic reflection, which were attributed to the magnetic ordering of the Mn^{3+} moments. Firstly, a strong A type reflection (*h+k=even*, *l=odd*) was seen with an incommensurate propagation vector that is consistent with the one reported in section 4.2. Secondly, a much weaker G type reflection (*h+k=odd*, *l=odd*) was seen for temperatures below 20 K. No F type (*h+k=even*, *l=even*) or C type (*h+k=odd*, *l=even*) antiferromagnetic reflection were detected. Ordering of the Tb^{3+} moments was seen below 7 K, however the paper does not give the wavevector. The existence of only the A and G type satellites lead Quezel *et al.* [119] to the conclusion that below 40 K the Mn sublattice had a sine-wave magnetic structure, with the moments parallel to the *b*-axis. The Tb^{3+} moments were also determined to have a sine-wave structure, with the moments pointing along two symmetrical directions within the *a*-*b* plane. The next study of $TbMnO_3$'s magnetic structure was made by Blasco *et al.* [125] in 2000. In this work Blasco and co-workers investigated the crystallographic and magnetic structures of the Ca-doped compounds: $Tb_{1-x}Ca_xMnO_3$, where the value of x varied from 0 to 1. For this thesis, I will restrict myself to a discussion of the results for the *x=0* compound. Here, neutron powder diffraction measurements (taken at 16 K) revealed a strong A type antiferromagnetic reflection, which lead to the conclusion that the Mn^{3+} moments are ordered with a incommensurate sine-wave magnetic structure, in agreement with the conclusions of Quezel *et al.* [119]. Shortly after the discovery of $TbMnO_3$'s

multiferroic properties, the magnetic structure of this compound was re-investigated. In 2004 Kajimoto *et al.* [13] performed neutron diffraction on a single crystal of $TbMnO_3$. In addition to the strong A type and weaker G type reflection that had previously been identified, this work also found evidence for F and C type reflections, with all reflections being observed for temperatures below 42 K. These surprising results were interpreted as follows: for the A & G type reflections the Mn^{3+} moments were arranged in a sine-wave structure, which pointed along the b-axis. The Mn^{3+} moments for F & C type reflections were determined to point along either the c or a-axis. In addition to the fundamental (q) reflections, third harmonics ($3q$) of each type (except F type) of magnetic reflections at (h k$\pm 3q$ l) were detected. The authors concluded that the existence of these higher harmonics suggests that the magnetic structure is not an ideal sinusoidal wave. Finally, 1^{st} and 2^{nd} harmonic incommensurate reflections, corresponding to the ordering of the Tb^{3+} moments were observed for temperatures below 7 K. The existence of the Tb^{3+} 2^{nd} harmonic reflections remains an open question, as they could be attributed to the breaking of inversion symmetry or a charge distortion induced by the magnetic order.

The most recent neutron investigation into the magnetic structure of $TbMnO_3$ was undertaken by Kenzelmann and co-workers in 2005 [12]. Diffraction measurements performed on two single crystal samples detected only the A type and G type reflections, with 3^{rd} harmonic reflections being observed in the ferroelectric phase. Through representational analysis of their neutron diffraction data, Kenzelmann and co-workers determined that the magnetic structure of $TbMnO_3$ between 42 K and 28 K was best described by a single irreducible representation, namely Γ_3. This irreducible representation gives information on the symmetry of the magnetic structure (see appendix A for more information) and from this information it was established that, for this phase, the Mn^{3+} magnetic moments were sinusoidally modulated along the b-axis, as shown in figure 4.2(a). For the magnetic phase below 28 K, the best agreement between experimental data and symmetry models was found when two irreducible representations were included, namely Γ_2 and Γ_3. The Γ_3 representation produced the same magnetic structure as before, while the Γ_2 representation gave a magnetic structure where the Mn^{3+} moments are antiferromagnetically ordered along the c-axis. From the size of the moments along the b and c axes, it was

determined that the magnetic structure below 28 K was that of an elliptical cycloid, as show in figure 4.2(b). By comparing the proposed collinear and cycloidal magnetic structures, Kenzelmann and co-workers [12] proposed an elegant and appealing model, where the onset of ferroelectric polarisation is driven by the loss of inversion symmetry at the Mn sites, at the onset of the cycloidal magnetic order. This loss of inversion symmetry idea has been supported with the discovery of other compounds [118, 126] (i.e. $Ni_3V_2O_8$), where a ferroelectric transition has been observed to coincide with the appearance of a non-collinear magnetic structure that breaks inversion symmetry. Finally below 7 K, reflections corresponding to the separate ordering of the Tb^{3+} moments were detected. In addition to the results taken in zero external field, a number of diffraction measurements were taken in an external magnetic field which was parallel to the a-axis (H$\|$a). Results showed that up to at least 6 Tesla, the Mn^{3+} magnetic structure remains a cycloid in the ferroelectric phase. Results taken in this experimental arrangement also showed that for the collinear phase, the Tb^{3+} moments are disordered, while for the cycloidal phase, the Tb^{3+} moments are orientated along the a-axis. At this stage, it is important to comment on the inconsistencies within the various neutron diffraction data, concerning the different types of antiferromagnetic reflections that were observed. The original neutron diffraction work by Quezel *et al.* [119] and powder neutron diffraction by Blasco *et al.* [125], revealed strong A type and weak G type magnetic reflections only. However, single crystal neutron diffraction conducted by Kajimoto *et al.* [13] observed all four reflection types. Finally, the neutron investigation by Kenzelmann *et al.* [12] in 2005 again reported only A and G type reflections. A possible explanation for these inconsistencies is that the magnetic structures of $TbMnO_3$ may vary with the different growth and preparation conditions. However, all the neutron data agrees that the A type reflection is dominant in $TbMnO_3$.

In addition to these neutron studies, the magnetic structure of $TbMnO_3$ has been investigated by several groups [42, 127] using both non-resonant X-ray scattering and resonant X-ray scattering, in the vicinity of the Mn K (6539 eV) and Tb L_3 (7514 eV) absorption edges. The most comprehensive study was performed by Mannix *et al.* [42]. To begin with, non-resonant X-ray magnetic scattering (NRXMS) revealed the sample to be dominated by the A type reflection. Resonant scattering performed in the collinear magnetic

phase revealed the existence of both A and F type reflections at both the Mn K and Tb L_3 resonances. The temperature dependences of these reflections follow the relationship stated in section 4.2. These results led to the conclusion that the Tb $5d$ states were polarised by the ordering of the Mn sublattice, in both the cycloidal and collinear magnetic phases. Azimuthal dependences taken in the collinear phase, plus the lack of a NRXMS signal for the F type reflection, suggests that the A type reflection was the true magnetic reflection, while the F type reflection is associated with an induced charge multipole (orbital ordering). As the sample was cooled through 28 K into the cycloidal magnetic phase, an additional C type reflection was detected with resonant scattering performed at the Tb L_3 edge. This data was comprehensively analysed using the FDMNES code [128], and results from these X-ray scattering cross-section calculations have suggested the Tb $5d$ states *possibly* develop an anapolar moment in the cycloidal phase. Another RXS study of $TbMnO_3$ was performed by Voigt *et al.* [127], results from this study confirm that the Tb $5d$ electronic states are ordered in the collinear phase. Again the authors state that this ordering is due to a strong coupling of $3d$ Mn and $4f$ Tb electronic states via the $5d$ conduction band.

4.3 Cycloid magnets inducing ferroelectric polarisation

The simultaneous appearance of the cycloidal magnetic structure and ferroelectric polarisation provides an insight into how multiferroicity is induced in $TbMnO_3$. A ferroelectric polarisation in these materials is somewhat surprising, as at first inspection the conditions for magnetic and ferroelectric ordering would seem to be mutually exclusive [129]. As to develop magnetic ordering, a $3d$ transition element such as Mn would require partially filled $3d$ electronic states, while for a ferroelectric polarisation to develop, completely empty outer states are required. Clearly something unusual occurs at the ferroelectric phase transition for $TbMnO_3$ to be multiferroic.

4.3.1 The cycloidal magnetic ground state

$TbMnO_3$ is believed to be an example of a frustrated magnet, meaning that competing interactions between spins may prohibit a simple magnetically ordered ground state. The next logical question is therefore, can frustration be used to explain the cycloidal magnetic phase observed in $TbMnO_3$? Figure 4.3 is a diagram of a frustrated spin chain, with two magnetic exchange interactions. The first interaction (J_1) operates between nearest-neighbours and is ferromagnetic, i.e. $J_1<0$. The second interaction (J_2) occurs between next nearest-neighbours and is antiferromagnetic, i.e. $J_2>0$. The energy of this spin chain can be described using an isotropic (Heisenberg) Hamiltonian [130]:

$$H_n = \sum_n \left[J_1 \hat{S}_n \cdot \hat{S}_{n+1} + J_2 \hat{S}_n \cdot \hat{S}_{n+2} \right] \tag{4.1}$$

$\hat{S}_n$ is the spin of the n^{th} atomic site. If one expresses the angle between the magnetic moments of successive ions as θ, the energy of the system can be written as [131]:

$$E = -2Ns^2(J_1 \cos(\theta) + J_2 \cos(2\theta)) \tag{4.2}$$

N is the number of atoms in the spin chain. The minimum energy of this spin chain is found by differentiating equation 4.2 with respect to θ, and setting this equal to zero:

$$\begin{aligned} \tfrac{\partial E}{\partial \theta} = \quad & -2NS^2(-J_1 \sin(\theta) - 2J_2 \sin(2\theta)) = 0 \\ & 2NS^2(J_1 \sin(\theta) + 4J_2 \sin(\theta)\cos(\theta)) = 0 \\ & \therefore (J_1 + 4J_2 \cos(\theta)) \sin(\theta) = 0 \end{aligned} \tag{4.3}$$

One set of solutions to this equation is when $\sin(\theta) = 0$, which implies that θ=0 or θ=π. For these cases, the magnetic ordering will be ferromagnetic or antiferromagnetic respectively. A third solution can be found when:

$$\cos(\theta) = -\frac{J_1}{4J_2} \tag{4.4}$$

Thus when $\frac{J_2}{|J_1|}>\frac{1}{4}$, the Hamiltonian in equation 4.1 gives a classical ground state which is a magnetic cycloid (figure 4.3).

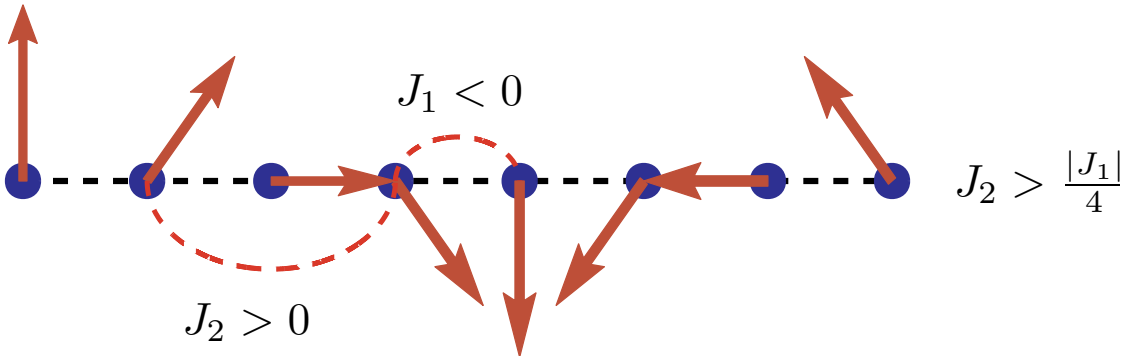

Figure 4.3: A frustrated spin chain with FM nearest-neighbour (J_1) and AFM next nearest-neighbour (J_2) interactions. For $J_2/|J_1|>1/4$ the ground state is a magnetic cycloid.

Further theoretical work has been undertaken to try to fully explain the mechanism which causes a ferroelectric polarisation in magnetoelectric multiferroics, such as $TbMnO_3$. This work has been conducted from both microscopic and phenomenological view points.

4.3.2 Phenomenological models

Starting with the phenomenological treatments. By calculating the Landau free energy expansion, Harris and co-workers [12, 118, 132] have shown that the magnetoelectric interaction, which has the symmetry of $TbMnO_3$'s paramagnetic phase, can be described by a trilinear coupling free energy term:

$$F_{me} = \sum_{\Gamma,\Gamma',\gamma} A_{\Gamma,\Gamma',\gamma}\sigma_{\Gamma}(\mathbf{q})\sigma_{\Gamma'}(\mathbf{q})^* P_{\gamma} \tag{4.5}$$

Where $\sigma_{\Gamma}(\mathbf{q})(\sigma_{\Gamma'}(\mathbf{q})^*)$ are the magnetic order parameters associated with the irreducible representations $\Gamma(\Gamma')$, also P_{γ} is the electrical polarisation in the γ Cartesian direction. Finally, $A_{\Gamma,\Gamma',\gamma}$ parameterises the interaction strength of the magnetoelectric coupling. Since the interactions in the free energy expansion have the symmetry of the paramagnetic phase, these interactions must be invariant under inversion. As the magnetic structure of the collinear phase is described by one irreducible representation (Γ_3), the

complex product of the two order parameters in equation 4.5 will be invariant under inversion. However, the ferroelectric polarisation will change its sign. Therefore, to leave the interaction invariant, $A_{\Gamma,\Gamma',\gamma}$ must be zero. Because $A_{\Gamma,\Gamma',\gamma}$ describes the magnetoelectric interaction strength, P_γ will also be zero. The magnetic structure of the cycloidal phase, by contrast, is described by two irreducible representations. For this case, there will be additional trilinear terms in the Landau expansion which include one order parameter that is associated with the Γ_3 representation and one with the Γ_2 representation (plus its complex conjugate). Therefore, to keep F_{me} invariant under inversion, the polarisation P_γ must transform as the product of the Γ_2 and Γ_3 irreducible representations. For $TbMnO_3$, this is only possible for a polarisation which is directed along the crystallographic c-axis.

In addition to the trilinear coupling explanation for the ferroelectric polarisation, Mostovoy [133] has shown from symmetry considerations, that the electric polarisation is related to a system's magnetic moments by:

$$\mathbf{P} \propto \gamma \mathbf{e_{ij}} \times (\mathbf{S_i} \times \mathbf{S_j}) \tag{4.6}$$

Where γ is a constant which is proportional to the spin-orbit coupling and super-exchange interactions. The vector $\mathbf{e_{ij}}$ is in the same direction as the spin structure's propagation vector and connects the spin sites i and j. Finally, the vector $\mathbf{S_i} \times \mathbf{S_j}$ is parallel to the spin rotation axis, in the case of $TbMnO_3$ this is the crystallographic a-axis. Thus, for a finite electric polarisation to develop, equation 4.6 shows that the following conditions must be met:

1. Adjacent magnetic moments must be coupled non-collinearly, so that $\mathbf{S_i} \times \mathbf{S_j} \neq 0$
2. The spin rotation axis ($\mathbf{S_i} \times \mathbf{S_j}$) is not parallel to the vector $\mathbf{e_{ij}}$

A cycloidal magnetic structure, of the kind predicted in $TbMnO_3$, satisfies both of these requirements. In addition, equation 4.6 shows that the direction of the electric polarisation will be perpendicular to the spin rotation axis and the direction of the propagation vector. For $TbMnO_3$ the direction of the predicted electric polarisation is the crystallographic c-axis, in agreement with experimental observations. The equation also predicts that

the direction of the polarisation may be reversed by a change in helicity of the magnetic cycloid. Finally, the equation also shows that the sinusoidal collinear magnetic structure, that $TbMnO_3$ is believed to adopt between 42 K and 28 K, cannot induce a ferroelectric polarisation. This is because $\mathbf{S_i} \parallel \mathbf{S_j}$, thus $\mathbf{S_i} \times \mathbf{S_j} = 0$. These phenomenological methods work well when describing the ferroelectric polarisation caused by a spin structure, which is not situated in an external magnetic field. In addition, when H$\|$c, the disappearance of the polarisation can be explained by the destruction of the cycloidal magnetic structure. However, the mechanism for the polarisation flop seen when H$\|$a or H$\|$b remains somewhat of an open question, and further experimental work is needed to confirm the nature of the ferroelectric order when P$\|$a for H$\|$a and H$\|$b. Even though this theoretical work gives a beautifully simplistic equation that can be used to identify other candidates for magnetoelectric compounds, it does not provide a microscopic picture of how the magnetic structure induces a ferroelectric polarisation. Thus it does not provide information on how to improve the characteristics, such as the strength of the polarisation or increasing the ordering temperature, for this type of multiferroics.

4.3.3 Microscopic models

The first attempt to describe, at a microscopic scale, how ferroelectricity is induced by a cycloidal magnetic structure was made by Katsura *et al.* [135]. This research considered a metal-oxygen-metal configuration, where the coupling between the two magnetic ions proceeds by indirect exchange interactions, through electron transfer between the metal ion's $3d$ and oxygen's $2p$ orbitals. By treating this electron transfer as a perturbation of the Coulomb Hamiltonian, Katsura and co-workers showed that for a non-collinear spin configuration between two neighbouring magnetic ions, a spin current $J \propto (S_1 \times S_2)$ is induced. This spin current leads to a finite electrical polarisation $P \propto e_{ij} \times J_j$, where e_{ij} is the unit vector connecting the two magnetic ions. Microscopically, electron-lattice interactions cause this polarisation by displacing the oxygen ligand, which is situated between two non-collinearly coupled magnetic moments of the metal ions. This effect can be regarded as the inverse of the Dzyaloshinskii-Moriya interaction, otherwise known as the Aharonov-Casher effect. Figure 4.4 depicts the oxygen displacement for a cycloidal

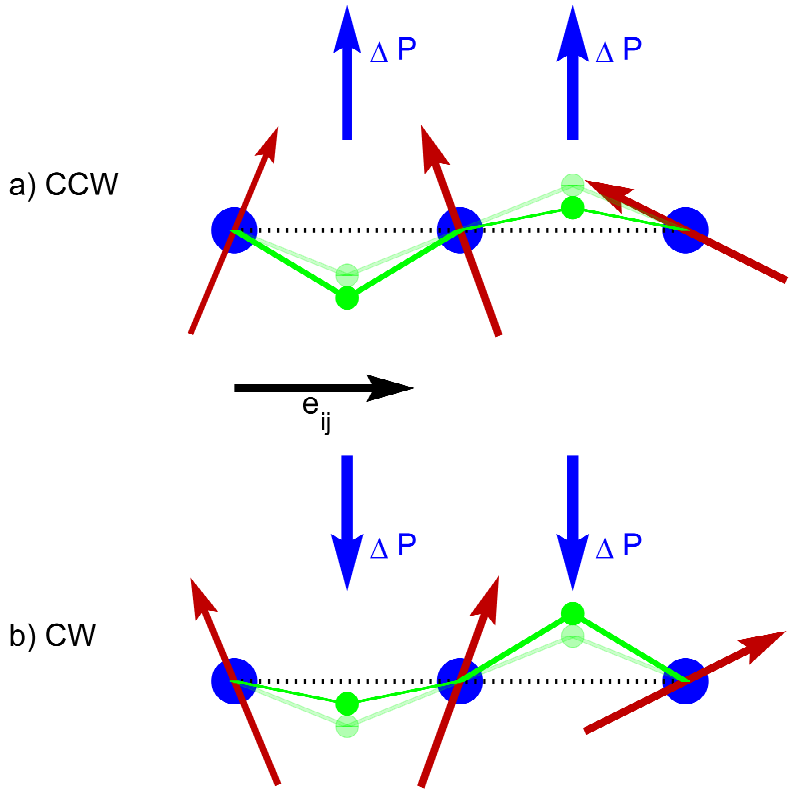

Figure 4.4: A schematic drawing of a) counter clockwise and b) clockwise magnetic cycloidal. The figure also shows the shift of oxygen ions (green) which are believed to cause an electric polarisation (blue arrows). The figure was copied from reference [134].

magnetic structure. As the figure shows, the direction of the local electric polarisation is uniform for a cycloid and therefore the total electric polarisation will be finite. For a canted antiferromagnet this would not be the case, as the electric polarisation of adjacent moments would cancel one another.

4.4 Resonant soft X-ray scattering

It has already been stated that resonant X-ray scattering has been used to study $TbMnO_3$ [42]. For these experiments, X-ray photons of energies greater than 3 keV were used. This corresponds to resonant scattering at the Mn K (6539 eV) and Tb L_3 (7514 eV) absorption edges. The work which I will describe in this Chapter relates to resonant scattering studies of $TbMnO_3$ with scattering of soft X-rays, at the four absorption edge energies: the Mn

L_2 (649.9 eV) and L_3 (638.7 eV) and Tb M_4 (1276.9 eV) and M_5 (1241.1 eV). The first question that must be asked is: why are additional RXS studies of $TbMnO_3$ needed, considering the amount of work that has already been conducted [42, 124, 127]? There are three reasons why this additional research is needed.

Firstly, the magnetic structure of $TbMnO_3$ was determined from only two types of antiferromagnetic reflections, namely the A and G type [12]. However, other neutron diffraction measurements have shown that all four types of antiferromagnetic reflections are present [13]. Therefore, measurements on the F and C type reflections may modify, perhaps significantly, the magnetic structure of $TbMnO_3$.

Secondly, when compared with other resonance enhancements of scattering, the K edge resonant enhancement for transition metals (including Mn) is extremely weak. For $TbMnO_3$ this means that any scattering recorded at the Mn K edge will also include a significant contribution from non-resonant magnetic scattering, complicating the result. One solution of this weak resonance signal is to study $TbMnO_3$ at the Tb L_3 resonance, where the enhancement is much greater. This however presents a complication, as the electric-dipole resonance for this edge is probing the Tb $5d$ electronic states. Thus, to study the ordering of the electronic states of the Mn sublattice, one must rely on the assumption that the ordering of the Mn sublattice is affecting, in a way that can be understood, the distribution of the Tb $5d$ electronic states. The electric-dipole resonance enhancements at the Mn L_2 (649.9 eV) and Mn L_3 (638.7 eV), which fall within the soft X-ray regime, are sufficiently large to not suffer from the intensity problem discussed above. Therefore, one does not need to study the Mn electronic states through the Tb resonance. This larger resonance enhancement is due to a greater overlap of the Mn $2p$ and $3d$ orbital wavefunctions.

The third reason why this new RXS study is needed is concerned with which electronic states one can study. As I have stated before (section 2.3.2), for the electric-dipole resonance, the quantum mechanical selection rules state that the angular quantum number l of the electron's initial state may change by plus or minus one only ($\Delta l = \pm 1$). Practically for $TbMnO_3$ this means the electric-dipole transitions for the high energy RXS studies are: Mn K ($1s \rightarrow 4p$) and Tb L_3 ($2p_{3/2} \rightarrow 5d$). Thus, RXS experiments per-

formed at these energies probe the Mn $4p$ and Tb $5d$ delocalised electronic band states, respectively. RXS performed in the vicinity of the Mn L_2 and L_3 and the Tb M_4 and M_5 resonant energies correspond to the following electric-dipole transitions: Mn L_2 (649.9 eV: $2p_{1/2} \rightarrow 3d$), Mn L_3 (638.7 eV: $2p_{3/2} \rightarrow 3d$), Tb M_4 (1276.9 eV: $3d_{3/2} \rightarrow 4f$), Tb M_5 (1241.1 eV: $3d_{5/2} \rightarrow 4f$). As such, there is a clear benefit in utilising RXS at these energies, as they provide information, in a model independent way, on the localised Mn $3d$ and Tb $4f$ electronic states, and it is these states which contain the magnetic moments. In this sense, these resonant soft X-ray scattering studies are complementary to both the previous neutron diffraction and high energy RXS studies.

When compared to the studies performed at high energies, there are however, several complications for RXS at these soft energies. The most fundamental problem associated with soft X-ray scattering is that due to the significantly lower energy, the Ewald sphere of reciprocal space that one may access is severely limited. For the case of $TbMnO_3$, this means that only the F type satellite peak may be accessed with photons equal in energy to the Mn L_2 and L_3 edges. In addition, the 2^{nd} harmonics of the F and C type satellite reflections also fall within the Ewald sphere, see figure 4.5(a). At the Tb M_4 and M_5 resonant energies, the A, C, F and G satellites can in principle be accessed (see figure 4.5(b)). Another complication associated with soft X-rays is the ease at which they are absorbed, in fact soft X-rays are readily absorbed by air. Experiments are therefore required to be conducted under a Ultra High Vacuum (UHV). Even under UHV conditions, the penetration depth of soft X-ray photon varies from 100 Å to 500 Å, depending on the photon energy. Thus, when compared to neutron measurements or X-ray measurements taken at significantly higher energies, one is not studying the same region of the crystal with RXS of soft X-rays. The need for UHV conditions also places several practical limitations on the diffractometers. As a result, soft X-ray diffractometers are generally less advanced than their hard X-ray counterparts. For example, the base temperature possible for soft X-ray diffractometers are generally no lower than 10 K. In addition, motorised azimuthal scans are not possible for all diffractometers, and polarisation analysis of the scattered beam is not common.

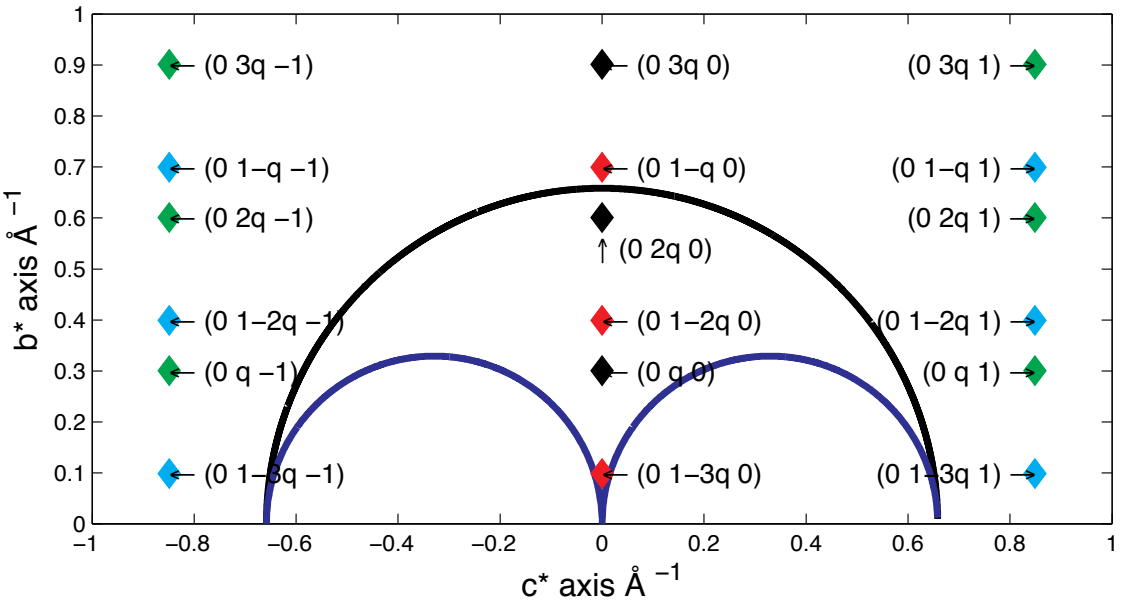

(a)

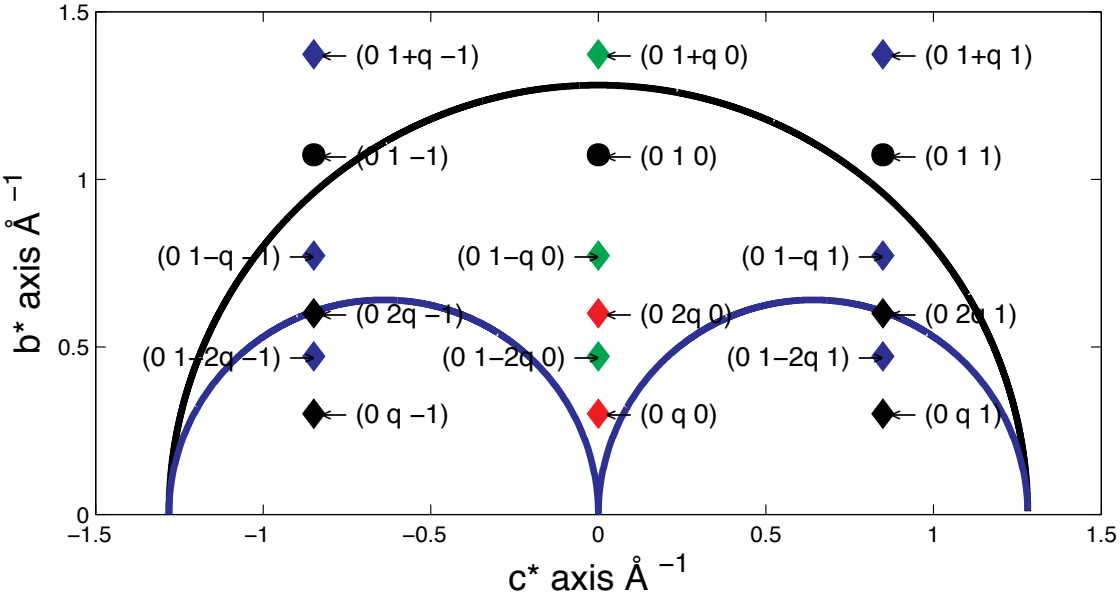

(b)

Figure 4.5: Reciprocal space diagrams of the *b*-face surface normal $TbMnO_3$ crystal at 4.5(a) the Mn L_3 and 4.5(b) the Tb M_4 resonant energies.

4.5 Experimental details

4.5.1 Crystal growth and orientation

In order to conduct this investigation, single crystals of $TbMnO_3$ with dimensions 2×2×1 mm^3 were grown at the University of Oxford, using the flux growth method. Two crystal samples were used, one was cut with a [0 1 0] direction as the surface normal, while the other was cut with a [0 0.28 1] direction as the surface normal. The [0 1 0] orientation allows access to F and C type reflections at the Mn L energies, while the [0 0.28 1] allows access to the A type reflection at the Tb M energies. Samples were polished to a flat, shiny surface with 0.1μm diamond followed by 0.02μAl_2O_3 pastes. The samples were mounted on the diffractometer with the surface normal and [001] direction pointing within the scattering plane. The origin of the azimuthal angle (ψ) also corresponds to the same orientation.

4.5.2 Experimental locations

Experiments were performed at three beamlines, 5U.1 at the Synchrotron Radiation Source (Daresbury Laboratory, Warrington, UK), ID08 at the European Synchrotron Radiation Facility (Grenoble, France) and XM11A at the Swiss Light Source (Paul Scherrer Institut, Villigen, Switzerland). Below is a brief description of each beamline.

Beamline 5U.1

The beamline is situated at the end of a variable-gap undulator, which produces a beam of photons over an energy range of 60-1500 eV. The undulator produces photons which may be vertically, horizontally or circularly polarised. For these experiments, the incident X-rays were approximately 90% linearly polarised, with an incident flux in the order of 10^{11} photons s^{-1} at the focal point. The diffractometer has a horizontal cylinder axis with a concentrically mounted two-circle stage for independent sample (θ) and detector (2θ) rotations, this gives a vertical scattering plane. In addition to the θ and 2θ motors, the

detector can be translated in a perpendicular direction to the vertical scattering plane, thus giving the diffractometer a pseudo χ motion. Inside the vacuum vessel, the sample was placed on the end of a cold finger which was conected to a liquid-helium cryostat, this gave a base temperature of 22 K. The diffractometer operated at a base pressure of 10^{-9} to 10^{-10} mbar. This beamline was used to collect the temperature dependence of the scattering.

Beamline ID08

This beamline is situated at the end of two variable-gap undulators, which are capable of producing photons over an energy range of 400-1600 eV. For the energies used in these experiments, the undulator produces $\sim 100\%$ linearly polarised X-rays ,with an incident flux of $\sim 10^{12}$ photons s^{-1} at the focal point. The beamline has an energy resolution up to 350 meV. The vertical scattering diffractometer had four circles of rotation: θ, 2θ, χ and ψ. This beamline was used because of its superior flux, high incident photon energy resolution and motorised azimuthal stage, to determine the photon energy and azimuthal dependencies of the scattering. The diffractometer operated at a base pressure of 10^{-10} mbar, and a liquid helium cryostat was used to cool the sample via the cold finger. This gave a base temperature of 18 K.

Beamline XM11A

Like the beamlines described previously, XM11A uses a variable-gap undulator to produce highly polarised X-rays over an energy range of 90-2000 eV. Again these X-rays can be vertically, horizontally or circularly polarised. The degree of polarisation and flux of the incident photons are comparable to the other beamlines. The RESOXS endstation is a four-circle diffractometer [136], which can be used in both vertical and horizontal scattering geometries. For this experiment, the horizontal scattering geometry was chosen. The sample was mounted onto the outside of a constant flow liquid helium cryostat which has a base temperature of 10 K, although for this experiment, a base temperature of 20 K was required. The diffractometer operated at a base pressure of 10^{-10} mbar. Polarisation

analysis of the scattered beam, for photon energies <1 keV, was achieved through the use of a W/C multilayer. The azimuthal angle (ψ) could be adjusted manually, by an external rod.

4.6 Experimental results

4.6.1 Identification of the incommensurate reflections

Initial surveys of the [0 1 0] orientated crystal, in the cycloidal phase (22 K) revealed the existence of a 1^{st} harmonic F type satellite peak (denoted as (0 q 0)), for both Mn L resonant energies, at a reciprocal space position of (0 0.285 b^* 0). In addition, two 2^{nd} harmonic satellite reflections corresponding to F type (0 $2q$ 0) and C type (0 1-$2q$ 0) ordering, were seen (again at both Mn L energies) at reciprocal space positions of (0 0.568 b^* 0) and (0 0.445 b^* 0), respectively. Scans parallel to b^* across the three incommensurate reflections were taken as a function of temperature, at both the Mn L_2 and L_3 resonant energies. Results revealed that all three reflections were present above the ferroelectric ordering temperature of 28 K. Examples of all three incommensurate reflections, at the Mn L_2 and L_3 resonances and in both magnetic phases are shown in figure 4.6. As the figure shows, the thermal evolution of the incommensurate propagation vector is most clearly shown for the (0 q 0) reflection. The longitudinal scans of the two 2^{nd} harmonic reflections are weaker and thus it is difficult to accurately determine the thermal evolution of these reflections, however these results do confirm that both 2^{nd} harmonic reflections exist above 28 K. The position of these reflections establish a value for the incommensurate propagation vector, for the cycloidal phase, of q=0.28±0.005 b^*. By fitting the three satellite reflections to a Lorentzian line shape, again this was done using the non-linear least squares fitting approach, the correlation lengths at both the L_2 and L_3 energies and in both magnetic phases were determined to be:

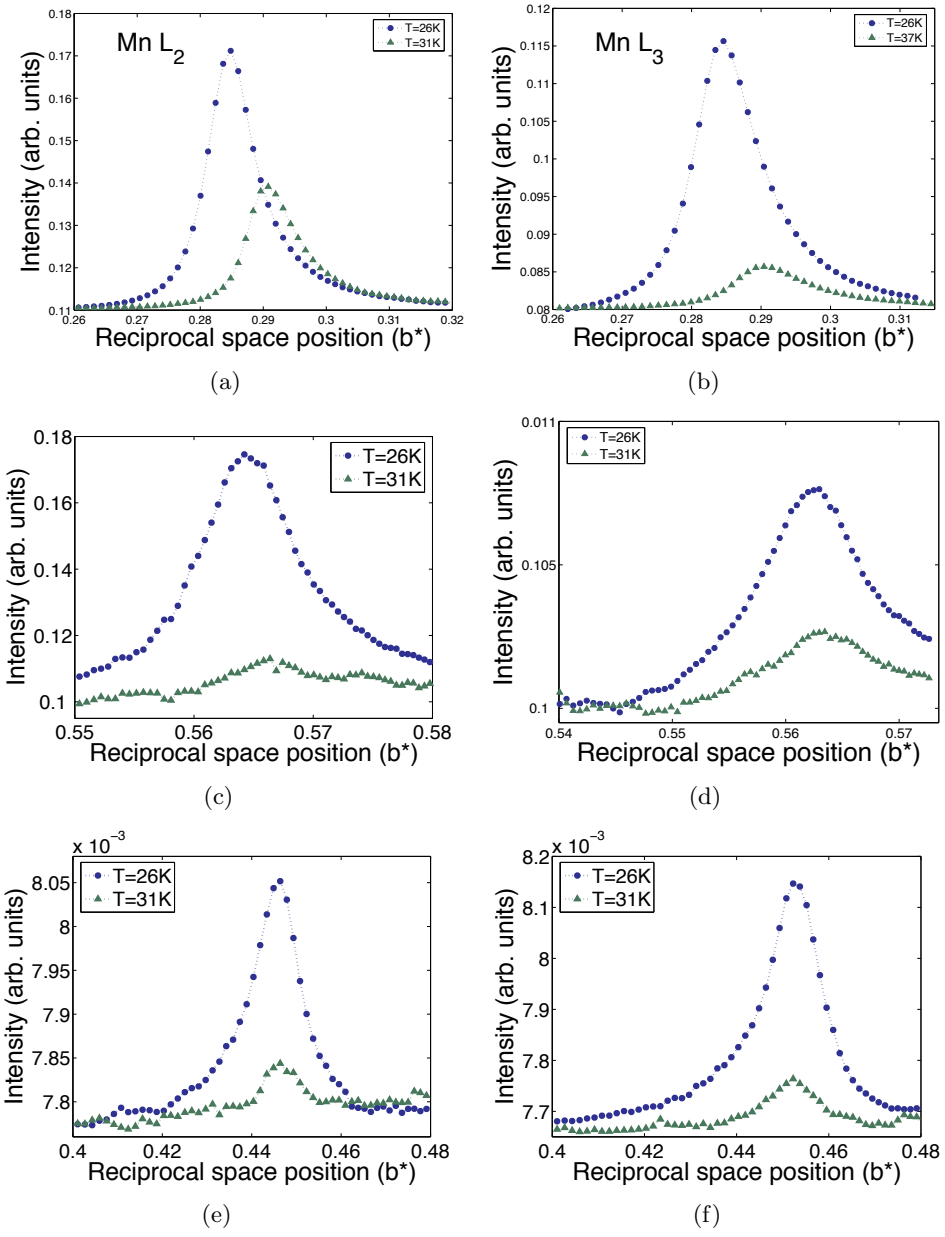

Figure 4.6: Examples of longitudinal scans parallel to the b^* reciprocal space axis. Results were are taken in the cycloidal (blue data points) and collinear (green data points) magnetic phases. Figure 4.6(a) is a scan across the (0 q 0) reflection taken with photon energies equal to the Mn L_2 resonance, while figure 4.6(b) is a scan across the same reflection taken with photon energies equal to the Mn L_3 resonance. Figure 4.6(c) is a scan across the (0 $2q$ 0) reflection taken with photon energies equal to the Mn L_2 resonance. Figure 4.6(d) is a scan across the same reflection taken with photon energies equal to the Mn L_3 resonance. Finally, figure 4.6(f) is scan across the (0 1-$2q$ 0) reflection taken with photon energies equal to the Mn L_2 resonance, and figure 4.6(f) is a scan across the same reflection taken with photon energies equal to the Mn L_3 resonance.

	T=26 K		T=30 K	
	Mn L_2	Mn L_3	Mn L_2	Mn L_3
(0 q 0)	217 Å	177 Å	208 Å	160 Å
(0 2q 0)	207 Å	180 Å	256 Å	178 Å
(0 1-2q 0)	161 Å	148 Å	199 Å	185 Å

Table 4.1: The correlation length (ζ) is defined to be: $\zeta = \frac{1}{\kappa}$, where κ is the characteristic half width of the Lorentzian profile in reciprocal lattice units. Results are given to three significant figures.

These results demonstrate that the X-rays probed a significant number of unit cells within the crystal, hence these measurements are not particularly surface sensitive. No significant change was observed in the correlation lengths of these reflections at the transition between the cycloidal and collinear magnetic phases.

For resonant scattering at the Tb M resonant energies, figure 4.5(b) shows that, in contrast to the results taken at the Mn L resonant energies, where only the F type and 2^{nd} harmonic C type satellite reflections may be observed, all four reflection types (A,C,F and G) may in principle be accessed. To observe the A type reflection, the [0 1 0] crystal sample was replaced by the [0 0.28 1] oriented sample. To start with, comprehensive surveys in the collinear phase of both crystal samples failed to locate any reflections. Upon cooling into the cycloidal phase, a strong well-defined A type satellite reflection was seen in the [0 0.28 1] sample, at both Tb M energies. Examples of longitudinal scans across the (0 q 1) reflection, taken with photon energies equal to the Tb M_4 and M_5 resonant energies, are shown in figure 4.7.

In addition to the A type (0 q 1) reflection, extensive surveys (in the cycloidal phase) of the [0 1 0] oriented sample revealed only a weak (when compared to the A type reflection) F type (0 q 0) and a slightly stronger C type (0 1-q 0) reflection. Both reflections were strongest at the Tb M_5 resonant energy, and were only observed for temperatures less than 26 K. For this azimuthal angle (b-c scattering plane), these reflections were seen with vertically (π) polarised photons only. In addition, no 2^{nd} harmonic reflections were observed. Examples of longitudinal scans across the (0 1-q 0) and (0 q 0) reflections, at the Tb M_5 resonant energy, are shown in figure 4.8.

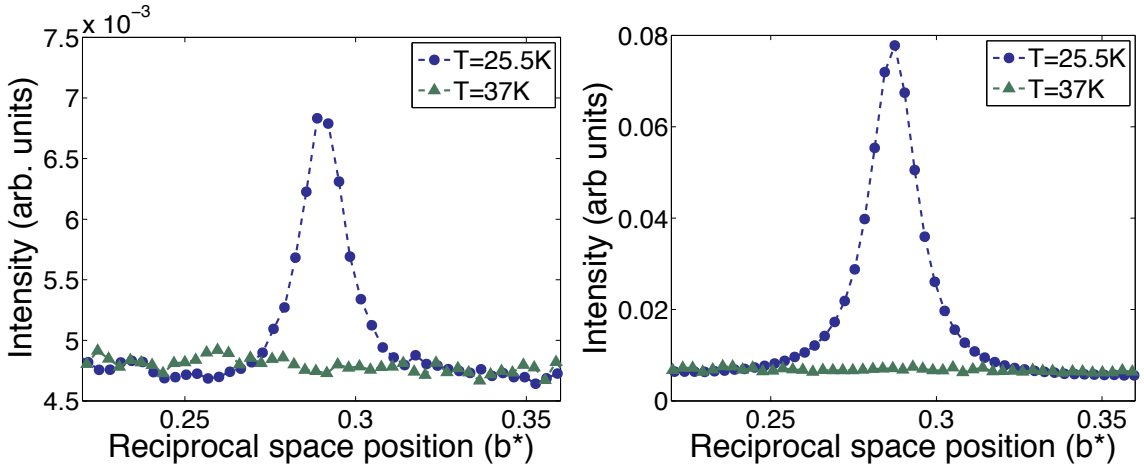

(a) (b)

Figure 4.7: Longitudinal scans of the (0 q 1) reflection taken in the cycloidal (blue data points) and collinear (green data points) magnetic phases. Figure 4.7(a) correspond to scans taken with photon energies equal to the Tb M_4 resonant energy. Figure 4.7(b) corresponds to longitudinal scans taken with photon energies equal to the Tb M_5 resonant energy.

The lack of an oxygen K-edge resonant reflection

A brief search for F type (0 q 0) reflection, with photon energies in the vicinity of the oxygen K-edge (543.1 eV: $1s \rightarrow 2p$), was unsuccessful in identifying any reflections. A reflection at the oxygen K-edge is indicative of hybridisation between Mn $3d$ and oxygen $2p$ orbitals. A lack of a reflection at this absorption edge could therefore mean that there is no hybridisation. However, this seems extremely unlikely considering the fact that hybridisation is needed to describe the ferroelectric polarisation in $TbMnO_3$ [135]. A more likely explanation for the lack of the oxygen K-edge reflection, is that the inversion symmetry of the Mn octahedron environment suppresses this resonant reflection. In fact, unpublished RXS research on $TbMn_2O_5$ has shown that a reflection from the oxygen K-edge arises from the Mn^{3+} ions which are located within the lower symmetry pyramid environments. But no oxygen K-edge resonance was observed for the Mn^{2+} ions situated in the higher symmetry octahedron environments.

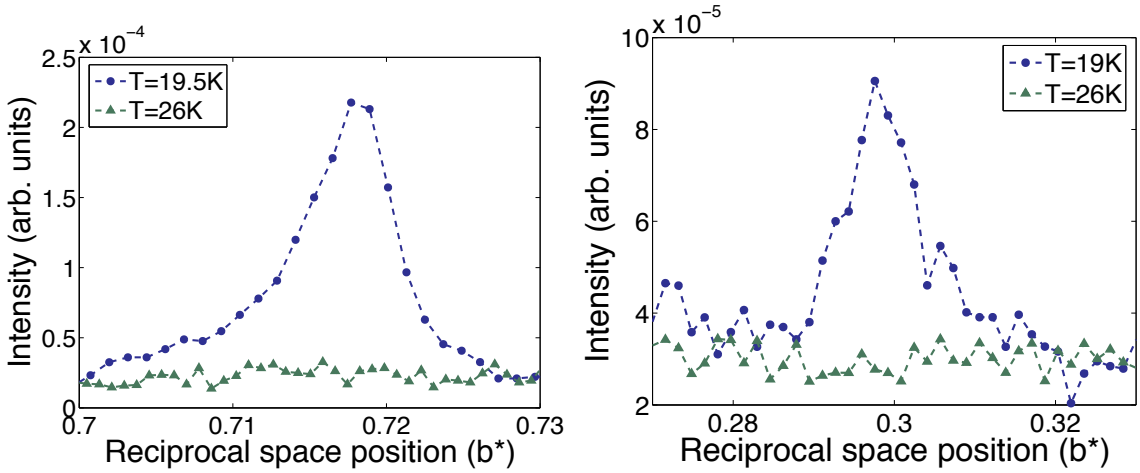

(a) (b)

Figure 4.8: Figure 4.8(a) shows longitudinal scans of the (0 1-q 0) reflection, taken at 19.5 K (blue data points) and 26 K (green data points). Figure 4.8(b) shows longitudinal scans of the (0 q 0) reflection taken at 19 K (blue data points) and 26 K (green data points). Scans were taken with vertically polarised photons, at an energy equal to the Tb M_5 resonance.

4.6.2 Mn L edges, energy scans and temperature dependencies

Figure 4.9 shows the scattering strength, as a function of incident X-ray photon energy, in the vicinity of the Mn L_2 and L_3 energies, at fixed wavevectors corresponding to the position of the (a) (0 q 0), (b) (0 2q 0) and (c) (0 1-2q 0) reflections. Scans were taken in both the cycloidal and collinear magnetic phases. The figure shows a clear resonance enhancement of scattering for all three reflections, at both Mn L edge energies, and in both the cycloidal and collinear magnetic phases. This indicates that the Mn 3d electronic states are ordered, in both magnetic phases.

A more detailed analysis of the effects of temperature, on the scattering strength of these three incommensurate reflections is shown in figure 4.10. Again, scans parallel to b^*, across the reflections (at both Mn L resonant energies) were taken as the temperature was increased from a base temperature of T$\sim$25 K. The vertical arrows shown in figure 4.9 indicate the exact energies at which the temperature dependences were recorded.

Let us first consider the results taken for the (0 q 0) F type reflection. The scans of

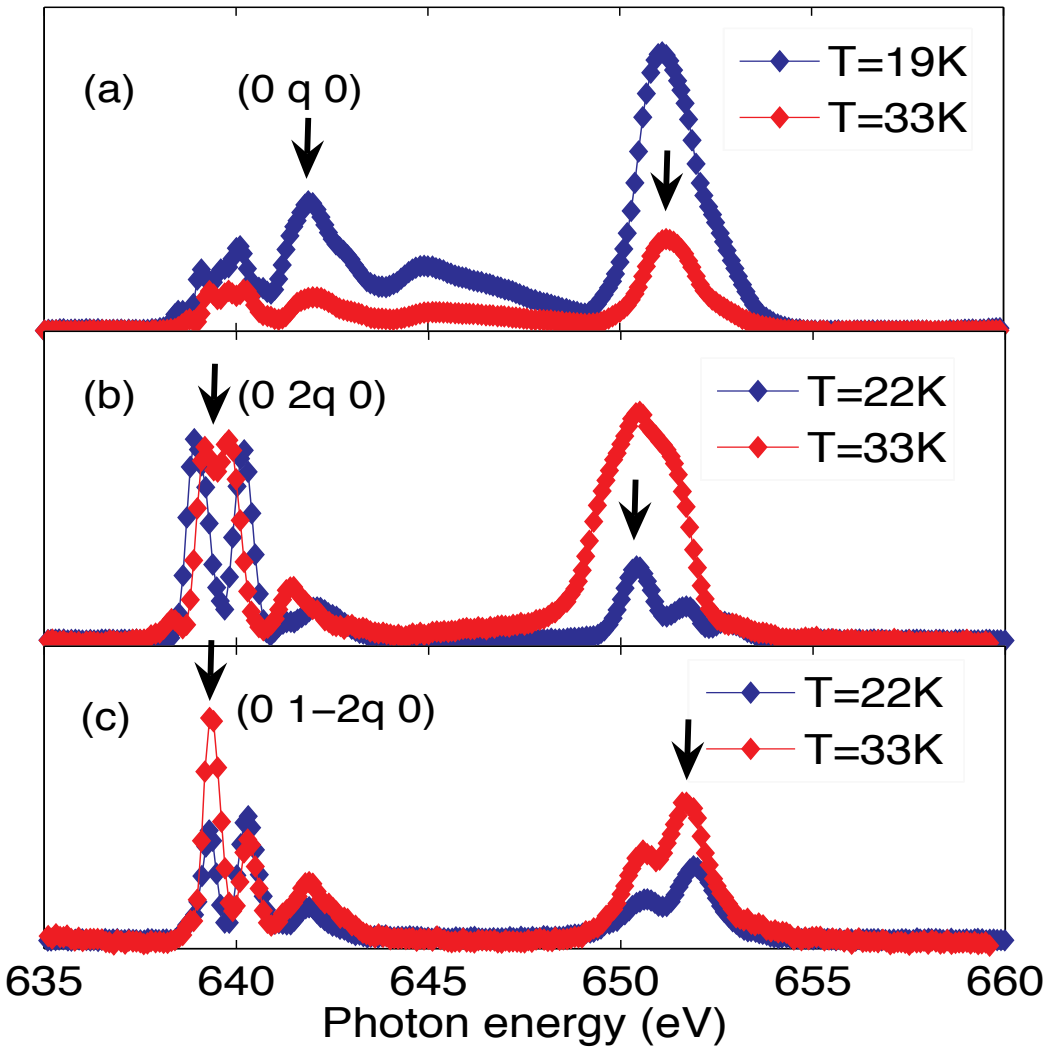

Figure 4.9: Mn L edge incident photon energy scans, at the fixed wavevectors of (a) the (0 q 0), (b) the (0 2q 0) and (c) the (0 1-2q 0) reflections. Scans were taken in both the cycloidal and collinear magnetic phases, with horizontally polarised (σ) incident photons. The vertical arrows indicate the energies at which a temperature dependences were recorded. The collinear phase energy scans of the (0 2q 0) and (0 1-2q 0) reflections have been normalised in intensity to the corresponding cycloidal phase scans, at the Mn L_3 resonance. Results show a clear resonance for all three reflections, in both phases. The multiple features, seen in these energy scans, are most likely due to crystal field effects which lift the degeneracy of the Mn 3d electronic states. This indicates that the Mn 3d electronic states show long range order for at least two types of reflections.

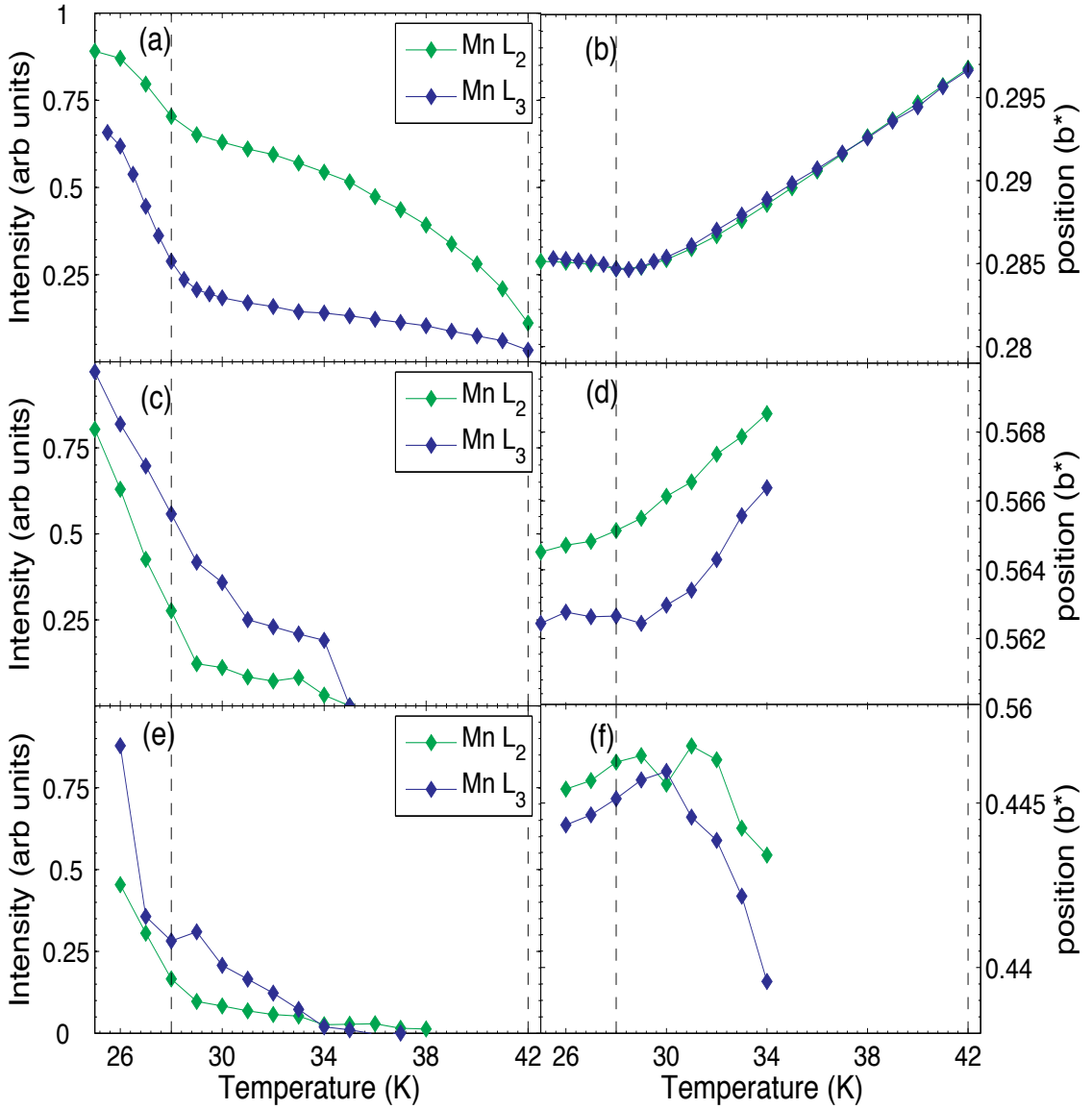

Figure 4.10: The temperature dependence of the (0 q 0) reflection, (a) the integrated intensity and (b) the position at the Mn L_2 and L_3 energies. The (0 2q 0) reflection, (c) the integrated intensity and (d) the position. The (0 1-2q 0) reflection, (e) the integrated intensity and (f) the position. Scans were taken with horizontally polarised (σ) incident photons. The integrated intensity and position of the reflection were obtained by fitting a Lorentzian function to the peak profiles.

scattering strength as a function of incident photon energy (energy scans) of this reflection, reveal strong resonant enhancements of the scattering cross-section at both the Mn L_2 and L_3 edge energies. Apart from the overall reduction in intensity for the results taken in the collinear phase, the energy spectra of the two magnetic phases are very similar. A strong single resonant feature is observed at the Mn L_2 edge, while the energy line shape, in the vicinity of the Mn L_3 edge, displays much more fine structure, with the main resonant feature at an incident photon energy of 642 eV. This fine structure is caused by the splitting of the Mn $3d$ electronic states, which is due to the crystal field. It should be noted that a number of resonant soft X-ray scattering studies have been made of several related rare-earth manganite compounds, which are not multiferroic [31, 33, 137]. Results from all of these studies have shown that, for both the magnetic and orbital ordered reflections, the resonant feature at the Mn L_3 edge is always strongest. This is clearly not the case for the (0 q 0) reflection observed in this study.

In order to investigate the scattering cross-section of the (0 q 0) reflection as a function of temperature, longitudinal scans of this reflection at both Mn L resonant enhancements were taken as the temperature is increased from T=25 K. Figure 4.10 gives (a) the integrated intensity and (b) the position in reciprocal lattice units of this reflection, versus temperature. For the results taken in the cycloidal phase, the propagation vector is only weakly temperature dependent with $q \approx 0.285 \pm 0.005\ b^*$. As the temperature is increased through 28 K into the collinear phase, the propagation vector increases linearly. This relationship holds as the temperature is increased, until T=42 K, where q reaches a maximum value of $q \approx 0.295 \pm 0.005\ b^*$. Above 42 K, the reflection is not observed. This trend is consistent with that deduced from previous neutron [12] and hard X-ray scattering [42] experiments. The reflection's scattering intensity, as a function of temperature (figure 4.10(a)), shows that the evolution in intensity differs between measurements performed at the Mn L_2 and L_3 resonant energies. At the transition between the two magnetic phases, a larger change in the scattering intensity is seen at the L_3 edge, than the L_2 edge. In other words, the Mn L_2/L_3 branching ratio is temperature dependent. A temperature dependent branching ratio has previously been observed in $DyFe_4Al_8$, where it was attributed to the effect of magneto-elastic coupling [138].

Turning to 2^{nd} harmonic incommensurate reflections, which have reciprocal space positions of: (0 0.568 b^* 0) and (0 0.445 b^* 0). It has already been stated that these reflections correspond to the 2^{nd} harmonic (0 2q 0) F type and (0 1-2q 0) C type satellite reflections, respectively. As with the (0 q 0) reflection, the incident photon energy scans of these reflections reveal significant resonant enhancements, at both the Mn L_2 and L_3 edges and in both the cycloidal and collinear phases. The spectra line shape of both 2^{nd} harmonic reflections differ to the (0 q 0) reflection, this is not unexpected as the scattering from 2^{nd} harmonic reflections arise from a different F_{lm} factor to the 1^{st} harmonic reflection. The single feature observed at the Mn L_2 edge for the (0 q 0) reflection is replaced by two distinct features. For the Mn L_3 resonances, the main feature of the (0 q 0) reflection at E=642 eV is much weaker, while the multiple features at E$\sim$640 eV are, in comparison, much stronger and replaced by two main features at energies either side of 640 eV. Furthermore, unlike the energy spectra of the (0 q 0) reflection, there are significant differences between the cycloidal and collinear phase energy spectra of the (0 2q 0) and (0 1-2q 0) reflections. For the (0 2q 0) reflection, figure 4.9(b) shows a large difference in the Mn L_2/L_3 branching ratio between the two phases. In addition, for the spectrum recorded in the collinear phase, the multiple features observed at the L_2 edge seem to almost merge into one feature. Interestingly, the change in branching ratio seen in figure 4.9(b) is not shown in the temperature dependence (figure 4.10(c)). I am unsure why this is the case. One possible explanation could be a change in energy of the incident photons, due to a shift in the beamline monochromator. Therefore, the scattering from this reflection may not have been measured at exactly the same energy for all temperatures. The position of the (0 2q 0) reflection, shown in figure 4.10(d), gives the correct trend for the evolution of the incommensurate propagation vector (q), where q is approximately independent of temperature below 28 K, with $q \approx 0.283 \pm 0.005b^*$ (Mn L_2) and $q \approx 0.281 \pm 0.005b^*$ (Mn L_3). Above 28 K, q increases linearly with temperature up to 35 K. Above 35 K the reflection was not observed. The fact that this reflection was not observed for temperatures between 35 K and 42 K could be due to the shift in incident photon energy as described previously. Another possible explanation, is that at the Mn L_2 energy, the reflection may have exceeded the 5U.1 diffractometer's maximum value of the θ and 2θ angles.

The energy spectra of the (0 1-2q 0) C type reflection are shown in figure 4.9(c). These spectra are similar to those of the (0 2q 0) reflection, except that the scattering intensities of the two features at the Mn L_2 resonance is reversed. Upon warming into the collinear phase, like the (0 2q 0) reflection, significant changes are detected in the incident photon energy spectra at the Mn L_3 resonance. This can be seen in a relative increase in the intensity of scattering at an energy slightly lower than 640 eV. In addition, a reduction in the scattering intensity of scattering slightly above 640 eV, is also seen. Apart from the reduction in scattering intensity, little change is seen in the energy scans taken in both phases at the Mn L_2 resonance. Finally, the temperature dependence of this reflection's integrated intensity and position are given in figures 4.10 (e) and (f) respectively. Figure 4.10 (e) shows that upon warming from a base temperature of 25 K, the intensity decreases in a non linear fashion, reaching zero at 35 K. Again, the reason for this lower transition temperature, could be due to an unnoticed shift of the incident photon energy. No significant change in intensity is observed at the ferroelectric phase transition (T=28 K). The general evolution of the reflection's position as a function of temperature (Figure 4.10 (f)), is in agreement with the evolution of the magnetic propagation vector [12], i.e. the reflection moves to a lower position in b^* as the temperature is increased, therefore the magnitude of q increases with temperature. Having said this, the actual values of the propagation vector q, are slightly lower than the values determined for the (0 q 0) F type reflection, 0.2775 b^*→0.2810 b^* (Mn L_2) and 0.2795 b^*→0.2805 b^* (Mn L_3).

In conclusion, the strong electric-dipole resonances, combined with the sharpness of the (0 q 0) reflection in reciprocal space, establishes that the Mn 3d electronic states display long range order in both the cycloidal and collinear phases. Also, the incident photon energy scans of this reflection show minimal changes of the electronic structure, apart from the reduction in intensity. In addition to the Mn 3d states long range ordering, the thermal evolution of the wavevector q, shown in figure 4.10(b), is extremely similar to the thermal evolution of the previously determined magnetic wavevector $\mathbf{q}$ [12]. This suggests that the RXS in these experiments, is most likely magnetic in origin.

Results from the two 2^{nd} harmonic satellite reflections of (0 2q 0) and (0 1-2q 0) are not as easy to interpret. The thermal evolution of these two reflections positions is in

general agreement with the evolution of the magnetic wavevector **q** [12], incident photon energy scans (figures 4.9 (a) and (b)) indicate significant changes in the Mn 3*d* electronic states between the cycloidal and collinear phases. However, to obtain further information from these energy scans, detailed modelling of the electronic structure is required. This modelling is beyond the scope of this current work.

4.6.3 Tb M edges, energy scans and temperature dependencies

I will now discuss the results taken with photon energies in the vicinity of Tb M_4 and M_5 absorption edges (1240 eV and 1270 eV respectively). As I have already stated, for the collinear magnetic phase, no incommensurate reflections were observed with photon energies equal to the Tb M_4 and M_5 absorption edges. Thus all results discussed in this section were recorded below 28 K, in the cycloidal magnetic phase.

Figure 4.11 shows a scan of the incident photon energy at the fixed wavevector of the A type reflection (denoted as (0 q 1)), in the cycloidal phase (T=22 K). The figure shows a significant resonant enhancement of the scattered beam, with multiple features at both absorption edges, however the Tb M_5 resonant enhancement is much stronger. As was the case for the reflections that were measured at the Mn L edges, the magnitude of the incommensurate propagation vector evolves as a function of temperature. For the A type reflection, the new crystal orientation means that the reflection becomes off specular. However, experimental limitations on 5U.1, made it impossible to resolve accurately the evolution of this reflection's position as a function of temperature. Therefore, only the reflection's scattering intensity, as a function of temperature, is presented (figure 4.12(a)). The intensity of the reflection was calculated as before. This temperature dependence was recorded with incident photon energies equal to the main Tb M_5 feature as seen in figure 4.11 (vertical arrow). No temperature dependence was recorded with photons at the Tb M_4 energy, as it was felt that the resonant feature here was too weak. In addition, we know from our initial scans that no reflection exists at this energy in the collinear phase. As figure 4.12(a) clearly shows, the intensity of scattering at the M_5 edge drops rapidly and linearly with increasing temperature, with a zero in intensity at T=28 K.

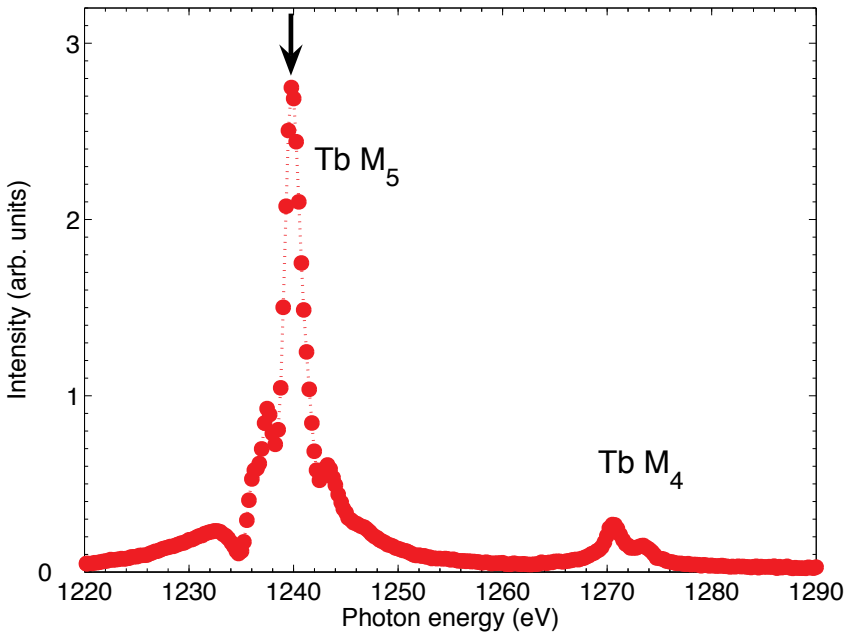

Figure 4.11: An incident photon energy scan, at fixed wavevector of the (0 q 1) reflection. The vertical arrow indicates the energy at which a temperature dependence was recorded. The scan was taken with horizontally polarised (σ) incident photons.

Also shown (figure 4.12(b)), is the intensity of the C type (0 1-q 0) reflection, recorded with π-polarised incident photons which were equal in energy to the Tb M_5 resonance. As the temperature was increased from a base temperature of 19 K (this temperature dependence was recorded at the ID08 beamline, hence the lower base temperature), the intensity of scattering decreases, with zero intensity being observed for T$\geq$25 K. The position of this reflection seems to remain constant with increasing temperature, which agrees with previous results for the propagation wavevector q for this temperature range. However, because of the relative weakness of this reflection, it is difficult to be certain about this. Finally, the F type reflection at these energies was too weak for a temperature dependence to be recorded.

In summary, the energy scans and temperature dependences taken at the Tb M edges clearly show, that for the A type (0 q 1) reflection, the Tb $4f$ band is highly influenced by the cycloidal magnetic order. However, the same reflection was absent in the collinear phase, indicating that there is no long range ordering of the Tb $4f$ states for this phase. This data supports Kenzelmann's neutron diffraction model [12], which concludes that the

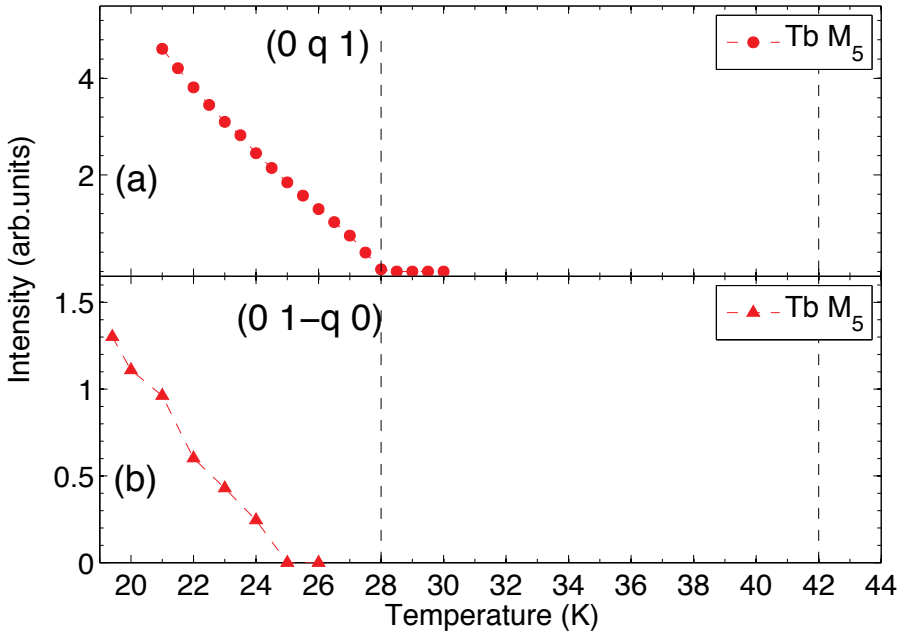

Figure 4.12: The integrated intensity temperature dependence of (a) the (0 q 1) incommensurate reflection at the Tb M_5 energy (1240 eV),taken with horizontally polarised (σ) photons, and (b) the (0 1-q 0) incommensurate reflection. Again this was recorded with photons equal in energy to the Tb M_5 energy (1240 eV), taken with vertically polarised (π) incident photons.

Tb $4f$ states should be disordered in the collinear phase. The absence of Tb $4f$ ordering in the collinear phase, suggests that ordering of the Tb $5d$ electronic states, as seen with hard X-rays [42, 127], was due to a polarisation by the Mn sublattice. In addition to strong Tb M edge resonances observed for the A type reflection, much weaker Tb M edge resonant reflections, corresponding to the F type (0 q 0) and C type (0 1-q 0) reflections, were observed in the cycloidal phase. The fact that these two reflections were detected with π-incident X-rays only and are much weaker, suggests a difference between the magnetic structures of the various types of reflections.

4.6.4 Mn L edges, azimuthal and polarisation dependencies

The (0 q 0) reflection.

In order to investigate the symmetry of the Mn $3d$ electronic states, the intensity of the (0 q 0), (0 $2q$ 0) and (0 1-$2q$ 0) reflections, as a function of azimuthal angle (ψ), were recorded. These results were taken during two experimental runs at the ID08 beamline. In addition, incident photon energy scans of the (0 q 0) and (0 $2q$ 0) reflections with polarisation analysis of the scattered beam, were recorded at the XM11A beamline.

For the [0 1 0] orientated sample, the azimuthal origin ($\psi = 0°$) corresponds to the situation where the [0 0 1] direction points within the scattering plane. Hence for $\psi = 0°$ the scattering is in the $b - c$ crystallographic plane, while for $\psi = 90°$ the scattering points within the $a - b$ crystallographic plane. The azimuthal dependence of the three reflections seen at the Mn L_2 and L_3 resonances were determined by transverse (θ) and longitudinal ($\theta - 2\theta$) scans of each reflection as the sample was rotated about the U_3 axis (see figure 2.1) in steps of 10°. These scans were taken at a number of specific energies that correspond to distinct features seen in the incident photon energy scans of each reflection (see inserts of azimuthal figures). If these reflections are magnetic in origin, then their azimuthal dependencies can be used to determine the magnitude of magnetic moments along the different crystallographic axes. This can be achieved by making the following substitutions:

$$\begin{aligned} \hat{z_1} &= \hat{z_c}\cos\psi + \hat{z_a}\sin\psi \\ \hat{z_2} &= \hat{z_c}\sin\psi + \hat{z_a}\cos\psi \\ \hat{z_3} &= \hat{z_b} \end{aligned} \tag{4.7}$$

For the 1^{st} harmonic reflection, the substitutions shown in equation 4.7 are inserted into the square of the second matrix of equation 2.32:

$$I \propto \begin{pmatrix} 0 & z_1\cos\theta + z_3\sin\theta \\ z_3\sin\theta - z_1\cos\theta & -z_2\sin 2\theta \end{pmatrix}^2 \tag{4.8}$$

Therefore the magnitude of magnetic moments along the different crystallographic axes can be determined for σ-polarised incident photons by fitting the azimuthal dependence with the function:

$$I \propto (\hat{z_c}\cos\psi + \hat{z_a}\sin\psi + \hat{z_b}\sin\theta)^2 \tag{4.9}$$

For the 2^{nd} harmonic reflection, the same substitutions are inserted into the square of the third matrix of equation 2.32:

$$I \propto \begin{pmatrix} {z_2}^2 & -z_2(z_1\sin\theta - z_3\cos\theta) \\ z_2(z_1\sin\theta + z_3\cos\theta) & -\cos^2\theta({z_1}^2\tan^2\theta + {z_3}^2) \end{pmatrix} \tag{4.10}$$

Thus the magnitude of magnetic moments along the different crystallographic axes can be determined for σ-polarised incident photons by fitting the azimuthal dependence with the function:

$$I \propto \left((\hat{z_c}\sin\psi + \hat{z_a}\cos\psi)^4 + ((\hat{z_c}\sin\psi + \hat{z_a}\cos\psi)(\hat{z_c}\cos\psi + \hat{z_a}\sin\psi\sin\theta - \hat{z_b}\cos\theta))^2\right) \tag{4.11}$$

Figures 4.13 and 4.14 show the azimuthal dependence of the (0 q 0) reflection for the cycloidal (T=26 K) and collinear (T=32 K) phases respectively. The intensity of the reflections were determined by fitting a Lorentzian line profile for the measurements taken in the cycloidal phase, however for the measurements taken in the collinear phase it was found that the reflection was not symmetrical about the peak, therefore the intensities were calculated using a numerical integration algorithm (called peakt in Spec1d). In addition figures 4.15 and 4.16 show the incident photon energy scans of the same reflection, with polarisation analysis, in the cycloidal (T=20 K) and collinear (T=32 K) phase respectively,

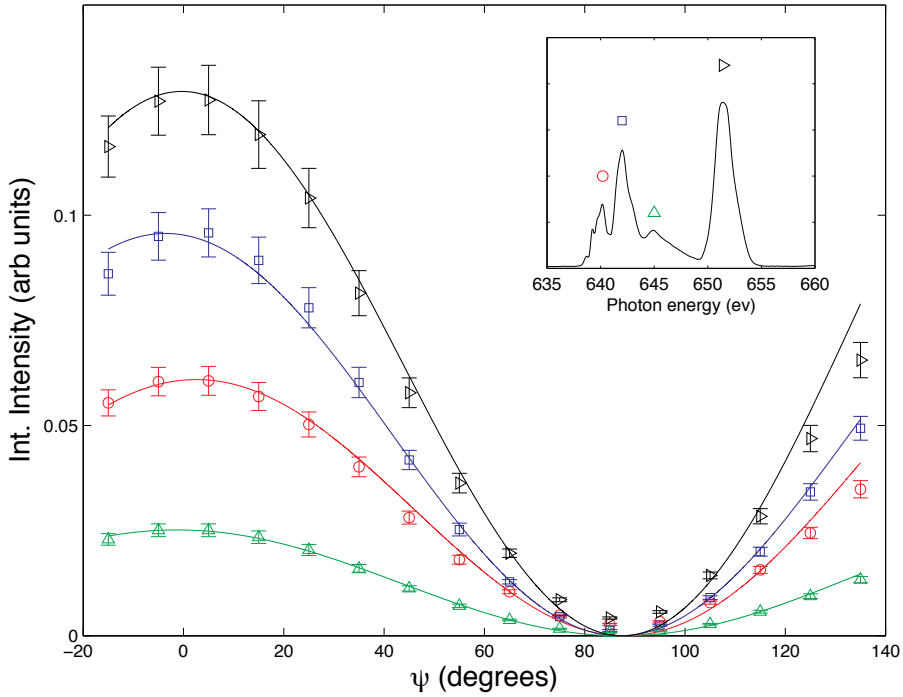

Figure 4.13: Azimuthal dependence of the (0 q 0) reflection at a temperature of 25 K. The scan was taken with horizontally polarised (σ) incident photons and fitted with equation 4.9.

at (a) & (b) $\psi = 0°$ and (c) & (d) $\psi = 90°$. These energy scans were taken with both σ and π polarised incident photons.

Returning to the azimuthal dependences of the (0 q 0) reflection, results taken in both phases show a reasonable agreement with a $\cos^2\psi$ relationship, for all features. Apart from the overall reduction in intensity, there does not seem to be any significant changes between the azimuthal dependences recorded in the cycloidal (figure 4.13) and collinear (figure 4.14) phases. Thus it seems that the symmetry of this reflection is the same for both magnetic phases. This is a somewhat surprising result, however it does seem to agree with the energy scans shown in figure 4.9(a). If this reflection is magnetic in origin as believed, then the magnetic structure for this reflection cannot be the one proposed by Kenzelmann *et al.* [12]. There are two main reasons for this statement. Firstly, for the results taken at 25 K (figure 4.13), one would expect a constant background on top of a $\cos^2\psi$ relationship. This is because for the cycloidal magnetic structure, there will always be a component of the magnetic moment in the scattering plane. However as figure

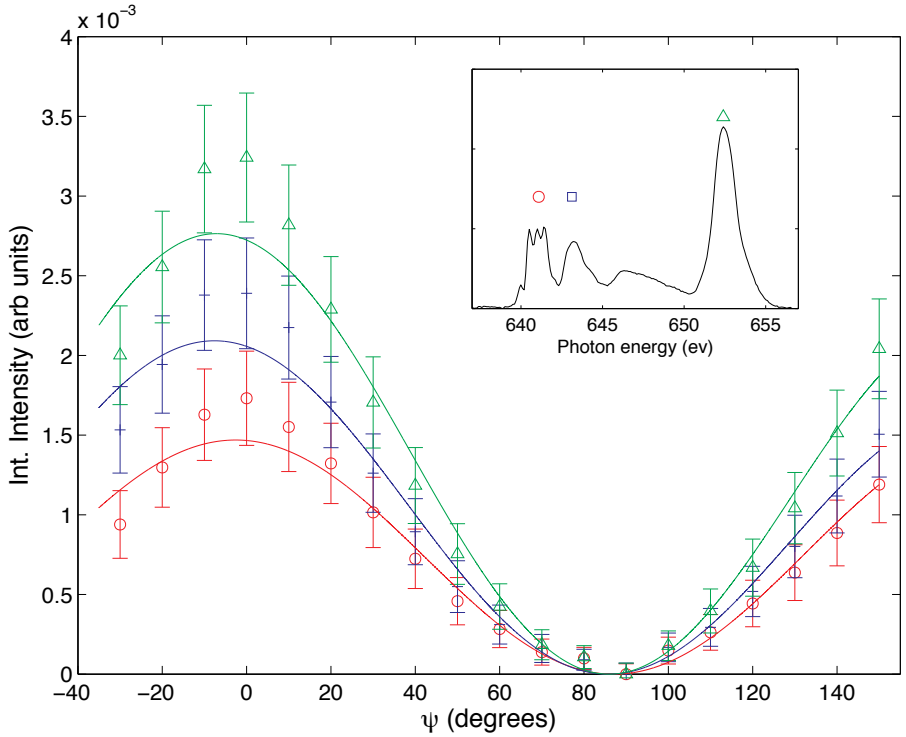

Figure 4.14: Azimuthal dependence of the (0 q 0) reflection at a temperature of 32 K. The scan was taken with horizontally polarised (σ) incident photons and fitted with equation 4.9.

4.13 shows, there is no constant background, the intensity of the reflection goes to zero as $\psi \rightarrow 90°$. Secondly, for the proposed collinear magnetic structure (sinusoidally modulated moments pointing parallel to the b-axis), the magnetic moments always point within the scattering plane, regardless of the azimuthal angle. Therefore one would expect to see a flat azimuthal dependence, which was independent of ψ, figure 4.14 shows that this clearly is not the case. One could argue that the relationship seen in figure 4.14 could be due to a miss cut crystal surface, such that some component of the crystallographic b-axis would be parallel to the crystal surface. However if this were the case, one would still expect to see a significant azimuthal independent background, but figure 4.14 clearly shows this not to be the case.

Further evidence that the (0 q 0) reflection does not represent the magnetic structure proposed by Kenzelmann and co-workers can be seen in the energy scans shown in figure 4.15. If one assumes that the scattering from this reflection is still magnetic in origin, then

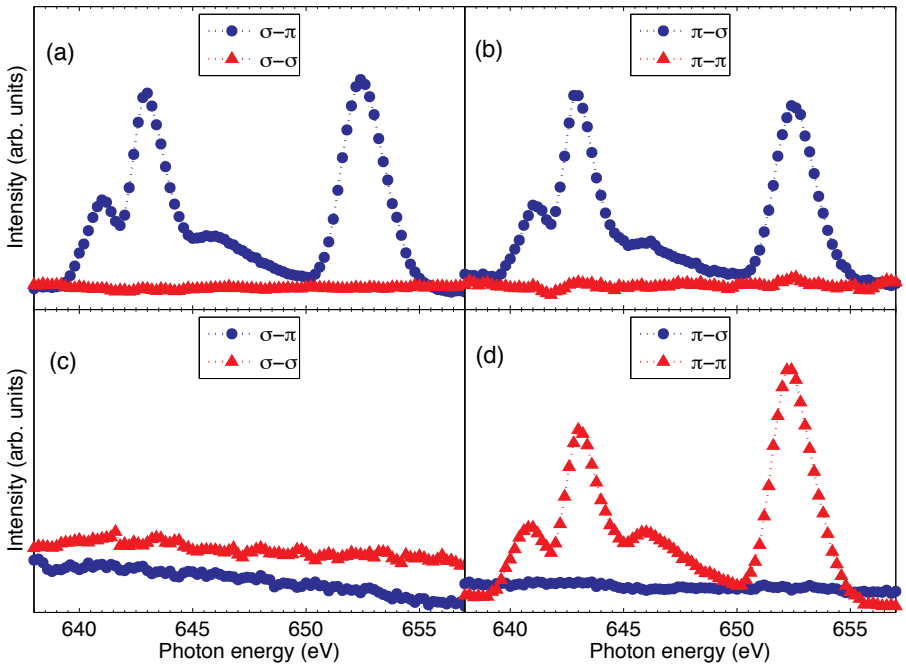

Figure 4.15: Incident photon energy scans at a fixed wavevector corresponding to the (0 q 0) reflection. These scans were taken at a temperature of 20 K and at the azimuthal angles of $\psi = 0°$ ((a) & (b)) and $\psi = 90°$ ((c) & (d)).

the electric-dipole cross-section for a 1^{st} harmonic antiferromagnetic reflection, given by equation 4.8, can be used to describe the polarisation dependence shown in figures 4.15 and 4.16.

For $\psi = 90°$, the following directions correspond to the crystallographic axes, $\hat{U_1} = \hat{a}$, $\hat{U_2} = \hat{c}$ and $\hat{U_3} = -\hat{b}$. If the magnetic moments point within the b-c plane, as is the case for the proposed cycloidal magnetic structure, then $\hat{z_1} = 0$ and $\hat{z_2} \neq 0$, $\hat{z_3} \neq 0$, therefore one would expect a signal in the $\sigma - \pi'$, $\pi - \sigma'$ and $\pi - \pi'$ scattering channels. As figure 4.15 (c) and (d) shows, at this azimuthal angle, a signal is only seen in the $\pi - \pi'$ channel.

If the magnetic structure for this reflection is not the one proposed by Kenzelmann and co-workers, then what is it?

By fitting the azimuthal dependencies of the (0 q 0) reflection (figures 4.13 and 4.19) to equation 4.9, the magnitude of the magnetic moments along the different crystallographic axes can be extracted. Results from these fits are shown in tables 4.2 and 4.3. The general

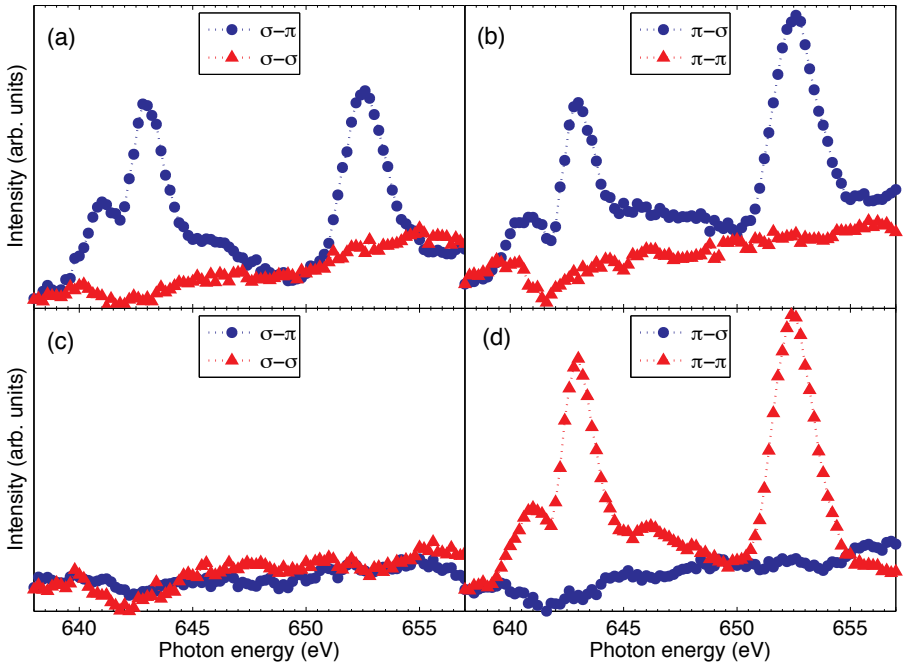

Figure 4.16: Incident photon energy scans at a fixed wavevector corresponding to the (0 q 0) reflection. These scans were taken at a temperature of 32 K and at the azimuthal angles of $\psi = 0°$ ((a) & (b)) and $\psi = 90°$ ((c) & (d)).

results from this fitting shows that, for both phases, the magnetic moments point along the crystallographic c-axis.

Energy	$\hat{z}_1$	$\hat{z}_2$	$\hat{z}_3$
640 eV	0.01±0.02	0.06±0.05	0.29±0.01
642 eV	0.02±0.01	0.01±0.02	0.33±0.01
645 eV	0.01±0.01	0.01±0.02	0.18±0.01
651 eV	0.01±0.04	0.04±0.1	0.40±0.01

Table 4.2: Values of $\hat{z}_1$, $\hat{z}_2$ and $\hat{z}_3$ obtained from fitting the azimuthal dependence of the (0 q 0) reflection at T=25K to equation 4.9.

This c-axis magnetic structure is supported by the polarisation dependent energy scan, shown in figures 4.15 and 4.16. As equation 4.8 shows, a magnetic structure with moments parallel to c-axis, would give scattering in the $\sigma - \pi'$ and $\pi - \sigma'$ channels for $\psi = 0°$, and in the $\pi - \pi'$ channel only for $\psi = 90°$. Additional energy scans taken in both magnetic phases, at $\psi = 180°$ and $\psi = 270°$, were identical to the energy scans at $\psi = 0°$ and $\psi = 90°$ respectively.

Energy	$\hat{z_1}$	$\hat{z_2}$	$\hat{z_3}$
641 eV	0.01±0.01	0.01±0.01	0.04±0.01
643 eV	0.01±0.01	0.01±0.01	0.04±0.01
651 eV	0.01±0.01	0.01±0.01	0.05±0.01

Table 4.3: Values of $\hat{z_1}$, $\hat{z_2}$ and $\hat{z_3}$ obtained from fitting the azimuthal dependence of the (0 q 0) reflection at T=32K to equation 4.9.

It is important to remember that Mannix *et al.* [42] did not see a signal in the rotated $\sigma - \pi'$ scattering channel for an F type reflection, with non-resonant X-ray scattering. A signal in the rotated channel for NRXS is definitive proof that a reflection has a magnetic component. Even without a non-resonant scattering signal, the azimuthal dependences and polarisation analysis of the incident photon energy scan of the F type (0 q 0) reflection, strongly suggest a antiferromagnetic structure with the moments parallel to the crystallographic c-axis. The result also suggests the same magnetic structure, for both the cycloidal and collinear magnetic phases, for this F type reflection.

The (0 2q 0) reflection.

A azimuthal dependence of the (0 2q 0) reflections is given in figure 4.17, the data was recorded in the cycloidal magnetic phase at a temperature of 25 K and fitted with the function given in equation 4.11. In addition, incident photon energy scans, with polarisation analysis of the scattered beam at (a) & (b) $\psi = 0°$ and (c) & (d) $\psi = 90°$ are shown for the (0 2q 0) reflection (figure 4.18). Again these results were taken in the cycloidal phase (T=20 K). Due to time constraints, no azimuthal dependences or energy scans with polarisation analysis for the collinear phase were taken.

The next question is: can these azimuthal dependences be explained by the simple c-axis antiferromagnetic structure of the (0 q 0) reflection?

Fitting the azimuthal dependence to equation 4.11 showed that the majority of the magnetic momentum points along the a-axis (see table 4.4).

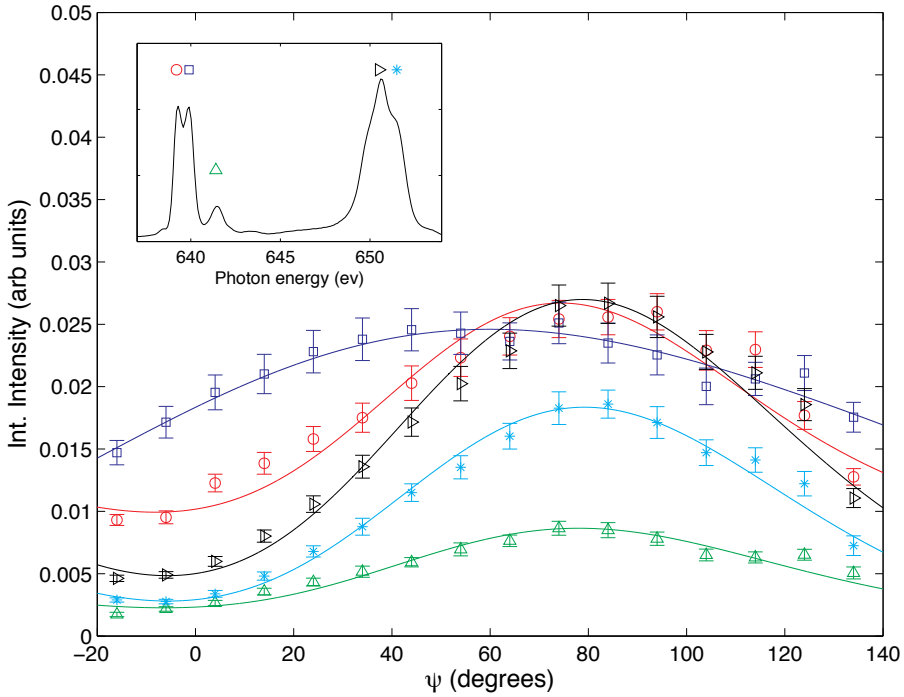

Figure 4.17: Azimuthal dependence of the (0 $2q$ 0) reflection at a temperature of 25 K. The scan was taken with horizontally polarised (σ) incident photons.

Energy	$\hat{z}_1$	$\hat{z}_2$	$\hat{z}_3$
639 eV	0.05±0.01	0.05±0.01	0.35±0.01
641.5 eV	0.03±0.01	0.05±0.01	0.28±0.01
650.5 eV	0.04±0.01	0.05±0.01	0.38±0.01
651.5 eV	0.03±0.01	0.04±0.01	0.35±0.01

Table 4.4: Values of $\hat{z}_1$, $\hat{z}_2$ and $\hat{z}_3$ obtained from fitting the azimuthal dependence of the (0 $2q$ 0) reflection at T=25K to equation 4.11. Values from the energy feature at 640 eV are not included.

Thus the azimuthal dependences shown in figure 4.17, with the exception of the resonant feature at 640.5 eV, suggest a magnetic structure with the majority of the magnetic moments pointing parallel to the c-axis. It is important to note however, that for a c-axis magnetic structure there should be zero scattering intensity when $\psi = 0°$. Therefore, the non-zero scattering intensity at $\psi = 0°$ shown in figure 4.17 is possibly due to charge distortions that arise from the magnetic structure.

Further evidence that the resonant feature at 640.5 eV is not consistent with a c-axis magnetic structure, can be found in figure 4.18. For the simple c-axis magnetic structure, inspection of equation 4.10 suggests that at $\psi = 0°$, one would only see a signal in the $\pi - \pi'$ scattering channel. Figure 4.18 however, shows that in addition to the $\pi - \pi'$ scattering, a significant resonant signal is seen at the Mn L_3 edge in the $\sigma - \sigma'$ scattering channel. Rotating ψ by 90°, equation 4.10 now states that a simple c-axis antiferromagnetic structure would only produce a resonant scattering signal in the $\sigma - \sigma'$ channel. However, figure 4.17(d) shows that, in addition to the Mn L_2 and L_3 resonances seen in the $\sigma - \sigma'$ scattering channel, a resonant feature is also observed again at the Mn L_3 edge in a different channel, this time the $\pi - \pi'$. What this signal represents is somewhat of a mystery, the feature at 640.5 eV could be charge scattering due to a displacement of the lattice, which has been induced by the magnetic ordering. Such reflections have been detected by Mannix *et al.* [42], however there is no reason why this charge scattering would resonate.

The (0 1-2q 0) reflection.

I will now discuss the azimuthal dependence of the C type (0 1-2q 0) reflection. Like the (0 2q 0) reflection, results were only taken in the cycloidal magnetic phase (T=25 K). Figure 4.19 shows this reflection's cycloidal phase azimuthal dependence. The figure shows that, with exception of the feature at 640.3 eV, a similar azimuthal dependence is seen for the different energies. For the feature at 640.3 eV, it is unclear what the azimuthal dependence represents. However, it may again be a combination of magnetic ordering and a charge distortion, as described for the (0 2q 0) reflection. Obviously, these azimuthal

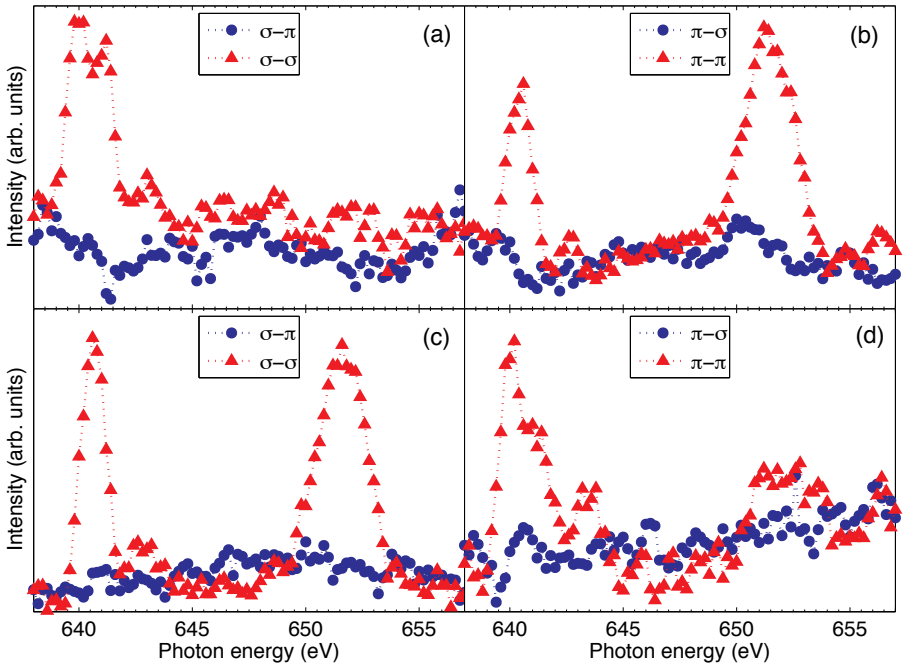

Figure 4.18: Incident photon energy scans at a fixed wavevector corresponding to the (0 2q 0) reflection. These scans were taken at a temperature of 20 K and at the azimuthal angles of $\psi = 0°$ ((a) & (b)) and $\psi = 90°$ ((c) & (d)).

dependencies cannot be attributed to the simple c-axis magnetic structure discussed previously, as the dependence in figure 4.19 is ≈90° out of phase with the expected azimuthal dependence (figure 4.17). However, by fitting the azimuthal dependence to equation 4.11, the magnitude of the magnetic moments along the different crystallographic axes, were determined to be:

Energy	$\hat{z}_1$	$\hat{z}_2$	$\hat{z}_3$
639 eV	0.26±0.01	0.03±0.01	0.05±0.02
650.3 eV	0.16±0.02	0.02±0.01	0.03±0.02
651.8 eV	0.21±0.01	0.03±0.01	0.04±0.02

Table 4.5: Values of $\hat{z}_1$, $\hat{z}_2$ and $\hat{z}_3$ obtained from fitting the azimuthal dependence of the (0 1-2q 0) reflection at T=25K to equation 4.11. The azimuthal fit for the feature at 640.3 eV is not included in the table.

Results from the fitting on the (0 1-2q 0) reflection show that, with the exception of feature at 640.3 eV, the majority of the magnetic moments point along the crystallographic a-axis. However, it is clear that these fits are not as accurate as for the previous azimuthal dependencies. It is also clear that the period is not equal to 90°. Whether this is due

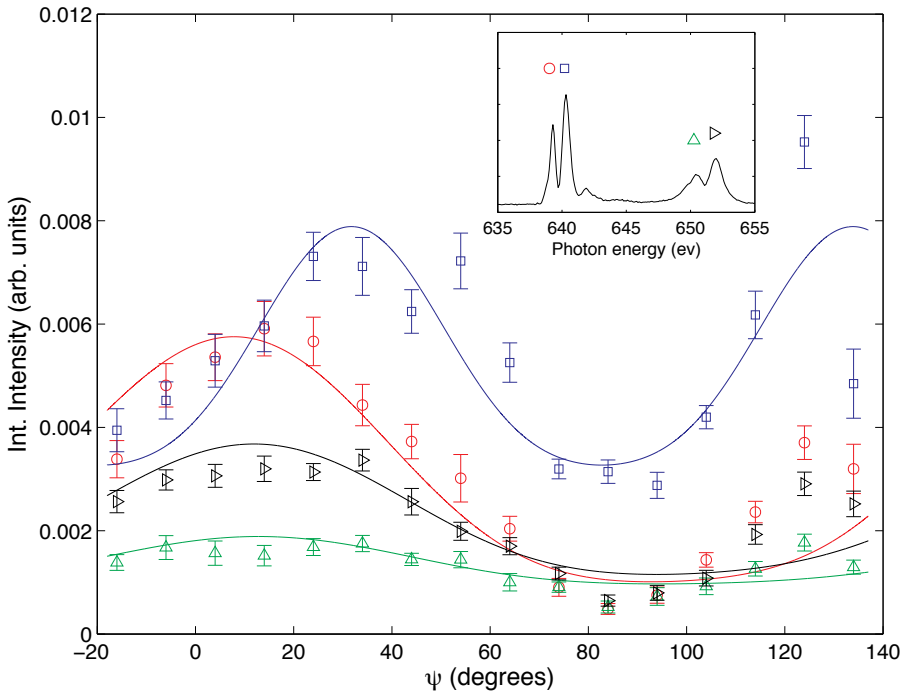

Figure 4.19: The azimuthal dependence of the (0 1-2q 0) reflection at a temperature of 25 K. The scan was taken with horizontally polarised (σ) incident photons. With the exception of the feature at 640.3 eV, the azimuthal dependencies were fitted with equation 4.11. The fit for the azimuthal dependence of the feature a 640.3 eV is just a guide to the eye. Results from the fitting to equation 4.11 are given in table 4.5.

to systematic errors, such as a precession of the crystal, or has some physical significance remains an open question. To resolve this issue energy scans with polarisation analysis would be very helpful. For example, if the scattering in the σ-σ' and σ-π' polarisation channels at ψ=0° was recorded, then one could use equation 4.10 to determine if the magnetic moments point solely along the crystallographic a-axis (scattering in the σ-σ' channel only) or there are additional components pointing along the other axes (scattering in both channels).

In conclusion, the resonant signal seen in the (0 2q 0) reflection, is likely to be a combination of magnetic scattering from a structure with the moments parallel to the c-axis and another resonant signal at the Mn L_3 edge which is non-magnetic in origin. Such a charge distortion also explains why the azimuthal dependences do not reach zero in intensity, as $\psi \rightarrow 0°$. The cycloidal phase azimuthal dependence of the 2^{nd} harmonic C type reflection at (0 1-2q 0), suggest however, an antiferromagnetic structure with the Mn moments aligned along the a-axis. For both the 2^{nd} harmonic reflections, there is an energy feature close to 640.5 eV which seems to show a different symmetry. What these features represent is somewhat of a mystery. One possibility is that they are charge distortions arising from the magnetic ordering, however there is no simple reason why these features would resonate. Without detailed electronic structure calculations [139], I am unable to positively identify the origin of these features.

Azimuthal dependences for the A type (0 q 1) and C type (0 1-q 0) satellite reflections, with photon energies equal to the Tb M_4 and M_5 absorption edges were also attempted. Unfortunately due to undetermined problems with the ID08 beamline, no meaningful results were produced. In addition it was not possible to perform polarisation analysis of scattered beam, as the Tb M edges are greater in energy than 1 keV, the maximum energy at which polarisation analysis could be performed.

4.7 Discussion

It is important to remember when interpreting these results, the collinear and cycloidal magnetic structures proposed by Kenzelmann and co-workers were based solely upon measurements of the A type and G type antiferromagnetic reflections. For the work described in this Chapter, only F type and C type reflections were studied, at the Mn L_2 and L_3 edges. Therefore, these results may not conflict with Kenzelmann's proposed magnetic structure. Instead, it is proposed that the results presented in this Chapter represent additional Fourier components of one coherent magnetic structure, which includes the Kenzelmann magnetic structure [15], not different antiferromagnetic domains as suggested by Mannix *et al.* [42].

There are several different reasons why it is believed that these reflections arise from a single coherent magnetic structure, rather than different antiferromagnetic domains. Firstly, the incommensurate wavevector of these reflections, have the same value and thermal evolution as previously published research [11, 12, 42]. Secondly, results from the F type (0 q 0) reflection indicate magnetic transitions at 28 K and 42 K. Thirdly, the sample shows ordering of the Tb $4f$ orbitals at 28 K for the A type (0 q 1) reflection, again this agrees with Kenzelmann's neutron diffraction work [12], and rules out the possibility that the sample is somehow not multiferroic.

The next logical question to ask is: how do the results presented in this Chapter alter the magnetic structure of $TbMnO_3$?

Starting with the magnetic phase above 28 K, results from F type reflections (0 q 0) and (0 $2q$ 0), indicate that there is an additional canting of the Mn magnetic moments, from the b-axis towards the c-axis. As this Fourier component is observed at l=even values, this canting is ferromagnetically ordered along the c-axis. The angle of canting was estimated to be 5°. This value was determined from the intensities of the F type and A type reflections, as measured by the neutron scattering work of Kajimoto *et al.* [13]. This low value for the canting could also explain the lack of NRXMS scattering seen in Mannix *et al.'s* [42] work, as the magnetic moment which arises from this canting, and

is seen in the F type reflection will be much weaker than the NRXMS signal from the A type reflection. It is important to note that this additional magnetic component is consistent with the Γ_3 irreducible representation. The basis vector of the Γ_3 irreducible representation for magnetic moments aligned along the c-axis is:

$$V_3^z = m_1^z + am_2^z + m_3^z + am_4^z \tag{4.12}$$

This basis vector shows that for the Γ_3 irreducible representation, the c-axis magnetic moment components are ferromagnetically aligned. The new magnetic structure of the high temperature magnetic phase is shown in figure 4.20 (a) & (b).

For the low temperature magnetic structure, in addition to the c-axis canting described above, azimuthal dependencies of the 2^{nd} harmonic C type reflection at (0 1-2q 0) suggests there is an additional a-axis Fourier component. There may also be an a-axis magnetic moment component in the high temperature magnetic structure, however due to the lack of azimuthal data in this phase, this cannot be confirmed. Since the (0 1-2q 0) reflection is a satellite reflection of the (0 1 0) forbidden reflection, these a-axis magnetic components will be canted antiferromagnetically along the b-axis. From the intensities of the azimuthal dependencies of the (0 $2q$ 0) and (0 1-$2q$ 0) reflections, the ratio of the a-axis to c-axis canting is estimated to be $\approx 2/3$. This modified magnetic structure is show in figures 4.20 (c) & (d). This antiferromagnetic a-axis canting is allowed by both the Γ_2 and Γ_3 irreducible representations, the symmetry of coupling between the magnetic moments for both representations are:

$$\begin{aligned} V_2^x &= m_1^x - am_2^x + m_3^x - am_4^x \\ V_3^x &= m_1^x - am_2^x - m_3^x + am_4^x \end{aligned} \tag{4.13}$$

The difference between the two basis vectors, is that the Mn magnetic moments are coupled ferromagnetically along the c-axis for the Γ_2 representation, and antiferromagnetically along the c-axis for the Γ_3 representation. Since for C type reflections l=even, the coupling must be ferromagnetic along the c-axis, meaning that the Γ_2 representation is the one that

describes the symmetry of this a-axis component. It should be noted that S. Wilkins was the first to calculate these additional magnetic components.

4.7.1 Conclusion

Using the technique of resonant X-ray scattering with photon energies in the vicinity of the Mn L_2 and L_3 absorption edges, I have probed the Mn $3d$ electron states of three specific incommensurate reflections. Two of these reflections correspond to a F type antiferromagnetic structure. Azimuthal dependencies and polarisation analysis of the scattered photons, show that the Mn magnetic moments are aligned along the crystallographic c-axis, in both the supposed collinear and cycloidal magnetic phases. It is therefore believed that this c-axis magnetic component modifies the magnetic structures derived by Kenzelmann *et al.* [12]. Previous neutron diffraction data [13] was used to estimate that this c-axis magnetic structure produces a canting of the Mn magnetic moments, from the b-axis towards the c-axis of 5° for both magnetic phases. This additional Fourier component of the magnetic structure, is described by the Γ_3 irreducible representation.

Cycloidal phase azimuthal dependencies of the third incommensurate reflection, which corresponds to a C type antiferromagnetic structure, reveal a component of the magnetic structure, with the Mn moments aligned along the crystallographic a-axis. It was estimated that the ratio of this a-axis component to the c-axis canting component was $\approx 2/3$. The a-axis magnetic component was described by the Γ_2 irreducible representation.

These results show that the ferroelectric polarisation in $TbMnO_3$ arises from a phase transition between two non-collinear magnetic structures, not between a collinear and a non-collinear magnetic structure as was previously believed. It is also important to highlight the fact that the (0 1-2q 0) reflection is present above 28 K, in the non-ferroelectric phase. Although this reflection is too weak for an azimuthal dependence to be measured. Symmetry arguments suggest it still corresponds to an a-axis component, which would still be represented by a Γ_2 component, thus both irreducible representations would be present above 28 K. As this new high temperature magnetic structure has the extra canting of the magnetic moments, and is represented by two irreducible representations, both the Lan-

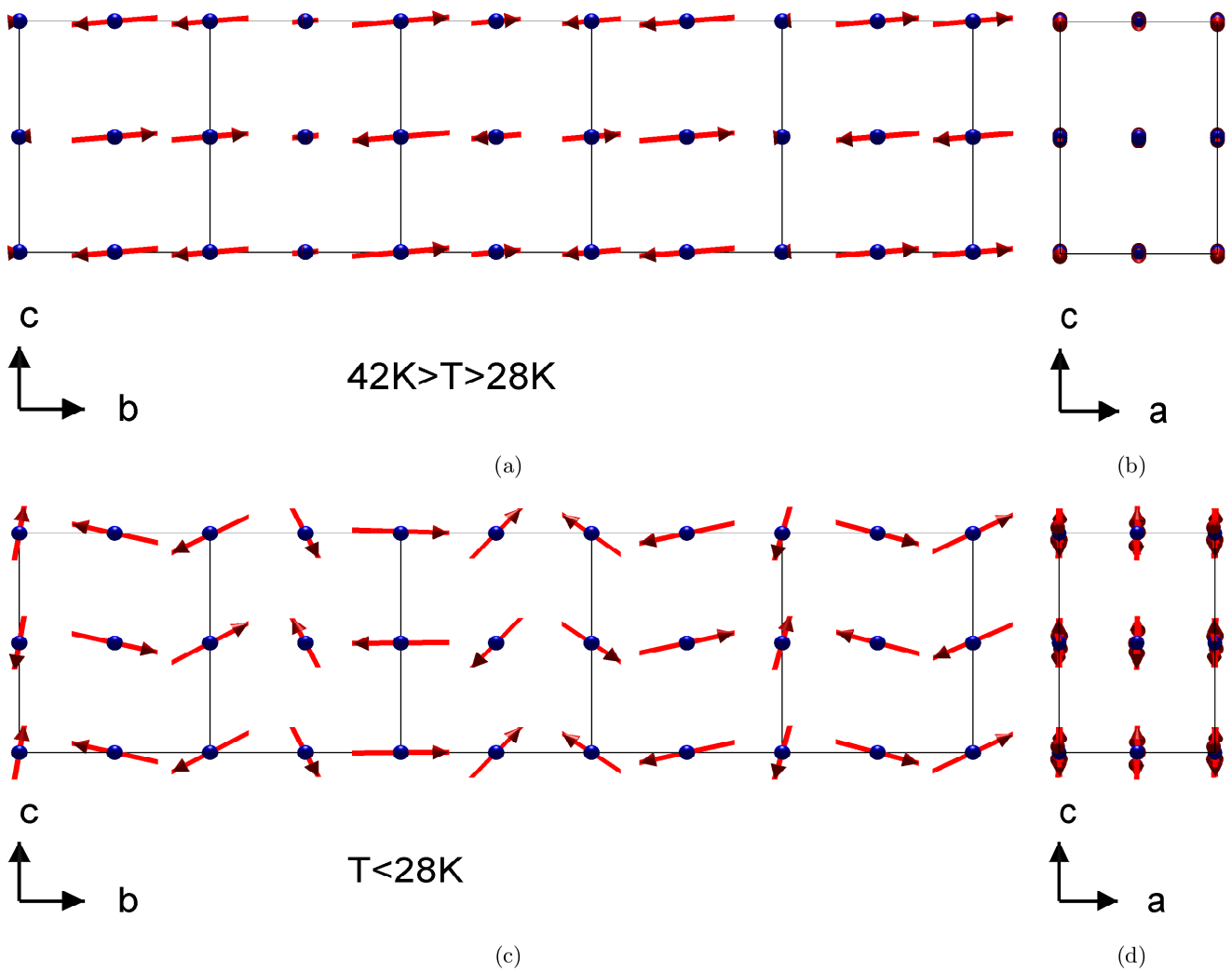

Figure 4.20: Upper panels: the modified magnetic structure of $TbMnO_3$, as projected onto the (a) $b-c$ and (b) $a-c$ crystallographic planes, for the high temperature magnetic phase between 42 K and 28 K. Lower panels: the modified magnetic structure of $TbMnO_3$, as projected onto the (c) $b-c$ and (d) $a-c$ crystallographic planes, for the low temperature magnetic phase below 28 K.

dau free energy analysis of Harris [132] and the symmetry work of Mostovoy [133], suggest that this phase may also be ferroelectric. Indeed if one calculates the electric polarisation for this new magnetic structure using equation 4.6, then a polarisation is predicted to appear along the c and a crystallographic axes for each b-axis chain of magnetic moments. However, polarisations which are equal in magnitude but point in the opposite directions, are predicted for alternative levels of the b-axis chain of magnetic moments. What is more, since these additional magnetic moments are coupled ferromagnetically along the c-axis, the application of a electric field parallel to the c-axis will not pole the sample, as in the case for the cycloidal magnetic structure. Therefore, this magnetic structure does not produce a macroscopic ferroelectric polarisation. In terms of the Landau free energy method derived by Harris [132], this corresponds to the magnetic structures of the different irreducible representations being in phase with one another. This makes sense as the magnitude of the canted moments is derived from the magnitude of the b-axis magnetic moments. For such an in-phase magnetic structure, Harris predicts that no ferroelectric polarisation is induced [132].

Finally, measurements at the Tb M_4 and M_5 edges of various antiferromagnetic incommensurate reflections, revealed that the Tb $4f$ electronic states were ordered in the ferroelectric phase, with the A type (0 q 1) reflection, showing the strongest scattering response. This result is in agreement with the magnetic structure model proposed by Kenzelmann *et al.* [12]. This result also suggests that the ordering of the Tb $5d$ electronic states above 28 K, which has been reported by the hard X-ray scattering studies of Mannix *et al.* [42] and Voigt *et al.* [127], is due to a polarisation by the Mn sublattice.

Chapter 5

X-ray scattering studies of multiferroic $DyMnO_3$

Shortly after the discovery of ferroelectricity in $TbMnO_3$, a second compound: $DyMnO_3$, was also found to be multiferroic. Again the ferroelectric polarisation points along the crystallographic c-axis [11]. As both compounds exist in the same orthorhombic crystal structure, and contain similar elements, it is believed that the mechanism for inducing the ferroelectric polarisation is the same for both $TbMnO_3$ and $DyMnO_3$. Intriguingly however the size of the electric polarisation in $DyMnO_3$ is twice that of $TbMnO_3$. Also, the strength of the magnetic field needed to rotate the electric polarisation is significantly reduced in $DyMnO_3$, when compared to $TbMnO_3$ [11].

For the penultimate chapter of this thesis, I will describe a series of X-ray scattering experiments on the multiferroic compound, $DyMnO_3$. These experiments were conducted with both non-resonant X-rays, and with photon energies in the vicinity of the Mn K (6.553 keV) and Dy L_3 (7.79 keV) resonant enhancements. Results taken at the Mn K resonance identified both A and F type antiferromagnetic reflections, which have temperature dependencies that are consistent with previous research [11]. The azimuthal dependence of the A-type reflection, suggested a b-c cycloidal magnetic structure for the Mn^{3+} magnetic moments. Furthermore, the azimuthal dependence of the F-type reflection

suggested a canting of the Mn^{3+} magnetic moments towards the c-axis. This is similar to what has been seen in $TbMnO_3$ [15]. In addition, two other types of satellite reflections were identified at the Mn K edge. However, due to their temperature and/or polarisation dependence, it is unlikely that these reflections correspond to the magnetic ordering of the Mn^{3+} magnetic moments. Finally, results taken at the Dy L_3 resonance, identified both A and F type reflections. However, several unidentified reflections were also detected. Moreover, the commensurate ordering of the Dy^{3+} magnetic moments below 6.5 K, which has previously been reported [16] was not observed. These results are compared to similar X-ray scattering studies of $TbMnO_3$ [127, 42], and interestingly there were some significant differences between these two multiferroic compounds, which are described in detail in section 5.3. Whether these differences are due to real physical effects or a bad crystal sample remains unclear however.

5.1 Multiferroic $DyMnO_3$

The crystal structure of $DyMnO_3$ is again an orthorhombically distorted perovskite (space group: *Pbnm*, crystal symmetry: *mmm*), with the lattice parameters a=5.28 Å, b=5.84 Å and c=7.38 Å [140]. Figure 4.1 shows the crystal structure of $TbMnO_3$, this structure is almost identical to that of $DyMnO_3$. Like $TbMnO_3$, the manganese ions in $DyMnO_3$ exist in a Mn^{3+} spin state and the MnO_6 octahedron is Jahn-Teller active. Finally the dysprosium exists in a Dy^{3+} spin state. Because of naturally occurring dysprosium's high elastic neutron absorption, neutron studies of $DyMnO_3$'s magnetic structure have been limited. Therefore, the exact nature of the ME coupling mechanism in this compound is still somewhat of an open question. Even so, $DyMnO_3$ is believed to exist in the following magnetic phases [11].

Above a transition temperature of 39 K, $DyMnO_3$ is both paramagnetic and paraelectric. As the temperature passes through 39 K, it is believed that the manganese sublattice undergoes a phase transition to a sinusoidally modulated antiferromagnetic structure, which is similar to the collinear phase seen in $TbMnO_3$. The onset of this collinear phase can be classified by the appearance of an incommensurate propagation vector (q)

along the crystallographic b-axis, (0 q 0). At 39 K this propagation vector has a value of $\sim$0.36 b^* [11]. However, unlike $TbMnO_3$, as the temperature is reduced to 18 K, the propagation vector q increases *not* decreases in magnitude. At 18 K, q reaches a maximum value of $\sim$0.385 b^*. Upon reaching 18 K, $DyMnO_3$ undergoes a second magnetic phase transition, where it is believed that the Mn sublattice forms an incommensurate cycloidal spin structure, similar to $TbMnO_3$. q is approximately constant upon a further decrease in temperature. As for the case of $TbMnO_3$, a ferroelectric polarisation which is parallel to the c-axis, spontaneously develops. The value of this polarisation is 2×10^{-3} C m^{-2}, approximately twice the value of the ferroelectric polarisation seen in $TbMnO_3$ [11]. Upon a further decrease in temperature to 6.5 K, Feyerherm and co-workers [16] have reported that the Dy^{3+} moments form a simple antiferromagnetic state, which has a propagation vector of (0 $\frac{1}{2}$ 0). See section 5.1.1.

The ferroelectric responses of $DyMnO_3$ to an external magnetic field is similar to that of $TbMnO_3$. However, there are some differences which are highlighted in figure 5.1. As the figure shows, for H$\|a$ and H$\|b$ the direction of ferroelectric polarisation in $DyMnO_3$ is rotated by 90° degrees so that P$\|a$, this is the same as $TbMnO_3$. However, for $DyMnO_3$, the magnetic field strength required to induce this change of polarisation direction is significantly less than the required field strengths for $TbMnO_3$ [11]. In addition, for H$\|$ c no magnetic or electric transitions are seen for magnetic field strengths up to 10T. The ferroelectric polarisation remains parallel to the c-axis, although a suppression of both the magnitude of P$\|c$ and the cycloidal phase ordering temperature (T_N), is seen [11]. For the magnetic field configurations: H$\|$a and H$\|$c there is no change in the propagation vector q with the change in the direction of polarisation [141]. This is in contrast to what is seen in $TbMnO_3$. A probable reason is that, unlike $TbMnO_3$, the propagation vector for $DyMnO_3$ is not sufficiently close to a commensurate value for a transition to a commensurate propagation vector to be energetically favourable.

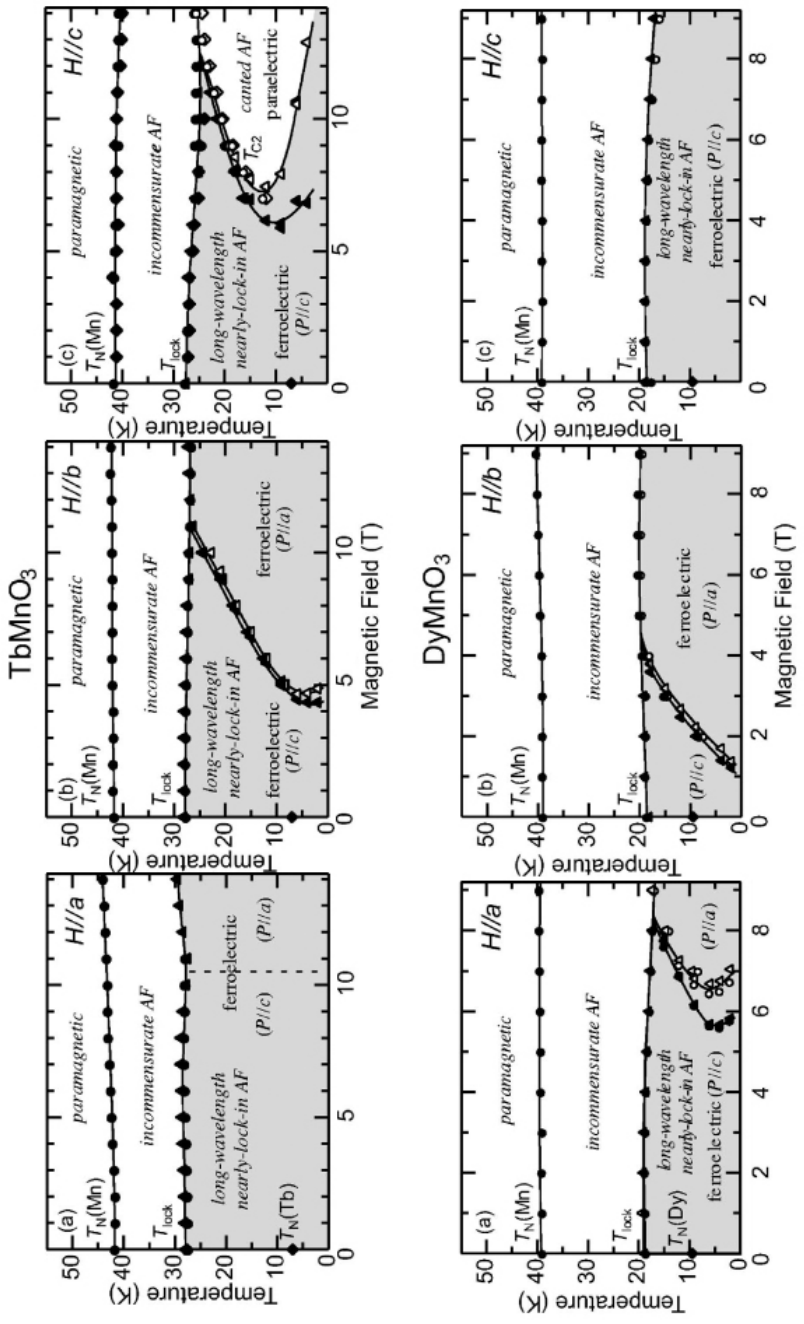

Figure 5.1: The magnetoelectric phase diagram of $TbMnO_3$ (upper panels) and $DyMnO_3$ (lower panels) with a magnetic field (H) along the a **(a)**, b **(b)** and c **(c)** axes. The grey areas represent the ferroelectric phases, while the circle, triangle and diamond data points correspond to measurements of the dielectric constant, pyroelectric (or magnetoelectric) current and magnetisation, respectively [11].

5.1.1 The magnetic phases of $DyMnO_3$

At the time of writing, only one set of neutron diffraction measurements has been published. This work studied the magnetic structure of a powder sample of $DyMnO_3$ [142]. This was made possible by replacing the naturally occurring dysprosium with an isotope (^{162}Dy), which has a smaller neutron absorption cross section. Below 40 K, a series of A-type magnetic satellite reflections were observed. These peaks were attributed to the magnetic ordering of the Mn sublattice. As the temperature was reduced, the peak's intensity and value for the incommensurate propagation vector increased. As the temperature passed through 15 K, an additional set of satellite reflections corresponding to G-type ordering were observed. These G-type peaks were much weaker than the A-type satellite peaks. The observation of strong A-type and weak G-type satellite peaks is similar to what Quezel *et al* [119] and Kenzelmann *et al* [12] observed in $TbMnO_3$. Rietveld analysis of the powder diffraction data, in a temperature range between 6.5 K and 13 K, gave unphysically large values for the moment of the Mn^{3+} atoms. This led Prokhnenko and co-workers to the conclusion that there must be an additional contribution to the magnetic ordering from the Dy^{3+} spins. Finally, below a temperature of 6.5 K, a reduction in intensity of the A-type satellite reflection was accompanied by the appearance of the commensurate magnetic reflection. This was attributed to ordering of the Dy^{3+} spins, having a propagation vector of $(0\ \frac{1}{2}\ 0)$.

To fully investigate the ordering of the Dy^{3+} electronic states, the same research group has undertaken a number of resonant X-ray scattering (RXS) studies [142, 16]. These measurements were taken using RXS of linearly polarised X-ray photons, with energies in the vicinity of the Dy L_3 absorption edge (7.790 keV). In agreement with their neutron diffraction work, commensurate magnetic ordering below 6.5 K was observed. This ordering was accompanied by an incommensurate lattice modulation, which had a propagation vector of q_{Dy}=0.905 b^*. Unlike $TbMnO_3$, the low temperature ordering of the lanthanoid ion also has an effect on the Mn sublattice. Specifically, the magnitude of the Mn induced lattice modulation of $(0\ 2q\ 0)$ is suppressed and shifts in position from 0.78 b^* to 0.81 b^*. Interestingly, this RXS work does not include measurements on the 1^{st} harmonic magnetic

reflection which should be located at a reciprocal space position of $k \approx 0.38 b^*$. Finally, a recent resonant X-ray scattering study of $DyMnO_3$, at the Dy M_5 (1292 eV) resonant enhancement [17], has shown that the Dy $4f$ electronic states form a collinear magnetic structure between 39 K and 18 K, while below 18 K the Dy $4f$ states form a cycloidal magnetic structure. Both these magnetic structures have the same wavevector as the Mn magnetic structure. This result is in stark contrast to what is seen in $TbMnO_3$ [14, 15, 12].

5.2 Experimental details

As several resonant X-ray scattering experimental studies of the magnetic ordering in $DyMnO_3$ have already been conducted, why are additional studies on $DyMnO_3$ required? As most of the RXS measurements [16] were conducted with photon energies in the vicinity of the Dy L_3 (7.79 keV) absorption edges, where the electric-dipole transition is $2p_{3/2} \rightarrow 5d$. The resonant X-ray scattering at these absorption edges is sensitive to the extended Dy $5d$ band structure of $DyMnO_3$. This means that conclusions regarding the manganese magnetic order, must rely on the assumption that the magnetic ordering of the Mn sublattice induces the ordering of the Dy^{3+} electronic states, in a way that may be understood. The commensurate ordering of the Dy^{3+} states at low temperatures also complicates the situation. In addition, the recent RXS work [17] conducted at the Dy M_5 edge, where the electric-dipolar transition is $3d \rightarrow 4f$, probes localised Dy $4f$ electronic states only.

For the experiments described in this chapter, the large incident photon flux available at the beamlines used, made it possible to study the magnetic ordering at the Mn K absorption edge, where the electric-dipole transition is $1s \rightarrow 4p$. In addition, RXS studies were also performed at the Dy L_3 absorption edge. Thus, for this experiment, one is able to separate the contributions to the magnetic ordering from both magnetic elemental species. The separation of the contributions to the magnetic ordering from the different elemental species is important, as there is significant evidence [17] that the Dy^{3+} magnetic moments may order, with the same propagation vector as the Mn moments in all magnetic phases, and may form a cycloidal structure below 18 K. Thus, it seems reasonable to conclude that

the Dy moments play a much more active role in the multiferroic properties of $DyMnO_3$, when compared to the Tb^{3+} moments in $TbMnO_3$ [142].

5.2.1 Crystal growth and orientation

Single crystals of $DyMnO_3$, with dimensions $4\times2\times1$ mm^3, were grown and cut with the [010] direction as surface normal, by a group led by Professor Y. Tokura, Department of Applied Physics, University of Tokyo, Japan. The sample was mounted, so that the [001] crystallographic direction lay within the scattering plane (ψ=0°). The in-plane orientation was determined from a Laue pattern using the *Orient Express* simulation program (see figure 5.3). Unlike the resonant soft X-ray scattering experiments described in the previous chapter, the Ewald sphere of reciprocal space, for both the resonant and non-resonant energies used in these experiment, allows access to all four types of antiferromagnetic reflections (A,C,F and G type). The out-of-plane orientation was found once the crystal was placed on the beamlines. Figure 5.2 shows a rocking curve of the (0 4 0) reflection, which was taken on the ID20 beamline. The reflection was fitted with a Lorentzian profile and gave a full width at half maximum of 0.0763°, which shows that the crystal has a good mosaic.

5.2.2 Experimental locations

Experiments were performed at two beamlines: ID20 and I16. The ID20 beamline [41] is located at the European Synchrotron Radiation Facility (Grenoble, France). The beamline is capable of providing X-ray photons in the energy range of 3-25 keV. The energy resolution of this beamline is approximately 8 eV for 9 keV photons. The Micro-Controle twelve-circle diffractometer, located in experimental hutch one (EH1), was used for these experiments. The diffractometer was used in the 4-circle (FOURC) mode. For EH1, the X-ray beam has a focus size of $\sim250\mu m$(V)$\times\sim300\mu m$ (H). The sample was mounted inside a closed circle refrigerator, with a ^{4}He Joule-Thomson evaporation stage, in the vertical scattering geometry. This displex is capable of reaching a base temperature of 1.8 K. (A fuller description of this beamline is given is section 2.3.3.) Initial surveys with photon

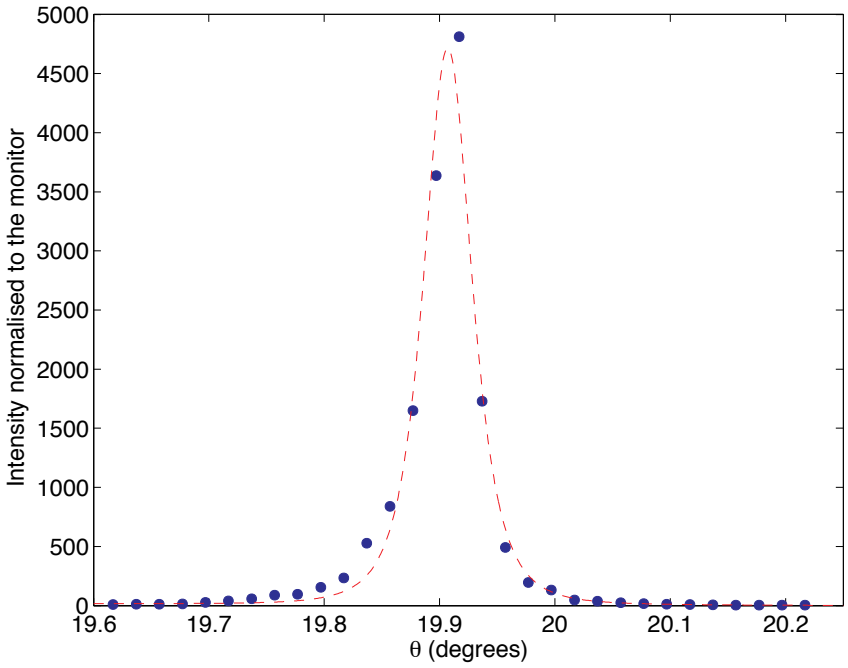

Figure 5.2: A rocking curve of the (0 4 0) reflection, at a temperature of 15K. The results were taken on the ID20 beamline. The reflection was was fitted with a Lorentzian profile and gave a full width at half maximum of 0.0763°.

energies in the vicinity of the Mn K and Dy L_3 absorption energies, of the crystal's incommensurate magnetic ordering, were performed at this beamline. For non-resonant and resonant scattering at the Mn K edge, a Cu(220) crystal was used to perform polarisation analysis of the scattered beam. For measurements taken at the Dy L_3 edge, a Pt(222) crystal was used. The intensity of scattering as a function of temperature, incident photon energy and azimuthal angle, of certain reflections, were recorded during this experimental run. The second experiment was conducted at the brand new I16 beamline at the Diamond light source (Didcot, UK). Unlike ID20, this beamline receives its photons from only one linear undulator. However, both the energy range and flux are comparable to ID20. The energy range is 3-25 keV and the (calculated) flux at 6 keV is 10^{14} photons s^{-1}, at the focal point. The focus size of the X-ray beam (with focusing mirrors) was $\leq 50\mu m$(V)$\times \leq 200\mu m$(H) and the energy resolution of the incident beam at 8 keV is ≤ 2 eV. The sample was mounted onto a Newport, six-axis Kappa-geometry diffractometer. A low temperature helium cryostat (base temperature 4 K) was used to cool the sample. For this experiment, the (0 6-q 1) A-type reflection was studied with both non-resonant scat-

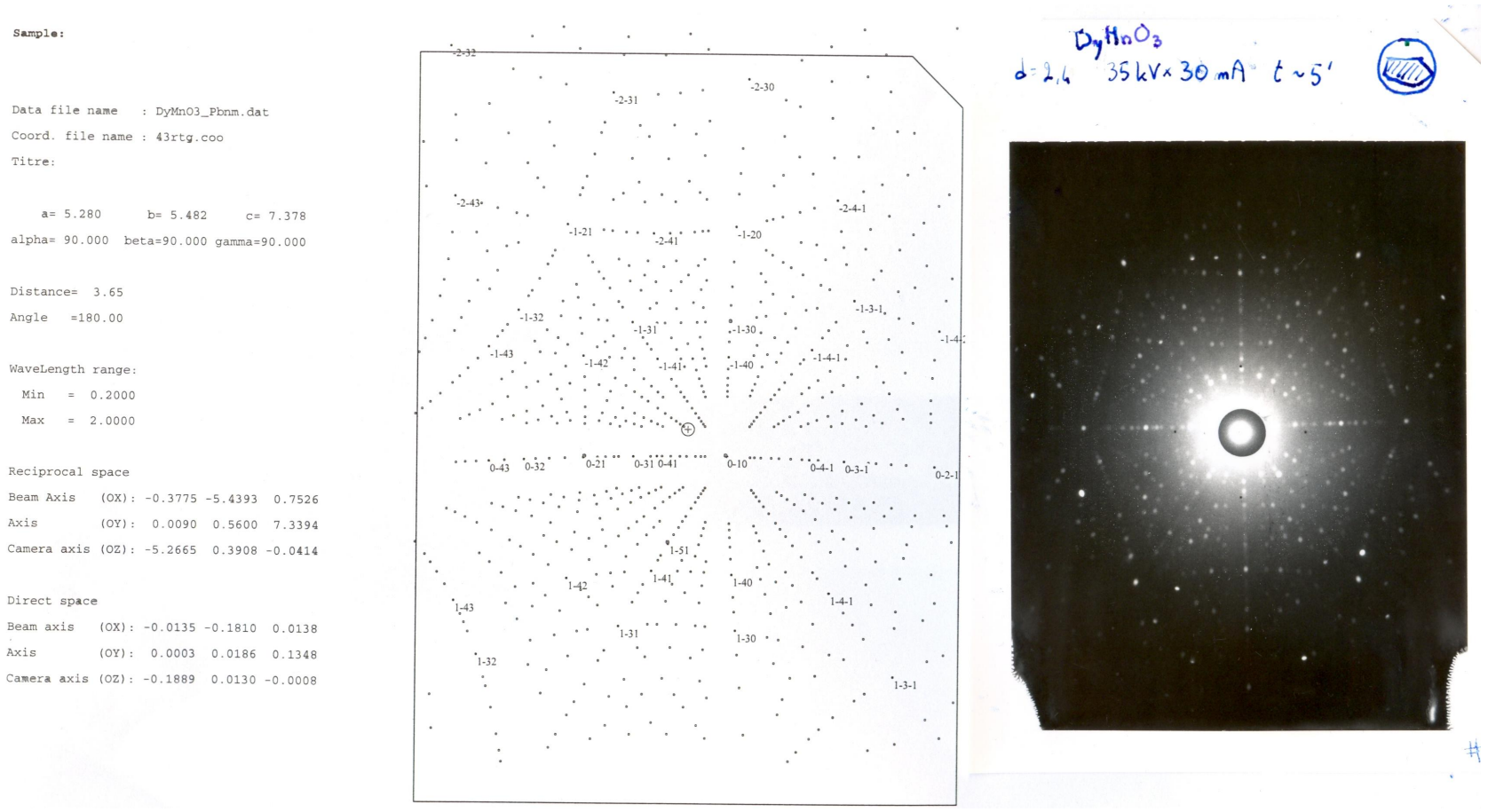

Figure 5.3: A Laue pattern photograph and *Orient Express* simulation used to orientate the $DyMnO_3$ sample.

tering (results were collected with a photon energy of 6.5 keV, 53 eV below the absorption edge) and resonant scattering in the vicinity of the Mn K edge. Polarisation analysis of the scattered beam was performed using a Cu(220) crystal.

5.3 Experimental results

Before describing the experimental results, it is important to calculate the cross-talk between the σ-σ' and σ-π' scattering channels. For results taken in the vicinity of the Mn K resonance, the photon energy was 6.553 keV. By using Bragg's law, one can calculate the scattering angle of the Cu(220) polarisation analyser (θ_{pol}):

$$\lambda = hc/energy = 4.1356 \times 10^{-15} \times 3 \times 10^{8}/6.553 = 1.89 \times 10^{-10}$$

$$\sin(\theta_{pol}) = \lambda/(2d) = 1.89 \times 10^{-10}/(2 \times 1.281 \times 10^{-10}) = 0.739 \quad (5.1)$$

$$\therefore \theta_{pol} = 47.65^{\circ}$$

Here, d is the lattice spacing of the Cu(220) polarisation analyser. Therefore, the cross-talk between the two scattering channels is: $\cos^2(2 \times 47.65)$=0.009 or 0.9%.

Figure 5.4 shows longitudinal scans along the b^* direction, for (0 k 0) and (0 k 1), where 4< k <5. These scans were taken with a incident photon energy in the vicinity of the Mn K edge, at a temperature of 15 K.

Figure 5.4 (a) is a longitudinal scan along [0k0], for 4< k <5, in the $\sigma - \pi'$ scattering channel. The first peak labelled as **A**, is in the correct position for a 2^{nd} harmonic C-type antiferromagnetic reflection, (0 5-2q 0), where q=0.376±0.005 b^*. This value of q is in agreement with previous work [11]. Rocking curves of the two peaks labelled as **B** and **C** in figure 5.4 (a), were extremely wide, indicating that these peaks were in fact powder lines of structural reflections. Finally, the peak labelled as **D** was located at a position of (0 4.748 0). This corresponds to the 2^{nd} harmonic F-type antiferromagnetic reflection,

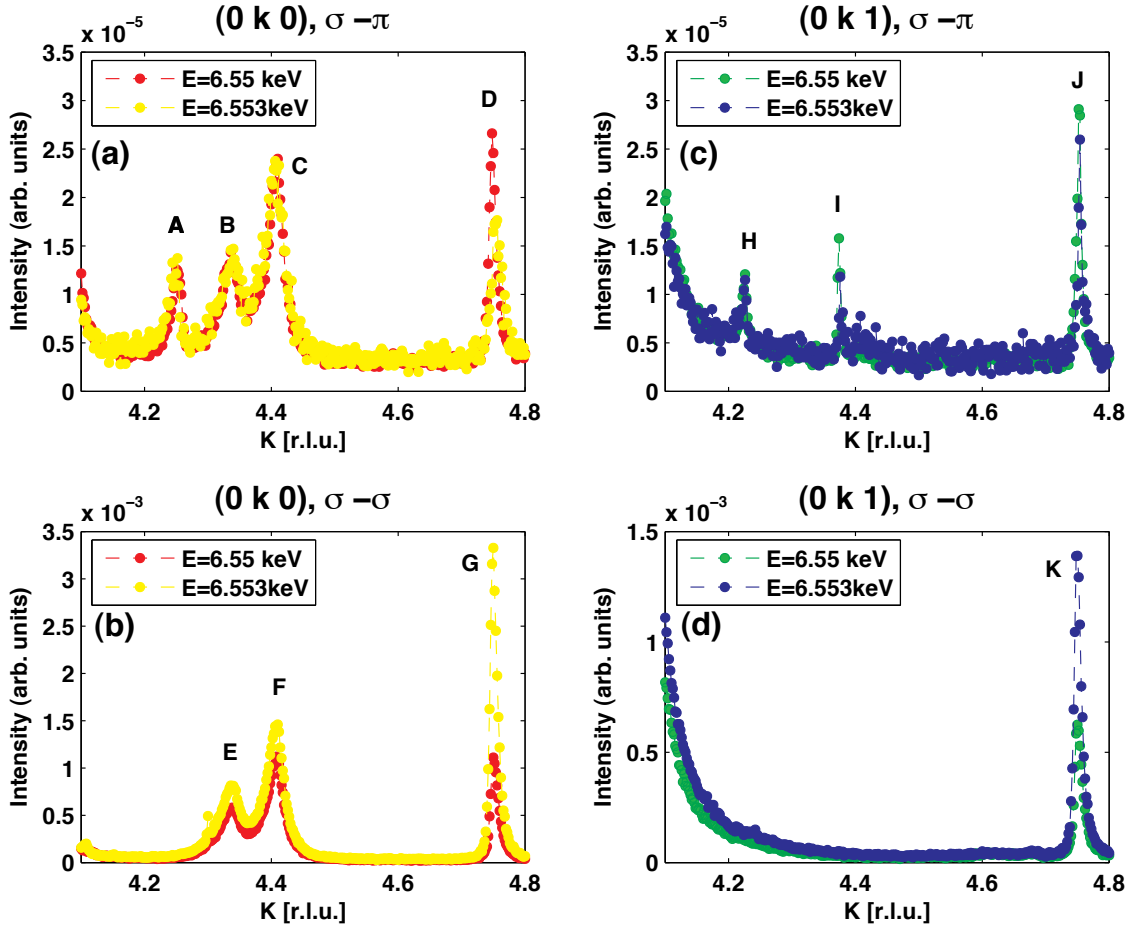

Figure 5.4: Longitudinal scans along the b^* reciprocal lattice direction, at l=*0*, for (a) the $\sigma - \pi'$ and (b) the $\sigma - \sigma'$ scattering channels, and at l=*1* for (c) the $\sigma - \pi'$ and (d) the $\sigma - \sigma'$ scattering channels. All scans were taken with incident photon energies close to the Mn K edge resonance (i.e. 6.553 keV) and off resonance (i.e. 6.5 keV). All scans were taken at 15 K. Data was recorded at the ID20 beamline.

(0 4+2q 0), giving an incommensurate wavevector value of q=0.374±0.005 b^*. Again this is in agreement with previously published results [11]. Figure 5.4 (b) is a longitudinal scan scan along [0k0], for 4< k <5, in the $\sigma - \sigma'$ scattering channel. The peaks labelled as **E** and **F** are the same powder lines as the peaks labelled as **B** and **C** in figure 5.4 (a). Again the peak labelled **G**, corresponds to the 2^{nd} harmonic F-type antiferromagnetic reflection, (0 4+2q 0), labelled previously as **D**. Interestingly, the 2^{nd} harmonic C-type antiferromagnetic reflection, (0 5-2q 0), is not seen in this scattering channel.

Figures 5.4 (c) & (d), show a second set of longitudinal scans, this time along [0k1] with

4< k <5. Figure 5.4 (c) corresponds to the results taken in the $\sigma - \pi'$ scattering channel while figure 5.4 (d) shows the scattering in the $\sigma - \sigma'$ scattering channel. For the features shown in figure 5.4 (c), the reflection labelled **H** is located at (0 4.225 1). Interestingly the reflection does not correspond to the 2^{nd} harmonic G-type incommensurate antiferromagnetic reflection, (0 5-2q 1). Also a feature is not seen at the same position in the $\sigma - \sigma'$ channel. The reflection labelled as **I** was located at a position of (0 4.375 1), this reflection clearly corresponds to the 1^{st} harmonic A-type antiferromagnetic reflection, (0 4+q 1), with q=0.375±0.005 b^*. Finally the reflection labelled as **J** was seen at the reciprocal space position of (0 4.752 1), this corresponds to the 2^{nd} harmonic A-type antiferromagnetic reflection, (0 4+2q 1) and gives a incommensurate wavevector value of q=0.376±0.005 b^*. This is the same reflection as seen in the $\sigma - \sigma'$ scattering channel (figure 5.4 (d)), where it is labelled as **K**.

5.3.1 The A-type incommensurate reflection

I will now discuss the two reflections which were observed at the reciprocal space positions of (0 4.374 1) and (0 4.752 1), for T=15 K. The first of these reflections was seen in the $\sigma - \pi'$ scattering channel only, while the second reflection was detected in both channels. By referring to the polarisation dependence of the electric-dipolar resonance (see equations 2.32), one may conclude that these peaks correspond to the A-type (0 4+q 1) and (0 4+2q 1) reflections, giving propagation wavevector values of q=0.374±0.005 b^* and q=0.376±0.005 b^*, respectively.

In addition, the A-type reflection of (0 6-q 1) was studied with both resonant and non-resonant X-rays at I16. The reason for this change, is that geometric factors mean this reflection is more intense than the (0 4+q 1) reflection. As the reflection was seen 'off resonance' in the $\sigma - \pi'$ scattering channel, the reflection must be magnetic in origin. Figure 5.5 shows the incident photon energy scans of the (0 6-q 1) reflection for both magnetic phases. The energy scans show a small resonant enhancement of the scattered beam for energies close to the Mn K edge resonance (6.55 keV). I believe that these scans show two separate resonant features. Firstly, an electric-dipole transition at an

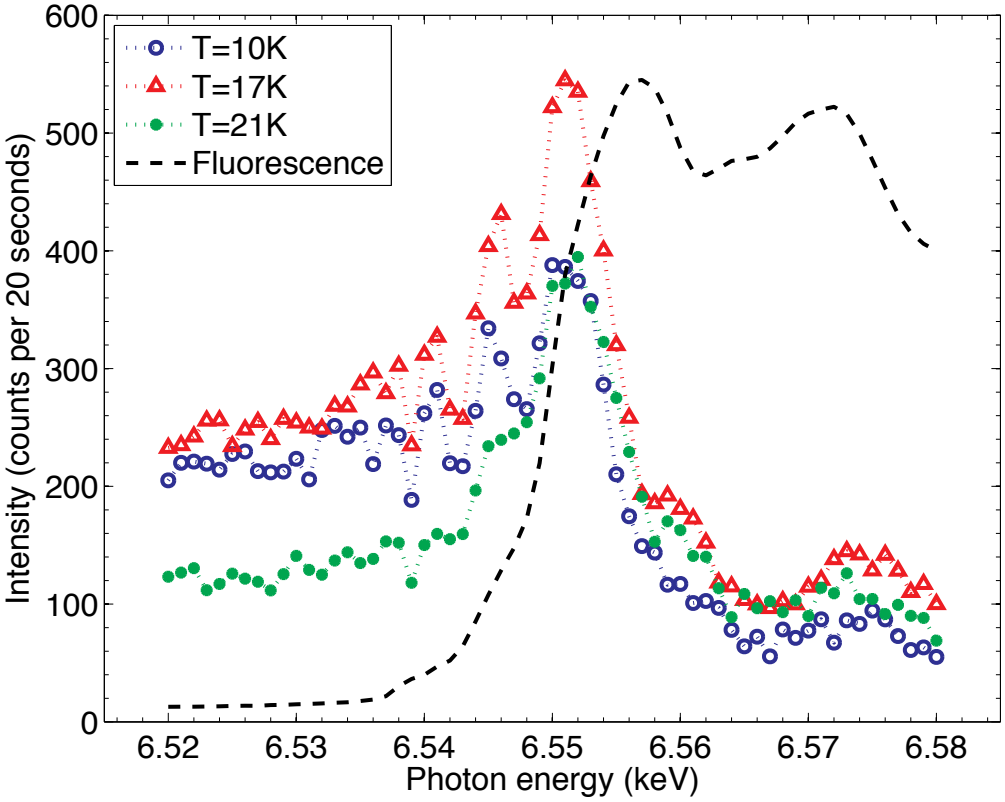

Figure 5.5: Incident photon energy scans in the vicinity of the Mn K edge for the (0 6-q 1) reflection, taken at various temperatures (see legend). A fluorescence spectrum is also shown. These results were recorded at I16.

energy of 6.551 keV, and secondly, an electric-quadrupole transition at the slightly lower energy of 6.546 keV. A similar electric-quadrupole transition has also been detected in $TbMnO_3$ [127]. Interestingly, the resonant enhancement seems to be stronger at 17 K than 10 K. This could be due to the separate magnetic commensurate ordering of the Dy^{3+} ions, which has been shown to suppress the magnetic ordering of the Mn sublattice [16]. Finally, the transition into the collinear magnetic phase causes an overall reduction in the non-resonant scattering, but seems to have minimal effect on the main resonant feature at 6.551 keV. However, the supposed electric-quadrupole feature seems to have disappeared. Interestingly, similar measurements taken on $TbMnO_3$ show a much larger resonant enhancement at the Mn K edge for this reflection type [127, 42].

Temperature dependences of the (0 4+q 1), (0 4+2q 1) and (0 6-q 1) reflections were recorded at both beamlines (figure 5.6). For the (0 4+q 1) reflection, scattering was

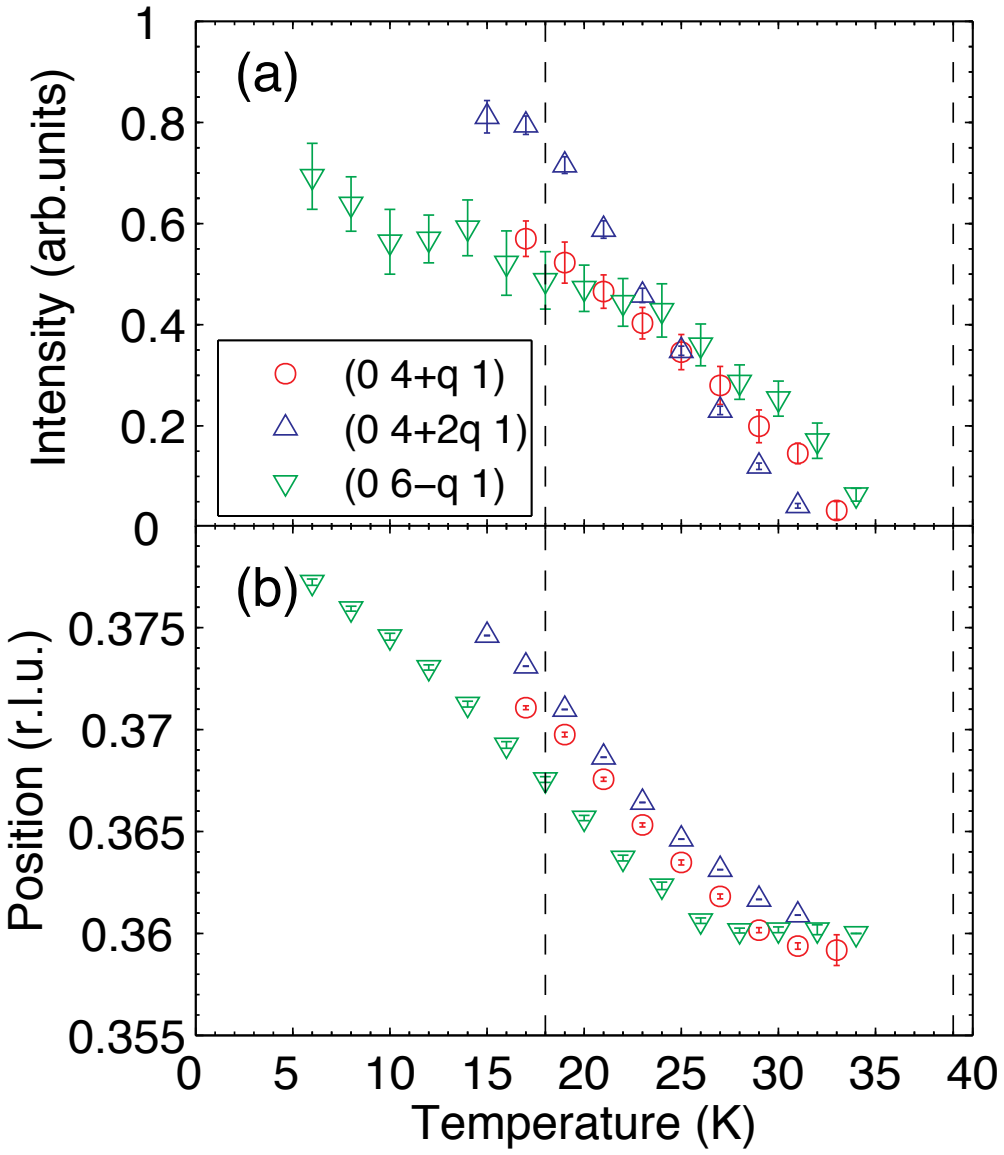

Figure 5.6: Temperature dependences of (a) the intensity and (b) the position of three A-type incommensurate reflections. The intensity of each reflection was determined by fitting Lorentzian profile to the data using the Spec1d non-linear least squares fitting program. The red circle data points correspond to Mn K edge resonant scattering from the (0 4+q 1) reflection, in the $\sigma - \pi'$ scattering channel. The blue triangle data points correspond to the non resonant scattering from the (0 4+2q 1) reflection, in the $\sigma - \sigma'$ scattering channel. Finally, the green triangle data points correspond to Mn K edge resonant scattering from the (0 6-q 1) reflection, in the $\sigma - \pi'$ scattering channel. The results show the correct trend for the position of the incommensurate reflections [11]. Data was recorded at the ID20 beamline for the (0 4+q 1) and (0 4+2q 1) reflections, and at ID16 to the (0 6-q 1) reflection.

performed with resonantly scattered photons, while non-resonant photons were used for the (0 6-q 1) reflection. Figure 5.6 shows that both reflections exist up to a temperature of 35 K. There is still some discrepancy between the temperature dependences shown here and the ordering temperature as reported from other techniques (39 K). The evolution of these reflections positions, however, is in good agreement with published data [11]. The 2^{nd} harmonic A-type reflection of (0 4+2q 1) was also studied at ID20. Scattering was seen in both polarisation channels, while incident photon energy scans (for both scattering channels) revealed an absorption edge with no resonant enhancements, as also seen in $TbMnO_3$ by Mannix *et al* [42]. Thus, this reflection occurs due to lattice distortions, which are induced by the magnetic structure. The appearance of this reflection in the $\sigma - \pi'$ scattering channel could possibly be due to a cross-talk from the polarisation analyser crystal. However, the strength of the reflection in the $\sigma - \pi'$ seems much stronger than 0.9%. Even so, I cannot think of a reasonable explanation for why there is scattering in the $\sigma - \pi'$ channel, for a non-resonant 2^{nd} harmonic reflection. A magnetic structure which is not perfectly sinusoidally modulated, may produce a 3^{rd} harmonic reflection, but not a 2^{nd} harmonic. The temperature dependence of this 2^{nd} harmonic reflection showed no scattering signal above 32 K, while the propagation vector position showed the correct trend decreasing in q as the temperature was increased.

Figure 5.7 shows the azimuthal dependence of the A-type antiferromagnetic reflection, (0 4+q 1). Again the intensity of each reflection was determined by fitting Lorentzian profile to the data, using the Spec1d non-linear least squares fitting program. To account for any change in scattering strength, due to the precession of the crystal as it was rotated in ψ, the azimuthal dependence of the (0 4 1) Bragg reflection was also recorded at the same values of ψ. The azimuthal dependence of the (0 4+q 1) reflection was then normalised by the (0 4 1) reflection.

On first inspection, the results shown in figure 5.7 are somewhat confusing, as when compared to the azimuthal dependences shown in chapter 4, this azimuthal dependence seems rather flat. However, it is important to remember that the (0 4+q 1) reflection is off specular. Therefore, this will change the definitions of z_1, z_2 and z_3 with respect to the crystallographic axes. In addition, figure 5.5 shows that there is a significant amount

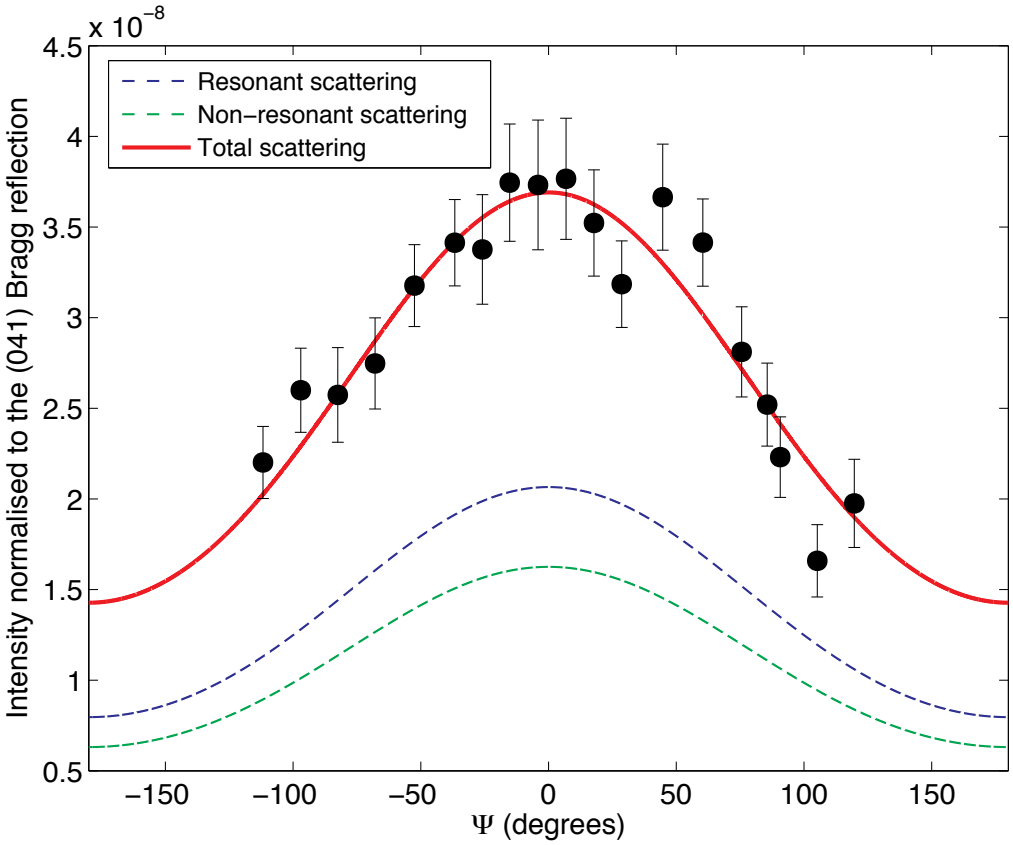

Figure 5.7: The azimuthal dependence of the (0 4+q 1) reflection in the $\sigma - \pi'$ scattering channel, at a temperature of 15 K. The reflection's intensity at each azimuthal angle was normalised to the corresponding intensity of the (0 4 1) Bragg reflection. The origin of the azimuthal dependence corresponds to scattering in the b-c crystallographic plane. The data is fitted with both a resonant scattering (blue line), and non-resonant scattering (green line). The red line corresponds to the combination of the two fits. Data was recorded at the ID20 beamline.

of non-resonant magnetic scattering for this reflection. With these two factors in mind, the azimuthal dependence of the (0 4+q 1) reflection was fitted with a combination of the resonant and non-resonant scattering cross sections with a starting ratio of 1:1.

$$I \propto (2\sin^2\theta[(L_1 + S_1)\cos\theta + S_3\sin\theta])^2 + (z_1\cos\theta + z_3\sin\theta)^2 \tag{5.2}$$

Here L and S correspond to the respective spin and angular moments of the magnetic species, while z is the magnetic moment derived from the resonant scattering. In addition the magnetic moment directions m_1, m_2 and m_3 are defined with respect to the

crystallographic axes as:

$$\begin{aligned} m_1 &= (-0.975m_b + 0.223m_c)\cos(\psi) + m_a \sin(\psi) \\ m_2 &= m_a \cos(\psi) + (-0.975m_b + 0.223m_c)\sin(\psi) \\ -m_3 &= 0.223m_b + 0.975m_c \end{aligned} \tag{5.3}$$

See appendix B for further information on how these relationships were calculated.

The result of this fitting is shown in figure 5.7, with the blue line representing the resonant azimuthal dependence. The green line representing the non-resonant azimuthal dependence, and the solid red line shows the overall fit. The figure shows a good agreement between the experimental data and the azimuthal dependency (χ^2_{red}=1.096). Results from the fit give resonant values for the magnetic moment direction of: z_a=0, z_b=2×10^{-4} and z_c=6×10^{-4}. Results for the non resonant values were: S_a=0, S_b=2×10^{-4} and S_c=5×10^{-4}. As these magnetic moments are from a transition metal element, it was assumed that the orbital angular magnetic moment was quenched [131]. Thus this azimuthal dependence seems to suggest a *b*-*c* cycloidal type magnetic structure for the A-type reflection.

5.3.2 The F-type incommensurate reflection

The position F-type 1st harmonic reflection, (0 4+q 0) was obscured by powder lines (see figure 5.4 (a) & (b)). However, a twin reflection corresponding to (0 4-q 0), at a reciprocal space position of (0 3.625 0) was observed in the $\sigma - \pi'$ scattering channel. The position of this reflection gives a value for the propagation vector q of 0.375 b^*, this agrees well with published data [11].

Incident photon energy scans of this reflection, taken in the cycloidal (T=15 K) and collinear (T=25 K) phases, are shown in figure 5.8. Results reveal a significant resonant enhancement of the scattering intensity in the vicinity of the Mn K absorption edge, the resonant enhancement is much stronger for this F-type reflection, when compared to the A-type reflection (figure 5.5). In addition, a second smaller peak is seen in the collinear phase at a energy of 6.533 keV. Whether this feature is due to the Mn electronic structure

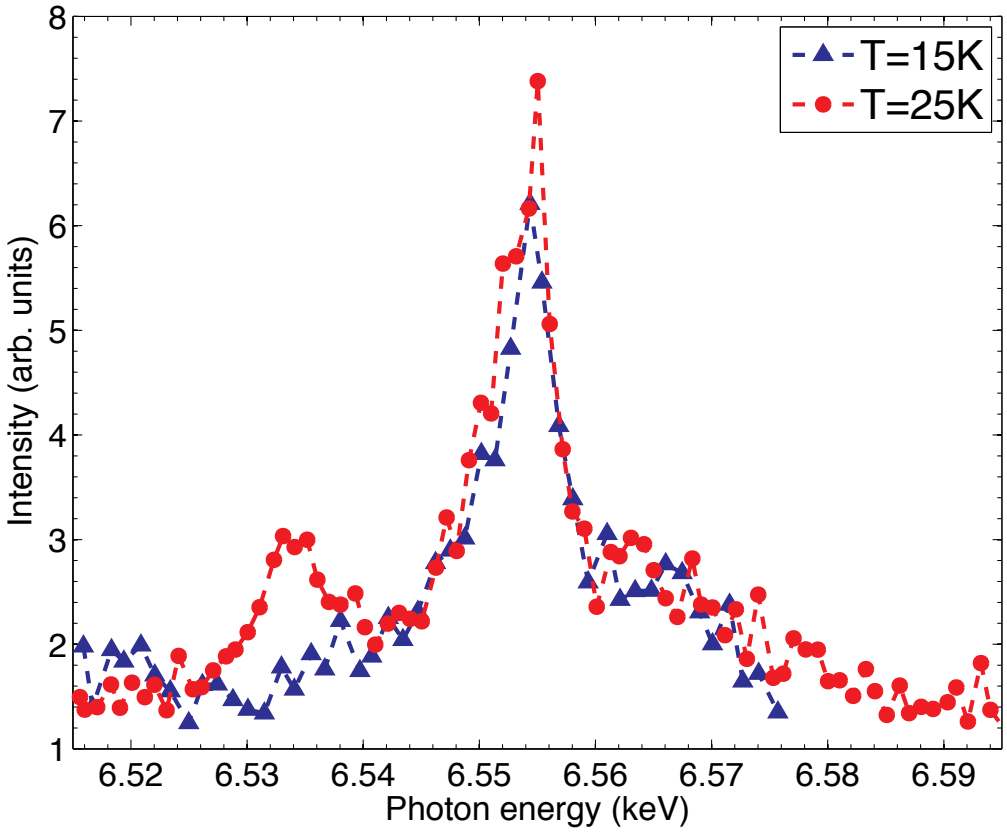

Figure 5.8: Incident photon energy scans, at a fixed wavevector corresponding to the (0 4-q 0) reflection. The scans were taken in both the cycloidal (T=15 K) and collinear (T=25 K) magnetic phases, in the $\sigma - \pi'$ scattering channel. Data was recorded at the ID20 beamline.

or multiple scattering remains an open question, as no other collinear phase energy scans of this reflection were recorded. In addition, a strong reflection was identified at a reciprocal space position of (0 4.748 0), for T=15 K. Because of its position, the reflection was classified as the F-type 2^{nd} harmonic peak, (0 4+2q 0), where q=0.374 b^*. Like the 2^{nd} harmonic A-type reflection, this F-type reflection has no resonant enhancement at the Mn K edge, suggesting again that the reflection arises from a lattice distortion which is caused by the magnetic structure. Scattering from this reflection was observed in both the $\sigma - \sigma'$ and $\sigma - \pi'$ scattering channels. Again the signal in the $\sigma - \pi'$ channel is most likely due to a cross-talk from the polarisation analyser.

The temperature dependence of both the (0 4-q 0) and (0 4+2q 0) reflections, are shown

in figure 5.9. Results were taken with incident photon energies equal to 6.554keV in the $\sigma - \pi'$ and $\sigma - \sigma'$ scattering channels, for the respective reflections. As the figure shows, both reflections are not observed for temperatures greater than 31 K. This disagrees with published data, which states that the paramagnetic/collinear phase transition is at 39 K [11]. The thermal evolution of the reflection's position does agree with previous work however, as the incommensurate propagation vector q, changes from 0.375 $b*$ to 0.362 $b*$, but again no 'lock in' transition was observed.

Finally an azimuthal dependence of the (0 4-q 0) reflection, at a temperature of 15 K, is shown in figure 5.10. Scans were recorded in the $\sigma - \pi'$ scattering channel. Again the intensity of the reflection at each azimuthal angle was determined by fitting a Lorentzian profile to the data, using the Spec1d non-linear least squares fitting program. These intensities were then normalised to the azimuthal dependence of the (0 4 0) Bragg reflection to account for the precision of the crystal sample. The origin of the azimuthal angle was defined as the b-c crystallographic plane.

The data was fitted with the same 1^{st} harmonic electric-dipolar scattering cross section, that was used to fit the azimuthal dependence of the (0 q 0) reflection in $TbMnO_3$ (equation 5.4):

$$I \propto (\cos\theta(\hat{z_c}\cos\psi + \hat{z_a}\sin\psi) + \hat{z_b}\sin\theta)^2 \tag{5.4}$$

Results from the fitting show a $\cos^2(\psi)$ azimuthal dependence, which suggests a c-axis magnetic structure. This is similar to what was seen for the 1^{st} harmonic F-type reflection for $TbMnO_3$. When compared to figure 4.13 (the azimuthal dependence of the (0 q 0) reflection in $TbMnO_3$), it is clear that the quality of data is not as good. Thus it is difficult to be as confident regarding the magnetic structure of this reflection.

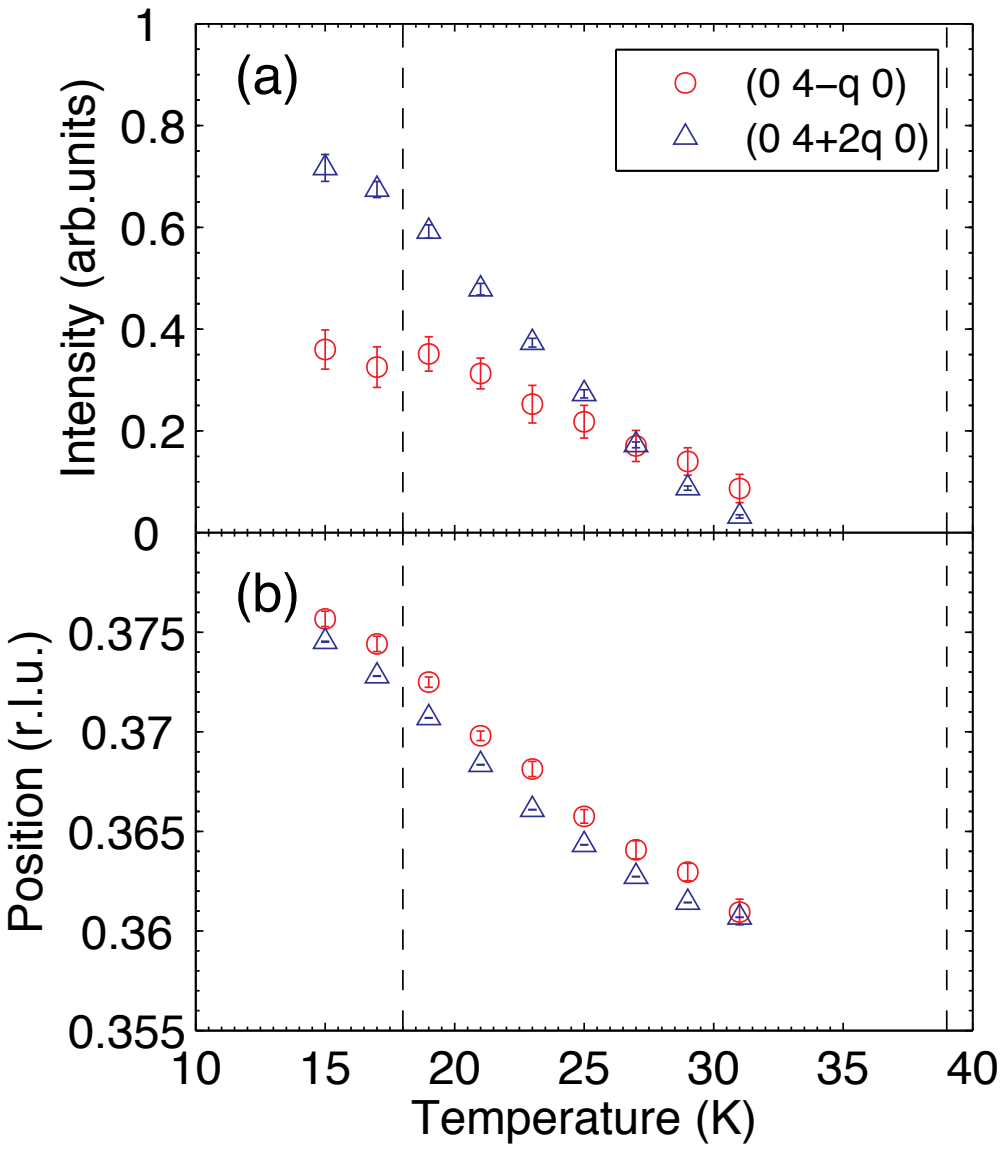

Figure 5.9: Temperature dependences in the $\sigma - \pi'$ scattering channel for the (0 4-q 0) reflection, and the $\sigma - \sigma'$ scattering channel for the (0 4+2q 0) reflection. Both reflections were measured with a photon energy in the vicinity of the Mn K edge. The figure shows (a) the integrated intensity and (b) the position of the reflection as the temperature is increased from 15 K, no reflection was observed above 31 K. The intensity of each reflection was determined by fitting a Lorentzian profile. Data was recorded at the ID20 beamline.

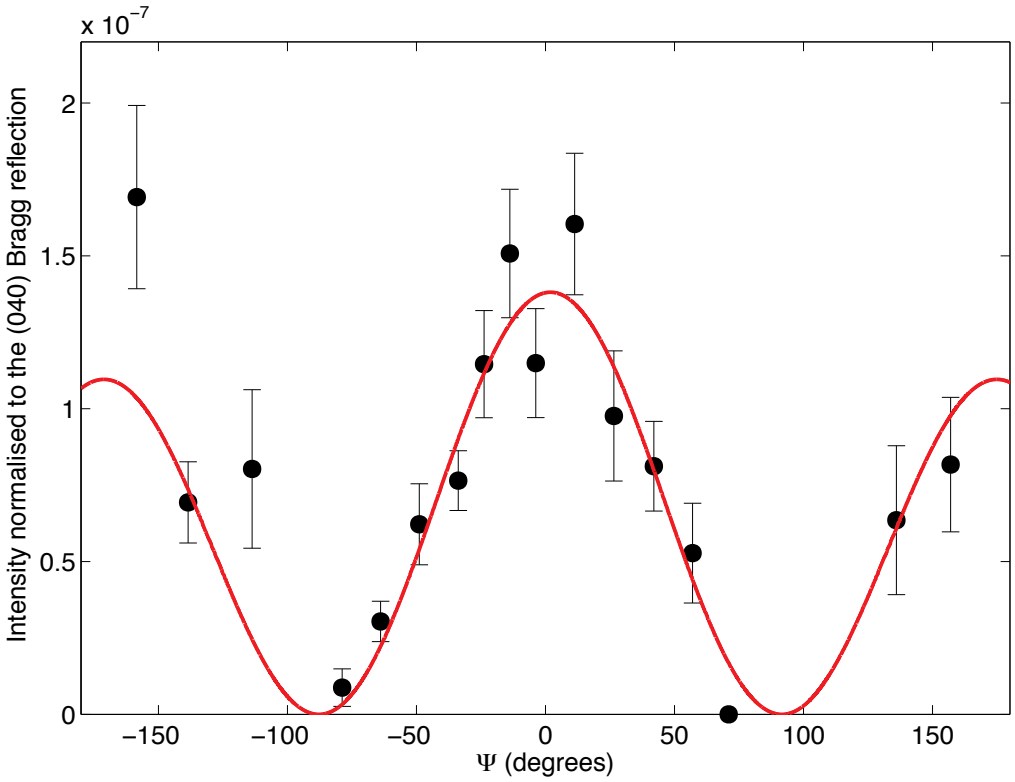

Figure 5.10: The Mn K edge resonant scattering azimuthal dependence of the (0 4-q 0) reflection. Results were taken at a temperature of 15 K, in the $\sigma - \pi'$ scattering channel. The reflection's intensity, at each azimuthal angle, was normalised to the corresponding intensity of the (0 4 0) Bragg reflection. ψ=0° corresponds to scattering in the b-c crystallographic plane. Data was recorded at the ID20 beamline.

5.3.3 Other satellite reflections

Turning to the reflection at a reciprocal space position of (0 4.248 0). Initially this reflection was identified as a 2^{nd} harmonic C-type reflection: (0 5-2q 0), with the correct incommensurate propagation vector value of q=0.376±0.005 b^* [11]. This reflection is only seen in the rotated $\sigma - \pi'$ polarisation channel. In addition, there is no sign of a 1^{st} harmonic reflection at q=(0 ∼4.62 0). Rocking curves of the feature reveal a sharp reflection, dismissing the possibility that this was a powder line. Scans of the intensity of scattering as a function of incident photon energy for this reflection reveal a clear resonance (figure 5.11). In addition to this reflection, a sister reflection was located at (0 ∼3.7 0), which possibly corresponds to the C-type reflection, (0 3+2q 0). Energy scans of this sister reflection

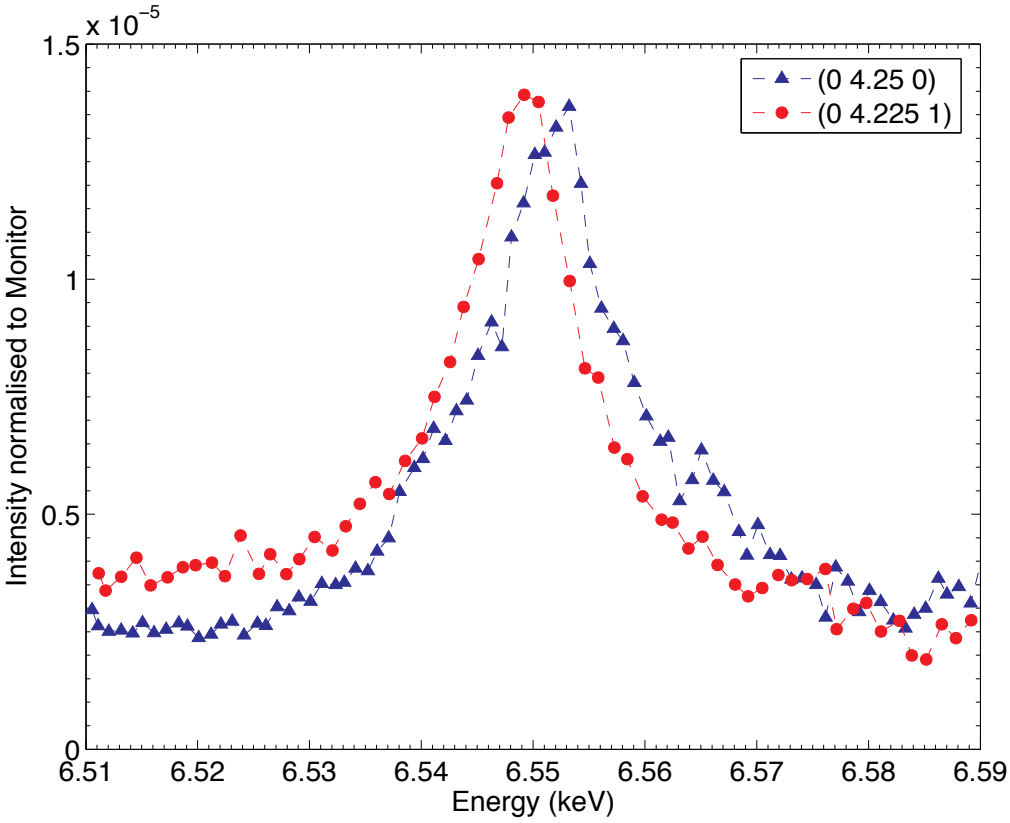

Figure 5.11: Incident photon energy scans at a fixed wavevector corresponding to the reflections at (0 4.248 0) (blue data points) and (0 4.225 1), (red data points). The scans were taken in the cycloidal (T=15 K) magnetic phase, in the σ-π' scattering channel. Data was recorded at the ID20 beamline.

show a similar resonance profile. Due to time constraints, no azimuthal or temperature dependences were taken of either of these reflections. Combining these observations with the fact that there is a clear resonant scattering signal, suggests that this reflection cannot be a 2^{nd} harmonic magnetic reflection. My reasoning for this statement is as follows, the cross section for scattering from a 2^{nd} harmonic magnetic reflection is:

$$F^{(2)} \begin{pmatrix} {z_2}^2 & -z_2(z_1 \sin\theta - z_3 \cos\theta) \\ z_2(z_1 \sin\theta + z_3 \cos\theta) & -\cos^2\theta({z_1}^2 \tan^2\theta + {z_3}^2) \end{pmatrix} \tag{5.5}$$

Thus no signal in the $\sigma - \sigma'$ channel indicates that z_2=0. However, the z_2 moment direction also appears at the front of the $\sigma - \pi'$ scattering term, thus for the scattering to be magnetic in origin, the $\sigma - \pi'$ scattering at this azimuthal angle would also have to be zero.

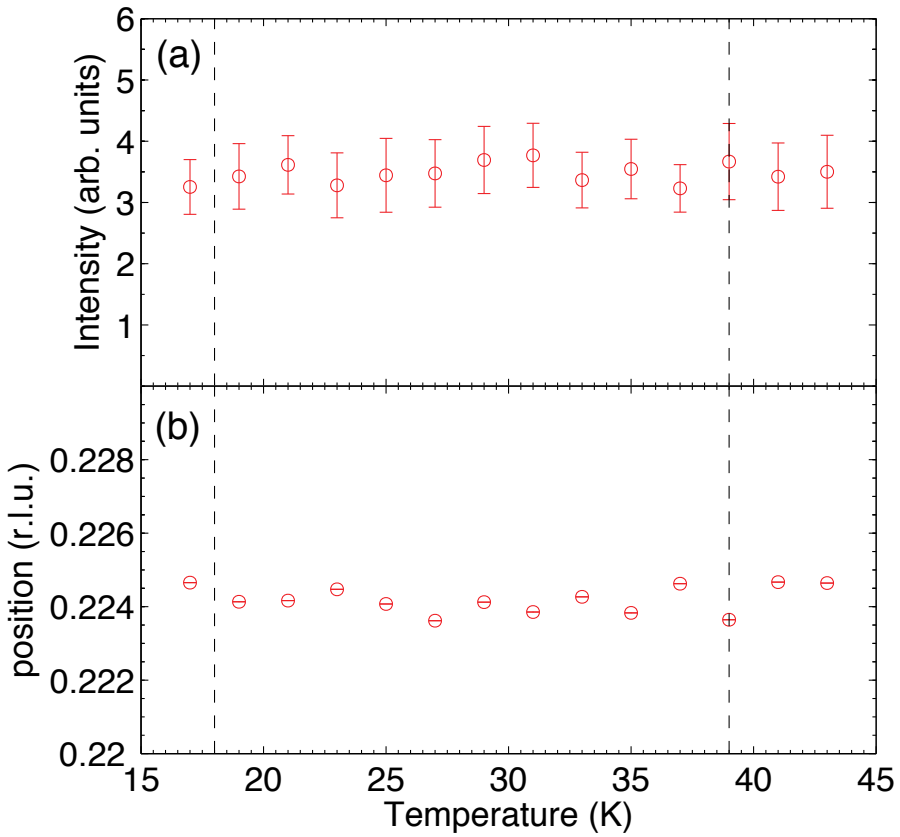

Figure 5.12: Temperature dependence of the reflection at (0 4.225 1) in the $\sigma-\pi'$ scattering channel. The figure shows (a) the integrated intensity and (b) the position of the reflection as the temperature is increased from 15 K. The intensity of each reflection was determined by fitting a Lorentzian profile. Data was recorded at the ID20 beamline.

The reflection observed at (0 4.225 1), was only detected in the rotated $\sigma - \pi'$ scattering channel. Again, rocking curves of this reflection gave a sharp peak, indicating that this is a real feature and not a powder line. The fact that this reflection was only seen in the rotated scattering channel, suggests that this is not the 2^{nd} harmonic reflection of the antiferromagnetic G-type reflection of (0 5-2q 1). In addition, the position of this reflection would give a value for the propagation vector q of 0.3875 b^*, which is significantly different from the value of q obtained from the other incommensurate reflections. An incident energy scan in the vicinity of the Mn K edge was taken at a temperature of 15 K, in the $\sigma - \pi'$ scattering channel (figure 5.11). The reflection shows a strong resonance in the $\sigma - \pi'$ scattering channel, with a peak in energy at 6.549 keV and a significant non-resonant

background. A temperature dependence (in the $\sigma - \pi'$ channel) was taken with a photon energy of 6.549 keV, over the range: 15 K≤T≤43 K. The result is shown in figure 5.12.

Results from the temperature dependence of this reflection reveal that this feature is in fact independent of the sample's magnetic phases. This conclusion can be drawn for two reasons: Firstly, this reflection exists above the paramagnetic phase transition at 39 K. One would expect to see the reflection disappear at temperature on or below this phase transition. Secondly, the reflection's position seems to be independent of temperature. One can therefore draw the conclusion that this ordering represented by this reflection, is not linked to the magnetic propagation vector q.

5.3.4 Measurements taken at the Dy L_3 resonance edge

RXS measurements were also performed with photon energies in the vicinity of the Dy L_3 absorption edge, at a base temperature of 2 K. Figure 5.13 shows the results of longitudinal scans, in both the $\sigma - \sigma'$ and $\sigma - \pi'$ scattering channels, along (a) [0k0] and (b) [0k1], with 3.1< k <3.9. For all scans, the energy of the X-rays were equal to the Dy L_3 resonant enhancement (7.792 keV).

The scan reveals multiple features, some of which can be attributed to the order of the manganese sublattice, namely the reflections labelled, **L**, **O**, **P** and **S**. However, the other reflections labelled in figure 5.13 could not be identified. Rocking curves of these unidentified reflections were sharp, however, indicating that they are not powder lines. Interestingly these measurements did not show any commensurate ordering of the Dy magnetic moments. Such commensurate ordering has previously been reported by Feyerherm *et al* [16] using the same experimental technique.

Starting with figure 5.13 (b). The reflection detected at a reciprocal space position (0 3.62 1), which is labelled as **S**, corresponds to the 1^{st} harmonic A-type reflection, (0 4-q 1), where q=0.38±0.005 b^*. The scattering strength as a function of incident photon energy, for this reflection, is shown in figure 5.14. As the figure shows, there is a resonant enhancement for this reflection, however it is much weaker than the enhancement for the

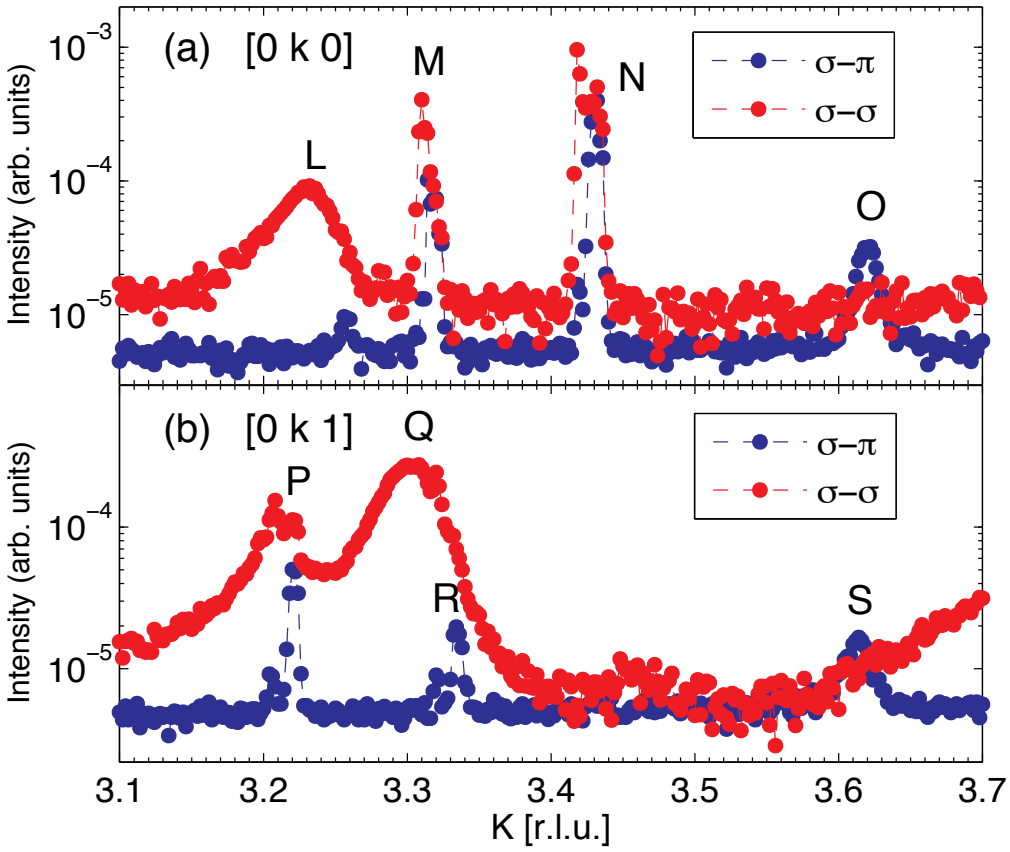

Figure 5.13: Longitudinal scans along (a) [0k0] and (b) [0k1], for 3.1< k <3.7. Data was taken at a temperature of 2 K, in $\sigma - \sigma'$ (red data points) and the $\sigma - \pi'$ (blue data points) scattering channels. The energy of X-ray photons used was equal to the Dy L_3 absorption edge (7.792 keV). Data was recorded at the ID20 beamline.

F-type reflection (see below).

The feature labelled as **P** in figure 5.13 (b), corresponds to the A-type 2^{nd} harmonic reflection, (0 4-2q 1), with q=0.39±0.005 b^*. Due to time constraints however, no temperature dependence or scattering intensity as a function of photon energy were recorded.

The peak labelled **O** in figure 5.13, (a) was located at a reciprocal space position of (0 3.62 0) and corresponds to the F-type 1^{st} harmonic reflection, (0 4-q 0), with q=0.38±0.005 b^*. In addition, a twin reflection, (0 4+q 0) was also located at (0 4.38 0). The scattering from these reflections, as a function of energy, are shown in figure 5.15.

The figure shows that there is a clear resonant enhancement of the scattering for both

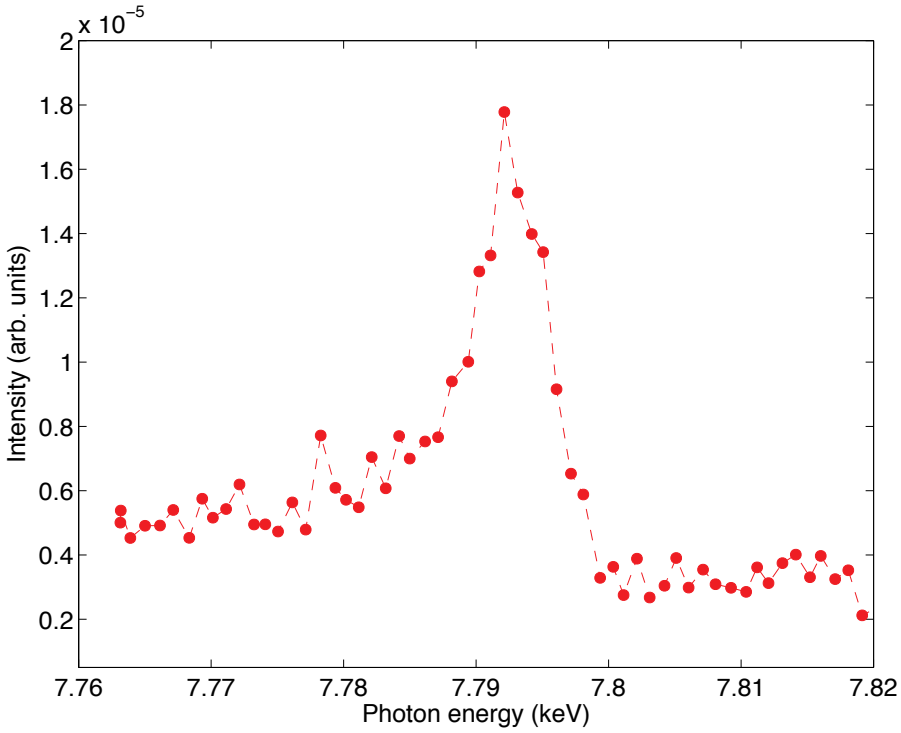

Figure 5.14: Scattering strength as a function of incident photon energy in the vicinity of the Dy L_3 absorption edge, for the reflection at (0 4-q 1). The scan was taken at a temperature of 2 K, in the $\sigma - \pi'$ scattering channel. Data was recorded at the ID20 beamline.

reflections. However, the two reflections have different energy profiles. This remains to be explained.

In addition to these 1^{st} harmonic reflections, figure 5.13 (a) also shows a reflection at (0 3.25 0), which is labelled as **L**. This feature corresponds to the 2^{nd} harmonic F-type reflection, (0 4-2q 0), where q=0.379±0.005 b^*. Due to time constraints however, no temperature dependence or scattering intensity as a function of photon energy for this reflection was taken.

5.4 Conclusion

Results from these experiments are somewhat difficult to interpret, with the results taken at the Mn K edge showing the correct incommensurate wavevector for the A and F type

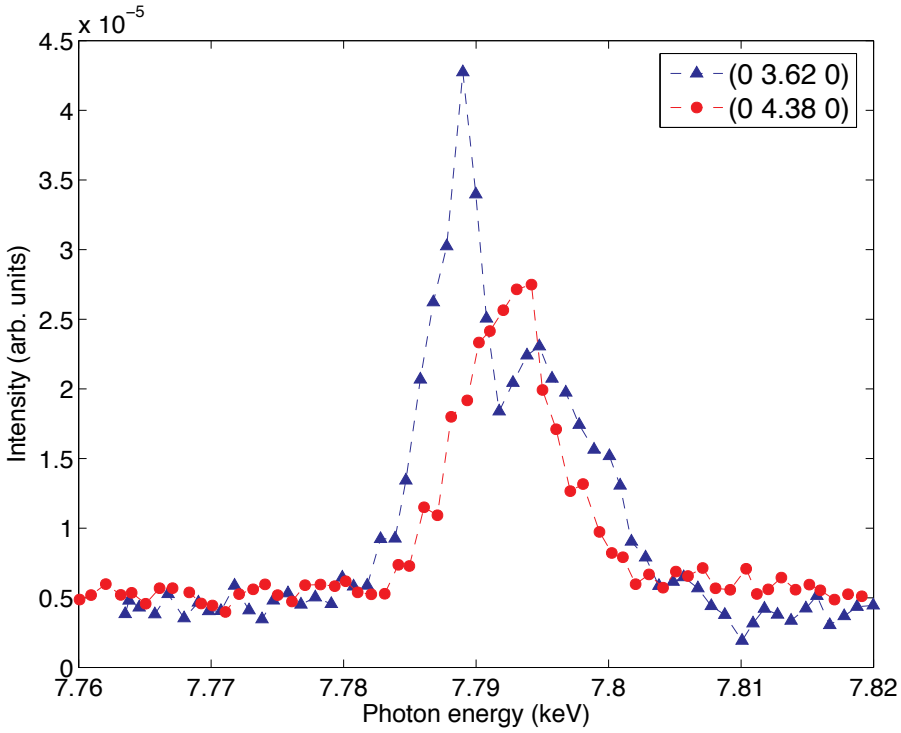

Figure 5.15: Scattering strength as a function of incident photon energy in the vicinity of the Dy L_3 absorption edge, for the (0 4-q 1) and (0 4+q 1) reflections (blue and red data points respectively). The scan was taken at a temperature of 2 K, in the $\sigma - \pi'$ scattering channel. Data was recorded at the ID20 beamline.

reflections. However, other incommensurate reflections were also detected with photon energies in the vicinity of the Mn K edge. These reflections are much more difficult to understand.

Starting with the A-type reflection, the non-resonant scattering seen in the rotated $\sigma - \pi'$ scattering channel confirms that this type of reflection is magnetic in origin. Incident photon energy scans of this reflection in the cycloidal phase show a weak resonance on top of a significant non-resonant background. This conflicts with RXS results on $TbMnO_3$ which show a much stronger resonant enhancement [127]. As the temperature is increased into the collinear phase the signal from non-resonant scattering reduces noticeably. In addition to the 1^{st} harmonic reflection, a corresponding 2^{nd} harmonic A-type reflection was also observed in both the scattering channels. This reflection is believed to arise from a lattice distortion caused by the magnetic structure. Thus, the signal in the rotated $\sigma - \pi'$

scattering channel is most likely due to cross-talk in the polarisation analyser. Temperature dependences show that both the 1^{st} and 2^{nd} harmonic A-type reflections disappear above 33 K. While this temperature is significantly less than the previously reported collinear/paramagnetic phase transition at 39 K [11], both reflections' incommensurate wavevectors (q) have the correct value and shows the correct thermal evolution. Azimuthal dependences of the (0 4+q 1) reflection suggest a b-c cycloid for the Mn magnetic moments, at 15 K. This is probably the main result of these experiments, as it microscopically shows, for the first time, that the Mn spins form a cycloid in $DyMnO_3$'s ferroelectric phase. Thus confirming a common mechanism for the induction of a ferroelectric polarisation in both $TbMnO_3$ and $DyMnO_3$. It should be noted however, that as a significant amount of scattering from this reflection is non-resonant in nature. Therefore, some of the azimuthal dependence may arise from magnetic scattering from the Dy^{3+} magnetic moments, which have also been shown to form a cycloid below 19 K [17].

The 1^{st} harmonic F-type reflections, (0 4±q 0) were also identified. Incident photon energy scans of these reflections revealed a significant Mn K-edge resonance, indicating that the Mn $4p$ electronic states are ordered in both the cycloidal and collinear phases. The lack of non-resonant measurements mean that one cannot confirm the origin of this reflection. If one assumes that the reflection is magnetic in origin, then the azimuthal dependence of this reflection suggests a c-axis canting of the Mn magnetic moments. This result is in agreement with the F-type reflection measured in $TbMnO_3$ (see section 4.13). However, because of the poor data quality, one cannot rule out other magnetic structures. The corresponding 2^{nd} harmonic reflection (with the correct propagation vector) was observed in both scattering channels. Again this reflection is believed to arise from a lattice distortion caused by the magnetic structure. Thus the signal in the rotated $\sigma - \pi'$ scattering channel is again, most likely due to cross-talk in the polarisation analyser.

The supposed C-type 2^{nd} harmonic reflection, (0 5-2q 0), gave the correct value of the incommensurate propagation vector (q) at 15 K. Significantly, no scattering was seen in the $\sigma - \sigma'$ scattering channel, indicating that this is not the same type of 2^{nd} harmonic reflection as the A or F type reflections. In addition, no 1^{st} harmonic reflection was identified. This leads to the conclusion that this reflection does not represent a 2^{nd} harmonic magnetic

reflection. One possibility is that this reflection may be commensurate of the form (0 $4\pm\tau$ 0), where τ=0.25 b^*. Although it is unusual for two completely different F-type reflections to exist. Without azimuthal and temperature dependences, this reflection is difficult to characterise. It is my belief that this C-type reflection might possibly represent scattering from structural distortions [29]. Finally, the reflection at (0 4.225 1) could not be identified as the G-type 2^{nd} harmonic reflection, (0 5-2q 1). This is because the temperature dependence of this reflection cannot be connected to the magnetic ordering in $DyMnO_3$. The polarisation dependence (the peak is seen in the $\sigma - \pi'$ scattering channel only) and sharp rocking curve, rule out the possibility that this is a powder line. I am unsure what this reflection represents, however the clear resonant enhancement of scattering shown in figure 5.11, indicates that the reflection is connected to the ordering of the Mn 4p electronic states.

For the results taken with photon energies in the vicinity of the Dy L_3 edge, at a temperature of 2 K, both A and F type reflections correspond to the magnetic ordering of the Mn sublattice. These reflections were shown to resonate. However, the lack of temperature or azimuthal dependences mean that one cannot draw any solid conclusions about their nature. In addition, several unidentified reflections were also observed at the Dy L_3 resonance. None of these reflections corresponds to the commensurate ordering of the Dy magnetic moments, as reported by Feyerherm *et al* [16]. It is tempting to believe that these conflicting results are due to a poor $DyMnO_3$ crystal sample. However, since our crystal has the correct lattice parameters and value for the incommensurate propagation vector (q), it would be extremely unusual for this to be the case.

Chapter 6

Overall conclusion

Over the course of my Ph.D. I have participated in several successful experimental studies. Firstly, I have performed one of the first investigations of the lattice dynamics in a single crystal sample of the '1111' class of iron pnictides. Results from this research have hinted at a strong coupling between the lattice and spin degrees of freedom. In addition, the resonant soft X-ray scattering studies of $TbMnO_3$ have revealed extra, previously unidentified, components of the magnetic structure. The resonant X-ray studies of $DyMnO_3$ did not produce any definite conclusions. However, these experiments did reveal some unexpected results that warrant further investigation. For the final Chapter of this thesis I will summaries the conclusions of these experimental studies, and explain their importance with respect to understanding the unusual properties of these materials. I will also describe the further research and data analysis that are needed to advance this understanding.

6.1 IXS measurements of the phonon modes in $SmFeAsO_{1-x}F_y$

Paramagnetic phase, inelastic X-ray scattering dispersion measurements along the [100] direction of SmFeAsO and $SmFeAsO_{0.60}F_{0.35}$, revealed an unusual renormalisation upon fluorine doping of two out of three optical phonon modes, that are in the vicinity of an energy transfer of 23 meV. Moreover, the two optical phonon modes which show the doping

induced renormalisations, specifically the B_{1g} and in-phase A_{1g}, are sensitive to the magnetic iron sublattice. What is more, the third optical mode, the out-of-phase A_{1g} mode, which is not sensitive to the magnetic iron sublattice, shows no doping induced renormalisation. This result suggests there is a strong spin-lattice coupling in these compounds. Such a coupling is a potentially important result, as it suggests that the coupling between the electronic system and the lattice proceeds via antiferromagnetic fluctuations. This unconventional form of electron-phonon coupling might provide the key to understanding the high T_c in the iron pnictides.

Because of their importance, these results have been published in *Physical Review B* as a rapid communication and editor's suggestion [9]. In this paper, it is speculated that the doping induced renormalisations are an effect of a resonance in the electronic system. A similar resonance, which is believed to arise from an enhancement of the dynamic magnetic susceptibility, due to Fermi surface nesting, has been detected in the '122' class of compounds [72, 73]. However, the results given in this thesis show, for the first time, that a similar resonance feature may also be present in the '1111' compounds. This suggests that a coupling between the lattice and magnetic degrees of freedom may be a universal feature of the iron pnictides. Again, this supports the idea of electron-phonon coupling being enhanced by antiferromagnetic fluctuations. These results offer an insight into the lattice dynamics of the iron pnictides, however additional theoretical and experimental work is needed to confirm the importance of these dynamics in the pnictide's low temperature ground states.

Firstly, it has been established that the optical mode renormalisations are not due to structural relaxations that were predicted by D.F.T calculations [98]. What is more, spin polarised D.F.T. calculations have been shown to be better at replicating the phonon spectra of '122' pnictide compounds [85]. It therefore seems reasonable to suggest that spin polarised D.F.T. calculations of a '1111' compound would be helpful in identifying the source of the optical mode renormalisations, that are shown in this thesis.

Secondly, measurements of the lattice dynamics across the respective magnetic (120 K) and superconducting (55 K) transitions in SmFeAsO and $SmFeAsO_{0.60}F_{0.35}$, would be an

ideal way to test the hypothesis, that strong spin-lattice coupling is responsible for the high T_c in the iron pnictides. In addition, all IXS dispersion measurements that have been recorded so far, have been along the [100] direction only. However, the Fermi surface nesting, that is believed to linked to the superconductivity, lies along the [110] direction. In addition, the magnetic resonance observed in the '122' compounds is also found along the same crystallographic direction [73]. Therefore, it is also extremely important to measure the IXS dispersion along this new direction as: a) the strongest phonon renormalisations should be observed here, and b) the shape of the dynamical magnetic susceptibility is known for this direction. Thus, by measuring the phonon dispersion along this new direction one could also obtain direct information on the momentum dependent coupling of the lattice to the electron spins.

At the time of writing this thesis, I have just conducted an experiment to measure the superconducting crystal's dispersion along the [110] direction at room temperature (295 K) and 5 K. Unfortunately, I have not been able to fully analyse the results yet, however an example spectra is shown in figure 6.1. The figure clearly shows that at 5 K there is an increase in phonon scattering intensity for the 23 meV phonons. Surprisingly, an increase in the phonon scattering intensity is also seen for the phonon modes at an energy transfer around 35 meV, these high energy phonons are believed to correspond to pure oxygen modes. It should be noted that these two IXS spectra have not been normalised to Bose factor: $1/(1-e^{-E/k_BT})$. However, one would expect the intensity of phonon scattering to decrease with temperature, due to this renormalisation. While the connection between this increase in phonon scattering intensity and superconductivity remains an open question, these results do provide compelling evidence for further investigations.

6.2 Resonant X-ray scattering studies of $TbMnO_3$

The technique of resonant X-ray scattering was used to probe the ordering of the localised Mn $3d$ and Tb $4f$ electronic states in multiferroic $TbMnO_3$. Results from these experiments showed, in a model independent way, additional Fourier components of the magnetic structure which were previously unknown. Specifically, a canting of 5° of the manganese

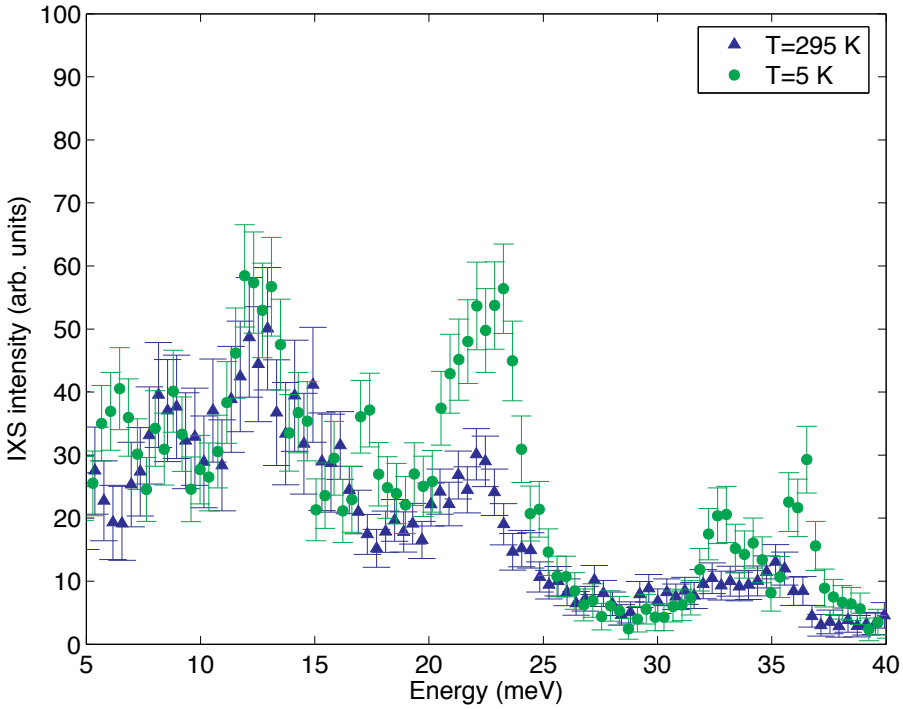

Figure 6.1: IXS spectra at q=(0.2 0.2 0). One spectra was recorded at 295 K (blue data points) and other at 5 K (green data points). A comparison between the two spectra show that at 5K there is an enhancement in phonon scattering intensity at energy transfers around 23 meV and 35 meV.

magnetic moments towards the crystallographic c-axis was detected in both phases. In addition, a canting towards the crystallographic a-axis was also confirmed for the cycloidal phase, however this canting could also exist above 28K. This means that the ferroelectric ordering in the $TbMnO_3$ arises from a phase transition between two non-collinear magnetic structures, and not between a collinear and non-collinear structure, as previously believed. The results of this study do not change the basic principles of how the ferroelectric polarisation in $TbMnO_3$ is induced. However, I still believe that it provides an important result. So important in fact, that this work has produced two journal articles, which have been published in *The Journal of Condensed Matter Physics* as a Fast Track Communication [14] and *Physical Review Letters* [15]. The importance of this study is therefore twofold:

Firstly, the 'original' magnetic structure of $TbMnO_3$ was derived from representational analysis of just two types of antiferromagnetic reflections (A and G types) [12]. However,

neutron diffraction work has shown that all four types of antiferromagnetic reflections exist [13]. Therefore, the study presented in this thesis clarifies what the additional reflections (F and C types) represent and ascertains whether they are important with respect to the magnetoelectric coupling in this class of multiferroic compounds. While the results of this study show that the A and C type reflections do not significantly alter $TbMnO_3$'s magnetic structure, they do provide extra conditions for the theoretical work, used to explain how a ferroelectric polarisation is induced in $TbMnO_3$.

Secondly, for most resonant soft X-ray scattering studies, the small volume of reciprocal space that may be probed, means that for most compounds, only one reflection may be studied, for example [30, 31, 143]. $TbMnO_3$ is therefore an example of a system where multiple reflections may be studied, and can be viewed as a case study of how resonant scattering of soft X-rays may be used to extract a great deal of information from such a small volume of reciprocal space.

The research on $TbMnO_3$ has been extremely successful, although there are still several important measurements which, due to time constraints, have not been recorded. For example, it has been speculated that the a-axis canting of the manganese magnetic moments exists above the ferroelectric phase transition at 28K. However, an azimuthal dependence of the (0 1-2q 0) reflection above 28K is needed to confirm this. In addition, recent resonant soft X-ray scattering research on the similar multiferroic compound: $DyMnO_3$, has suggested that the Dy magnetic moments also form a cycloidal magnetic structure in the ferroelectric phase [17]. It would therefore be interesting to record the azimuthal dependence of the (0 q 1) reflection at the Tb M_5 resonant enhancement below 28K, to see what symmetry the Tb $4f$ moments posses, in this phase. Finally, modelling of the different reflection's scattering strength, as a function of incident photon energy (figure 4.9), would also provide useful information on the local crystal field environment of the Mn ions (something that I plan to do in the future). Such modelling could be performed with *Hilbert++* [139], a ligand field program. However, to achieve this I will need absorption spectra of the crystal sample in the different magnetic phases. It is my hope, that if this modelling is successful, I will be able to publish the results in another journal article.

6.3 X-ray magnetic scattering studies of $DyMnO_3$

Unlike the results presented in the previous two chapters, resonant X-ray scattering studies of multiferroic $DyMnO_3$, did not provide any new information on the magnetic ordering of this compound. The experimental studies did identify A and F type antiferromagnetic reflections, with the correct value for the incommensurate propagation vector. The azimuthal dependencies of these reflections suggested cycloidal and c-axis canted magnetic structures, respectively. These results are consistent with research on $TbMnO_3$ [12, 15]. It should also be noted that these results are the first measurements which show, microscopically, that the Mn magnetic moments form a cycloidal magnetic structure in $DyMnO_3$'s ferroelectric phase. However, other satellite reflections that were observed, with a Mn K resonant enhancement, do not correspond to the incommensurate magnetic structure of $DyMnO_3$. Without further experimental results, i.e. temperature and azimuthal dependencies, it is impossible to determine what these reflections represent. Furthermore, results taken at 2K with a photon equal in energy to the Dy L_3 resonant enhancement were even more confusing. It should be noted at this stage that these results were taken with a brand new polarisation analyser crystal, therefore some of these confusing results may be explained by the crystal analyser having a bad mosaic. However, this does not explain the lack of a commensurate reflection that had previously been detected [16].

Even though the results from these experiments offered no new information on the magnetic ordering, I still think it is important to continue the RXS research on $DyMnO_3$, perhaps with a new crystal sample. The main reason for this is that the vast majority of research on the magnetic ordering in $DyMnO_3$ has been published by one research group [16, 142, 17], presumably working from one batch of crystals. It is therefore important to independently clarify their results.

Appendix A

Appendix: Irreducible representations of $TbMnO_3$

To determine the magnetic structure of a crystal sample, one needs two pieces of information. Firstly, the magnetic wavevector(s), denoted by $\mathbf{q}$, and secondly the symmetry of the coupling between the different magnetic ions, within the crystallographic unit cell. The first piece of information is usually determined experimentally, through scattering techniques such as neutron diffraction. The second piece of information is determined with the help of group theory, which gives the possible magnetic structures that are allowed by the crystal's symmetry.

For the case of $TbMnO_3$, Kenzelmann and co-workers [12] used group theory representational analysis to determine the different magnetic structures above and below the ferroelectric phase transition at 28K. Representational analysis is a method that gives the allowed magnetic symmetries (known as basis vectors), which are associated with the different irreducible representations Γ_ν (the most basic way of combining the symmetry elements of a specific crystallographic structure).

The basic method of representational analysis is as follows, for further information readers should refer to [144]. From the point group of the crystal structure ($\mathbf{g}$), one has a number of symmetry elements, i.e. rotational axis, mirrors planes etc. From all the symmetry

elements, one determines which elements leave the magnetic wavevector $\mathbf{q}$ invariant (the translational parts of the symmetry elements are not included). These invariant symmetry elements give a subgroup of the point group, which is denoted as $\mathbf{g_q}$. The irreducible representations of the subgroup $\mathbf{g_q}$ can be written in a character table, which describes how each rotational part (mirror planes can be thought of as 2-fold rotational axis) of the symmetry operators work on the magnetic ions. The next step is to include the translational parts of the symmetry elements in the irreducible representations, now the irreducible representations are of the little group $\mathbf{G_q}$ of the space group, $\mathbf{G}$. If $\mathbf{q}$ is a interior point of the Brillouin zone (as is the case for $TbMnO_3$), then the irreducible representations of $\mathbf{G_q}$ can be calculated using the relationship[144]:

$$\Gamma_\nu(\omega_i, t_i) = e^{-i\mathbf{q}\cdot\mathbf{t_i}}\gamma_\nu(\omega_i) \tag{A.1}$$

Where Γ_ν is an irreducible representation of $\mathbf{G_q}$, γ_ν is an irreducible representation of $\mathbf{g_q}$, and $\mathbf{q}$ is the wavevector. Finally, ω_i and t_i are the respective rotational and translational parts of the symmetry operators. From the character table of $\mathbf{G_q}$, one can then determine the basis vectors (V_ν^α), and therefore, how the spins of the different magnetic ion sites are related for the different irreducible representations:

$$V_\nu^\alpha = \sum_\epsilon \Gamma_\nu \epsilon \cdot m_\nu^\alpha \tag{A.2}$$

Here ϵ is the symmetry operator, and m_ν^α is the Fourier component of magnetic moment projection along the different crystallographic axes ($\alpha = x, y, z$).

I will now calculate the basis vectors for $TbMnO_3$.

$TbMnO_3$ exists in the space group $Pbnm$, its magnetic ordering wavevector is, $\mathbf{q} = [0\ 0.28\frac{2\pi}{b}\ 0]$. The $Pbnm$ space group has a point group of D_{2h} and 8 symmetry operator. Of these 8 symmetry operators 4 leave $\mathbf{q}$ invariant, these 4 operators are: [132].

1. The identity operator (I).

2. A 2-fold rotation about the y axis centred around $x = 1/4, z = 1/4$, followed by a translation of $b/2$ along y ($2y$).

3. A mirror plane in z at $z = 1/4$ (m_{xy}).

4. A glide plane with a mirror at $x = 3/4$, followed by a translation of $b/2$ (m_{yz}).

In matrix format the rotational part of these symmetry operators are:

$$
\begin{aligned}
I &= \begin{pmatrix} 1 & 0 & 0 \\ 0 & 1 & 0 \\ 0 & 0 & 1 \end{pmatrix} \\
2_y &= \begin{pmatrix} -1 & 0 & 0 \\ 0 & 1 & 0 \\ 0 & 0 & -1 \end{pmatrix} \\
m_{xy} &= \begin{pmatrix} 1 & 0 & 0 \\ 0 & 1 & 0 \\ 0 & 0 & -1 \end{pmatrix} \\
m_{yz} &= \begin{pmatrix} -1 & 0 & 0 \\ 0 & 1 & 0 \\ 0 & 0 & 1 \end{pmatrix}
\end{aligned}
\tag{A.3}
$$

Thus the point group $\mathbf{g}$=D_{2h} is reduced to the subgroup $\mathbf{g_q}$=C_{2v}.T he character table of this point subgroup is given below.

Table A.1: Character table of the point group C_{2v} for $TbMnO_3$. This table was taken from Kenzelmann *et al.* [12].

	I	2_y	m_{xy}	m_{yz}
Γ_1	1	1	1	1
Γ_2	1	1	-1	-1
Γ_3	1	-1	1	-1
Γ_4	1	-1	-1	1

In addition to the rotational/inversion parts, some of the symmetry operators have translational parts. Which are:

$$
\begin{aligned}
I &= \begin{pmatrix} 0 \\ 0 \\ 0 \end{pmatrix} \\
2_y &= \begin{pmatrix} 1/2 \\ 1/2 \\ 1/2 \end{pmatrix} \\
m_{xy} &= \begin{pmatrix} 0 \\ 0 \\ 1/2 \end{pmatrix} \\
m_{yz} &= \begin{pmatrix} 1/2 \\ 1/2 \\ 0 \end{pmatrix}
\end{aligned}
\tag{A.4}
$$

The next step is to determine the character table for the little Group $\mathbf{G_q}$, using equation A.1. The I and m_{xy} symmetry operators have no translations parallel to the wavevector, therefore their phase factor ($e^{i\mathbf{q}\cdot\mathbf{t_i}}$) will zero. However, the 2_y and m_{yz} symmetry operators have translations parallel to the wavevector ($b/2$). Therefore, their phase factors will be, $e^{iq_y\pi}$, where q_y=0.28 b^*. Hence the character table for the little group $\mathbf{G_q}$ is:

The final step before determining the basis vectors, is to calculate how the symmetry operators transform the Fourier components of the magnetic moment projections, $m^{\alpha}_{q,j}$,

Table A.2: Character table of the little group $\mathbf{G_q}$ for $TbMnO_3$, where $a = e^{iq_y\pi}$.

	I	2_y	m_{xy}	m_{yz}
Γ_1	1	a	1	a
Γ_2	1	a	-1	-a
Γ_3	1	-a	1	-a
Γ_4	1	-a	-1	a

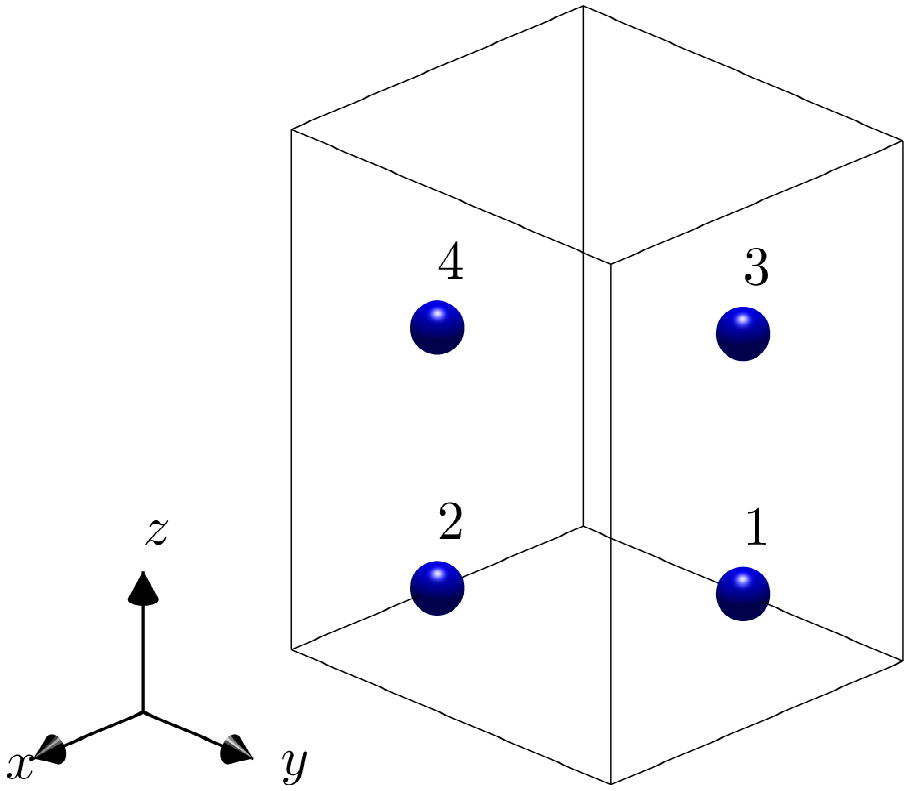

Figure A.1: The four Mn crystallographic positions in $TbMnO_3$.

where $\alpha = x, y, z$, and $j = 1, 2, 3, 4$ corresponds to the four Mn crystallographic sites. For $TbMnO_3$ the Mn crystallographic sites are at, (1) (0 $\frac{1}{2}$ 0), (2) ($\frac{1}{2}$ 0 0), (3) (0 $\frac{1}{2}$ $\frac{1}{2}$), (4) ($\frac{1}{2}$ 0 $\frac{1}{2}$) (see figure A.1).

Therefore:

- I takes the Mn at site 1 to site 1.
- 2_y takes the Mn at site 1 to site 4.
- m_{xy} takes the Mn at site 1 to site 3.

- m_{yz} takes the Mn at site 1 to site 2.

The symmetry elements 2_y, m_{xy} and m_{yz} will leave the respective spin direction along y, z and x invariant, but will invert the other components. Hence:

$$\begin{array}{ccc} 2_y(m_1^x) = -m_4^x & 2_y(m_1^y) = m_4^y & 2_y(m_1^z) = -m_4^z \\ m_{xy}(m_1^x) = -m_3^x & m_{xy}(m_1^y) = -m_3^y & m_{xy}(m_1^z) = m_3^z \\ m_{yz}(m_1^x) = m_2^x & m_{yz}(m_1^y) = -m_2^y & m_{yz}(m_1^z) = -m_2^z \end{array} \tag{A.5}$$

Using equation A.2, one can now write the basis vectors for the spin components along the x, y and z directions for the four irreducible representations. Put simply the equations shown below give the symmetry of coupling between the 4 Mn magnetic moments, for each irreducible representation.

The symmetry of magnetic moment coupling, as described by the Γ_1 irreducible representation:

$$\begin{aligned} V_1^x &= m_1^x + am_2^x - m_3^x - am_4^x \\ V_1^y &= m_1^y - am_2^y - m_3^y + am_4^y \\ V_1^z &= m_1^z - am_2^z + m_3^z - am_4^z \end{aligned} \tag{A.6}$$

The symmetry of magnetic moment coupling, as described by the Γ_2 irreducible representation:

$$\begin{aligned} V_2^x &= m_1^x - am_2^x + m_3^x - am_4^x \\ V_2^y &= m_1^y + am_2^y + m_3^y + am_4^y \\ V_2^z &= m_1^z + am_2^z - m_3^z - am_4^z \end{aligned} \tag{A.7}$$

The symmetry of magnetic moment coupling, as described by the Γ_3 irreducible representation:

$$\begin{aligned} V_3^x &= m_1^x - am_2^x - m_3^x + am_4^x \\ V_3^y &= m_1^y + am_2^y - m_3^y - am_4^y \\ V_3^z &= m_1^z + am_2^z + m_3^z + am_4^z \end{aligned} \tag{A.8}$$

The symmetry of magnetic moment coupling, as described by the Γ_4 irreducible represen-

tation:

$$\begin{aligned} V_4^x &= m_1^x + am_2^x + m_3^x + am_4^x \\ V_4^y &= m_1^y - am_2^y + m_3^y - am_4^y \\ V_4^z &= m_1^z - am_2^z - m_3^z + am_4^z \end{aligned} \tag{A.9}$$

$TbMnO_3$ may now take a magnetic structure associated with one or more irreducible representation. For example, the general magnetic structure for the Γ_3 representation can be:

$$c_1V_3^x + c_2V_3^y + c_3V_3^z \tag{A.10}$$

Where c_1,c_2,c_3 are constants. Equation A.10 shows that the magnetic moments can point in any direction, this direction will depend upon physical parameters (exchange interactions and anisotropy). However, the coupling between the magnetic moments on the four different Mn sites are determined by the symmetry of the irreducible representation. For example, in its collinear phase, the Mn magnetic moments in $TbMnO_3$ point along the *b*-axis. Therefore the magnetic structure will be described by:

$$V_3^y = m_1^y + am_2^y - m_3^y - am_4^y \tag{A.11}$$

This states that the moments at sites 1 and 2 are ferromagnetically aligned along the *b*-axis, however, the factor $a{=}e^{iq_y\pi}$ will modulate the size of the magnetic moment. The moments at sites 3 and 4 are aligned in the opposite direction to those at sites 1 and 2, and again are modulated by the factor $a{=}e^{iq_y\pi}$. Therefore the magnetic moments at sites 1 and 3 will have the same magnitude, put will point in the opposite direction, the same is true for the magnetic moments at sites 2 and 4. This symmetry describes a longitudinal sine-wave modulated magnetic structure with a phase shift[1] between the Bravais sublattice. The description given is one of a collinear magnetic structure shown in figure 4.2(a) of the main text.

For the low temperature magnetic phase, an additional irreducible representation (Γ_2) was needed to describe the neutron diffraction results [12]. For this magnetic phase the

[1]In this case, a phase shift means the magnetic moment is modulated by the factor $a{=}e^{iq_y\pi}$, this produces in a change of magnitude and possibly the direction of the moment.

Mn moment direction of the Γ_2 representation was determined to lie along the c-axis. Therefore, the symmetry of this additional magnetic magnetic component will be:

$$V_2^z = m_1^z + am_2^z - m_3^z - am_4^z \tag{A.12}$$

For the Mn moment component pointing along the c-axis, the moments at sites 1 and 2 will point in the same direction. Again there is a difference in the phase of the moments, which is described by the phase factor. The same is true for the moments at sites 3 and 4, but the moments are antiferromagnetically aligned along the c-axis. When the Γ_2 and Γ_3 structures are combined, this gives an elliptical cycloid as shown in figure 4.2(b) of the main text.

Appendix B

Appendix: Calculating U_1,U_2,U_3 for the (0 4.375 1) peak

If one assumes that surface normal direction is: [0 4.371 1] in reciprocal space. Then, by using the standard reciprocal lattice transformations (equation B.1), the surface normal direction can be converted into real space:

$$\begin{aligned} \mathbf{a_1^*} &= 2\pi \frac{\mathbf{a_2}\times\mathbf{a_3}}{\mathbf{a_1}\cdot(\mathbf{a_2}\times\mathbf{a_3})} \\ \mathbf{a_2^*} &= 2\pi \frac{\mathbf{a_3}\times\mathbf{a_1}}{\mathbf{a_1}\cdot(\mathbf{a_2}\times\mathbf{a_3})} \\ \mathbf{a_3^*} &= 2\pi \frac{\mathbf{a_1}\times\mathbf{a_2}}{\mathbf{a_1}\cdot(\mathbf{a_2}\times\mathbf{a_3})} \end{aligned} \tag{B.1}$$

Where

$$\begin{aligned} \mathbf{a_1} &= na\hat{x} \\ \mathbf{a_2} &= mb\hat{y} \\ \mathbf{a_3} &= wc\hat{z} \end{aligned} \tag{B.2}$$

Here *a,b,c* are the real space lattice parameters, and *n,m,w* are just a set of multiplication constants.

From now on, we are only interested in $\mathbf{a}_2^*$ and $\mathbf{a}_3^*$ as the Miller index h is zero. The first step in determining the real space surface normal, is to insert the relationships given by equation B.2 into equation B.1. If one does this and remembers that the *Pbmn* space group has an orthogonal basis, then reciprocal lattice parameters reduce simply to:

$$\begin{aligned} \mathbf{a_2^*} &= \tfrac{2\pi}{mb}\hat{y} \\ \mathbf{a_3^*} &= \tfrac{2\pi}{wc}\hat{z} \end{aligned} \tag{B.3}$$

Now, by setting $\mathbf{a}_2^*$ equal to 4.375 and $\mathbf{a}_3^*$ equal to 1, one can rearrange equation B.3 to give the values of mb and wc respectively. The numerical values are: mb=1.4362Å and wc=2πÅ . So the real space surface normal of this peak is: [0 1.4362 2π]. This vector can be normalised to a magnitude of 1 by dividing by the modulus of the vector i.e. $\sqrt{(1.4362)^2 + (2\pi)^2}$=6.4452. Therefore, the final result is: -U_3=[0 0.223 0.975].

From this result it is easy to see that: U_1=[0 -0.975 0.223] and U_2=[100], as now: $U_1 \cdot U_2 = U_1 \cdot U_3 = U_2 \cdot U_3 = 0$.

Therefore, one can now set the magnetic moment directions (z_1,z_2,z_3) in terms of the crystallographic axes:

$$\begin{aligned} z_1 &= (-0.975z_b + 0.223z_c)\cos(\psi) + z_a \sin(\psi) \\ z_2 &= z_a \cos(\psi) + (-0.975z_b + 0.223z_c)\sin(\psi) \\ -z_3 &= 0.223z_b + 0.975z_c \end{aligned} \tag{B.4}$$

Bibliography

[1] Kamihara, Y., Watanabe, T., Hirano, M., and Hosono, H. *Journal of the American chemical society* **130**(11), 3296–3297 (2008).

[2] Torikachvili, M. S., Bud'ko, S. L., Ni, N., and Canfield, P. C. *Phys. Rev. Lett.* **101**(5), 057006 (2008).

[3] Alireza, P. L., Chris Ko, Y. T., Gillett, J., Petrone, C. M., Cole, J. M., Lonzarich, G. G., and Sebastian, S. E. *J. Phys. Condens. Matter* **21**(1), 012208 (2009).

[4] Zaanen, J. *Nature* **457**(7229), 546–547 (2009).

[5] Singh, D. J. and Du, M. H. *Phys. Rev. Lett.* **100**(23), 237003 (2008).

[6] Le Tacon, M., Krisch, M., Bosak, A., Bos, J. W. G., and Margadonna, S. *Phys. Rev. B* **78**(14), 140505 (2008).

[7] Shukla, A., Calandra, M., d'Astuto, M., Lazzeri, M., Mauri, F., Bellin, C., Krisch, M., Karpinski, J., Kazakov, S. M., Jun, J., Daghero, D., and Parlinski, K. *Phys. Rev. Lett.* **90**(9), 095506 (2003).

[8] Baron, A. Q. R., Uchiyama, H., Tanaka, Y., Tsutsui, S., Ishikawa, D., Lee, S., Heid, R., Bohnen, K.-P., Tajima, S., and Ishikawa, T. *Phys. Rev. Lett.* **92**(19), 197004 (2004).

[9] Le Tacon, M., Forrest, T. R., Rüegg, C., Bosak, A., Walters, A. C., Mittal, R., Rønnow, H. M., Zhigadlo, N. D., Katrych, S., Karpinski, J., Hill, J. P., Krisch, M., and McMorrow, D. F. *Phys. Rev. B* **80**(22), 220504 (2009).

[10] Kirmura, T., Goto, T., Shintani, H., Ishizaka, K., Arima, T., and Tokura, Y. *Nature* **426**(6962), 55–58 (2003).

[11] Kirmura, T., Lawes, G., Goto, T., Tokura, Y., and Ramirez, A. *Phys. Rev. B* **71**(22), 224425 (2005).

[12] Kenzelmann, M., Harris, A. B., Jonas, S., Broholm, C., Schefer, J., Kim, S. B., Zhang, C. L., Cheong, S.-W., Vajk, O. P., and Lynn, J. W. *Phys. Rev. Lett* **95**(8), 087206 (2005).

[13] Kajimoto, R., Yoshizawa, H., Shintani, H., Kimura, T., and Tokura, Y. *Phys. Rev. B* **70**(1), 012401 (2004).

[14] Forrest, T. R., Bland, S. R., Wilkins, S. B., Walker, H. C., Beale, T. A. W., Hatton, P. D., Prabhakaran, D., Boothroyd, A. T., Mannix, D., Yakhou, F., and McMorrow, D. F. *J. Phys. Condens. Matter* **20**(42), 422205 (2008).

[15] Wilkins, S. B., Forrest, T. R., Beale, T. A. W., Bland, S. R., Walker, H. C., Mannix, D., Yakhou, F., Prabhakaran, D., Boothroyd, A. T., Hill, J. P., Hatton, P. D., and McMorrow, D. F. *Phys. Rev. Lett.* **103**(20), 207602 (2009).

[16] Feyerherm, R., Dudzik, E., Aliouane, N., and Argyriou, D. N. *Phys. Rev. B* **73**(18), 180401 (2006).

[17] Schierle, E., Soltwisch, V., Schmitz, D., feyerherm, R., Maljuk, A., Yokaichiya, F., Argyriou, D. N., and Weschke, E. *arXiv.org:0910.5663* (2009).

[18] Als-Nielsen, J. and McMorrow, D. *Elements of Modern X-ray Physics*. John Wiley & Sons, (2001).

[19] Blume, M. *Journal of Applied Physics* **57**(8), 3615–3618 (1985).

[20] Platzman, P. M. and Tzoar, N. *Phys. Rev. B* **2**(9), 3556–3559 (1970).

[21] Shull, C. G. and Smart, J. S. *Physical Review* **76**(8), 1256–1257 (1949).

[22] Low, F. E. *Phys. Rev.* **96**(5), 1428–1432 (1954).

[23] Gell-Mann, M. and Goldberger, M. L. *Phys. Rev.* **96**(5), 1433–1438 (1954).

[24] de Bergevin, F. and Brunel, M. *Phys. Lett. A* **39**(2), 141–142 (1972).

[25] de Bergevin, F. and Brunel, M. *Acta Cryst. Sect. A* **37**(3), 314–324 (1981).

[26] Blume, M. and Gibbs, D. *Phys. Rev. B* **37**(4), 1779–1789 (1988).

[27] Hill, J. P. *Magnetic scattering studies of the three dimensional random field Ising model*. PhD thesis, M.I.T., (1992).

[28] Namikawa, K., Ando, M., Nakajima, T., and Kawata, H. *Journal of the physical society of Japan* **54**(11), 4099–4102 (1985).

[29] Zimmermann, M. v., Nelson, C. S., Kim, Y.-J., Hill, J. P., Gibbs, D., Nakao, H., Wakabayashi, Y., Murakami, Y., Tokura, Y., Tomioka, Y., Arima, T., Kao, C.-C., Casa, D., Venkataraman, C., and Gog, T. *Phys. Rev. B* **64**(6), 064411 (2001).

[30] Grenier, S., Hill, J. P., Gibbs, D., Thomas, K. J., v. Zimmermann, M., Nelson, C. S., Kiryukhin, V., Tokura, Y., Tomioka, Y., Casa, D., Gog, T., and Venkataraman, C. *Phys. Rev. B* **69**(13), 134419 (2004).

[31] Wilkins, S. B., Spencer, P. D., Hatton, P. D., Collins, S. P., Roper, M. D., Prabhakaran, D., and Boothroyd, A. T. *Phys. Rev. Lett.* **91**(16), 167205 (2003).

[32] Wilkins, S. B., Caciuffo, R., Detlefs, C., Rebizant, J., Colineau, E., Wastin, F., and Lander, G. H. *Phys. Rev. B* **73**(6), 060406 (2006).

[33] Wilkins, S. B., Stojic, N., Beale, T. A. W., Binggeli, N., Castleton, C. W. M., Bencok, P., Prabhakaran, D., Boothroyd, A. T., Hatton, P. D., and Altarelli, M. *Phys. Rev. B* **71**(24), 245102 (2005).

[34] Rae, A. *Quantum Mechanics*. Institute of Physics Publishing, fourth edition edition, (2002).

[35] Altarelli, M. In *Magnetism: A Synchrotron Radiation Approach,* Beaurepaire, E and Bulou, H and Scheurer, F and Kappler, JP, editor, volume 697 of *Lecture notes in physics*, 201–242, (2006).

[36] Hannon, J. P., Trammell, G. T., Blume, M., and Gibbs, D. *Phys. Rev. Lett.* **61**(10), 1245–1248 (1988).

[37] Trammell, G. T. *Phys. Rev.* **126**(3), 1045–1054 (1962).

[38] Hannon, J. P. and Trammell, G. T. *Phys. Rev.* **186**(2), 306–325 (1969).

[39] Hill, J. P. and McMorrow, D. F. *Acta Cryst. Sect. A* **52**(2), 236–244 (1996).

[40] Gibbs, D., Harshman, D. R., Isaacs, E. D., McWhan, D. B., Mills, D., and Vettier, C. *Phys. Rev. Lett.* **61**(10), 1241–1244 (1988).

[41] Paolasini, L., Detlefs, C., Mazzoli, C., Wilkins, S., Deen, P. P., Bombardi, A., Kernavanois, N., de Bergevin, F., Yakhou, F., Valade, J. P., Breslavetz, I., Fondacaro, A., Pepellin, G., and Bernard, P. *Journal of Synchrotron Radiation* **14**(Part 4), 301–312 (2007).

[42] Mannix, D., McMorrow, D. F., Ewings, R. A., Boothroyd, A. T., Prabhakaran, D., Joly, Y., Janousova, B., Mazzoli, C., Paolasini, L., and Wilkins, S. B. *Phys. Rev. B* **76**(18), 184420 (2007).

[43] Egger, H., Hofmann, W., and Kalus, J. *Applied Physics A, Materials science & processing* **35**(1), 41–45 (1984).

[44] Burkel, E., Peisl, J., and Dorner, B. *Europhys. Lett.* **3**(8), 957–961 (1987).

[45] Dorner, B., Burkel, E., Illini, T., and Peisl, J. *Z. Phys. B: Condens. Matter* **69**(2-3), 179–183 (1987).

[46] Krisch, M. and Sette, F. In *Light scattering in solids IX*, volume 108 of *Topics in applied physics*, 317–369. (2007).

[47] Minutes of the 1955 Annual Meeting Held at New York City, January 27-29, . *Phys. Rev.* **98**(4), 1144–1209 (1955).

[48] Zachariasen, H. *The theory of X-ray diffraction in crystals.* John Wiley and sons, Inc, Hoboken, New Jersey, USA, (1944).

[49] Verbeni, R., Sette, F., Krisch, M., Bergmann, U., Gorges, B., Halcoussis, C., Martel, K., Masciovecchio, C., Ribois, J., Ruocco, G., and Sinn, H. *Journal of Synchrotron radiation* **3**(Part 2), 62–64 (1996).

[50] http://www.esrf.eu/UsersAndScience/Experiments/DynExtrCond/ID28. .

[51] Sette, F., Ruocco, G., Krisch, M., Masciovecchio, C., and Verbeni, R. *Physica Scripta* **T66**, 48–56 (1996).

[52] Zhigadlo, N. D., Katrych, S., Bukowski, Z., Weyeneth, S., Puzniak, R., and Karpinski, J. *J. Phys. Condens. Matter* **20**(34), 342202 (2008).

[53] Kamihara, Y., Hiramatsu, H., Hirano, M., Kawamura, R., Yanagi, H., Kamiya, T., and Hosono, H. *Journal of the American chemical society* **128**(31), 10012–10013 (2006).

[54] Takahashi, H., Igawa, K., Arii, K., Kamihara, Y., Hirano, M., and Hosono, H. *Nature* **453**(7193), 376–378 (2008).

[55] Zhi-An, R., Wei, L., Jie, Y., Wei, Y., Xiao-Li, S., Zheng-Cai, L., Guang-Can, C., Xiao-Li, D., Li-Ling, S., Fang, Z., and Zhong-Xian, Z. *Chinese Physics Letters* **25**(6), 2215–2216 (2008).

[56] Ishida, K., Nakai, Y., and Hosono, H. *J. Phys. Soc. Japan* **78**(6), 062001 (2009).

[57] Ren, Z.-A., Che, G.-C., Dong, X.-L., Yang, J., Lu, W., Yi, W., Shen, X.-L., Li, Z.-C., Sun, L.-L., Zhou, F., and Zhao, Z.-X. *Europhys. Lett.* **83**(1), 17002 (2008).

[58] Ahilan, K., Ning, F. L., Imai, T., Sefat, A. S., Jin, R., McGuire, M. A., Sales, B. C., and Mandrus, D. *Phys. Rev. B* **78**(10), 100501 (2008).

[59] Dong, J., Zhang, H. J., Xu, G., Li, Z., Li, G., Hu, W. Z., Wu, D., Chen, G. F., Dai, X., Luo, J. L., Fang, Z., and Wang, N. L. *Europhys. Lett.* **83**(2), 27006 (2008).

[60] Luetkens, H., Klauss, H. H., Kraken, M., Litterst, F. J., Dellmann, T., Klingeler, R., Hess, C., Khasanov, R., Amato, A., Baines, C., Kosmala, M., Schumann, O. J., Braden, M., Hamann-Borrero, J., Leps, N., Kondrat, A., Behr, G., Werner, J., and Buechner, B. *Nature Materials* **8**(4), 305–309 (2009).

[61] Zhao, J., Huang, Q., de la Cruz, C., Li, S., Lynn, J. W., Chen, Y., Green, M. A., Chen, G. F., Li, G., Li, Z., Luo, J. L., Wang, N. L., and Dai, P. *Nature Materials* **7**(12), 953–959 (2008).

[62] Drew, A. J., Niedermayer, C., Baker, P. J., Pratt, F. L., Blundell, S. J., Lancaster, T., Liu, R. H., Wu, G., Chen, X. H., Watanabe, I., Malik, V. K., Dubroka, A., Roessle, M., Kim, K. W., Baines, C., and Bernhard, C. *Nature Materials* **8**(4), 310–314 (2009).

[63] Welp, U., Xie, R., Koshelev, A. E., Kwok, W. K., Cheng, P., Fang, L., and Wen, H. H. *Phys. Rev. B* **78**(14), 140510 (2008).

[64] Li, P., Balakirev, F. F., and Greene, R. L. *Phys. Rev. B* **75**(17), 172508 (2007).

[65] Yuan, H. Q., Singleton, J., Balakirev, F. F., Baily, S. A., Chen, G. F., Luo, J. L., and Wang, N. L. *Nature* **457**(7229), 565–568 (2009).

[66] Zabolotnyy, V. B., Inosov, D. S., Evtushinsky, D. V., Koitzsch, A., Kordyuk, A. A., Sun, G. L., Park, J. T., Haug, D., Hinkov, V., Boris, A. V., Lin, C. T., Knupfer, M., Yaresko, A. N., Buechner, B., Varykhalov, A., Follath, R., and Borisenko, S. V. *Nature* **457**(7229), 569–572 (2009).

[67] Liu, C., Kondo, T., Palczewski, A. D., Samolyuk, G. D., Lee, Y., Tillman, M. E., Ni, N., Mun, E. D., Gordon, R., Santander-Syro, A. F., Bud'ko, S. L., McChesney, J. L., Rotenberg, E., Fedorov, A. V., Valla, T., Copie, O., Tanatar, M. A., Martin, C., Harmon, B. N., Canfield, P. C., Prozorov, R., Schmalian, J., and Kaminski, A. *Physica C-Superconductivity and its applications* **469**(9-12), 491–497 (2009).

[68] McMillan, W. L. *Physical Review* **167**(2), 331–344 (1968).

[69] Lee, P. A. and Wen, X.-G. *Phys. Rev. B* **78**(14), 144517 (2008).

[70] Si, Q. and Abrahams, E. *Phys. Rev. Lett.* **101**(7), 076401 (2008).

[71] Dai, X., Fang, Z., Zhou, Y., and Zhang, F.-C. *Phys. Rev. Lett.* **101**(5), 057008 (2008).

[72] Christianson, A. D., Goremychkin, E. A., Osborn, R., Rosenkranz, S., Lumsden, M. D., Malliakas, C. D., Todorov, I. S., Claus, H., Chung, D. Y., Kanatzidis, M. G., Bewley, R. I., and Guidi, T. *Nature* **456**(7224), 930–932 (2008).

[73] Lumsden, M. D., Christianson, A. D., Parshall, D., Stone, M. B., Nagler, S. E., MacDougall, G. J., Mook, H. A., Lokshin, K., Egami, T., Abernathy, D. L., Goremychkin, E. A., Osborn, R., McGuire, M. A., Sefat, A. S., Jin, R., Sales, B. C., and Mandrus, D. *Phys. Rev. Lett.* **102**(10), 107005 (2009).

[74] Ding, H., Richard, P., Nakayama, K., Sugawara, K., Arakane, T., Sekiba, Y., Takayama, A., Souma, S., Sato, T., Takahashi, T., Wang, Z., Dai, X., Fang, Z., Chen, G. F., Luo, J. L., and Wang, N. L. *Europhys. Lett.* **83**(4), 47001 (2008).

[75] Kirtley, J., Tsuei, C., Sun, J., Chin, C., Yu-Jahnes, L., Gupta, A., Rupp, M., and Ketchen, M. *Nature* **373**(6511), 225–228 (1995).

[76] Lee, C. H., Iyo, A., Eisaki, H., Kito, H., Fernandez-Diaz, M. T., Ito, T., Kihou, K., Matsuhata, H., Braden, M., and Yamada, K. *J. Phys. Soc. Japan* **77**(8), 083704 (2008).

[77] Mukuda, H., Terasaki, N., Kinouchi, H., Yashima, M., Kitaoka, Y., Suzuki, S., Miyasaka, S., Tajima, S., Miyazawa, K., Shirage, P., Kito, H., Eisaki, H., and Iyo, A. *J. Phys. Soc. Japan* **77**(9), 093704 (2008).

[78] Zhang, C. J., Oyanagi, H., Sun, Z. H., Kamihara, Y., and Hosono, H. *Phys. Rev. B* **78**(21), 214513 (2008).

[79] Liu, R. H., Wu, T., Wu, G., Chen, H., Wang, X. F., Xie, Y. L., Ying, J. J., Yan, Y. J., Li, Q. J., Shi, B. C., Chu, W. S., Wu, Z. Y., and Chen, X. H. *Nature* **459**(7243), 64–67 (2009).

[80] Boeri, L., Dolgov, O. V., and Golubov, A. A. *Phys. Rev. Lett.* **101**(2), 026403 (2008).

[81] Allen, P. B. and Dynes, R. C. *Phys. Rev. B* **12**(3), 905–922 (1975).

[82] Carbotte, J. P. *Rev. Mod. Phys.* **62**, 1027 (1990).

[83] Christianson, A. D., Lumsden, M. D., Delaire, O., Stone, M. B., Abernathy, D. L., McGuire, M. A., Sefat, A. S., Jin, R., Sales, B. C., Mandrus, D., Mun, E. D., Canfield, P. C., Lin, J. Y. Y., Lucas, M., Kresch, M., Keith, J. B., Fultz, B., Goremychkin, E. A., and McQueeney, R. J. *Phys. Rev. Lett.* **101**(15), 157004 (2008).

[84] Mittal, R., Pintschovius, L., Lamago, D., Heid, R., Bohnen, K.-P., Reznik, D., Chaplot, S. L., Su, Y., Kumar, N., Dhar, S. K., Thamizhavel, A., and Brueckel, T. *Phys. Rev. Lett.* **102**(21), 217001 (2009).

[85] Hahn, S. E., Lee, Y., Ni, N., Canfield, P. C., Goldman, A. I., McQueeney, R. J., Harmon, B. N., Alatas, A., Leu, B. M., Alp, E. E., Chung, D. Y., Todorov, I. S., and Kanatzidis, M. G. *Phys. Rev. B* **79**(22), 220511 (2009).

[86] Egami, T., Fine, B., Parshall, D., Subedi, A., and Singh, D. *arXiv.org:0907.2734* (2009).

[87] Ewings, R. A., Boothroyd, A. T., McMorrow, D. F., Mannix, D., Walker, H. C., and Wanklyn, B. M. R. *Phys. Rev. B* **77**(10), 104415 (2008).

[88] Mittal, R., Su, Y., Rols, S., Chatterji, T., Chaplot, S. L., Schober, H., Rotter, M., Johrendt, D., and Brueckel, T. *Phys. Rev. B* **78**(10), 104514 (2008).

[89] Mittal, R., Su, Y., Rols, S., Tegel, M., Chaplot, S. L., Schober, H., Chatterji, T., Johrendt, D., and Brueckel, T. *Phys. Rev. B* **78**(22), 224518 (2008).

[90] Litvinchuk, A. P., Hadjiev, V. G., Iliev, M. N., Lv, B., Guloy, A. M., and Chu, C. W. *Phys. Rev. B* **78**(6), 060503 (2008).

[91] Rahlenbeck, M., Sun, G. L., Sun, D. L., Lin, C. T., Keimer, B., and Ulrich, C. *Phys. Rev. B* **80**(6), 064509 (2009).

[92] Chauviere, L., Gallais, Y., Cazayous, M., Sacuto, A., Measson, M. A., Colson, D., and Forget, A. *Phys. Rev. B* **80**(9), 094504 (2009).

[93] Fukuda, T., Baron, A. Q. R., Shamoto, S.-i., Ishikado, M., Nakamura, H., Machida, M., Uchiyama, H., Tsutsui, S., Iyo, A., Kito, H., Mizuki, J., Arai, M., Eisaki, H., and Hosono, H. *J. Phys. Soc. Japan* **77**(10), 103715 (2008).

[94] Mazin, I. I., Johannes, M. D., Boeri, L., Koepernik, K., and Singh, D. J. *Phys. Rev. B* **78**(8), 085104 (2008).

[95] Zhao, S. C., Hou, D., Wu, Y., Xia, T. L., Zhang, A. M., Chen, G. F., Luo, J. L., Wang, N. L., Wei, J. H., Lu, Z. Y., and Zhang, Q. M. *Science & Technology* **22**(1), 015017 (2009).

[96] Hadjiev, V. G., Iliev, M. N., Sasmal, K., Sun, Y. Y., and Chu, C. W. *Phys. Rev. B* **77**(22), 220505 (2008).

[97] Martinelli, A., Ferretti, M., Manfrinetti, P., Palenzona, A., Tropeano, M., Cimberle, M. R., Ferdeghini, C., Valle, R., Bernini, C., Putti, M., and Siri, A. S. *Superconductor Science and Technology* **21**(9), 095017 (2008).

[98] Noffsinger, J., Louie, G., Cohen, L., and G., F. *Phys. Rev. Lett.* **102**(14), 147003 (2009).

[99] Seber, G. A. F. and Wild, C. J. *Nonlinear Regression.* John Wiley & Sons, (1989).

[100] Marini, C., Mirri, C., Profeta, G., Lupi, S., Di Castro, D., Sopracase, R., Postorino, P., Calvani, P., Perucchi, A., Massidda, S., Tropeano, G. M., Putti, M., Martinelli, A., Palenzona, A., and Dore, P. *Europhys. Lett.* **84**(6), 67013 (2008).

[101] Higashitaniguchi, S., Seto, M., Kitao, S., Kobayashi, Y., Saito, M., Masuda, R., Mitsui, T., Yoda, Y., Kamihara, Y., Hirano, M., and Hosono, H. *Phys. Rev. B* **78**(17), 174507 (2008).

[102] Yin, Z. P., Lebegue, S., Han, M. J., Neal, B. P., Savrasov, S. Y., and Pickett, W. E. *Phys. Rev. Lett.* **101**(4), 047001 (2008).

[103] Yildirim, T. *Physica C-Superconductivity and its applications* **469**(9-12), 425–441 (2009).

[104] Yndurain, F. and Soler, J. M. *Phys. Rev. B* **79**(13), 134506 (2009).

[105] Yaresko, A. N., Liu, G.-Q., Antonov, V. N., and Andersen, O. K. *Phys. Rev. B* **79**(14), 144421 (2009).

[106] Hur, N., Park, S., Sharma, P. A., Ahn, J. S., Guha, S., and Cheong, S.-W. *Nature* **429**(6990), 392–395 (2004).

[107] Schmid, H. *Bulletin of Materials Science* **17**(7), 1411–1414 (1994).

[108] Rontgen, W. C. *Ann. Phys. Chem.* **271**, 264–270 (1888).

[109] Curie, P. *J. Phys. (Paris)* **3**, 393415 (1894).

[110] Maxwell, J. C. *Phil. Trans. R. Soc. Lond.* **155**, 459512 (1865).

[111] Dzyaloshinskii, I. *Soviet Physics JETP* **10**(3), 628–629 (1960).

[112] Astrov, D. *Soviet Physics JETP* **11**(3), 708–709 (1960).

[113] Ascher, E., Rieder, H., Schmid, H., and Stossel, H. *Journal of Applied Physics* **37**(3), 1404–1405 (1966).

[114] Smolenskii, G. A., Agranovskaia, A. I., Popov, S. N., and Isupov, V. A. *Soviet Physics-Technical Physics* **3**(10), 1981–1982 (1958).

[115] Smolenskii, G., Isupov, V., and Agronovskaya, A. *Soviet Physics-Solid State* **1**(1), 150–151 (1959).

[116] Khomskii, D. *Journal of Magnetism and Magnetic Materials* **306**(1), 1–8 (2006).

[117] Wang, J., Neaton, J., Zheng, H., Nagarajan, V., Ogale, S., Liu, B., Viehland, D., Vaithyanathan, V., Schlom, D., Waghmare, U., Spaldin, N., Rabe, K., Wuttig, M., and Ramesh, R. *Science* **299**(5613), 1719–1722 (2003).

[118] Lawes, G., Harris, A. B., Kimura, T., Rogado, N., Cava, R. J., Aharony, A., Entin-Wohlman, O., Yildirim, T., Kenzelmann, M., Broholm, C., and Ramirez, A. P. *Phys. Rev. Lett.* **95**(8), 087205 (2005).

[119] Quezel, S., Tcheou, F., Rossatmignod, J., Quezel, G., and E., R. *Physica B & C* **86**, 916 (1977).

[120] Yamasaki, Y., Sagayama, H., Goto, T., Matsuura, M., Hirota, K., Arima, T., and Tokura, Y. *Phys. Rev. Lett* **98**, 147204 (2007).

[121] Fabrizi, F., Walker, H. C., Paolasini, L., de Bergevin, F., Boothroyd, A. T., Prabhakaran, D., and McMorrow, D. F. *Phys. Rev. Lett.* **102**(23), 237205 (2009).

[122] Aliouane, N., Argyriou, D. N., Strempfer, J., Zegkinoglou, I., Landsgesell, S., and v. Zimmermann, M. *Phys. Rev. B* **73**(2), 020102 (2006).

[123] Arima, T., Goto, T., Yamasaki, Y., Miyasaka, S., Ishii, K., Tsubota, M., Inami, T., Murakami, Y., and Tokura, Y. *Phys. Rev. B* **72**(10), 100102 (2005).

[124] Argyriou, D. N., Aliouane, N., Strempfer, J., Zegkinoglou, I., Bohnenbuck, B., Habicht, K., and v. Zimmermann, M. *Phys. Rev. B* **75**, 020101 (2007).

[125] Blasco, J., Ritter, C., García, J., de Teresa, J. M., Pérez-Cacho, J., and Ibarra, M. R. *Phys. Rev. B* **62**, 5609–5618 (2000).

[126] Yamasaki, Y., Miyasaka, S., Kaneko, Y., He, J.-P., Arima, T., and Tokura, Y. *Phys. Rev. Lett* **96**(20), 207204 (2006).

[127] Voigt, J., Persson, J., Kim, J. W., Bihlmayer, G., and Bruckel, T. *Phys. Rev. B* **76**, 104431 (2007).

[128] Joly, Y. *Phys. Rev. B* **63**(12), 125120 (2001).

[129] Hill, N. *J. Phys. Chem. B* **104**, 6694 (2000).

[130] Cheong, S.-W. and Mostovoy, M. *Nature Materials* **6**, 13 (2007).

[131] Blundell, S. *Magnetism in Condensed Matter*. Oxford University Press, (2001).

[132] Harris, A. B. *Phys. Rev. B* **76**(5), 054447 (2007).

[133] Mostovoy, M. *Phys. Rev. Lett.* **96**(6), 067601 (2006).

[134] Kimura, T. *Annual Review of Materials Research* **37**, 387–413 (2007).

[135] Katsura, H., Nagaosa, N., and Balatsky, A. V. *Phys. Rev. Lett* **95**(5), 057205 (2005).

[136] Jaouen, N., Tonnerre, J., Kapoujian, G., Taunier, P., Roux, J., Raoux, D., and Sirotti, F. *Journal of Synchrotron Radiation* **11**(Part 4), 353–357 (2004).

[137] Thomas, K. J., Hill, J. P., Grenier, S., Kim, Y.-J., Abbamonte, P., Venema, L., Rusydi, A., Tomioka, Y., Tokura, Y., McMorrow, D. F., Sawatzky, G., and van Veenendaal, M. *Phys. Rev. Lett* **92**(23), 237204 (2004).

[138] Langridge, S., Paixao, J., Bernhoeft, N., Vettier, C., Lander, G., Gibbs, D., Sorensen, S., Stunault, A., Wermeille, D., and Talik, E. *Phys. Rev. Lett.* **82**(10), 2187–2190 (1999).

[139] Mirone, A. *arXiv.org:0706.4170* (2007).

[140] Mori, T., Aoki, K., Kamegashira, N., Shishido, T., and Fukuda, T. *Materials Letters* **42**(1), 387–389 (2000).

[141] Strempfer, J., Bohnenbuck, B., Mostovoy, M., Aliouane, N., Argyriou, D. N., Schrettle, F., Hemberger, J., Krimmel, A., and von Zimmermann, M. *Phys. Rev. B* **75**(21), 212402 (2007).

[142] Prokhnenko, O., Feyerherm, R., Dudzik, E., Landsgesell, S., Aliouane, N., Chapon, L. C., and Argyriou, D. N. *Phys. Rev. Lett* **98**, 057206 (2007).

[143] Wilkins, S. B., Stojic, N., Beale, T. A. W., Binggeli, N., Castleton, C. W. M., Bencok, P., Prabhakaran, D., Boothroyd, A. T., Hatton, P. D., and Altarelli, M. *Phys. Rev. B* **71**(24), 245102 (2005).

[144] Rossat-Mignod, J. *Methods of experimental physics, vol. 23, p. 69.* Academic Press, New York, London, (1987).